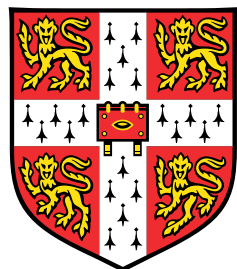


# **Three-dimensional peridynamic modelling of quasi-brittle structural elements**



**Mark Christopher Hobbs**

Department of Engineering  
University of Cambridge

This dissertation is submitted for the degree of  
*Doctor of Philosophy*

Christ's College

May 2021



## **Declaration**

I hereby declare that except where specific reference is made to the work of others, the contents of this dissertation are original and have not been submitted in whole or in part for consideration for any other degree or qualification in this, or any other university. This dissertation is my own work and contains nothing which is the outcome of work done in collaboration with others, except as specified in the text and Acknowledgements. This dissertation contains fewer than 65,000 words including appendices, bibliography, footnotes, tables and equations and has fewer than 150 figures.

Mark Christopher Hobbs  
May 2021



## Acknowledgements

I would like to begin by thanking my supervisor, Dr John Orr, for his advice and encouragement during my research. I am grateful that John gave me the freedom to take this project in any direction that I wished to do so. I would also like to thank Dr David Miranda for guiding me at the start of my PhD journey. Without his advice and help, my progress during the first year would have likely been much slower.

I wish to express my deepest gratitude to Dr Gabriel Hattori, who has always been available to provide excellent advice and guidance on a wide range of topics. Gabriel has answered my many questions without complaint, and I am incredibly thankful for his support and friendship.

I must also thank the EPSRC Centre for Future Infrastructure and Built Environment for funding this research and providing a supportive environment to develop as a researcher and make lifelong friendships. Particular thanks must go to Dr Rod Lynch.

I am indebted to Ben Boys for his excellent work during his fourth year project and subsequent efforts. Ben has undoubtedly laid the foundation for my future research.

I have thoroughly enjoyed my time in Cambridge, and I am grateful to friends outside of the engineering department, particularly at Christ's College and those that I have met through sport. Outside of Cambridge, I would like to thank my family and close friends for their unwavering support. Finally, I would like to thank Jasmin for everything she does for me.



## Abstract

The peridynamic theory provides a promising theoretical framework for developing robust numerical models capable of simulating the complex fracture processes in quasi-brittle materials. However, there is a lack of detailed validation studies in the literature, and significant work remains to quantify the predictive accuracy and generality of a peridynamic model.

This thesis presents the development and validation of a three-dimensional bond-based peridynamic framework for modelling quasi-brittle structural elements. By following a rigorous validation process and carefully selecting validation problems that test a wide range of fundamental behaviours, a robust examination of the model is provided, and new insights into the capabilities of the bond-based model are gained.

This thesis begins with an examination of existing constitutive laws and a new non-linear softening model is introduced. Predictions with the newly proposed non-linear model improve upon existing laws. In an attempt to explain the cause of discrepancies between experimental and numerical results, it was determined that the application of surface correction factors increases the energy required to produce a fracture surface. This is the first time that this effect has been described, and a correction scheme is proposed that is simple to implement and yields improved results.

It is demonstrated that a bond-based peridynamic model can accurately capture the size effect in quasi-brittle materials. This is the first time that a peridynamic model has been used to examine the size effect and provides an important check on the validity of the numerical model. The thesis ends with an examination of the predictive accuracy and generality of the model against nine reinforced concrete beams that exhibit a wide range of failure modes. The shear-span-to-depth ratio is systematically varied from 1 to 8 to facilitate a study of different load-transfer mechanisms and failure modes. This is the first study to rigorously validate the predictive capability of a peridynamic model against a series of problems.

The model is validated using published experimental data, and the predictive accuracy is equivalent to well-established numerical methods whilst offering several benefits that justify further research and development.



# Table of contents

<b>List of figures</b>	<b>xv</b>
<b>List of tables</b>	<b>xix</b>
<b>Nomenclature</b>	<b>xxi</b>
<b>1 Introduction</b>	<b>1</b>
1.1 Background . . . . .	1
1.2 Problem statement . . . . .	4
1.3 Aims and objectives . . . . .	5
1.4 Outline of thesis . . . . .	5
<b>2 Literature review</b>	<b>7</b>
2.1 Quasi-brittle materials . . . . .	7
2.1.1 Load-deformation response . . . . .	8
2.1.2 Fracture process zone . . . . .	8
2.1.3 Structural size effect . . . . .	10
2.1.4 Modes of fracture . . . . .	11
2.1.5 Fracture models . . . . .	11
2.2 Reinforced concrete . . . . .	12
2.2.1 Flexural failure . . . . .	12
2.2.2 Shear failure . . . . .	13
2.2.3 Limitations of empirical design codes . . . . .	15
2.3 Numerical methods . . . . .	17
2.3.1 Discontinuous approaches . . . . .	18
2.3.2 Continuous approaches . . . . .	19
2.3.3 Lattice and particle models . . . . .	22
2.3.4 Summary of numerical methods . . . . .	22
2.4 Peridynamics . . . . .	23

2.4.1	Development of peridynamics for quasi-brittle materials . . . . .	24
2.4.2	Research gaps . . . . .	24
2.5	Validation . . . . .	30
2.5.1	Validation hierarchy . . . . .	30
2.5.2	Validation metrics . . . . .	32
2.5.3	Model validation procedure . . . . .	32
2.6	Summary . . . . .	33
<b>3</b>	<b>Peridynamic theory of solid mechanics</b>	<b>35</b>
3.1	Introduction . . . . .	35
3.2	Bond-based peridynamic theory . . . . .	37
3.2.1	Peridynamic continuum model . . . . .	37
3.2.2	Constitutive model . . . . .	40
3.2.3	Damping . . . . .	47
3.3	State-based peridynamic theory . . . . .	48
3.4	Constitutive laws . . . . .	50
3.5	Non-locality . . . . .	50
3.5.1	Origins of non-locality . . . . .	50
3.5.2	Physical meaning of the horizon . . . . .	52
<b>4</b>	<b>Numerical solution method</b>	<b>53</b>
4.1	Introduction . . . . .	53
4.2	Spatial integration . . . . .	54
4.2.1	Spatial discretisation . . . . .	55
4.2.2	Volume correction . . . . .	56
4.2.3	Horizon, grid resolution, and numerical convergence . . . . .	58
4.3	Explicit time integration . . . . .	60
4.3.1	Euler-Cromer scheme . . . . .	61
4.3.2	Numerical stability . . . . .	62
4.3.3	Quasi-static analysis . . . . .	63
4.4	Boundary conditions . . . . .	65
4.4.1	Force boundary condition . . . . .	66
4.4.2	Displacement boundary condition . . . . .	66
4.5	Surface correction factors . . . . .	67
4.5.1	Volume correction method . . . . .	68
4.6	Implicit time integration . . . . .	69
4.6.1	Static formulation . . . . .	69

4.6.2	Local and global stiffness matrix . . . . .	70
4.6.3	Solution procedure . . . . .	72
4.7	Reducing computational expense . . . . .	75
4.7.1	Parallel processing . . . . .	75
4.7.2	Family member search and data structures . . . . .	76
4.8	Code structure . . . . .	77
4.8.1	Input module . . . . .	77
4.8.2	Core computational kernel . . . . .	77
4.8.3	Post-processing module . . . . .	78
<b>5</b>	<b>Modelling of quasi-brittle materials</b>	<b>81</b>
5.1	Introduction . . . . .	81
5.2	Failure process . . . . .	82
5.3	Constitutive laws . . . . .	83
5.3.1	Linear . . . . .	84
5.3.2	Bilinear . . . . .	85
5.3.3	Trilinear . . . . .	87
5.3.4	Non-linear . . . . .	90
5.3.5	Concrete fracture energy . . . . .	93
5.3.6	Summary . . . . .	93
5.4	Comparison of constitutive laws . . . . .	94
5.4.1	Validation problem . . . . .	94
5.4.2	Results . . . . .	96
5.5	Critical stretch corrections . . . . .	100
5.5.1	The problem . . . . .	100
5.5.2	Integration accuracy in three-dimensions . . . . .	102
5.5.3	Numerical examination of discrete fracture energy . . . . .	106
5.5.4	Critical stretch correction scheme . . . . .	110
5.5.5	Results . . . . .	111
5.6	Mesh sensitivity study . . . . .	113
5.7	Examination of damage energy dissipation . . . . .	116
5.8	Mixed-mode problem . . . . .	120
5.9	Discussion and future work . . . . .	125
5.10	Conclusions . . . . .	126

<b>6 Size effect</b>	<b>129</b>
6.1 Introduction . . . . .	129
6.2 Structural size effect . . . . .	130
6.2.1 What is size effect? . . . . .	130
6.2.2 Size effect mechanisms . . . . .	130
6.2.3 Size effect laws . . . . .	131
6.2.4 Numerical methods . . . . .	133
6.3 Numerical framework . . . . .	134
6.4 Mode I problem . . . . .	134
6.4.1 Results: notched cases . . . . .	136
6.4.2 Results: unnotched case . . . . .	137
6.4.3 Energy dissipation . . . . .	142
6.5 Mixed-mode problem . . . . .	143
6.5.1 Results . . . . .	144
6.6 Discussion and future work . . . . .	148
6.6.1 Spatial variability of material properties . . . . .	148
6.6.2 Load path following . . . . .	149
6.6.3 Localisation limiter . . . . .	150
6.6.4 Additional comments . . . . .	150
6.7 Conclusions . . . . .	151
<b>7 Shear failure</b>	<b>153</b>
7.1 Introduction . . . . .	153
7.2 Numerical framework . . . . .	154
7.2.1 Steel constitutive model . . . . .	154
7.2.2 Interface constitutive model . . . . .	155
7.3 Model validation . . . . .	156
7.3.1 Stuttgart shear tests . . . . .	157
7.3.2 Results . . . . .	161
7.4 Discussion . . . . .	171
7.4.1 Shear-transfer actions . . . . .	171
7.4.2 Loading system . . . . .	175
7.4.3 Discretisation . . . . .	176
7.4.4 Material parameters . . . . .	176
7.4.5 Comparison with design codes . . . . .	177
7.4.6 Importance of further validation . . . . .	177
7.4.7 Summary . . . . .	178

7.5 Conclusions . . . . .	179
<b>8 Conclusions and future work</b>	<b>181</b>
8.1 Conclusions . . . . .	181
8.1.1 Constitutive model . . . . .	181
8.1.2 Mode I and mixed-mode fracture . . . . .	182
8.1.3 Size effect . . . . .	182
8.1.4 Shear strength . . . . .	183
8.1.5 Mesh sensitivity . . . . .	184
8.1.6 Physical meaning of the horizon . . . . .	185
8.1.7 Critical stretch corrections . . . . .	186
8.2 Future work . . . . .	186
8.3 A comment on the importance of validation . . . . .	189
<b>References</b>	<b>191</b>
<b>Appendix A Code performance</b>	<b>209</b>



# List of figures

1.1	Number of citations per year for the original paper of Silling [203] . . . . .	3
2.1	Stress-strain response: (a) perfectly brittle material, (b) quasi-brittle material.	8
2.2	Fracture process zone in a quasi-brittle material. . . . .	9
2.3	Fracture modes . . . . .	11
2.4	Cohesive crack model . . . . .	12
2.5	Flexural and shear failure . . . . .	12
2.6	Typical four-point bending test setup . . . . .	14
2.7	Shear transfer actions . . . . .	14
3.1	Stress tensor in a continuous solid . . . . .	36
3.2	Peridynamic continuum and kinematics of particle pair and bond-based pairwise force function . . . . .	37
3.3	Constitutive model . . . . .	40
3.4	A three-dimensional body subjected to isotropic expansion. . . . .	42
3.5	A three-dimensional body subjected to simple shear. . . . .	43
3.6	Schematic of a constant influence function for a two-dimensional peridynamic model . . . . .	44
3.7	Influence functions . . . . .	45
3.8	Schematic of the energy release rate $G_0$ computation . . . . .	47
3.9	State based peridynamic model . . . . .	49
3.10	Schematic of bond based, ordinary, and non-ordinary material response .	50
4.1	Horizon of node $\mathbf{x}_i$ in the discretised configuration . . . . .	55
4.2	Regular and irregular mesh . . . . .	56
4.3	Spatial integration . . . . .	56
4.4	Volume correction . . . . .	57
4.5	Volume correction factor $v_c$ against distance . . . . .	58
4.6	$m$ -convergence and $\delta$ -convergence . . . . .	59

4.7	Influence of the local damping coefficient on the convergence speed . . . . .	64
4.8	Applied displacement against time . . . . .	65
4.9	Development of a contact surface . . . . .	67
4.10	Material point horizons . . . . .	67
4.11	Schematic to illustrate the computation of surface correction factors. . . . .	69
4.12	Sparsity structure of the global stiffness matrix $[\mathbf{K}]_{global}$ . . . . .	71
4.13	Implicit scheme with load-control . . . . .	74
4.14	Quasi-static explicit solver with displacement-controlled loading . . . . .	79
5.1	Tensile stress-strain curve for concrete . . . . .	83
5.2	Linear damage model ( $f$ - $s$ ) . . . . .	84
5.3	Bilinear damage model ( $f$ - $s$ ) . . . . .	85
5.4	Trilinear damage model ( $f$ - $s$ ) . . . . .	87
5.5	Bilinear tension softening constitutive law ( $\sigma$ - $w$ ) . . . . .	87
5.6	Non-linear damage model ( $f$ - $s$ ) . . . . .	90
5.7	Non-linear tension softening constitutive law ( $\sigma$ - $w$ ) . . . . .	91
5.8	Schematic of the experimental setup - mode I fracture tests . . . . .	95
5.9	Load-CMOD response for Beam 4 ( $d = 50$ mm): unnotched, fifth-notched, and half-notched . . . . .	96
5.10	Comparison of load-CMOD results predicted using different constitutive laws	99
5.11	Load-CMOD response for the unnotched beam ( $d = 50$ mm) using a trilinear constitutive law with and without surface correction factors. . . . .	102
5.12	$m$ -convergence of the discrete volume approximation . . . . .	103
5.13	$m$ -convergence of the discrete strain energy density approximation . . . . .	104
5.14	Comparison of micro-modulus functions: (a) constant influence function; (b) triangular influence function (conical) . . . . .	104
5.15	$m$ -convergence of the discrete strain energy density approximation using a conical influence function . . . . .	106
5.16	Discretised unit cube . . . . .	107
5.17	Bonds that cross the theoretical unit fracture surface within a unit cube . .	108
5.18	$5\text{m} \times 5\text{m} \times 5\text{m}$ cube . . . . .	108
5.19	Bonds that cross the theoretical unit fracture surface centred within a $5\text{m} \times 5\text{m} \times 5\text{m}$ cube . . . . .	109
5.20	Bonds that cross a theoretical fracture surface at the edge of a peridynamic body . . . . .	109
5.21	Load-CMOD results with critical stretch corrections . . . . .	112
5.22	Mesh sensitivity study . . . . .	114

5.23	Numerical fracture path . . . . .	115
5.24	Numerical softening damage . . . . .	117
5.25	Region of damage energy dissipation at peak load . . . . .	119
5.26	Numerical fracture process zone . . . . .	120
5.27	Schematic of the experimental setup - mixed-mode fracture tests . . . . .	121
5.28	Load-CMOD response for the mixed mode fracture tests . . . . .	122
5.29	3D crack paths for the mixed-mode fracture tests . . . . .	123
5.30	Numerical softening damage for the mixed-mode fracture tests . . . . .	124
5.31	Experimental and numerical crack paths for the mixed-mode fracture tests .	124
6.1	Size effect laws in a log-log scale: (a) Type 1 (unnotched case); (b) Type 2 (notched case) . . . . .	132
6.2	Numerical softening damage for the half-notched specimens . . . . .	137
6.3	Load-CMOD response for the mode I fracture tests . . . . .	140
6.4	Nominal strength versus depth (characteristic dimension) for the mode I fracture tests . . . . .	141
6.5	Region of damage energy dissipation at peak load for unnotched members .	143
6.6	Numerical softening damage for notch eccentricity $\mu d = 0.3125d$ . . . . .	145
6.7	Numerical softening damage for notch eccentricity $\mu d = 0.625d$ . . . . .	145
6.8	Experimental and numerical crack paths for the mixed mode fracture tests ( $d = 160\text{mm}$ ) . . . . .	146
6.9	Experimental and numerical crack paths for the mixed mode fracture tests ( $d = 320\text{mm}$ ) . . . . .	146
6.10	Load-CMOD response for the mixed-mode fracture tests . . . . .	147
7.1	Microplastic model ( $f$ - $s$ ) . . . . .	155
7.2	Kani's shear valley . . . . .	158
7.3	Experimental setup - Stuttgart shear tests . . . . .	159
7.4	Discretised cross-section . . . . .	160
7.5	Failure behaviour in beams tested by Leonhardt and Walther [135] . . . . .	161
7.6	Shear force and moment at failure against $a_v/d$ . . . . .	163
7.7	Numerical fracture pattern at failure using the normal mesh . . . . .	163
7.8	Numerical fracture pattern at failure for Beam 3, 5, and 7 using the fine mesh	164
7.9	Beam 3 load-displacement curve ( $a_v/d = 2$ ) . . . . .	166
7.10	Beam 5 load-displacement curve ( $a_v/d = 3$ ) . . . . .	168
7.11	Beam 7 load-displacement curve ( $a_v/d = 5$ ) . . . . .	170
7.12	Fracture paths in Beam 7 using the fine mesh . . . . .	170

7.13 Deformed shape of Beam 7 at failure . . . . .	170
7.14 Principal compressive strain distribution in Beam 1 . . . . .	173
7.15 Comparison of experimental and numerical load-displacement curves . . . .	178

# List of tables

2.1	Review of the development of peridynamics for quasi-brittle materials . . . . .	26
3.1	Influence functions $\omega$ and their corresponding constant $c$ for a three-dimensional peridynamic material . . . . .	45
5.1	Constitutive model parameters. Refer to Table 5.2 for a summary of the constitutive equations. . . . .	97
5.2	Constitutive equations . . . . .	97
5.3	Width of the region of damage energy dissipation at peak load (mm) . . . . .	118
6.1	Member dimensions . . . . .	136
6.2	Width of the region of damage energy dissipation at peak load (mm). Mesh resolution $\Delta x = 5$ mm. . . . .	142
7.1	Stuttgart Shear Tests - experimental parameters . . . . .	159
7.2	Simulation Parameters. Stretch is a dimensionless scalar. . . . .	160
7.3	Comparison of experimental results, design code predictions, and numerical predictions . . . . .	162
A.1	Input file data . . . . .	210



# Nomenclature

## General

$\ddot{\mathbf{u}}$	Acceleration
$\dot{\mathbf{u}}$	Velocity
$\varepsilon$	Strain
$\lambda$	Lame's elastic constant
$\mathcal{R}$	Spatial region
$\nabla$	Divergence operator
$\rho$	Density
$\rho$	Reinforcement ratio
$\sigma$	Stress
$\sigma_n$	Nominal strength
$\mathbf{u}$	Displacement
$a_v$	Shear span
$d$	Beam depth
$E$	Elastic modulus
$f_c$	Compressive strength
$f_t$	Tensile strength
$G$	Shear modulus

$G_F$	Material fracture energy
$G_f$	Initial fracture energy
$k$	Bulk modulus
$t$	Time
$\nu$	Poisson's ratio
$w$	Crack width
$W_{CCM}$	Strain energy density - classical theory

**Peridynamic Theory**

$\alpha$	Volume correction factor
$\eta$	Relative deformed vector ( $\eta_1, \eta_2, \eta_3$ )
$\xi$	Initial relative position vector ( $\xi_1, \xi_2, \xi_3$ )
$\Delta t$	Time step
$\Delta x$	Mesh resolution
$\delta$	Horizon radius
$\lambda$	Bond stiffening factor
$\mathcal{H}_x$	Neighbourhood of material point $x$ (particle family)
$\mu$	History dependent scalar
$\omega$	Influence function
$\Phi$	Total macroelastic energy
$\mathbf{b}$	Body force per unit volume
$\mathbf{f}$	Pairwise force function
$\mathbf{x}$	Material point
$\underline{\mathbf{F}}$	Deformation state
$\underline{\mathbf{T}}$	Force state

---

$\varphi$	Damage
$C$	Damping coefficient
$c$	Micromodulus (bond stiffness)
$c_d$	Damaged bond stiffness
$d$	Softening parameter
$f$	Scalar bond force
$G_0$	Peridynamic energy release rate
$s$	Stretch
$s_0$	Linear elastic limit
$s_c$	Critical stretch
$V$	Volume
$w$	Micropotential
$W_x$	Macroelastic energy density
$W_{PD}$	Strain energy density - peridynamic theory

### Acronyms / Abbreviations

<i>fib</i>	Fédération internationale du béton – International Federation for Structural Concrete
ACI	American Concrete Institute
ADR	Adaptive Dynamic Relaxation
CMOD	Crack Mouth Opening Displacement
CPU	Central Processing Unit
CSC	Compressed Sparse Column format
CSCT	Critical Shear Crack Theory
CZM	Cohesive Zone Model

EC2	Eurocode 2
FA	Full Area
FEA	Finite Element Analysis
FEM	Finite Element Method
FPZ	Fracture Process Zone
GPU	Graphics Processing Unit
HPC	High Performance Computing
HPX	High Performance ParallelX
LAMMPS	Large-scale Atomic/Molecular Massively Parallel Simulator
LEFM	Linear Elastic Fracture Mechanics
MCFT	Modified Compression Field Theory
MPI	Message Passing Interface
OpenCL	Open Computing Language
OpenMP	Open Multi-Processing application programming interface
PA	Partial Area
PMB	Prototype Microelastic Brittle model
RC	Reinforced Concrete
ULS	Ultimate Limit State

# **Chapter 1**

## **Introduction**

### **1.1 Background**

#### **Over-design**

There is a pressing need to address the over-design of reinforced concrete structures. The utilisation of structural concrete members is often low, and structural material wastage in the order of 50% is common [170]. There is significant scope for reducing material usage and associated carbon emissions by combining smarter structural design with innovative construction methods. Concrete structural elements are predominantly prismatic (cross-sectional area is constant along the member length). The reasons are twofold: (1) prismatic reinforced concrete members are simple and economical to construct, and (2) decades of experimental work has provided a comprehensive understanding of their behaviour. Using innovative construction methods, such as fabric formwork, it is possible to design and build efficient non-prismatic concrete members that use up to 40% less concrete than prismatic members of equivalent strength [171]. These material savings have been achieved by creating structural members whose geometry reflects the requirements of their loading envelope. The potential benefits of using more efficient structural forms are clear but the available analysis tools dictate the possible designs. Accurate analysis methods are crucial to ensuring the safety and reliability of highly efficient structural members.

#### **Shear design**

Predicting the shear capacity of reinforced concrete members is notoriously difficult and codified design methods are generally based on empirical formulas derived from the testing of prismatic beams. Non-prismatic members fall outside of conventional design codes and current methods for determining their structural response and ultimate limit state (ULS)

behaviour are inadequate. These difficulties have been highlighted in a number of papers. Rombach et al. [193] investigated the shear design of prismatic concrete members without shear reinforcement and compared results from existing experimental shear databases to design codes and numerical models. The authors concluded that no consistent mechanical model exists for the design of reinforced concrete members without shear reinforcement. There are large discrepancies between experimental results and analytical models, indicating that existing approaches for shear design have a large amount of uncertainty. In an earlier paper, Rombach and Nghiep [192], investigated the shear design of variable depth beams (haunched beams) and noted that there was only a very limited number of investigations conducted regarding the shear capacity of variable depth beams. Orr et al. [172] further investigated the shear behaviour of non-prismatic beams, testing nineteen beams designed using three different approaches. The results showed that the assumptions made in some design codes can lead to unconservative predictions of shear strength for non-prismatic members.

Shear failure is typically a sudden brittle failure, underlying the importance of correctly predicting the load carrying capacity and failure mechanism [84]. As our understanding of shear behaviour in reinforced concrete has improved, it has become clear that older structures do not always conform with modern standards. Extensions to the functional lifespan of a structure and increased loading requirements necessitate accurate structural assessments.

It is crucial for the safety and serviceability of reinforced concrete structures that reliable design models are available. Empirical approaches lack generality and are only applicable to the range of problems for which they were developed. Numerical models offer higher flexibility and can overcome the severe limitations of empirical methods.

## Numerical methods

A wide range of numerical methods are available for modelling the failure behaviour of reinforced concrete members. Computational approaches for modelling fracture can be broadly divided into three categories: discrete crack models, smeared crack models (continuum damage mechanics), and lattice and particle models. It is difficult to determine the leading method due to a lack of validation studies that methodically examine a range of failure modes.

Collins et al. [54] presented a difficult benchmark problem to evaluate the blind predictive accuracy of reinforced concrete models. Engineers were invited to predict the shear strength of a very deep beam and 66 entries were received from academia and industry. The overall winner of the contest used a smeared crack approach and a fracture mechanics-based cohesive crack model, implemented in the commercial finite element code ATENA. The shear strength

predicted by the winner was 745 kN, and the experimental value was 685 kN, a prediction error of +9%. Červenka et al. [225] provide further details of the winning model. Shear strength predictions from the 66 participants were evenly distributed from 250 kN to 3773 kN, further demonstrating the challenge of predicting shear strength. Whilst numerical models have been applied successfully, accurately predicting the load capacity and failure mode for complex reinforced concrete members remains an open problem. Robust numerical models, capable of accurately capturing the structural behaviour of reinforced concrete elements of any geometry, under any loading condition are still needed.

## Peridynamics

The peridynamic theory of solid mechanics, introduced by Silling [203] in 2000, provides a promising theoretical framework for developing robust numerical models capable of simulating the complex failure behaviour of quasi-brittle materials and structures. There has been a growing interest and recognition of the potential of the peridynamic theory as it provides a powerful framework for capturing a wide range of constitutive responses, and damage and fracture are an emergent property of the theory. Fig. 1.1 illustrates the exponential growth in interest in peridynamics from the research community and industry.

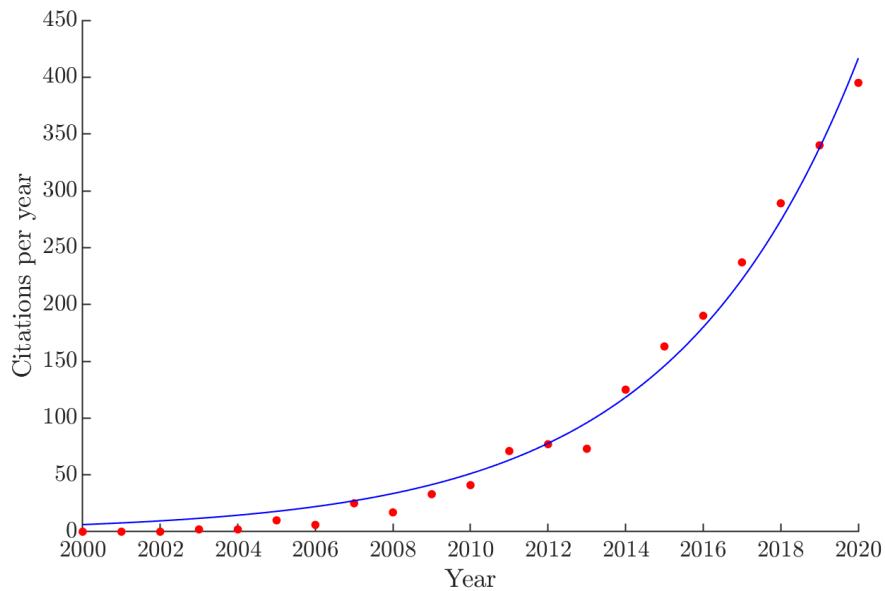


Fig. 1.1 Number of citations per year for the original paper of Silling [203]. The fitted curve is an exponential function.

Peridynamic models possess a number of advantageous features for modelling the failure of quasi-brittle materials:

1. The peridynamic theory replaces the partial differential equations of the classical theory of solid mechanics with integral equations. The governing equations do not require a spatially continuous and differentiable displacement field and damage localisation and fracture naturally emerge. No additional assumptions or techniques are required for modelling damage and fracture.
2. The classical theory assumes that all forces are contact forces that act across zero distance (local theory). The peridynamic theory is a non-local theory in which material points interact with each other directly over finite distances. The failure of quasi-brittle materials is characterised by the accumulation of damage over a significant volume of material before localising into a discontinuity that generally propagates along a complex three-dimensional path. The fracture of quasi-brittle materials is a process in which non-locality is known to be important [17].
3. The fundamental feature of any model capable of correctly capturing the structural size effect is the presence of some form of characteristic length (length scale) [18].
4. Non-planar three-dimensional crack paths are captured with ease. This is important when considering complex problems such as reinforced slabs.
5. A key advantage of using a bond-based peridynamic model is the simplicity of the constitutive model. In a standard continuum-based framework, constitutive models generally require numerous parameters that have no physical basis and must be determined using a calibration procedure.

Significant work remains to quantify the confidence and predictive accuracy of peridynamic models. Diehl et al. [69] reviewed benchmark experiments for the validation of peridynamic models. They identified 39 publications that compare numerical predictions from peridynamic simulations against experimental data and there were only four examples of benchmark tests that addressed the behaviour of concrete. Furthermore, Diehl notes that the majority of papers calibrate model parameters against a single experiment and only a few addressed further validation. The lack of robust validation studies is a concern that is limiting the application of peridynamic models.

## 1.2 Problem statement

Accurately predicting the response and load capacity of reinforced concrete structural elements remains an open challenge. Existing design practices rely on empirical formulas and

large safety factors. This approach will not be sufficient to meet the demands of ambitious design targets that aim to minimise material usage. Improving material efficiency through smarter design is recognised as a key strategy for reducing carbon emissions [4].

Improving material utilisation requires accurate analysis methods to ensure the safety and reliability of efficient structures. Progress is hindered by a lack of models that are sufficiently general to tackle the design of novel structural forms. The peridynamic theory provides a promising theoretical framework for developing robust numerical models capable of simulating the complex fracture processes in quasi-brittle materials. However, there is a lack of detailed validation studies in the literature and significant work remains to quantify the confidence and predictive accuracy of peridynamic models.

### 1.3 Aims and objectives

The aim of this thesis is to develop a three-dimensional bond-based peridynamic framework for modelling quasi-brittle structural elements and to quantify the predictive accuracy of the model by employing a thorough validation procedure. The predictive capabilities and generality of the bond-based peridynamic model have yet to be examined in detail. The objectives are to:

1. Validate the developed numerical framework against experimental data and compare results with advanced numerical methods.
2. Carefully select experimental tests that provide a robust examination of the model and deliver new insights into the capabilities and deficiencies of the peridynamic model.
3. Quantify the predictive accuracy of existing constitutive laws. If existing laws are found to be unsatisfactory, develop a new constitutive model that can accurately predict the behaviour of quasi-brittle materials.

### 1.4 Outline of thesis

**Chapter 2** reviews the relevant literature and establishes the context in which this work was conceived. The limitations of empirical design codes and existing numerical methods are detailed before reviewing the development of peridynamics for quasi-brittle materials and structures.

**Chapter 3** presents the peridynamic theory. The bond-based peridynamic theory is the main focus of the chapter and the state-based theory is briefly reviewed. A detailed examination of the origins of non-locality is provided.

**Chapter 4** describes the development of a three-dimensional bond-based peridynamic code. The implementation details are examined and all choices are explained.

**Chapter 5** examines the modelling of quasi-brittle materials using a three-dimensional bond-based peridynamic model. Existing constitutive laws are examined and compared, and a new non-linear softening law is introduced. Numerical results are compared with experimental data and advanced numerical methods. In addition, it is shown that the application of surface correction factors produces a toughening effect and a correction scheme is proposed that is simple to implement and yields improved results.

**Chapter 6** examines size effect in quasi-brittle materials. This is the first time that the capability of a peridynamic model to capture size effect has been investigated.

**Chapter 7** examines the predictive accuracy and generality of the model against nine reinforced concrete beams that exhibit a wide range of failure modes. The shear-span-to-depth ratio is systematically varied from 1 to 8 to facilitate a study of different load-transfer mechanisms and failure modes.

**Chapter 8** presents the main conclusions that can be drawn from this thesis and future work is proposed to build upon the findings of this project.

# Chapter 2

## Literature review

This chapter establishes the context of the research. The first section provides a review of the fundamentals of failure in quasi-brittle materials. This is followed by an examination of reinforced concrete structures. The limitations of empirical design codes are discussed before reviewing existing numerical methods. The deficiencies of existing numerical methods are detailed, and the need for new approaches becomes apparent. The peridynamic theory is then briefly introduced before reviewing the development of peridynamics for quasi-brittle materials and structures. Clear research gaps are identified, and the chapter concludes by examining concepts of model calibration and validation and defining the essential features of a robust validation procedure.

### 2.1 Quasi-brittle materials

This chapter begins with a review of the fundamentals of failure in quasi-brittle materials. Examples of quasi-brittle materials include concrete, rocks, ceramics, graphite, ice, bone and wood [21]. The primary focus of this work is on concrete structures but the developed numerical framework is applicable to any material that exhibits quasi-brittle behaviour.

Quasi-brittle structures are defined by the following: (1) failure is caused by fracture rather than plastic yield, and (2) the fracture front is surrounded by a large fracture process zone in which progressive distributed cracking or other damage takes place [15]. A further definition is provided by Bažant [18]: quasi-brittle materials are those that obey on a small scale the theory of plasticity (or strength theory), characterised by material strength or yield limit  $\sigma_y$ , and on a large scale the theory of linear elastic fracture mechanics, characterised by fracture energy  $G_f$ .

For a comprehensive review of fracture in quasi-brittle materials, the reader is referred to [154, 14, 79].

### 2.1.1 Load-deformation response

For a perfectly brittle material, the stress-strain curve is linear elastic and no permanent damage occurs up until the maximum stress is reached and a fracture forms (as illustrated in Fig. 2.1(a)). For a quasi-brittle material, the stress-strain relationship is characterised by non-linearities that occur before the peak load is reached and strain softening behaviour in the post-peak stage (as illustrated in Fig. 2.1(b)).

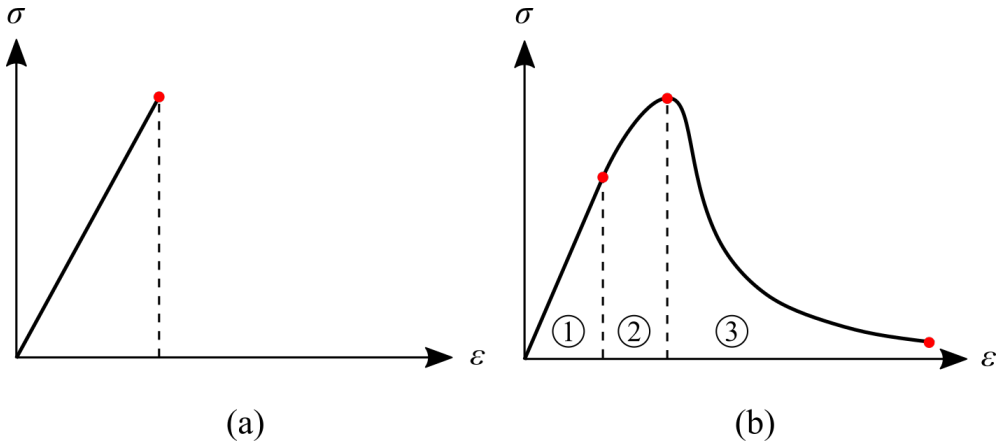


Fig. 2.1 Stress-strain response: (a) perfectly brittle material, (b) quasi-brittle material.

The mechanical behaviour of quasi-brittle materials can be divided into three distinct stages: (1) linear elastic behaviour, (2) development of distributed micro-cracking, and (3) localisation of damage and formation of macroscopic cracks [179]. During the initial stages of loading, the behaviour is linear elastic and there is no permanent damage. Upon unloading, the material will return to its original stress-free state. As the applied load is increased, the stress-strain response becomes non-linear. The non-linearities are a result of the development and growth of micro-cracks. At the peak load, distributed micro-cracks coalesce and localise into a single dominant macro-crack. The post-peak response exhibits strain-softening behaviour, where the stress gradually decreases as the deformation of the specimen increases.

### 2.1.2 Fracture process zone

When a fracture initiates and begins to propagate, the elastic strain energy stored in the structure is consumed by the fracture propagation. In quasi-brittle materials, energy is dissipated in a non-linear zone of micro-cracking that forms at the fracture front (as illustrated in Fig. 2.2). This damage zone is known as the fracture process zone (FPZ). The area of damage can extend well ahead of the discontinuity, and in some cases the size of the damage

zone is comparable to the structural size. There is no rigorous definition of the fracture process zone, but Otsuka and Date [175] define the fracture process zone as the region of the specimen inside which 95% of the total fracture energy is dissipated. This definition is generally accepted.

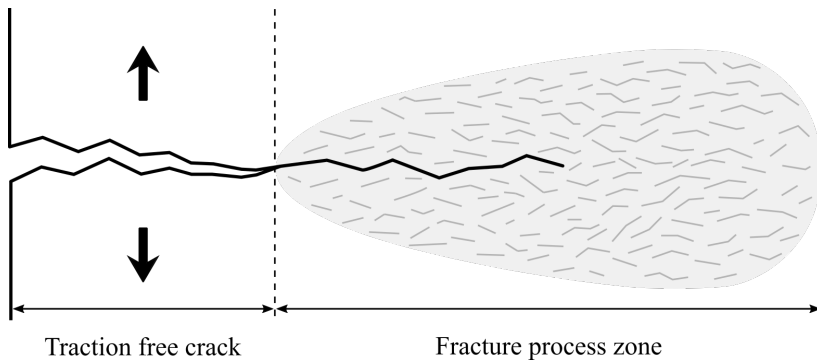


Fig. 2.2 Fracture process zone in a quasi-brittle material.

In heterogeneous materials, such as concrete, micro-cracking is a result of local stress concentrations that occur due to the complex and disordered nature of the microstructure. The size of the damage zone is related to the size of material inhomogeneities [18]. As the loading is increased, the micro-cracks coalesce and form a dominant macro-crack. The strain softening behaviour is a result of the growth and interaction of micro-cracks.

The formation and size of the fracture process zone has been studied extensively using experimental techniques, such as: X-ray imaging, acoustic emission analysis, scanning electron microscopy, and digital image correlation [175, 99, 106, 73]. Studying the development of the fracture process zone is difficult due to the small scale at which micro-cracking occurs and numerical methods have been used to understand the underlying mechanics. Examples include the work of Grassl et al. [96] and Benkemoun et al. [26].

Developing analytical models of fracture in quasi-brittle materials is difficult due to the simultaneous growth and interaction of many micro-cracks. Zhao et al. [245] recently introduced a micro-mechanics approach that can describe the transition from distributed damage to localisation in quasi-brittle materials. Analytical solutions of complete stress-strain curves were obtained for triaxial compression tests and the results are in good agreement with experimental data. Understanding the formation and evolution of the fracture process zone in quasi-brittle materials still remains an open problem.

### 2.1.3 Structural size effect

Strength-of-materials theories assume that failure occurs when a maximum stress is exceeded in a structure, and the limiting stress can be determined from small scale tests on representative material samples. Uniaxial tension, uniaxial compression and flexural tests are used to establish the limiting stress for different loading conditions. This simplistic view does not suffice for quasi-brittle materials [154].

Quasi-brittle materials exhibit a size effect. According to strength-of-materials theories, the maximum stress that a material can resist is independent of size when geometrically similar specimens are considered. Any deviation from predictions made using stress failure criteria is known as the structural size effect. The maximum stress that a quasi-brittle material can resist deviates significantly from predictions made using stress failure criteria, and large specimens fail at significantly lower stresses than small specimens.

There are two primary sources of size effect in quasi-brittle materials [14]: (1) release of stored energy (deterministic size effect), and (2) statistical variability in material properties (statistical size effect). The release of stored energy is by far the most important factor influencing the size effect on structural strength, and the statistical size effect is of secondary importance. The deterministic size effect is governed by the size of the fracture process zone (zone of energy dissipation) relative to the size of the structure. The statistical size effect is a result of the randomness of material properties and defects. The probability that a specimen contains a defect from which failure will initiate increases as the size of the specimen increases.

Understanding the structural size effect is essential for safe predictions of load capacity. The design of large scale structures relies on the properties of quasi-brittle materials measured in small scale laboratory tests. These properties must be extrapolated to structures that are one or two orders of magnitude larger than laboratory tests. Full scale tests are prohibitively expensive and reliable models that can capture structural size effect are needed. Accurately capturing the size effect is of utmost importance for the design of efficient structural forms with small margins of safety. Existing analytical formulas for predicting size effect in geometrically similar structures are extremely limited, and they generally employ empirical parameters that must be determined through best-fit procedures [155]. This section has been condensed to highlight the main features of structural size effect. A detailed review and examination of size effect is provided in Chapter 6.

### 2.1.4 Modes of fracture

In fracture mechanics, three modes of fracture are defined: normal (mode I), in-plane shear (mode II), and out-of-plane shear (mode III), as illustrated in Fig. 2.3. Tensile fracture (mode I) is by far the most common form of fracture observed in concrete and can in some cases occur in its pure form. Mode II and III fracture rarely occur in their pure form and some researchers have questioned the existence of pure mode II and III fracture [154]. Modes of failure are often a combination of the basic fracture modes and mixed-mode I and II fracture (a combination of tension and shear) is a common failure mode.

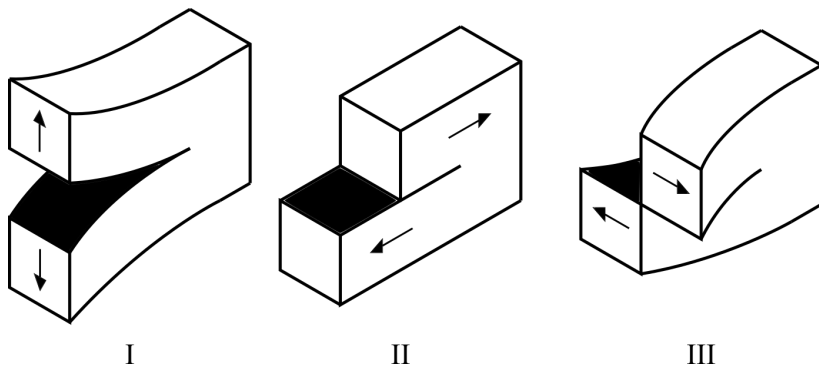


Fig. 2.3 Three principle fracture modes: normal (mode I), in-plane shear (mode II), and out-of-plane shear (mode III).

### 2.1.5 Fracture models

It has been well known since the early 1970s that the theory of linear elastic fracture mechanics (LEFM) is not suitable for modelling quasi-brittle materials. The LEFM theory has been developed under the assumption that the size of the fracture process zone is negligible. This assumption does not hold true for the vast majority of quasi-brittle structures, and LEFM is only valid for very large structures where the size of the fracture process zone is negligible, such as a concrete arch or gravity dam.

In 1976, Hillerborg et al. [113] made a major advance in concrete fracture modelling through the introduction of the cohesive crack model (illustrated in Fig. 2.4). The concept is relatively simple. The tensile stress-strain response of concrete is characterised by softening behaviour after the peak strength has been exceeded. This means that a crack is not immediately stress free after the tensile strength has been reached and there is a stress component that acts perpendicular to the crack face. The value of this stress component ( $\sigma$ ) is related to the crack width ( $w$ ) and gradually decreases as the crack width increases. For a detailed review of concrete fracture models, the reader is referred to the work of Bažant [10].

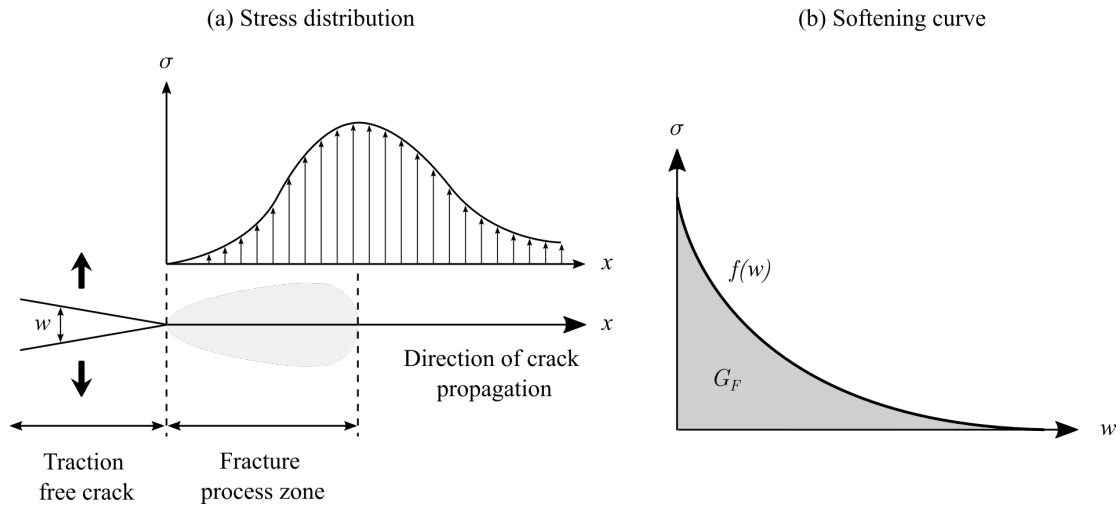


Fig. 2.4 Schematic of the cohesive zone at the crack tip and the traction-separation law ( $\sigma$ - $w$  relationship)

## 2.2 Reinforced concrete

The aim of this section is to provide a short overview of reinforced concrete failure modes and to make clear the limitations of design codes that rely on empirical methods. At the end of this section, the reader should appreciate the need for numerical models to aid the design of new efficient structural forms.

There are two common types of failure in reinforced concrete beams: flexural failure and shear failure (as illustrated in Fig. 2.5).

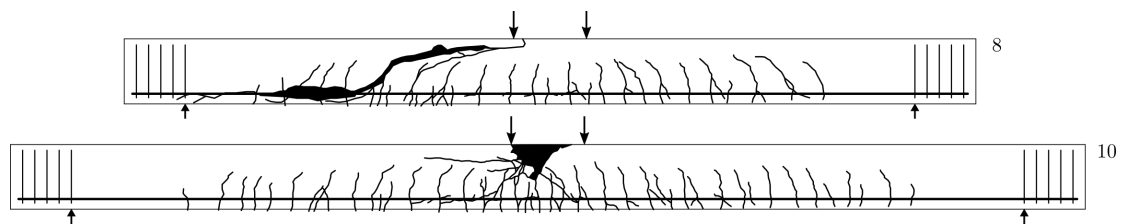


Fig. 2.5 Beam 8 and 10 from the Stuttgart shear tests [135]. Beam 8 fails in shear, and the failure behaviour is characterised by the formation of a diagonal shear crack. Beam 10 fails in flexure, and the failure behaviour is characterised by the crushing failure of concrete.

### 2.2.1 Flexural failure

Flexural failure of a reinforced concrete beam is characterised by ductile behaviour and large deflections. Flexural failure is desirable because it gives ample warning prior to structural

collapse. Narrow flexural cracks develop well before the ultimate load is reached, and if proper bond is provided, the steel and concrete will attain the same strain. As additional loading is applied, the width and length of the flexural cracks will gradually increase, and the area of the compression zone will decrease. This behaviour will become more pronounced after yielding of the reinforcing steel. The area of the compression zone will continue to decrease, and the compressive stresses will eventually reach a level where crushing failure of the concrete occurs [129].

The flexural behaviour of reinforced concrete members is well understood and the ultimate flexural strength (moment capacity) can be accurately predicted using analytical methods based on simplified rectangular stress blocks. The equivalent stress block introduced in 1937 by Whitney [229] forms the basis of modern design codes. Failure loads predicted by analytical methods match closely with experimental results and predictions of flexural strength with different design codes differ by no more than 10% [27]. See the work of Wu [231] for a review of theorems for flexural design of reinforced concrete members.

### 2.2.2 Shear failure

Shear failure of a reinforced concrete beam is characterised by small deflections and poor ductility. The longitudinal steel reinforcing bars do not reach the yielding strain and sudden collapse occurs upon the rapid development of a diagonal shear crack. Shear failure is highly undesirable, as it occurs suddenly with little to no prior warning of collapse (brittle failure). The sudden brittle nature of shear failure underlies the importance of correctly predicting the load carrying capacity and failure mechanism [84].

The shear behaviour of reinforced concrete members is much more complex than flexural behaviour and predictions of shear strength rely on empirical methods that lack a robust theoretical basis [55]. There is no consensus on the relational theory between shear capacity and the many influencing parameters. This uncertainty is highlighted by the variability that exists within different design codes. Bentz et al. [27] state that predictions of ultimate shear strength can vary by a factor of more than two when using different design codes, whilst the flexural strength predicted by the same codes does not vary by more than 10%.

Codified shear design procedures, such as Eurocode 2 (EC2) [43] and ACI 318-19 [2], use empirical formulas that have been determined by statistical regression of experimental data. Researchers have tested thousands of prismatic beams without web reinforcement (shear reinforcement) over a range of variables and the results have been used to determine empirical equations for calculating shear strength. Web reinforcement is generally ignored so that the fundamental shear-transfer actions can be studied. A typical four-point bending test setup is illustrated in Fig. 2.6. Four-point bending tests have the advantage of combining

two different loading conditions, pure bending between the applied loads, and constant shear force in the end sections [132]. For details of experimental databases, the reader is referred to the work of Bažant et al. [25] and Hattori et al. [108].

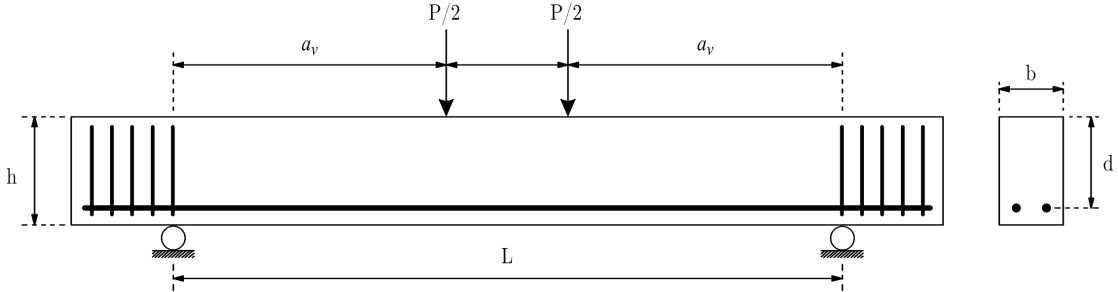


Fig. 2.6 Typical four-point bending test setup

### Shear-transfer mechanisms

The ultimate shear capacity is governed by the combined resistance to shear force offered by (1) arch or direct strut action, (2) the uncracked compressive zone, (3) aggregate interlock, (4) dowel action, and (5) the residual tensile strength in the fracture process zone. The free-body diagram shown in Fig. 2.7, illustrates the shear-transfer mechanisms in a reinforced concrete member without web reinforcement.

The existence of the different shear-transfer actions is generally agreed upon but the contribution of each action is still a matter of debate. The contribution of each action to the overall shear resistance is related to parameters such as shear span, beam depth, and reinforcement ratio. A number of recent papers have examined the contribution of the various shear-transfer actions in members without web reinforcement [46, 47, 119, 121, 111].

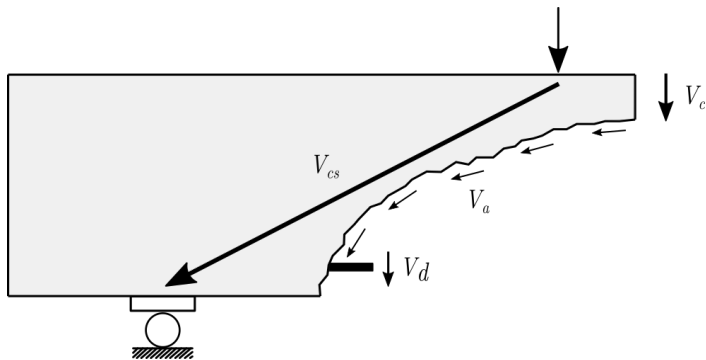


Fig. 2.7 Shear transfer actions in a reinforced concrete member: compressive strut  $V_{cs}$ , uncracked compressive zone  $V_c$ , aggregate interlock  $V_a$ , dowel actions  $V_d$ .

### Parameters that influence shear strength

There are multiple parameters that influence the shear strength of a reinforced concrete beam, such as: shear span  $a_v$ , beam depth  $d$ , concrete compressive strength  $f_c$ , reinforcement ratio  $\rho$ , and aggregate size.

Extensive testing has shown that the mode of shear failure is primarily dependent on the shear-span-to-depth ratio  $a_v/d$ , this is sometimes referred to as the shear slenderness. Kani [128] proved experimentally that the load transfer behaviour changes at a value of  $a_v/d$  approximately equal to 2.5. If the value of  $a_v/d$  is less than 2.5, beams develop an internal arch and shear capacity increases. For values of  $a_v/d$  greater than 2.5 and less than 6, arch action is negligible and sudden and brittle failure in diagonal tension is expected. Full flexural capacity is obtained for values of  $a_v/d$  greater than 6. The observations of Kani [128] were supported by experimental data from Leonhardt and Walther [135]. The exact value of  $a_v/d$  at which load transfer behaviour changes is dependent on the concrete compressive strength  $f_c$  and the reinforcement ratio  $\rho$ . Chapter 7 provides further details on the influence of  $a_v/d$  and includes detailed descriptions of the distinct shear failure modes.

Size effect has a significant influence on shear capacity. Bažant et al. [25] provided justification for incorporating size effect into the ACI code provisions for shear design of reinforced concrete beams. They demonstrated that predictions of shear capacity with different design codes did not show major differences for small beams but extrapolation to large beams resulted in very significant disagreements. Furthermore, predictions were unconservative and in some instances, design codes overpredicted shear strength by a factor of 2 or more. Size effect is deemed to be of major importance for beams deeper than approximately 1 m. Experimental data on beams of this size is limited, yet they are reasonably common in industrial applications.

The bond-slip behaviour at the steel-concrete interface also plays an important role for short beams ( $a_v/d < 2.5$ ), where arch action is dominant. Fenwick and Pauley [81] found that arch action can only occur at the expense of slip (complete loss of bond transfer). Arch action enhances the shear resistance of an unbonded beam beyond that of a bonded beam but also increases deflection. Accurately determining the structural response and shear capacity of a reinforced concrete member requires a clear understanding of the interface behaviour.

#### 2.2.3 Limitations of empirical design codes

Extending the scope of empirical equations beyond the verified range of parameters can result in unconservative predictions of shear strength. Non-prismatic members fall outside of conventional design codes and current methods for determining their structural response and

ultimate limit state (ULS) behaviour are inadequate. Rombach and Nghiep [192], investigated the shear design of variable depth beams (haunched beams) and noted that there was only a very limited number of investigations conducted regarding the shear capacity of beams with variable cross-sections. Orr et al. [172] further investigated the shear behaviour of non-prismatic RC beams, testing nineteen beams designed using three different approaches. The results showed that the assumptions made in some design codes can lead to unconservative predictions of shear strength for non-prismatic members.

To assess the ability of engineers to accurately estimate the structural response and shear strength of deep beam, Collins et al. [54] tested a 4 m deep beam and invited industry and academics to provide predictions. Based on ACI 318, the magnitude of the load at shear failure was predicted to be 2505 kN. The actual failure load was 685 kN. The ACI code prediction was approximately 3.7 times higher than the experimental value. EC2 also significantly overestimated the shear capacity of the beam; the magnitude of the load at shear failure was predicted to be 1351 kN. Traditional codified design methods can seriously overestimate the load capacity of members that are beyond the scope of empirical equations.

As our understanding of shear behaviour in reinforced concrete has improved, it has become clear that older structures do not always conform with modern standards. Many existing structures have far less shear reinforcement than that required by modern codes [111]. Extensions to the functional lifespan of a structure and increased loading requirements necessitate accurate structural assessments. It is crucial for the safety and serviceability of reinforced concrete structures that reliable design models are available.

The inadequacy of empirical methods has prompted the development of numerous theoretical approaches: variable angle truss model, strut-and-tie model [148, 149], critical shear crack theory (CSCT) [160, 161], and modified compression field theory (MCFT) [226]. The reader is referred to [121, 111, 84] for a review of state of the art shear strength models. The Canadian CSA A23.3-14 standard [60] is based on the modified compression field theory. The CSA code provides a conservative prediction of shear strength for the deep beam tested by Collins et al. [54]; the predicted shear capacity is 620 kN. This is within the ‘gold standard’ prediction range of  $\pm 10\%$ . In general, theoretical approaches are more reliable than empirical procedures, but the accuracy is dependent on various assumptions and there is still no widely agreed upon mechanical model to describe shear behaviour. It is possible that no such model will ever be discovered.

A need exists for a rational and general approach that can be applied to a wide range of problems that fall outside the scope of codified design methods. The importance of correctly predicting the load carrying capacity and failure mechanism of reinforced concrete structural elements is obvious due to the sudden and potentially catastrophic nature of shear failure.

The need for new approaches is becoming more pressing as the demand for new efficient structural forms grows. Numerical models offer higher flexibility and can overcome the severe limitations of empirical methods.

## 2.3 Numerical methods

Accurately modelling the initiation and propagation of fracture remains a long-standing problem in computational mechanics. The fundamental problem is the disagreement that arises between a fracture (spatial discontinuity) and the governing partial differential equations of solid mechanics that require a spatially continuous and differentiable displacement field.

Any numerical method based on the classical governing equations will require additional methods for modelling fracture behaviour. A successful technique can capture the initiation, direction, and velocity of a fracture and requires two essential elements:

1. The means of including fracture in the discretised continuum
2. The criterion for fracture initiation and growth (constitutive model)

Numerical modelling of fracture in quasi-brittle materials began in the late 1960s, with the seminal papers of Ngo and Scordelis [164] and Rashid [184], in which the discrete and smeared crack models were first introduced. A wide range of related approaches now exist for modelling quasi-brittle materials. Approaches for modelling fracture in quasi-brittle materials can broadly be categorised into three groups: continuous crack models, discontinuous crack models, and lattice and particle models.

Continuous and discontinuous crack models are extensions of the finite element method. Continuous approaches, such as the smeared crack model, modify the material properties of damaged areas. The stress-strain relationship of a solid element is modified to account for the degradation in stiffness that occurs when a material fractures. Discontinuous approaches, such as the discrete crack model, model cracks directly via a displacement-discontinuity at the interface of solid elements. A crack is assumed to form when the force normal to the element boundaries exceeds the maximum tensile strength. Lattice element models are a class of discrete models, in which the solid body is represented as a truss like assembly of discrete one-dimensional solid elements. Discrete particle models are another class of discrete model that simulate concrete at the meso-scale by modelling the interaction of adjacent coarse aggregates.

A brief and non-exhaustive review is provided of the most common methods for modelling fracture in quasi-brittle materials. The reader is referred to the work of Rabczuk [182] and

Mauludin and Oucif [150] for detailed reviews. Slobbe [211] provides a detailed review of the modelling of concrete fracture within the context of standard finite element approaches.

### 2.3.1 Discontinuous approaches

The discrete crack approach was first introduced in 1967 by Ngo and Scordelis [164]. The aim of the discrete crack model is to simulate the initiation and propagation of dominant cracks. The discrete crack approach alters the geometry of the solid continuum so that fractures can be modelled on the continuum boundary. A fracture is formed by separating mesh elements that previously shared a common edge. Cracking is assumed to occur when the nodal force that is normal to the element boundaries exceeds the maximum allowable tensile force. There is a resultant change in nodal connectivity at every stage of fracture propagation. This constant remeshing is time consuming and computationally expensive. A major improvement to the discrete crack approach was the introduction of automatic remeshing [120].

The initiation and propagation of fracture requires the provision of double-nodes along element edges (interface elements) that coincide with the fracture path. This requires knowledge of the expected fracture path and is generally based on experimental data or previous simulations. The need to define crack locations before analysis begins is a major limitation. Another option is to double all nodes initially and only nodes close to the fracture path will separate. This method is generally avoided as additional nodes increase computational expense. The discrete crack approach suffers from a mesh bias, as the fracture trajectory is constrained to following element boundaries.

In early work, the second essential element (the criterion for fracture initiation and direction of growth) was based on the theory of linear elastic fracture mechanics (LEFM). When the tensile stress normal to the element boundaries exceeded the maximum allowable tensile force, the elements would separate, and the direction of fracture propagation was assumed to be normal to that of the principal stress [10]. Plain concrete is not a perfectly brittle material and LEFM was shown to be inadequate for capturing the correct stress-strain characteristics of concrete [36].

This led to the introduction of the cohesive crack model (also known as the fictitious crack model) by Hillerborg et al. [113]. The cohesive crack model captures the progressive softening behaviour ahead of the crack tip in the fracture process zone (FPZ). The model is based on the hypothesis that the three-dimensional behaviour of a finite fracture process zone can be approximated by a unique one-dimensional decreasing function relating the crack opening displacement  $w$  (separation of crack faces) to the crack bridging stress  $\sigma$  at the crack tip [18]. The relationship between the crack bridging stress and the crack opening

displacement is often referred to as a traction-separation law. The cohesive zone model was originally developed for simulating mode I fracture but has been extended to account for mixed-mode fracture [102]. The simulation of mixed-mode cracks requires constant remeshing and the use of material parameters that are difficult to determine experimentally (mode II fracture energy).

Discontinuous approaches (such as the cohesive crack model) have a number of serious limitations: (1) The cohesive crack model is a uniaxial model and can not capture the triaxial stresses in the fracture process zone. The cohesive crack model is adequate for simple mode I problems, such as a notched beam, but is not suitable for more general problems where triaxial stress states arise. (2) Modelling a crack as an ideal straight line is not physically consistent. In reality, energy dissipation does not occur on the crack line, and actually occurs over a wide zone at the fracture front. (3) Extending from two to three-dimensions is difficult. (4) Discontinuous approaches are not well suited to modelling problems with multiple arbitrarily evolving cracks. The explicit tracking of fracture surfaces can become unmanageable for non-planar three-dimensional fracture problems. (5) External criteria are required to determine when and where a crack initiates, the speed of crack propagation, the direction of crack propagation, and to determine when crack branching occurs.

Discontinuous approaches, such as the cohesive crack model, model cracks directly via a displacement-discontinuity at the interface of solid elements. Discontinuous approaches require constant remeshing and refinement as a crack propagates. Additional approaches have been developed to model discontinuities in the displacement field, for example: the strong discontinuity approach [168, 169], and the extended finite element method [156]. The issues outlined above still exist and examples of application to complex three-dimensional problems are limited. The reader is referred to the work of Rabczuk [182] for further details. Due to the limitations of discontinuous approaches, adoption has been limited. Smeared approaches, discussed next, overcome many of the aforementioned limitations.

### 2.3.2 Continuous approaches

#### Smeared crack model

The smeared crack model was first introduced in 1968 by Rashid [184] and overcame many of the limitations of the discrete crack approach. The smeared crack approach does not alter the geometry of the continuum, but instead alters the material properties of damaged areas. The stress-strain relationship of an element is modified to account for the degradation in stiffness that occurs when solid bodies fracture.

A major advantage of a smeared approach over the cohesive crack model is the ability to model triaxial stress states in the FPZ [10]. Many constitutive models that can capture the stress-strain behaviour of concrete have been developed and applied within the framework of a smeared crack model, and Červenka et al. [223] provide a brief overview of these models. The simplest model assumes that failure occurs when the maximum principal stress in an element reaches the tensile strength of the material. For more complex triaxial stress states, models such as that introduced by Červenka and Papanikolaou [222] and Grassl et al. [97] can be used. These models combine fracture and plasticity models to describe the tensile and compressive behaviour of concrete. The direction of damage evolution can be modelled by degrading the Young's modulus  $E$  in the direction of the major principal stress [36].

Vorel et al. [228] recently compared four state of the art concrete constitutive models in a standard continuum-based framework. The average number of model parameters is 25, and many of these parameters have no credible justification. The complexity of continuum-based constitutive models is considered to be a weakness.

The primary shortcoming of the smeared crack approach is the strong dependence on mesh resolution and orientation. The spatial discretisation influences the numerical results: load-deflection response and crack paths. When using a material model with strain softening, strain localises in a band a single element wide and propagates along continuous mesh lines [38]. As the mesh resolution is refined the volume of the damage zone will approach zero. The energy dissipation will also tend to zero, and this results in a severe mesh dependence.

The crack band model was proposed by Bažant and Oh [12] to fix the problems of mesh sensitivity. The crack band approach, is essentially the smeared representation of the cohesive zone model. Mesh dependent behaviour is corrected by modifying the softening law so that the energy dissipated in a single mesh element is equal to a given value that depends upon the material fracture energy  $G_F$  and a material characteristic length  $l_c$  [48]. The concept of a material characteristic length is somewhat ambiguous and this will be discussed throughout this work. Note that a crack band model prevents zero energy dissipation upon refinement, but damage localisation still occurs in a single row of elements, even if the size of the elements becomes infinitely small [211]. The crack band model applied within the framework of a smeared crack model has become the standard approach for the modelling of fracture in concrete and reinforced concrete elements [223].

The crack band model solved the issue of mesh sensitivity when strain localises in a single band of elements and the mesh is aligned with the direction of crack propagation. But for more general cases, where the crack direction is not aligned with the mesh, the predicted crack paths still suffer from directional mesh bias [211]. Reliable predictions of structural

response, load capacity, and failure mechanisms for quasi-brittle structures are hindered by directional bias.

The crack band model does not fully resolve the fundamental difficulty of using a strain softening constitutive model and still suffers from mesh dependency, as demonstrated by Xenos and Grassl [232]. This is due to the loss of ellipticity in the governing partial differential equations induced by strain localisation (discontinuous deformation gradients). A number of models have been proposed to solve the aforementioned issues. These methods are collectively referred to as enriched, higher-order or regularised continuum models. Regularisation techniques introduce a characteristic length into the constitutive model, that enforces a minimum width of the strain localisation band (localisation limiters). Discontinuities are represented by smooth displacement and strain fields, and the loss of ellipticity induced by strain localisation is prevented. Examples of regularised continuum models include: nonlocal models [180, 124, 21], gradient-enhanced models [178, 39], viscous models [162, 212], and phase-field models [40, 153]. The reader is referred to the work of Slobbe [211] for a detailed review and discussion of smeared models and mesh dependence.

### **Reinforced concrete applications**

A smeared approach is more physically realistic for reinforced problems where damage is distributed [196]. Due to the heterogeneity of concrete and the presence of reinforcement, damage (micro-cracking) develops over a wide area subjected to high tensile stress. As the loading is increased, damage localises and multiple cracks form. Distinct from discontinuous approaches, smeared approaches capture the development of damage over a wide region [37].

The crack band model is the most successful approach for modelling the non-linear failure behaviour of reinforced concrete structures. Collins et al. [54] presented a difficult benchmark problem to evaluate the blind predictive accuracy of reinforced concrete models. The shear strength prediction submitted by Červenka Consulting was deemed to be the best of 66 participants with a simulation error of +9%. Červenka et al. [225] provide details of the winning crack band model. The model uses the combined fracture-plasticity constitutive model introduced by Červenka and Papanikolaou [222].

Červenka et al. [225] recognised that there were significant uncertainties in their winning numerical model and the final failure load was sensitive to the chosen model parameters. A parameter sensitivity study found that the uncertainty of the strength prediction was between -23% and +28%. Collins et al. [54] specified a ‘gold standard’ prediction range of  $\pm 10\%$ . The parameter sensitivity study of Červenka et al. [225] displayed much higher variability due to model and material uncertainties. Accurately predicting the shear strength of reinforced concrete elements remains an open problem.

### 2.3.3 Lattice and particle models

Discrete models are well suited for modelling the meso-structure of concrete. Lattice element models are a class of discrete models, in which the solid body is represented as a truss like assembly of discrete one-dimensional solid elements. Lattice based model have seen extensive interest from researchers for the modelling of fracture in quasi-brittle materials. Schlangen and van Mier [199] introduced a simple lattice model and modelled the concrete meso-structure by assigning different material properties to individual beam elements. Grassl et al. [96] demonstrated the predictive capabilities of lattice element models by accurately modelling the fracture process zone in concrete beams of different sizes. This approach requires a very high mesh resolution and is prohibitively computationally expensive for larger problems. A less computationally demanding approach was proposed by Bažant et al. [23]. Each node corresponds to the centre of an aggregate particle and neighbouring particles interact through axial interactions. This method is not capable of accurately modelling the fracture process zone in quasi-brittle materials.

Discrete particle models are another class of discrete model that simulate concrete at the meso-scale by modelling the interaction of adjacent coarse aggregates. Zubelewicz and Bažant [249] introduced a two-dimensional model that represents concrete as a system of rigid particles of various sizes that are separated by interface layers that are described by a force-displacement relation for the normal and tangential components. Cusatis et al. [62, 61] later introduced the improved lattice discrete particle model (LDPM). This models accounts for the three-dimensional rotation of particles, which can cause shearing and bending at aggregate interfaces. Eliáš et al. [75] and Eliáš and Vorechovský [74] have demonstrated the potential of this model by simulating a series of concrete beams in three-point bending, and examining the predicted fracture process zone and the probability distribution of the load capacity. The predicted results were in good agreement with experimental data.

The use of discrete models is mostly limited to plain concrete and there are very few studies that examine reinforced concrete problems. Aydin et al. [6] recently simulated the response of reinforced concrete members using a two-dimensional lattice element mode. The numerical results were in reasonable agreement with experimental data but significant work remains to validate this approach.

### 2.3.4 Summary of numerical methods

The crack band model in a smeared crack framework is by far the most popular and successful approach for modelling the non-linear behaviour of quasi-brittle materials and structures [223]. However, there are still numerous issues with smeared approaches, such as mesh

dependency and the use of complex constitutive models. Plus, damage localisation occurs in a single row of elements, even if the size of the elements becomes infinitely small. This is not physically consistent. In addition, the practical application of numerical models to real problems remains low due to the lack of comprehensive and robust validation studies. This view is supported by Vorel et al. [228].

The limitations of existing methods are a result of the mathematical deficiencies of the governing partial differential equations. Silling [203] proposed a non-local theory of solid mechanics, known as the peridynamic theory, that is formulated in terms of integral equations rather than partial differential equations. The governing equations do not require a spatially continuous and differentiable displacement field and damage localisation and fracture naturally emerge. The development of peridynamics for quasi-brittle materials is examined in the following section.

## 2.4 Peridynamics

Silling [203] proposed a non-local theory of solid mechanics, known as the peridynamic theory, that is formulated in terms of integral equations rather than partial differential equations. The governing equations do not require a spatially continuous and differentiable displacement field and damage localisation and fracture naturally emerge. To make a distinction between the peridynamic theory and other non-local theories, note that most non-local theories average some measure of strain within a neighbourhood of a material particle. The peridynamic theory dispenses with the concept of strain, which by its definition, requires the evaluation of partial derivatives of displacement [207].

There are two primary formulations of the peridynamic theory: bond-based [203] and state based theory [208]. In the original bond-based theory, the Poisson's ratio is limited to a fixed value. Silling et al. [208] later introduced a generalised state-based theory that overcomes the limitations of the original theory. The peridynamic theory is well established and has been successfully applied to a wide range of material failure problems. For a review of the peridynamic theory and its major applications, the reader is referred to the work of Javili et al. [122]. Chapter 3 and 4 provide a detailed treatment of the peridynamic formulation and its numerical solution.

This thesis focusses on bond-based peridynamics. It is a deliberate choice not to consider the more complex state-based theory and there are a number of reasons that justify this choice: (1) The simplest model should be examined first. Only if the model is found to be deficient should the complexity be increased. (2) The developed numerical framework serves as a good baseline from which to measure any improvements obtained from more sophisticated

models. (3) It is reasonable to trade off small improvements in predictive accuracy for the need to retain simplicity. (4) Bond-based models are computationally cheaper.

### 2.4.1 Development of peridynamics for quasi-brittle materials

This section provides a brief review of the development of peridynamics for quasi-brittle materials. The peridynamic theory provides a promising theoretical framework for developing robust numerical models capable of simulating the complex fracture processes in quasi-brittle materials. However, there is a lack of detailed validation studies in the literature and significant work remains to quantify the confidence and predictive accuracy of peridynamic models.

Table 2.1 presents a summary of the development of peridynamics for quasi-brittle materials. The list contained in the table is not exhaustive and there is a focus on foundational papers and more recent developments. The following points are considered to provide structure to the review: (1) model details - peridynamic formulation and constitutive model used, (2) benchmark problems - tests used to evaluate model accuracy, (3) validation metrics - how is the predictive accuracy quantified?

The reader is referred to Hattori et al. [108] for a detailed review of the development of peridynamics for reinforced concrete structures. Hattori provides further examples of works that use the state-based theory. Zhou and Wang [247] also provide a state-of-the-art review on the application of peridynamics to geomaterials. There are clear gaps in the existing literature and these are discussed in the next section.

### 2.4.2 Research gaps

There are relatively few papers that compare numerical results against experimental data, and when a comparison is made, the majority of papers calibrate model parameters against a single experiment, and only a few provide further validation. Diehl et al. [69] provided a review of benchmark experiments for the validation of peridynamic models and noted the same issue. The lack of robust validation studies is a concern that is limiting the application of peridynamic models. The following research gaps have been identified:

1. The vast majority of papers rely on qualitative validation and the predictive accuracy of the bond-based peridynamic model remains an open question. To quantify the predictive accuracy of a model, a robust validation procedure must be employed. The key elements of model validation are defined and discussed in section 2.5.

2. The vast majority of papers only consider two-dimensional models. Two-dimensional models are not adequate for complex reinforced problems, and three-dimensional models should be employed. Using a two-dimensional model, Sau et al. [198] found that predicted crack paths in a reinforced concrete beam were halted by reinforcing bars, but associated experimental data showed that the cracks should propagate around the bars.
3. A comparative study to quantify the predictive accuracy of existing constitutive laws for modelling quasi-brittle materials is needed. From the literature review, it is evident that there is no broadly accepted constitutive model for quasi-brittle materials. This suggests that there is still a large degree of uncertainty surrounding the predictive accuracy of existing constitutive laws.
4. Accurately capturing the structural size effect is essential for safe predictions of load capacity. The capability of a peridynamic model to capture size effect in quasi-brittle materials has not been investigated yet and remains a major question. As stated by Bažant [19], the capability to correctly reproduce the size effect is an important check on the validity of any computational model.
5. Correctly predicting the shear strength of a reinforced concrete element is an essential test for any numerical model due to the sudden and catastrophic nature of shear failure. To quantify the predictive accuracy of a peridynamic model, the model must be tested against a systematically arranged set of element-level benchmark tests that exhibit a wide range of failure modes.
6. The predicted results (load-deflection response, peak load and crack path) should be independent of the mesh resolution. This is a basic test of the adequacy of any numerical model. To the best of the authors knowledge, mesh sensitivity studies are missing from the existing literature.

The above gaps need to be addressed before large scale industry motivated problems can be examined using a peridynamic model.

Table 2.1 Review of the development of peridynamics for quasi-brittle materials

Author	Title	Model details	Benchmark problems	Validation metrics	Summary
Gerstle and Sau (2004) [91]	Peridynamic modeling of concrete structures	<ul style="list-style-type: none"> <li>Two-dimensional bond-based model</li> <li>Linear constitutive law</li> </ul>	<ul style="list-style-type: none"> <li>Uniaxial tension and compression test</li> <li>Anchor bolt pullout</li> <li>Reinforcing bar splice</li> </ul>	<ul style="list-style-type: none"> <li>Visual examination of the deformed shape</li> <li>No comparison with experimental data</li> </ul>	This a foundational paper and provides the first example of modelling concrete and reinforced concrete. Validation is qualitative but the predicted fracture behaviour demonstrated the promise of the method.
Huang et al. (2015)	An improved peridynamic approach for quasi-static elastic deformation and brittle fracture analysis [118]	<ul style="list-style-type: none"> <li>Two-dimensional bond-based model</li> <li>Linear constitutive law</li> </ul>	<ul style="list-style-type: none"> <li>Plain concrete cantilever</li> <li>Notched plain concrete cantilever</li> </ul>	<ul style="list-style-type: none"> <li>Deformed shape is compared to results from standard finite element models</li> <li>Predicted failure load of the cantilever is provided</li> <li>The predicted crack path is provided</li> <li>No comparison with experimental data</li> </ul>	This paper examined quasi-static problems using a bond-based model. The effect of the local damping coefficient on the accuracy and efficiency of elastic calculations was investigated. This work further demonstrated the potential of a peridynamic model to predict crack initiation and propagation in concrete structures.
Yaghoobi and Chorzepe (2015) [235]	Meshless modeling framework for fiber reinforced concrete structures	<ul style="list-style-type: none"> <li>Two-dimensional non-ordinary state-based model</li> <li>Exponential softening constitutive law</li> </ul>	<ul style="list-style-type: none"> <li>Fibre reinforced concrete plate with two opposing semi circular notches</li> <li>Notched plain and fibre reinforced concrete beam tested in three-point bending</li> <li>Fibre reinforced beam tested in four-point bending</li> </ul>	<ul style="list-style-type: none"> <li>Visual examination of damage for the plate test (tested in uniaxial tension)</li> <li>Numerical load-deflection data is provided for beam bending tests</li> </ul>	Comparison with experimental data is provided and the model is validated against a further test after calibration. The chosen validation problem (beam in three point bending) is almost identical to the calibration problem and is not sufficiently challenging.
Yang et al. (2018) [236]	Investigation on mode-I crack propagation in concrete using bond-based peridynamics with a new damage model	<ul style="list-style-type: none"> <li>Two-dimensional bond-based model</li> <li>Trilinear constitutive law</li> </ul>	<ul style="list-style-type: none"> <li>Eight notched concrete beams in three-point bending</li> <li>Wedge splitting test</li> </ul>	<ul style="list-style-type: none"> <li>Numerical load-CMOD data is provided for eight problems. The notch length and compressive strength are varied</li> <li>Comparison with results obtained using a cohesive zone model</li> <li>Comparison of different constitutive laws (linear, bilinear, trilinear)</li> </ul>	This paper provides perhaps the best example of validation available in the existing literature. A trilinear constitutive law is introduced and the model is validated against experimental data. The predictive accuracy of existing constitutive laws is examined.

Author	Title	Model details	Benchmark problems	Validation metrics	Summary
Li and Guo (2018)	Meso-fracture simulation of cracking process in concrete incorporating three-phase characteristics by peridynamic method [137]	<ul style="list-style-type: none"> <li>Two-dimensional bond-based model</li> <li>Linear constitutive law</li> <li>Mesoscopic model that considers heterogeneity and randomness of material properties</li> </ul>	<ul style="list-style-type: none"> <li>Concrete cube under uniaxial tension and compression</li> <li>Mode I and mixed-mode fracture in a notched concrete plate</li> <li>Notched beam in three-point bending</li> </ul>	<ul style="list-style-type: none"> <li>Predicted crack paths are compared to analytical solutions</li> <li>Normalised stress-strain curves and load-CMOD results are compared against experimental data</li> </ul>	<p>This paper introduced a mesoscopic model that considers heterogeneity and randomness of material properties. The predicted crack paths are in good agreement with analytical solutions. The stress-strain curves and load-CMOD results have been normalised to fit the experimental data (peak load). Normalising results is potentially misleading.</p>
Sau et al. (2019)	Peridynamic modelling of reinforced concrete structures [198]	<ul style="list-style-type: none"> <li>Two-dimensional micropolar bond-based model</li> <li>Linear constitutive law with yield plateau</li> </ul>	<ul style="list-style-type: none"> <li>Deep reinforced concrete beam in three-point bending</li> <li>Concrete beam in four-point bending with: (1) no reinforcement, (2) longitudinal reinforcement, and (3) longitudinal and shear reinforcement</li> </ul>	<ul style="list-style-type: none"> <li>Results for the deep beam were compared with the ACI code</li> <li>Predicted crack paths for the beams in four-point bending are compared to experimental data</li> </ul>	<p>This paper demonstrates the potential of a peridynamic model but the validation is mostly qualitative. Load-deflection data is not provided and comparisons with experimental values of strength are missing. Results for the deep beam were compared with the ACI code but due to the limitations of empirical design codes this a relatively poor validation metric.</p>
Das et al. (2019)	Simulating the fracture of notched mortar beams through extended finite-element method and peridynamics [64]	<ul style="list-style-type: none"> <li>Three-dimensional bond-based model</li> <li>Linear constitutive law</li> </ul>	<ul style="list-style-type: none"> <li>Notched mortar beam in three-point bending</li> </ul>	<ul style="list-style-type: none"> <li>The predicted crack path is provided</li> <li>The predicted failure load is compared against experimental data</li> </ul>	<p>This paper compares results obtained using a model based on the extended finite element method and a bond-based peridynamic model. A single example is provided and model parameters are calibrated to fit the experimental data. There are no validation cases.</p>
Rossi Cabral et al. (2019)	An alternative bilinear peridynamic model to simulate the damage process in quasi-brittle materials [194]	<ul style="list-style-type: none"> <li>Three-dimensional bond-based model</li> <li>Bilinear constitutive law</li> </ul>	<ul style="list-style-type: none"> <li>Sandstone uniaxial tension test</li> </ul>	<ul style="list-style-type: none"> <li>Numerical load-deflection data is provided and compared against experimental data</li> <li>Predicted crack paths are provided</li> </ul>	<p>This paper introduces a novel bilinear constitutive law that improves the flexibility of the model calibration and reduces the computational cost. A single calibration example is provided. There are no validation cases.</p>

Author	Title	Model details	Benchmark problems	Validation metrics	Summary
Tong et al. (2020)	A new bond model in peridynamic theory for progressive failure in cohesive brittle materials [219]	<ul style="list-style-type: none"> <li>Two-dimensional bond-based model</li> <li>Exponential softening constitutive law</li> </ul>	<ul style="list-style-type: none"> <li>Notched beam in three-point bending</li> <li>Double-edged-notched specimen in uniaxial tension and compression</li> <li>L-shaped mixed-mode fracture test</li> </ul>	<ul style="list-style-type: none"> <li>Predicted crack paths are compared against experimental data</li> <li>Numerical load-deflection data is provided and compared against experimental data</li> </ul>	This paper introduces a new exponential softening constitutive law and calibrates the proposed model against experimental data. Model parameters are adjusted to improve agreement between numerical and experimental results, therefore, the predictive accuracy of the model cannot be quantified.
Zhao et al. (2020)	A stochastic multiscale peridynamic model for corrosion-induced fracture in reinforced concrete [244]	<ul style="list-style-type: none"> <li>Two-dimensional bond-based model</li> <li>Linear constitutive law</li> <li>Randomly distributed material properties</li> </ul>	Corrosion induced fracture in reinforced concrete	<ul style="list-style-type: none"> <li>Predicted crack paths are compared against experimental data</li> </ul>	This paper presents a novel study of fracture in reinforced concrete due to rebar corrosion. The inclusion of randomness in the material properties improves the predicted crack paths. The qualitative examination of crack paths is the only validation metric used.
Diana et al. (2020)	Simulating fracture in rock using a micropolar peridynamic formulation [67]	<ul style="list-style-type: none"> <li>Two-dimensional micropolar bond-based model</li> <li>Trilinear constitutive law</li> </ul>	<ul style="list-style-type: none"> <li>Notched sandstone beams in three-point bending</li> <li>Centred and offset notches are examined to study mode I and mixed-mode fracture</li> </ul>	<ul style="list-style-type: none"> <li>Predicted crack paths are compared against experimental data</li> <li>Predicted failure loads and load-deflection curves are not provided</li> </ul>	This paper examines a number of notched sandstone beams. Centred and offset notches are examined to study mode I and mixed-mode fracture. The predicted crack paths are in good agreement with experimental data. No information is provided on the predicted structural response.
Hai and Ren (2020)	Computational investigation on damage of reinforced concrete slab subjected to underwater explosion [107]	<ul style="list-style-type: none"> <li>Three-dimensional bond-based model</li> <li>Linear constitutive law</li> </ul>	Dynamic response of a reinforced concrete slab subjected to an underwater explosion	<ul style="list-style-type: none"> <li>Predicted crack paths are compared to results obtained using a standard continuum damage model</li> <li>The predicted time history of relative velocity at two points on the slab are provided. Numerical results are compared to results obtained using a standard continuum damage model.</li> </ul>	This paper examined a single challenging problem. There is a lack of specifics and detailed validation is not provided. The results from the peridynamic model are comparable with those obtained using a standard model but there is no comparison against experimental data.

Author	Title	Model details	Benchmark problems	Validation metrics	Summary
Yu et al. (2020)	A generalized bond-based peridynamic model for quasi-brittle materials enriched with bond tension–rotation–shear coupling effects [239]	<ul style="list-style-type: none"> <li>Three-dimensional generalised bond-based model</li> <li>Non-linear softening constitutive law (energy-based failure model)</li> </ul>	<ul style="list-style-type: none"> <li>Plate under uniaxial tension</li> <li>Double-edge-notched specimen under uniaxial tension</li> <li>Double-edge-notched specimen under tension–shear combined loading</li> </ul>	<ul style="list-style-type: none"> <li>Predicted crack paths for double-edge-notched specimens are compared against experimental data</li> <li>Numerical force-displacement response is provided and compared against experimental data</li> </ul>	This paper builds on the existing bond-based theory and provides a new generalised model to couple the tension, rotation, and shearing behaviours of a peridynamic bond. A double-edge-notched specimen under uniaxial tension is used to calibrate the constitutive law and a single validation example is provided (double-edge-notched specimen under tension-shear combined loading).
Xu et al. (2021)	Peridynamic modeling of prefabricated beams post-cast with steel fiber reinforced high-strength concrete [234]	<ul style="list-style-type: none"> <li>Two-dimensional micropolar bond-based model with shear deformability</li> <li>Bilinear constitutive law</li> </ul>	<ul style="list-style-type: none"> <li>L-shaped mixed-mode fracture test</li> <li>Reinforced concrete beam in four-point bending. The test specimen was assembled using two precast reinforced concrete beams connected with a steel fibre reinforced high-strength concrete joint</li> </ul>	<ul style="list-style-type: none"> <li>Predicted crack paths are compared against experimental data</li> <li>Numerical load-deflection data is provided and compared against experimental data</li> </ul>	This paper examined a challenging industry motivated problem (joints between precast reinforced beams) and the results show reasonably good agreement with experimental data. A wider range of problems would need to be considered to validate the model and identify the cause of observed discrepancies.

## 2.5 Validation

Validation is the process of quantifying the predictive accuracy of a model through comparisons with experimental data. Validation is an ongoing process as complete validation over the entire domain of applicability is impossible. A model can only ever be validated for a specific set of problems. But by carefully selecting validation problems that test a wide range of fundamental behaviours, a better understanding of the predictive capabilities of a model can be gained.

Robust validation studies are currently missing in the peridynamic literature. The lack of proper validation studies is an issue that is prevalent throughout the peridynamic literature and is also observed in the wider computational mechanics literature. Diehl et al. [69] identified only 39 publications that compare numerical predictions from peridynamic simulations against experimental data. Diehl notes that the majority of papers calibrate model parameters against a single experiment and only a few addressed further validation. Without proper validation, it is not possible to quantify the predictive accuracy of a numerical model.

Calibration and validation are often conceptually misunderstood and many papers fail to make a clear distinction between the two. Definitions of verification, calibration, and validation are provided [218]:

**Verification** is the process of determining that numerical algorithms have been correctly implemented.

**Calibration** is the process of adjusting numerical or physical parameters in a model to improve agreement with experimental data. Calibration must be completed with caution to avoid tuning a model to fit a specific experiment.

**Validation** is the process of determining the degree to which a model is an accurate representation of the real world from the perspective of the intended uses of the model. The expected outcome of the validation process is the quantified level of agreement between experimental data and model prediction, as well as the predictive accuracy of the model.

### 2.5.1 Validation hierarchy

Many industrially motivated problems will exhibit complex failure behaviour influenced by multiple factors that might not be evident or precisely understood. Attempting to directly validate a model on a complex and unique problem will ultimately reveal little about the predictive accuracy. If there is any discrepancy between the experimental and numerical

results, it will be difficult, if not impossible, to isolate the source of error. Even if the agreement between the experimental and numerical data is good, the predictive accuracy might be poor when tested on further problems. Models must be systematically validated using a hierarchy of tests that examine fundamental behaviours and build confidence in the predictive capabilities. The International Federation for Structural Concrete (*fib*) published a guide to finite element modelling of reinforced concrete structures and they defined three different levels of validation for numerical models [82]:

### **Level 1: Model calibration with material parameters**

Level 1 of the validation hierarchy has been rigorously addressed within the existing literature and is, therefore, not the focus of this thesis. Examples of Level 1 problems include uniaxial compression and tension tests.

### **Level 2: Validation and calibration with systematically arranged element-level benchmark tests**

This work focusses on Level 2 of the validation hierarchy. There are very few examples of Level 2 validation in the existing peridynamic literature. To quantify the predictive accuracy of a model, the model must be tested against a systematically arranged set of element-level benchmark tests that encompass the range of behaviours that might be experienced. By determining the ratio of the measured to predicted capacity of a carefully selected set of experiments, a global safety factor can be determined and applied to the numerical results.

The importance of validation against a carefully selected set of experiments was demonstrated by Collins et al. [56]. Researchers were invited to predict the load capacity of four reinforced shear panels. The tests had been carefully selected so that they each exhibited different structural behaviour. None of the contestants were able to provide accurate predictions for more than two tests, thereby illustrating the importance of the selection of a systematically arranged set of validation experiments.

Level 2 tests should be reasonably simple with little chance for misinterpretation of the experimental data. These tests may be referred to as fundamental or element-level tests. Examples of Level 2 tests include: a systematic examination of geometrically similar beams of different sizes (to examine size effect) and a systematic examination of the effect of shear-span-to-depth ratio on shear strength.

### Level 3: Validation and calibration at a structural level

Level 3 validation requires the assessment of a model against complex and unique problems where the exact physical behaviour is perhaps not understood, for example, a very deep beam, such as that tested by Collins et al. [54], or non-prismatic beams, such as that tested by Orr et al. [172].

#### 2.5.2 Validation metrics

A validation metric is the basis for comparing the numerical results with experimental data. Validation metrics define the level of accuracy and precision of a simulation and must be chosen carefully. The load-deflection response is perhaps the most robust validation metric as it captures many common metrics such as, structural stiffness, load capacity, deformation at peak load and deformation at failure. The fracture behaviour is another important validation metric. Accurately predicting fracture behaviour requires a model that can capture the underlying physical mechanisms that govern crack propagation. Other more novel comparisons are possible; for example, the size of the zone of energy dissipation (fracture process zone) can be used as a validation metric.

#### 2.5.3 Model validation procedure

In this section, the essential features of a robust validation procedure are defined. This work adheres to the following principles:

1. To quantify the predictive accuracy of a model, the model must be tested against a systematically arranged set of element-level benchmark tests that encompass the range of behaviours that might be experienced. The importance of validating using a comprehensive series of test data that captures the range of critical behaviour characteristics cannot be overemphasised [82].
2. Experimental data must be divided into two sub-sets: (1) data for calibration, and (2) data for validation. Best practice is to use a single problem for calibration. The calibrated model parameters are then used to evaluate a range of test cases.
3. Material parameters that have been measured experimentally must not be adjusted. Only numerical parameters can be calibrated.
4. Performing a mesh sensitivity study is an essential part of any validation procedure. The predictive accuracy of a model cannot be quantified if the numerical results are

dependent on the mesh resolution. Note that mesh sensitivity studies are sometimes designated as part of the verification process.

## 2.6 Summary

As the demand for efficient structural forms grows, the need for accurate and robust predictions of structural strength and behaviour becomes more pressing. Methods that rely on empirical formulas will not suffice and no consistent mechanical model exists to describe shear behaviour. Numerical methods offer higher flexibility and can overcome the severe limitations of empirical methods.

Modelling the initiation and propagation of cracks is a long standing problem in computational mechanics. The limitations of existing methods are a result of the mathematical deficiencies of the governing partial differential equations. Silling [203] proposed a non-local theory of solid mechanics, known as the peridynamic theory, that is formulated in terms of integral equations rather than partial differential equations. The governing equations do not require a spatially continuous and differentiable displacement field and damage localisation and fracture naturally emerge.

The peridynamic theory provides a promising theoretical framework for developing robust numerical models, capable of simulating the complex fracture processes in quasi-brittle materials. Existing work on the development of peridynamics for quasi-brittle materials has demonstrated significant potential but much work remains to quantify the predictive accuracy and address large-scale industry motivated problems.



# Chapter 3

## Peridynamic theory of solid mechanics

### 3.1 Introduction

Peridynamics is an integral-type non-local theory of solid mechanics, first proposed in 2000 by Silling [203]. The term peridynamic comes from the Greek words *peri* and *dyna*, meaning *near* and *force* respectively, and the name alludes to the non-local nature of the theory. The peridynamic model defines material behaviour at a point in a continuum body as an integral equation of the surrounding displacement. This is in contrast to the classical theory of solid mechanics, where the material behaviour at a point is defined by partial differential equations. The classical theory is only valid if the body under analysis has a spatially continuous and differentiable displacement field. Spatial derivatives are not defined across discontinuities and the classical theory breaks down when a body fractures. The peridynamic theory does not include spatial derivatives and remains valid across discontinuities, allowing for the natural inclusion of fracture behaviour. In the classical theory of solid mechanics, linear momentum in a deformable solid body is conserved according to Eq. (3.1).

$$\rho \ddot{\mathbf{u}}(\mathbf{x}, t) = \nabla \cdot \boldsymbol{\sigma}(\mathbf{x}, t) + \mathbf{b}(\mathbf{x}, t) \quad (3.1)$$

Where  $\rho$  is density,  $\ddot{\mathbf{u}}$  is acceleration,  $\nabla$  is the divergence operator,  $\boldsymbol{\sigma}$  is the Cauchy stress tensor, and  $\mathbf{b}$  is the body force. The stress tensor defines the internal forces at a point in a solid, see Fig. 3.1. The peridynamic theory replaces the divergence of stress term with an integral function.

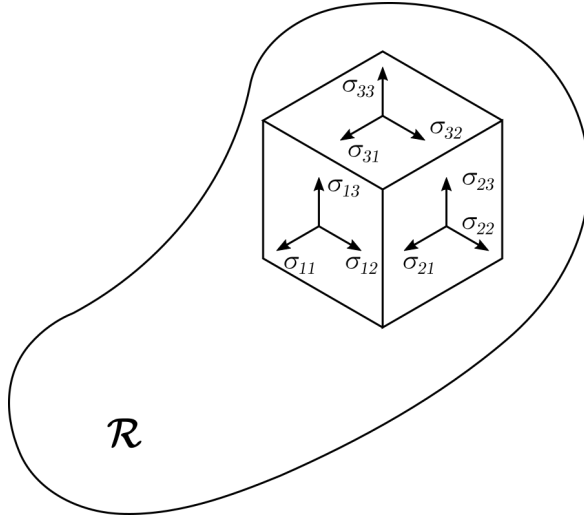


Fig. 3.1 Stress tensor in a continuous solid

The aim of peridynamics is to unify the mechanics of continuous media, continuous media with evolving discontinuities, and discrete particles, with a single consistent set of equations. This avoids the coupling of dissimilar mathematical systems and the basic equations allow for the natural inclusion of discontinuities, overcoming the problems inherent with classical continuum mechanics. The peridynamic theory is strongly non-local and material points interact across a finite length scale. In the classical theory, points only interact if they are separated by zero distance (all internal forces are contact forces), and the behaviour and influence of material points within a wider neighbourhood is ignored. The origins of non-locality and the physical justification are discussed in this chapter.

Fig. 3.2 illustrates a peridynamic continuum model. The peridynamic theory starts with the assumption that Newton's second law holds true for every infinitesimally small differential volume (continuum material particle) within a solid continuum body. Particles that are separated by a finite distance  $\delta$  in the reference undeformed configuration interact through a pairwise bond force density function  $\mathbf{f}$ . The pairwise bond force is described by a constitutive model that is a function of the material properties and the initial and deformed particle positions. In the original formulation, known as the bond-based peridynamic theory, the pairwise force function  $\mathbf{f}$  is assumed to be a function of the initial and deformed configuration between a pair of particles [203]. The assumption that particle pairs respond independently of all others places a limitation on the Poisson's ratio. This limitation led to the development of the state-based peridynamic theory [208]. In the state-based theory, the pairwise force function  $\mathbf{f}$  depends on the initial and deformed configuration between every pair of particles within the horizon of a material point. The peridynamic theory and its variations are introduced in this chapter.

## 3.2 Bond-based peridynamic theory

This section presents the bond-based peridynamic theory. Detailed mathematical treatments can be found in the literature [203, 207, 210]. A mechanically intuitive but less rigorous way of obtaining the governing equations can be found in [30].

### 3.2.1 Peridynamic continuum model

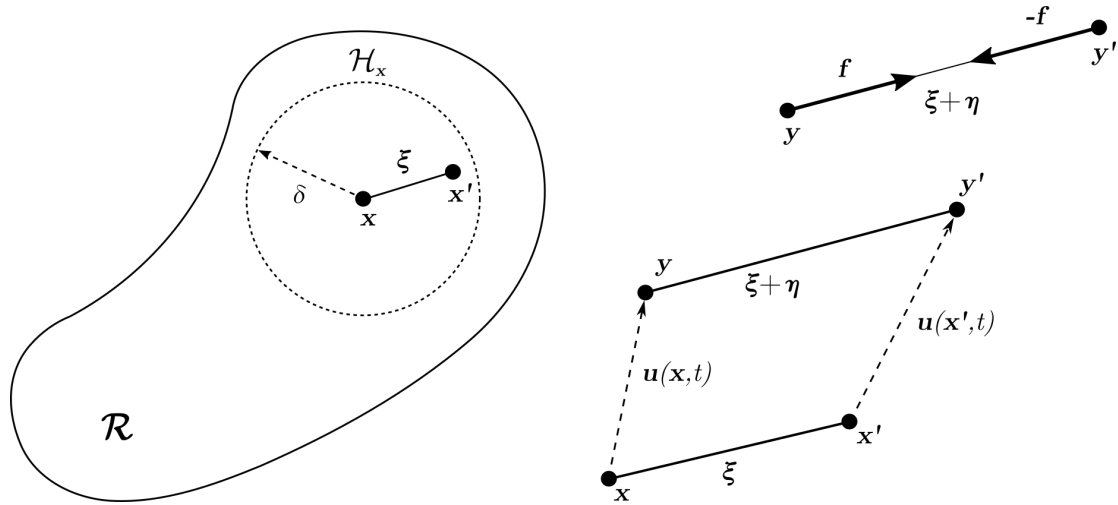


Fig. 3.2 Peridynamic continuum and kinematics of particle pair and bond-based pairwise force function

Assuming that a body occupies a spatial region  $\mathcal{R}$ , for any material point  $\mathbf{x} \in \mathcal{R}$ , a pairwise force function  $\mathbf{f}$  can be defined to describe the interaction between particles within a finite distance  $\delta$  of  $\mathbf{x}$ , at any time  $t$ , where  $\mathbf{u}$  represents the displacement of a material point (See Fig. 3.2).

$$\mathbf{f} = \mathbf{f}(\mathbf{x}, \mathbf{x}', \mathbf{u}(\mathbf{x}, t), \mathbf{u}(\mathbf{x}', t), t), \quad \mathbf{x}' \in \mathcal{R} : \|\mathbf{x}' - \mathbf{x}\| \leq \delta \quad (3.2)$$

The peridynamic equation of motion or a single material point  $\mathbf{x}$  at a point in time  $t$  is given by Newton's second law of motion, and is defined by Eq. (3.3).

$$\rho \ddot{\mathbf{u}}(\mathbf{x}, t) = \int_{\mathcal{H}_x} \mathbf{f}(\mathbf{u}(\mathbf{x}', t) - \mathbf{u}(\mathbf{x}, t), \mathbf{x}' - \mathbf{x}) dV_{\mathbf{x}'} + \mathbf{b}(\mathbf{x}, t) \quad (3.3)$$

$\rho$  is mass density,  $\ddot{\mathbf{u}}$  is particle acceleration,  $\mathbf{b}$  is body force per unit volume, and  $\mathcal{H}_x$  is the neighbourhood of material point  $\mathbf{x}$ . The size of the neighbourhood is defined by the

horizon length  $\delta$ . For a 3D problem, the material point neighbourhood will be a sphere, and for a 2D problem, the neighbourhood will be circular.

$$\mathcal{H}_x = \mathcal{H}_x(x, \delta) = \{x' \in \mathcal{R} : \|x' - x\| \leq \delta\} \quad (3.4)$$

The pairwise force function  $\mathbf{f}$  represents the force that particle  $x'$  exerts on particle  $x$  and contains all the constitutive information of the material under analysis. This interaction is commonly referred to as the peridynamic bond force. Particles separated by a distance greater than the horizon length  $\delta$  do not interact.

$$|\xi| > \delta \rightarrow \mathbf{f} = \mathbf{f}(u(x', t) - u(x, t), x' - x) = \mathbf{f}(\eta, \xi) = \mathbf{0} \quad (3.5)$$

The initial relative position vector of a pair of particles is denoted by  $\xi = x' - x$ , and the relative displacement vector is denoted by  $\eta = u' - u$ . The current relative position vector is given by  $\xi + \eta$  (see Fig. 3.2). The pairwise force function  $\mathbf{f}$  must satisfy the following conditions. To satisfy the conservation of angular momentum, the force vector must be parallel to the deformed bond.

$$\mathbf{f}(\eta, \xi) \times (\eta + \xi) = \mathbf{0} \quad (3.6)$$

The pairwise force function must also satisfy the balance of linear momentum, which corresponds to Newton's third law.

$$\mathbf{f}(-\eta, -\xi) = -\mathbf{f}(\eta, \xi) \quad (3.7)$$

### Micro-elastic material

If the pairwise force function  $\mathbf{f}$  can be derived from a scalar micropotential  $w$ , a material is said to be microelastic. This is a consequence of Stokes theorem and a more detailed explanation can be found in the original paper of Silling [203].

$$\mathbf{f}(\eta, \xi) = \frac{\partial w}{\partial \eta}(\eta, \xi) \quad (3.8)$$

Every bond gains energy when a body is deformed. The energy stored in a bond is known as the micropotential  $w$  and has units of energy per unit volume squared ( $J/m^6$ ). For a microelastic material, every pair of nodes is connected by a bond. Bonds are essentially springs, and they can possess linear or non-linear characteristics. Bond force is dependent only on the scalar distance between nodes in the deformed configuration. Micropotential

$w$  depends on the material properties and the deformed position of particles relative to the initial configuration.

The concept of microelasticity is only applied to single bonds connecting interacting nodes. This concept can be broadened to capture the behaviour of whole bodies and is referred to as macroelasticity ( $\text{J/m}^3$ ). The macroelastic energy density  $W_x$  associated with a material point  $x$  is defined by Eq. (3.9). Macroelastic energy density is also known as the strain energy density. The strain energy of a material point  $x$  is equal to the summation of the micropotential of all bonds connect to  $x$ . Each node owns half of the energy stored in a bond, this leads to the factor of  $1/2$  in Eq. (3.9).

$$W = \frac{1}{2} \int_{\mathcal{H}_x} w(\boldsymbol{\eta}, \boldsymbol{\xi}) dV_{\boldsymbol{\xi}} \quad (3.9)$$

The total macroelastic energy  $\Phi$  for a whole body is defined by Eq. (3.10). Alike to the classical theory of elasticity, work done by external forces on a body  $\mathcal{R}$  is stored in a recoverable form.

$$\Phi = \int_{\mathcal{R}} W(\mathbf{x}) dV \quad (3.10)$$

The micropotential  $w$  depends on the relative displacement vector  $\boldsymbol{\eta}$  only through the scalar distance between deformed particles, and a scalar valued function  $\hat{w}$  exists such that,

$$\hat{w}(y, \boldsymbol{\xi}) = w(\boldsymbol{\eta}, \boldsymbol{\xi}) \quad \forall \boldsymbol{\xi}, \boldsymbol{\eta} \quad y = |\boldsymbol{\xi} + \boldsymbol{\eta}| \quad (3.11)$$

By differentiating Eq. (3.11) with respect to  $\boldsymbol{\eta}$  and combining with Eq. (3.8), a general form of the pairwise force function  $\mathbf{f}$  can be derived, where  $f$  is a scalar-valued function defined by Eq. (3.13).

$$\frac{\partial w(\boldsymbol{\eta}, \boldsymbol{\xi})}{\partial \boldsymbol{\eta}} = \frac{\partial \hat{w}(y, \boldsymbol{\xi})}{\partial y} \frac{\partial y}{\partial \boldsymbol{\eta}} \quad (3.12)$$

$$\frac{\partial \hat{w}(y, \boldsymbol{\xi})}{\partial y} = f(y, \boldsymbol{\xi}) = f(|\boldsymbol{\xi} + \boldsymbol{\eta}|, \boldsymbol{\xi}) \quad (3.13)$$

$$\frac{\partial y}{\partial \boldsymbol{\eta}} = \frac{\boldsymbol{\xi} + \boldsymbol{\eta}}{|\boldsymbol{\xi} + \boldsymbol{\eta}|} \quad (3.14)$$

$$\mathbf{f}(\boldsymbol{\eta}, \boldsymbol{\xi}) = f(|\boldsymbol{\xi} + \boldsymbol{\eta}|, \boldsymbol{\xi}) \frac{\boldsymbol{\xi} + \boldsymbol{\eta}}{|\boldsymbol{\xi} + \boldsymbol{\eta}|} \quad (3.15)$$

The general form of the pairwise force function, Eq. (3.15), and the peridynamic equation of motion, Eq. (3.3), capture the entirety of the peridynamic model for a non-linear micro-elastic material. The magnitude of the force vector,  $f$ , is yet to be defined and this is addressed in the following section.

### 3.2.2 Constitutive model

The constitutive behaviour of a material within the bond-based peridynamic framework is expressed as a relationship between the scalar bond force  $f$  and stretch  $s$ . Bonds are essentially springs and they can possess linear or non-linear characteristics. The basic equations of peridynamics allow for the natural inclusion of discontinuities, overcoming the problems inherent with classical continuum mechanics. Damage is introduced into the constitutive model by breaking bonds when their stretch exceeds a critical value  $s_c$ . Silling and Askari [207] introduced the first peridynamic constitutive law, known as the prototype microelastic brittle (PMB) model. This model represents the behaviour of a linear elastic material and is depicted by Fig. 3.3. The model is defined by Eq. (3.16).

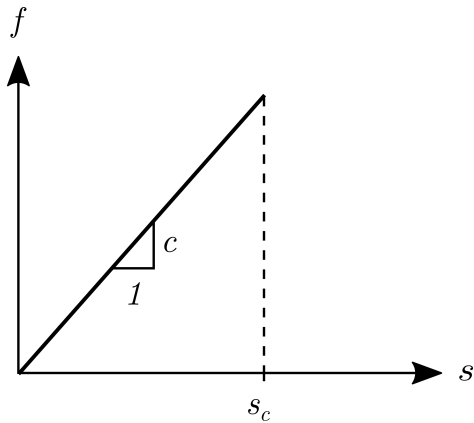


Fig. 3.3 Scalar bond force  $f$  as a function of bond stretch  $s$  in the linear elastic material model.

$$f(|\xi + \eta|, \xi) = cs\mu \quad (3.16)$$

The micromodulus  $c$  defines the stiffness of a pair-wise bond.  $c$  is generally a constant value and is often referred to as the bond stiffness or spring constant. It is assumed that the scalar bond force  $f$  is dependent only on the bond stretch  $s$ , defined by Eq. (3.17). Bond stretch  $s$  is positive when a peridynamic bond is under tension. The scalar bond force  $f$  does not depend on bond direction; therefore, the described material model is isotropic.

$$s = \frac{|\xi + \eta| - |\xi|}{|\xi|} \quad (3.17)$$

To enable the simulation of fracture, a method to capture the failure of bonds must be included in the material model. Damage is introduced by allowing bonds to break when a critical stretch value  $s_c$  is exceeded and  $\mu$  is a history dependent scalar-valued function used to capture the failure of bonds.  $\mu$  is equal to 1 when bond stretch is below the critical stretch value  $s_c$ , and 0 when a bond exceeds the critical stretch.

$$\mu = \begin{cases} 1 & \text{if } s < s_c \\ 0 & \text{if } s \geq s_c \end{cases} \quad (3.18)$$

Once a bond has broken, it can no longer sustain any tensile force. Damage is permanent and bond cannot be repaired. The material model is consequently history dependent. The linear elastic material model is isotropic in its initial state, but breakage of bonds results in an anisotropic response.

The pairwise force function is defined by Eq. (3.19). This equation is obtained by substituting Eq. (3.16) into Eq. (3.15).

$$\mathbf{f}(\eta, \xi) = cs\mu \frac{\xi + \eta}{|\xi + \eta|} \quad (3.19)$$

The next step is to determine the bond stiffness  $c$  and critical bond stretch  $s_c$ .

### **$c$ - micromodulus**

Only two material parameters characterise the linear damage model, the bond stiffness  $c$  and the critical bond stretch  $s_c$ . The peridynamic bond stiffness  $c$  contains all material specific information.  $c$  can be correlated with material properties from the classical theory of elasticity by equating the strain energy density of a unit volume in the peridynamic and classical theory. Consider a large homogeneous body under isotropic expansion, illustrated in Fig. 3.4. Bond stretch  $s$  is constant for all bonds  $\xi$ , and deformation  $\eta = s\xi$ . Defining  $\xi = |\xi|$  and  $\eta = |\eta|$ , it follows that  $\xi = s\eta$ . From Eq. (3.16),  $f = cs$ , therefore  $f = c\eta/\xi$ . Note that bond failure is not considered and  $\mu$  is ignored. Using the definition of the micropotential, Eq. (3.8), the energy stored in a bond can be determined as follows.

$$\mathbf{f}(\eta, \xi) = \frac{\partial w}{\partial \eta}(\eta, \xi) = \frac{c\eta}{\xi} \quad \rightarrow \quad w = \int \frac{c\eta}{\xi} d\eta = \frac{c\eta^2}{2\xi} = \frac{cs^2\xi^2}{2\xi} = \frac{cs^2\xi}{2} \quad (3.20)$$

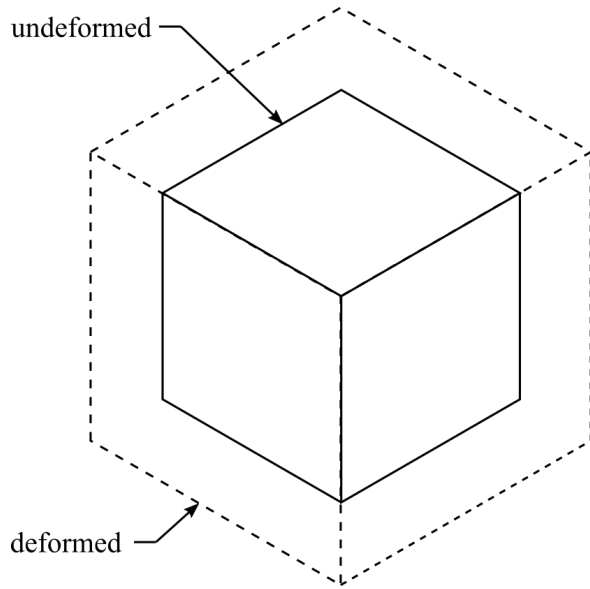


Fig. 3.4 A three-dimensional body subjected to isotropic expansion.

Substitute Eq. (3.20), the energy stored in a bond, into Eq. (3.9) to find the peridynamic strain energy density. The volume of a sphere is  $4\pi r^3/3$ , therefore the node horizon volume is  $V_\xi = 4\pi \xi^3/3$  if  $\delta = \xi$ . The change in volume  $dV_\xi$  with respect to a change in bond length  $\xi$  is defined as follows.

$$\frac{dV_\xi}{d\xi} = 3 \frac{4}{3} \pi \xi^2 \quad \rightarrow \quad dV_\xi = 4\pi \xi^2 d\xi \quad (3.21)$$

The peridynamic strain energy density can then be found as follows.

$$W_{PD} = \frac{1}{2} \int_{\mathcal{H}_x} w(\boldsymbol{\eta}, \boldsymbol{\xi}) dV_\xi = \frac{1}{2} \int_0^\delta \frac{cs^2 \xi}{2} 4\pi \xi^2 d\xi = \frac{1}{2} \left[ \frac{2\pi cs^2 \xi^4}{4} \right]_0^\delta = \frac{\pi cs^2 \delta^4}{4} \quad (3.22)$$

The peridynamic strain energy density is then equated to the strain energy density from the classical theory. The peridynamic bond stiffness  $c$  can then be found. The derivation of  $c$  in three-dimensions is provided. The strain energy density for a 3D isotropic elastic element subjected to equal tensile forces is given by Eq. (3.23). A detailed derivation of Eq. (3.23) is provided by Boresi et al. [35].

$$W_{CCM} = \frac{1}{2} [\lambda (\varepsilon_1 + \varepsilon_2 + \varepsilon_3)^2 + 2G(\varepsilon_1^2 + \varepsilon_2^2 + \varepsilon_3^2)] \quad (3.23)$$

Where  $\lambda$  is Lame's elastic constant and  $G$  is the shear modulus.

$$\lambda = \frac{\nu E}{(1+\nu)(1-2\nu)} \quad \text{and} \quad G = \frac{E}{2(1+\nu)} \quad (3.24)$$

Consider a cube subject to equal tensile forces along three orthogonal directions, with no change in shape, only volumetric expansion. The principle strains will be equal,  $\varepsilon_1 = \varepsilon_2 = \varepsilon_3 = \varepsilon_0$ . The stretch of a bond  $s$  in a peridynamic material will be equal to  $\varepsilon_0$ ,  $s = \varepsilon_0$ . Eq. (3.23) can be simplified.

$$W_{CCM} = \frac{1}{2}\lambda(3s)^2 + 3Gs^2 \rightarrow W_{CCM} = \frac{3}{2}(3\lambda + 2G)s^2 \quad (3.25)$$

Equating Eq. (3.22) and Eq. (3.25),  $W_{PD} = W_{CCM}$ .

$$\frac{\pi c s^2 \delta^2}{4} = \frac{3}{2}(3\lambda + 2G)s^2 \rightarrow c = \frac{12E}{\pi \delta^4 (2 - 4\nu)} \quad (3.26)$$

A second expression for  $c$  can be determined by considering the equivalence of strain energy  $W_{PD} = W_{CCM}$  for different states of deformation, for example, a simple shear state, as illustrated in Fig. 3.5, or a pure shear state. Further details can be found in the following references: [203, 146, 118]. Equating the two values of  $c$ , it can be found that the Poisson's ratio  $\nu$  is limited to 1/4 for the 3D case. Therefore, the peridynamic bond stiffness  $c$  for 3D problems is defined by Eq. (3.27).

$$c = \frac{12E}{\pi \delta^4} \quad (3.27)$$

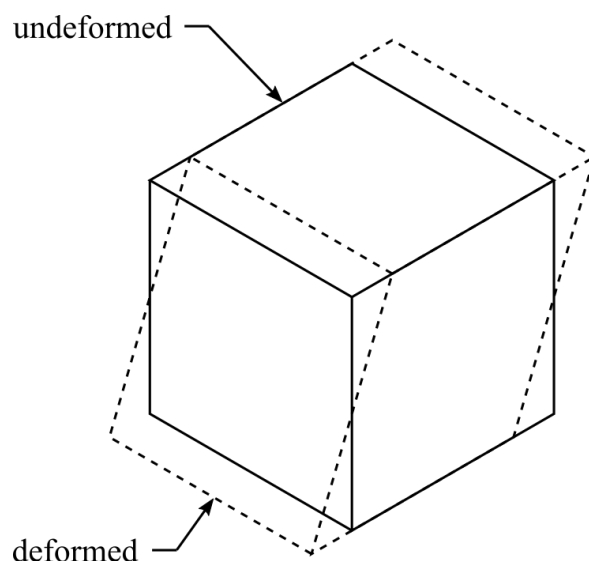


Fig. 3.5 A three-dimensional body subjected to simple shear.

The same procedure can be used to derive the bond constant for 2D plane stress and plane strain problems. The Poisson's ratio  $\nu$  is limited to 1/3 for plane stress problems, and 1/4 for plane strain and 3D problems. The bond stiffness constant for different problem types is defined by Eq. (3.28), where  $t$  is the thickness of the domain under analysis.

$$c = \begin{cases} \frac{12E}{\pi\delta^4} & \text{3D} \\ \frac{9E}{\pi t \delta^3} & \text{Plane stress} \\ \frac{48E}{5\pi t \delta^3} & \text{Plane strain} \end{cases} \quad (3.28)$$

The restriction on the Poisson's ratio has been addressed by the state-based peridynamic theory [208]. The bond-based model has also been revised to overcome the Poisson's ratio restriction [94]. The Poisson's ratio of concrete is generally between 0.1 to 0.2 and the limitation in the bond-based theory is unlikely to play a crucial role in the modelling of the ultimate limit state behaviour of concrete.

### $\omega$ - influence function

The effect of distance between nodes is not accounted for when determining the stiffness of a bond. The stiffness constant  $c$  is identical for all bonds within the horizon of a node and reduces to zero when the length of a bond exceeds the horizon length, see Fig 3.6. It has been argued that this does not provide an accurate representation of the physical reality of non-local forces [118, 51].

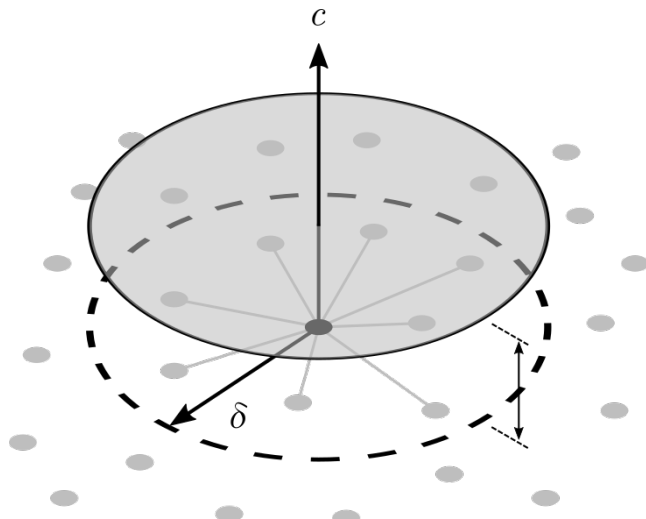


Fig. 3.6 Schematic of a constant influence function for a two-dimensional peridynamic model

By introducing an influence function  $\omega(\xi, \delta)$ , a micromodulus function  $c(\xi, \delta)$  can be defined that accounts for the distance between material points. The micromodulus function is defined by Eq. (3.29). The micromodulus function can be thought of as a weight function (kernel function) used in other non-local models such as smoothed-particle hydrodynamics.

$$c(\xi, \delta) = c(0, \delta)\omega(\xi, \delta) \quad (3.29)$$

Fig. 3.7 illustrates three different micromodulus functions. The influence function and corresponding constant  $c$  for a linear elastic material in three-dimensions are presented in Table 3.1. The presented influence functions capture a gradual decrease in stiffness as the bond length increases, reaching zero stiffness at the horizon boundary. This provides a more accurate representation of the physical nature of non-local forces [118]. It is shown in Chapter 5 that the use of a non-constant micromodulus function improves the numerical convergence of the peridynamic model. Other benefits are also discussed.

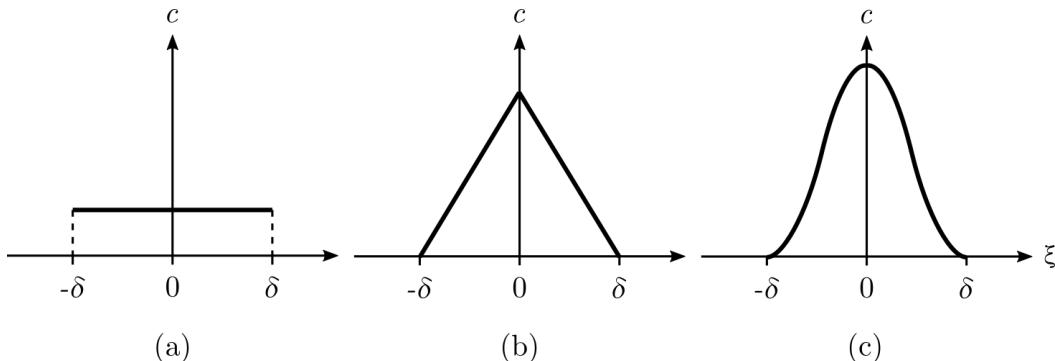


Fig. 3.7 Comparison of influence functions (scale is approximate): (a) constant influence function; (b) triangular influence function (conical); (c) quartic influence function

Table 3.1 Influence functions  $\omega$  and their corresponding constant  $c$  for a three-dimensional peridynamic material

Function type	$\omega(\xi, \delta)$	$c(0, \delta)$
Constant	1	$\frac{12E}{\pi\delta^4}$
Conical	$1 - \frac{\xi}{\delta}$	$\frac{60E}{\pi\delta^4}$
Quartic	$\left(\frac{\xi}{\delta}\right)^4 - 2\left(\frac{\xi}{\delta}\right)^2 + 1$	$\frac{72E}{\pi\delta^4}$

**$s_c$  - critical stretch**

The critical stretch value determines when a bond will fail. In the literature there are two common approaches for determining the value of  $s_c$ : (1) the critical stretch can be related to material parameters from the classical fracture theory, or (2) the critical stretch value can be determined by calibrating simulation results to test data. Silling and Askari [207] derived the critical stretch value in terms of the material fracture energy  $G_F$ . An infinitely large peridynamic body is completely separated into two halves and all the bonds that initially crossed the fracture surface are considered to have broken. The energy stored in a bond is defined by Eq. (3.20) and has units of energy per volume squared ( $\text{J}/\text{m}^6$ ). The energy required to break a bond is defined by Eq. (3.30). The energy required to break all bonds per unit fracture area in a three-dimensional peridynamic body is given by Eq. (3.31). The peridynamic energy release rate  $G_0$  has units of energy per unit area ( $\text{J}/\text{m}^2$ ). Refer to Fig. 3.8 for an explanation of this calculation. Note that this calculation uses a spherical coordinate system and is analogous to finding the volume of a sphere using triple integrals.

$$w_c = \frac{cs_c^2\xi}{2} \quad (3.30)$$

$$G_0 = \int_0^\delta \int_0^{2\pi} \int_z^\delta \int_0^{\cos^{-1}(z/\xi)} \left( \frac{cs_c^2\xi}{2} \right) \xi^2 \sin\phi d\phi d\xi d\theta dz \quad (3.31)$$

After evaluation of Eq. (3.31), the following definition of  $G_0$  is found.

$$G_0 = \frac{\pi cs_c^2 \delta^5}{10} \quad (3.32)$$

It is assumed that  $G_0$  is equal to the material fracture energy  $G_F$ . The material fracture energy can be obtained experimentally or through empirical equations. The critical bond stretch  $s_c$  for a three-dimensional peridynamic body can then be defined as follows.

$$s_c = \sqrt{\frac{10G_F}{\pi c \delta^5}} \quad (3.33)$$

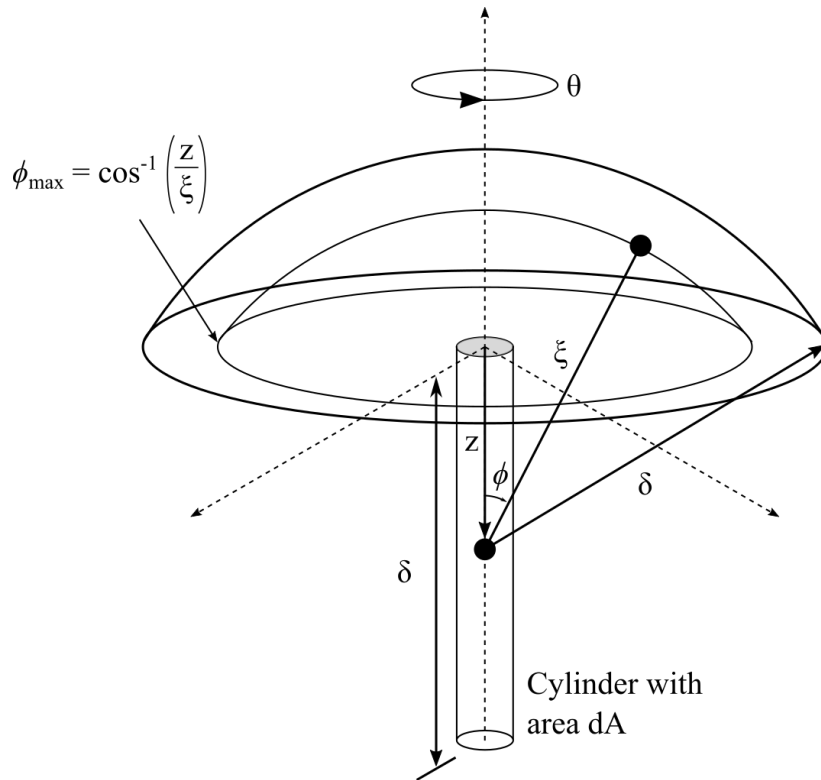


Fig. 3.8 Schematic of the energy release rate  $G_0$  computation

### $\varphi$ - damage

Introducing failure at the level of an individual bond leads to an unambiguous definition of damage at a material point. The damage of a peridynamic material at node  $\mathbf{x}$  is defined by Eq. (3.34) as the ratio of broken bonds to total number of bonds attached to node  $\mathbf{x}$ . Note that the value of  $\varphi$  will range from 0 to 1, where 0 indicates that the material is undamaged, and 1 represent a material point that has completely disconnected from all other material points.

$$\varphi(\mathbf{x}, t) = 1 - \frac{\int_{\mathcal{H}_x} \mu(\mathbf{x}, t, \xi) dV_\xi}{\int_{\mathcal{H}_x} dV_\xi} \quad (3.34)$$

### 3.2.3 Damping

All materials exhibit damping to some extent and damping should be included within the peridynamic model. Without damping, the solution will exhibit large oscillations about the equilibrium position. Damping can be introduced in two ways: (1) viscous damping, and (2) local damping. For fully dynamic problems, Kilic [130] introduced non-local viscous damping into the bond force function. The damping model introduced by Kilic is also

known as the Kelvin-Voight model for viscoelastic materials. For quasi-static problems, an additional damping term can be introduced into the governing motion equation, Eq. (3.35).

$$\rho \ddot{\mathbf{u}}(\mathbf{x}, t) = \int_{\mathcal{H}_x} \mathbf{f}(\mathbf{u}(\mathbf{x}', t) - \mathbf{u}(\mathbf{x}, t), \mathbf{x}' - \mathbf{x}) dV_{\mathbf{x}'} + \mathbf{b}(\mathbf{x}, t) - C \dot{\mathbf{u}}(\mathbf{x}, t) \quad (3.35)$$

The local damping coefficient  $C$  is a positive real constant with units of  $\text{kg}/\text{m}^3\text{s}$ . This method is sometimes referred to as dynamic relaxation. Local damping can cause unphysical effects in fully dynamic simulations. Consider a rigid body moving at constant velocity in a vacuum. According to Eq. (3.35), the body will eventually come to a complete stop without any external forces. The motion of a body should continue forever, unless some external force acts upon it. For quasi-static problems, dynamic effects are negligible and a local damping term can be used.

### 3.3 State-based peridynamic theory

The original bond-based peridynamic formulation is limited to modelling materials with a Poisson's ratio of  $1/4$ . This is due to restrictions on the pairwise force function  $\mathbf{f}$  that arise from basic mechanical considerations; the forces that act between any two particles must be of equal magnitude and act in opposite directions (the force vector must be parallel to the deformed bond). To overcome this limitation, Silling et al. [208] extended the bond-based theory with the introduction of force states  $\underline{\mathbf{T}}$  and deformation states  $\underline{\mathbf{F}}$ . This generalised theory is known as state-based peridynamics. In the state-based theory, the force state is a function of the reference and deformed state of all particles that lie within the horizons of a particle pair, see Fig. 3.9. In the ordinary state-based theory, there are no restrictions on the magnitude of the forces that act between particles. In the non-ordinary theory, there are no restrictions on the magnitude or the direction of the forces. Fig. 3.10 illustrates the response for bond-based and state-based material models.

The concept of a deformation state is used to construct correspondence models that can recreate any constitutive model from the classical theory. Correspondence models use the deformation state to approximate the deformation gradient tensor. The deformation gradient tensor is then used to calculate force contributions. Correspondence models provide a method for enhancing material models from classical theory with the inherent capability of peridynamics to model long-range forces and fracture [206]. State-based correspondence models have been used to successfully capture a variety of material behaviour, including linear elasticity, plasticity and fracture [122].

A number of papers have attempted to establish a link between the state-based peridynamic theory and meshfree methods [28, 87]. Under very specific circumstances it was shown by Ganzenmüller et al. [87] that smoothed-particle hydrodynamics (SPH) is equivalent to peridynamics. The authors emphasised that the mathematical foundations of peridynamics are clear and straightforward, and SPH requires *ad-hoc* procedures to ensure that linear and angular momentum are conserved and to approximate linear fields accurately.

The state-based peridynamic theory provides a general framework for modelling material failure, however state-based models are significantly more computationally expensive than bond-based models. This is one of several factors that has influenced the decision to only consider the bond-based theory in this work. Further justification for this decision is provided in section 2.4.

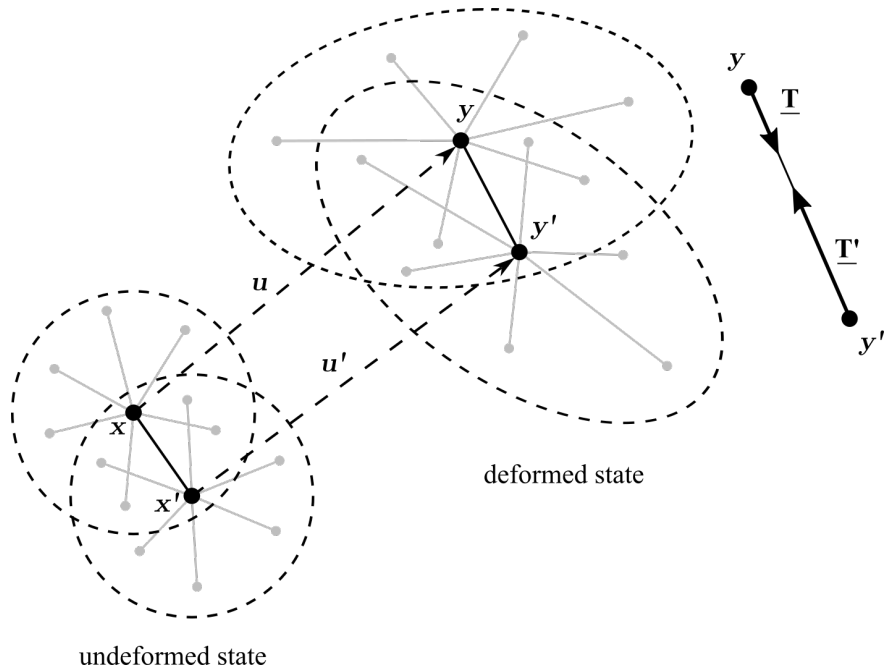


Fig. 3.9 State based peridynamic model

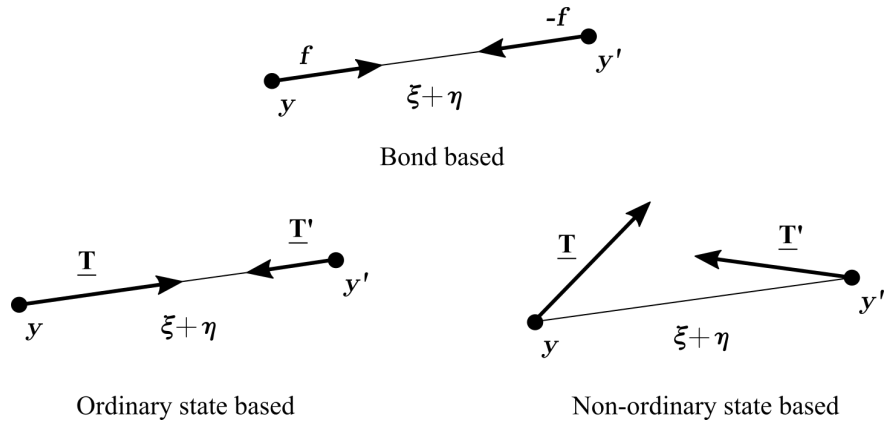


Fig. 3.10 Schematic of bond based, ordinary, and non-ordinary material response. Adapted from Silling et al. [208].

## 3.4 Constitutive laws

This chapter has provided a detailed explanation and derivation of the linear elastic damage law proposed by Silling and Askari [207]. The linear model is suitable for modelling the behaviour of ideal-brittle materials and has been used to accurately capture complex fracture patterns in glass and ceramic materials [104, 105]. It is generally assumed that the behaviour of a peridynamic bond should be consistent with the macroscopic material response. In small and medium sized structures, concrete acts as a quasi-brittle material and exhibits strain-softening behaviour when in tension. The linear damage model does not consider softening behaviour, and this limits its ability to capture the true behaviour of quasi-brittle structures. A number of constitutive laws have been proposed within the bond-based peridynamic framework to model the behaviour of quasi-brittle materials: bilinear [93, 243, 30, 194], trilinear [236], and decaying exponential [219] forms. Detailed studies on the predictive accuracy of constitutive laws for quasi-brittle materials are still needed and this is addressed in Chapter 5. A new non-linear softening law is introduced and the predictive accuracy of the proposed law is superior to existing constitutive laws.

## 3.5 Non-locality

### 3.5.1 Origins of non-locality

Is non-locality physically realistic? This is a common question often asked of the peridynamic theory and perhaps the most detailed treatment of this question is provided in Chapter 1 of [30]. The answer to this question depends on material properties and the geometrical

length scale. At the atomic and molecular levels, individual atoms interact through non-local forces. By definition, atoms are separated by a non-zero distance. At larger length scales, it is generally assumed that local models provide good approximations. Materials can be approximated as continuous, and all internal forces are contact forces. However, local approximations have severe limitations, even at meso and macroscopic length scales (the subject of this thesis). These limitations arise due to a number of factors.

Physical justification of non-locality was provided by Bažant [17], who demonstrated that damage in a heterogeneous material is non-local using micromechanics arguments. Crack nucleation and growth are the result of processes that occur at the microstructural level. The development of distributed micro-cracking and release of stored energy occurs prior to the localisation of damage and formation of macroscopic cracks [179]. This zone of damage moves with the crack front and can extend far ahead of the discontinuity. The size and volume of the damage zone is non-negligible and its influence must be accounted for. It is argued that the existence and importance of the interaction of spatially distributed micro-cracks implies non-locality. In addition, the simultaneous growth of many interacting micro-cracks in a stable manner is only possible within a non-local framework.

Bažant [17] also demonstrated that non-locality arises from the decision to model a material with distributed defects in terms of a smoothed displacement field. This idea has been extended to demonstrate that non-local interactions arise as a result of the homogenisation of heterogeneous materials, rather than through direct physical interactions across a finite distance. Typically, the elastic response of a heterogeneous material is addressed by applying the classical continuum equations with smoothed (homogenised) material properties. These properties are obtained from laboratory testing on specimens much larger than any internal length scale in the material. For example, determining the compressive strength of concrete cylinders. This approximation is acceptable for many problems but it ignores the reality that most materials are not perfectly uniform in composition. Using a similar procedure to Bažant [17], Silling [205] presented a derivation of how non-locality is implied by the use of a smoothed displacement field to model a heterogeneous microstructure. This work is based on a simple model of the mechanics of a composite. Using more abstract reasoning, Alali and Lipton [3] also proved that non-locality is an essential feature of homogenisation of heterogeneous materials.

There are a number of other factors that support the argument that non-local theories are more fundamental than local theories. Emmrich and Weckner [76] and Silling and Lehoucq [209] have shown that as the horizon radius approaches the limit of zero interaction distance ( $\delta \rightarrow 0$ ), the local solution is obtained. In this sense, non-local theories are more fundamental, and local models can be considered as a special case of non-local models.

Non-local models ensure that upon mesh refinement, the localisation of strain, damage, and energy dissipation does not occur in a zone of vanishingly small volume. This eliminates problems of mesh sensitivity and incorrect convergence that occur in local models [17]. Many existing numerical models incorporate a localisation limiter that is used to enforce a minimum width of strain localisation and is related to a material characteristic length [125, 211]. This is commonly known as regularisation and is necessary to prevent singularities and to ensure correct energy dissipation when a crack forms.

Finally, local models can not capture a size effect on material strength. Correctly reproducing size effect is an essential check on the validity of any model, and as stated by Bažant [18], the fundamental feature of any model capable of capturing size effect is the presence of some form of characteristic length (length scale). The characteristic length is generally assumed to be a material property that is related to the size of material inhomogeneities. The physical meaning of the horizon radius  $\delta$  is addressed in the following section. For further discussion on the physical justification of non-local models, the reader is referred to Bažant and Jirásek [21].

### 3.5.2 Physical meaning of the horizon

The physical meaning of the peridynamic horizon  $\mathcal{H}_x$  remains a subject of debate. Is the horizon a numerical constant or is it an intrinsic property of a material? Does it depend on the size scale of the model? Silling and Askari [207] state that the value of the horizon radius  $\delta$  is dependent on the physical nature of the problem under analysis. For problems at the nanoscale,  $\delta$  can be chosen to replicate the physical distance over which atoms interact. At the macroscale,  $\delta$  has no physical meaning and the most appropriate value can be selected (see section 4.2.3 for details). Rossi Cabral et al. [194] examined the physical meaning of the horizon, and introduced a material horizon related to a characteristic length of the material, and a numerical horizon that is chosen for convenience. For concrete the characteristic length is determined to be approximately 2.7 times the maximum aggregate size [22]. A clear physical interpretation of the material characteristic length is disputed and avoiding the use of a vaguely defined parameter would be advantageous [165, 155]. This work does not attribute any physical meaning to the horizon length.

The results presented in the following chapters demonstrate that non-locality is essential in a physically consistent model, but at the macroscale, the horizon radius  $\delta$  is not an intrinsic material property. This differentiates the peridynamic model from existing numerical approaches, and the use of an ambiguous characteristic length parameter is avoided.

# Chapter 4

## Numerical solution method

### 4.1 Introduction

The governing equations of peridynamics are solved numerically. The equation of motion is an integro-differential equation that is difficult to solve analytically. Analytical solutions exist but they are restricted to specific cases. Many problems of interest to engineers concern complex geometries with multiple materials and numerical techniques must be used to obtain solutions. Silling and Askari [207] were the first to describe a numerical method for solving dynamic problems within the peridynamic theory.

EMU, developed by Silling [204], was the first computational peridynamics code. At a high level, a peridynamic code consists of several distinct components: a routine for spatial integration (calculating bond forces and reducing to nodal forces), a time integration routine, a method for applying initial and boundary conditions, a damping method for obtaining steady-state solutions, a routine for applying surface corrections, a routine for bond damage evaluation and tracking, and a method for reading input data and saving output data [139]. Peridynamic models are computationally expensive due to the non-local nature of the governing equations. Simulating large problems, on the order of hundreds of thousands to tens of millions of particles, requires high performance computing resources. Strategies such as parallel computing are employed to minimise the computational expense. Details of the chosen methods are discussed in this chapter.

There are a limited number of actively developed open-source peridynamic codes. Peridynamics has been implemented within the classical molecular dynamics package LAMMPS (Large-scale Atomic/Molecular Massively Parallel Simulator). The peridynamics package in LAMMPS is known as PD-LAMMPS [176]. This was the first open-source peridynamics code. A more recent and capable package is the open-source code Peridigm [177]. Peridigm is the only open-source code available that is specifically designed for peridynamic simula-

tions. Peridigm is written in C++ and requires many dependencies. Its complexity presents a barrier to uptake amongst many engineers and academics.

There is a need for fast open-source code that is easy to use. A three-dimensional bond-based peridynamic code has been developed in MATLAB and C. The developed code makes use of shared memory parallelism using OpenMP. This chapter outlines the numerical framework and discusses implementation details. Boys et al. [41] have recently developed a lightweight, open-source, and high performance peridynamics package in Python. The author has contributed to the development and validation of this package. The developed toolbox utilises OpenCL and can execute on CPUs or GPUs. It is hoped that the package of Boys et al. [41] will become the industry standard and other researchers will contribute to its development.

## 4.2 Spatial integration

In peridynamics, the governing equations are based on spatial integration. This is in contrast to the classical theory, where the governing equations are based on spatial differentiation. This makes the peridynamic governing equation valid all over the domain of a body, even when spatial discontinuities are present. The discretisation of integrals plays an important role in the accuracy of peridynamic simulations. Silling and Askari [207] proposed a simple discretisation method for the peridynamic equation of motion, known as the meshfree method. In the meshfree method, the body is discretised into a regular grid of nodes and every node is assigned a corresponding cell, as illustrated in Fig. 4.1. The discretised form of the peridynamic equation of motion, Eq. (3.3), is given by Eq. (4.1). Where  $\mathbf{u}_i^n = \mathbf{u}(\mathbf{x}_i, t = n\Delta t)$ ,  $n$  signifies the  $n$ th time step,  $\Delta t$  is the time step size, and  $p$  represents any material particle in the horizon of node  $i$ .

$$\rho \ddot{\mathbf{u}}_i^n = \sum_p \mathbf{f}(\mathbf{u}_p^n - \mathbf{u}_i^n, \mathbf{x}_p - \mathbf{x}_i) dV_p + \mathbf{b}_i^n \quad (4.1)$$

Spatial integration over the horizon of a node is implemented numerically with a summation of integrals over all cells contained within the horizon boundary. A one-point quadrature method is applied over every cell. The centre point of every cell is used as a quadrature point, and the area (2D problems) or volume (3D problems) of a cell is used a weight. For some nodes, a fraction of the cell volume will sit across the horizon boundary and using the whole cell volume will lead to errors in the spatial integration. A volume correction procedure can be implemented to improve the accuracy of the spatial integration.

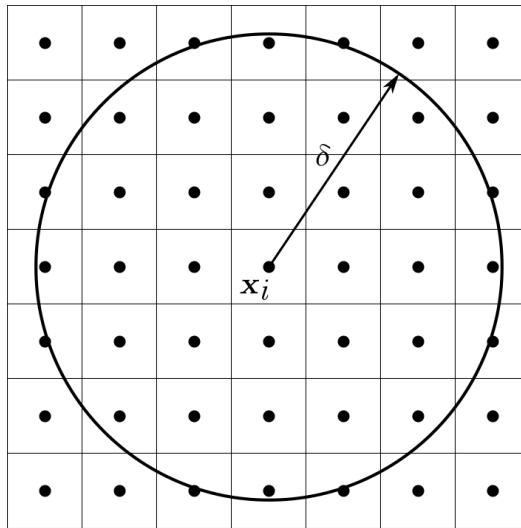


Fig. 4.1 Horizon of node  $x_i$  in the discretised configuration

The meshfree approach of Silling and Askari [207] has been used in the vast majority of existing work and is implemented in this thesis. The original meshfree method is popular due to its simplicity and relatively low computational cost. Note that this method is termed ‘meshfree’ or ‘meshless’ because a topological mesh is not required. It is convenient to refer to the grid of nodes that represent the computational domain as a mesh, and this terminology will be used throughout. Other discretisation approaches for the strong form of the peridynamic governing equation have been proposed within the literature and Seleson [200] provides a brief review.

### 4.2.1 Spatial discretisation

The accuracy and efficiency of spatial integration is linked to the discretisation of the continuum body. The spatial domain can be discretised using a regular or irregular grid of nodes, as illustrated in Fig. 4.2. A regular discretisation is the most common choice in the literature and offers a number of advantages: (1) simplicity of implementation, (2) easily defined cell areas/volumes, and (3) better convergence behaviour. However, regular grids have a number of disadvantages. Predicted crack paths show a degree of dependency on the mesh orientation [110, 70]. A finer spatial discretisation can alleviate this behaviour but increases computational expense. Henke and Shanbhag [110] also noted that the regularity of a mesh influences the predicted crack paths for symmetrical problems; cracks propagate along lines of symmetry. Accurately capturing complex geometries is also problematic and inaccuracies are particularly pronounced for curved geometries. These disadvantages can be mitigated by using an irregular mesh. Chen [49] quantitatively examined the effect of an

irregular mesh on the predictive accuracy of a peridynamic model. Chen did not consider failure as it is not strictly valid to apply failure criteria derived for a regular grid of nodes to problems with an irregular discretisation. Hu et al. [117] introduced an energy-based bond failure criteria appropriate for irregular meshes. Due to simplicity, all problems in this thesis are discretised using a regular mesh. This provides a good baseline from which to measure any improvements obtained from more sophisticated discretisation schemes.

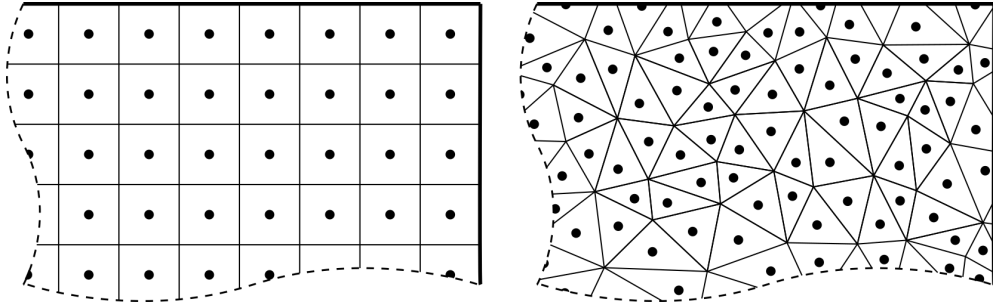


Fig. 4.2 Regular and irregular mesh

#### 4.2.2 Volume correction

The meshfree approach of Silling and Askari [207] suffers from accuracy issues due to the imprecise approximation of cell areas and volumes that intersect with horizon boundaries. If  $\xi \leq \delta$ , the weight of a quadrature point is taken to be the full area/volume of a cell. It is clear to see from Fig. 4.3 that this will result in an overestimation of the cell area/volume for several material points.

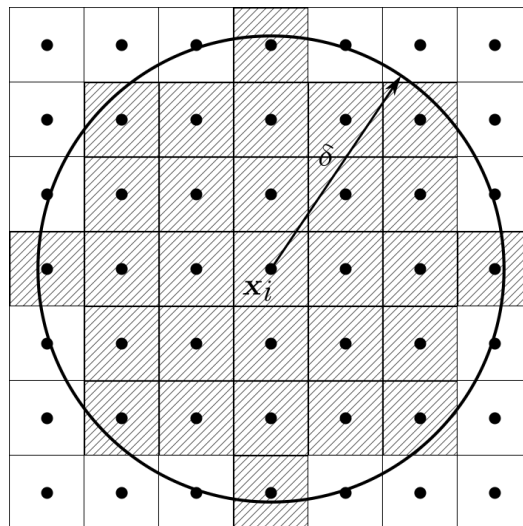


Fig. 4.3 Illustration of spatial integration using the meshfree method proposed by Silling and Askari [207]. The hashed areas highlight the computed area

A number of methods exist for improving the computation of cell areas/volumes that intersect with the horizon boundary. These methods are commonly known as volume correction procedures. Seleson [200] provides a detailed analysis of the various methods available for improving the accuracy of one-point quadrature schemes in two-dimensional peridynamic problems. This work has implemented the volume correction procedure introduced by Parks et al. [176], referred to as the PA-PDLAMMPS algorithm. If  $\xi \leq \delta - \Delta x/2$ , the weight is taken to be the full area/volume of a cell. If  $\delta - \Delta x/2 < \xi \leq \delta$ , a volume correction factor is introduced. Fig. 4.4 provides a schematic of the volume correction procedure. The volume correction factor  $v_c$  is defined by a simple linear relationship that provides a rough approximation of the partial area/volume. Fig. 4.5 illustrates Eq. (4.2).

$$v_c = \frac{\delta + \Delta x/2 - \xi}{\Delta x} \quad (4.2)$$

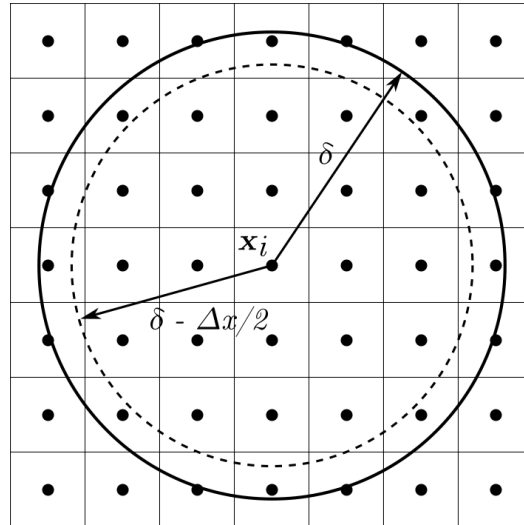


Fig. 4.4 The volume correction factor is applied to nodes that lie between  $\delta$  and  $\delta - \Delta x/2$

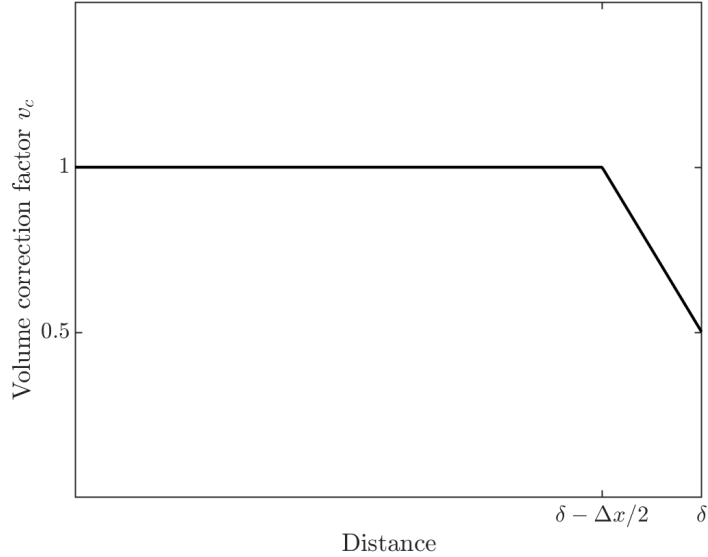


Fig. 4.5 Volume correction factor  $v_c$  against distance

The volume correction procedure introduced by Parks et al. [176] has been used because of its simplicity and compatibility with three-dimensional problems. It must be noted that improved volume correction procedures are available. Hu et al. [116] proposed a volume correction procedure that outperforms the PA-PDLAMMPS method [200]. Seleson [200] proposed an improved algorithm for two-dimensional problems based on the analytical calculation of partial areas. The extension of this analytical scheme to three-dimensional problems would be beneficial. Jones and Williams [126] state that there exists no unique analytical solution to the computation of the volume of intersection between spheres and cubes. They introduced a linear approximation for computing the intersection volume between a sphere and a cube. This approach could be utilised to improve the accuracy of spatial integration within a three-dimensional peridynamic model. Yu [241], Yu et al. [242] introduced an adaptive trapezoidal integration scheme with error control. Volume correction procedures are only applicable to regular meshes and extension to irregular meshes is yet to be explored. Yu et al. [242] states that the adaptive integration scheme could easily be extended to an irregular mesh.

### 4.2.3 Horizon, grid resolution, and numerical convergence

The horizon  $\delta$  and grid resolution  $\Delta x$  have a significant influence on the numerical accuracy and convergence. At the macroscale, the horizon is a numerical constant with no physical meaning. For a given value of  $\delta$ , the parameters in a peridynamic model can be chosen to

match a given set of physically measurable material properties. Therefore, an optimum value of  $\delta$  must be chosen that provides high accuracy whilst balancing computational expense.

The accuracy and convergence behaviour of a peridynamic model is complicated by the presence of a length scale. To determine an optimum value of  $\delta$ , an additional parameter  $m$  must be introduced.  $m$  is the ratio between the horizon radius and grid resolution ( $m = \delta/\Delta x$ ). Bobaru et al. [33] and Ha and Bobaru [104] define and discuss two fundamental types of convergence: (1)  $m$ -convergence:  $\delta$  is fixed and  $m \rightarrow \infty$ . This can also be stated as  $\delta$  is fixed and  $\Delta x \rightarrow 0$ . (2)  $\delta$ -convergence:  $m$  is fixed and  $\delta \rightarrow 0$ . This can also be stated as  $m$  is fixed and  $\Delta x \rightarrow 0$ . See Fig. 4.6 for a graphical representation of the types of convergence. A third type of convergence can be defined:  $\delta m$ -convergence. This is a combination of  $\delta$ - and  $m$ -convergence. See Bobaru et al. [33] for details.

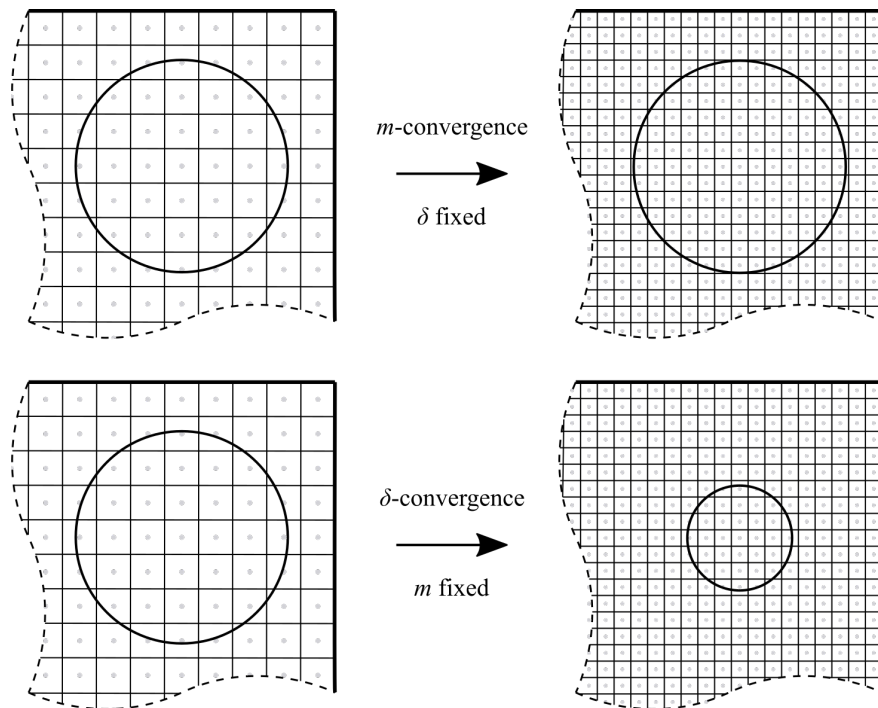


Fig. 4.6 Graphical representation of the two fundamental types of convergence:  $m$ -convergence and  $\delta$ -convergence.

Madenci and Oterkus [146] investigated the choice of  $m$  for macroscale problems. Six values of  $m$  were considered  $m = 1, 3, 5, 10, 25, 50$ . It was found that values of  $m = 1$  and  $m = 3$  achieved the highest accuracy when compared to the classical analytical solution for the displacement of a one-dimensional bar subjected to a defined initial strain. Values of  $m$  much larger than 3 lead to excessive wave dispersion and become extremely computationally expensive. When fracture behaviour is also considered, values of  $m$  less than 3 lead to grid

dependence on crack propagation [32, 146]. Hu et al. [116] and Seleson [200] examined the  $m$ -convergence behaviour for two-dimensional models. Higher values of  $m$  improve the spatial integration accuracy but  $m \approx 3$  provides an acceptable approximation.  $m$ -convergence behaviour is examined in three-dimensions in section 5.5.2. A value of  $m = \pi$  ( $\delta = \pi\Delta x$ ) is generally recommended for macroscale problems and is found extensively throughout the literature. The  $m$ -ratio is set to  $\pi$  for all problems in this thesis.

How is the mesh resolution selected? The spatial discretisation error is of the order  $\mathcal{O}(\Delta x^2)$  [207]. The discretisation error can be reduced by using a finer spatial discretisation, but this will result in an increase in computational expense, and a balance has to be found between accuracy and efficiency. Bobaru and Hu [32] and Zhao et al. [244] note that the size of the horizon should be defined by the smallest relevant geometrical feature. The ratio between the horizon radius and the grid resolution is fixed, therefore, the mesh resolution should be finer than the smallest relevant feature. For many problems, this is not reasonably practicable due to the need for very fine meshes and high computational expense. Mesh sensitivity ( $\delta$ -convergence) is examined in Chapters 5 and 7. To the best of the authors knowledge, the effect of mesh refinement on the predicted peak load and load-deflection response has not been examined within the literature. Numerical results should be independent of the mesh resolution. This is a basic test of the adequacy of any numerical model.

For further insight into the meaning and choice of the horizon, the reader is referred to Bobaru and Hu [32] and section 2.2.7 in [30].

### 4.3 Explicit time integration

The peridynamic equation of motion is in a dynamic form and explicit or implicit time integration schemes can be used to determine a solution. Explicit schemes are the most popular and widely used method in the peridynamic literature due to their easy implementation and computational efficiency. Explicit methods use the current state of the system to compute the future state. The response of the system is determined by advancing through a large number of small time steps. Continuous time is discretised into a finite number of uniform time steps  $t_1, t_2, t_3, \dots, t_n$  with a time step size  $\Delta t$ . Eq. (4.1) is applied directly to determine the nodal acceleration of every material point. The calculated nodal accelerations are then applied to every node to advance the solution from one time step to the next.

Explicit schemes are typically used for dynamic problems where inertial effects are important. They are robust and well suited to problems with large deformations and material failure. A disadvantage of explicit methods is that they are conditionally stable, which limits

the maximum allowable time step size [139]. Implicit methods are unconditionally stable, however, they require the solution of a large system of equations comprising both the current state of the system and a future state. This adds a significant degree of complexity and is computationally expensive. Implicit schemes are examined in section 4.6.

There are numerous explicit time integration schemes available. Commonly used schemes include: forward Euler method, midpoint method, Euler-Cromer and Velocity-Verlet. Chapter 3 of [95] summarises common methods for the numerical integration of the equations of motion. This work has implemented a Euler-Cromer algorithm [59]. The Velocity-Verlet scheme [215] was also implemented and preliminary numerical investigations indicated that the predictive accuracy was equivalent. It is not the purpose of this work to rigorously investigate explicit time integration schemes.

### 4.3.1 Euler-Cromer scheme

This section outlines the Euler-Cromer scheme used to produce all the results presented in this thesis.

#### 1. Calculate nodal accelerations $\ddot{\mathbf{u}}_i^n$

The first step is to calculate nodal accelerations  $\ddot{\mathbf{u}}_i^n$ , using Eq. (4.3).

$$\ddot{\mathbf{u}}_i^n = \frac{1}{\rho} \left[ \sum_p \mathbf{f}(\mathbf{u}_p^n - \mathbf{u}_i^n, \mathbf{x}_p - \mathbf{x}_i) dV_p + \mathbf{b}_i^n \right] \quad (4.3)$$

#### 2. Calculate nodal velocities $\dot{\mathbf{u}}_i^{n+1}$

The second step is to calculate nodal velocities  $\dot{\mathbf{u}}_i^{n+1}$  using Eq. (4.4).

$$\dot{\mathbf{u}}_i^{n+1} = \dot{\mathbf{u}}_i^n + \ddot{\mathbf{u}}_i^n \Delta t \quad (4.4)$$

#### 3. Calculate nodal displacements $\mathbf{u}_i^{n+1}$ and update nodal positions

The third step is to calculate nodal displacements  $\mathbf{u}_i^{n+1}$  using Eq. (4.5) and update nodal coordinates.

$$\mathbf{u}_i^{n+1} = \mathbf{u}_i^n + \dot{\mathbf{u}}_i^{n+1} \Delta t \quad (4.5)$$

#### 4. Calculate bond forces and update nodal acceleration $\ddot{u}_i^{n+1}$

Using the updated nodal positions, the bond forces are calculated by means of the constitutive model. The bond force array is reduced to an array of nodal forces. The nodal acceleration at time step  $n + 1$  can then be calculated using Eq. (4.3) and the process repeats. This procedure is repeated thousands or even millions of times.

#### 4.3.2 Numerical stability

Explicit time integration schemes become numerically unstable for large time steps  $\Delta t$ . To ensure numerical stability, small time steps are required and this can significantly increase simulation run time. Silling and Askari [207] derived a stability condition for the time step.

$$\Delta t_{crit} = \sqrt{\frac{2\rho}{\sum_p \Delta V_p c_{ip}}} \quad (4.6)$$

The critical time step is determined for every material point in the body, and the minimum value is taken.  $p$  iterates over all the material points in the neighbourhood of point  $i$ .  $\Delta V_p$  is the volume of the point  $p$ , and  $c_{ip}$  is the bond stiffness between the given point  $i$  and neighbour  $p$ . The critical time step should be multiplied by a safety factor,  $sf < 1$ . The safety factor helps to ensure numerical stability, this is especially important for non-linear problems. Eq. (4.6) was derived for a one dimensional peridynamic body. For two and three-dimensional bodies, Eq. (4.6) will provide a conservative estimation of the critical time step [30].

An alternative option for calculating the critical time step is the Courant-Friedrichs-Lowy approach [58].

$$\Delta t_{crit} = \frac{h}{c} \quad (4.7)$$

$h$  is a characteristic length associated with the spatial discretisation. For a regular discretisation,  $h$  is taken as the node spacing  $\Delta x$ .  $c$  is the wave speed and can be calculated using Eq. (4.8), where  $k$  is the bulk modulus.

$$c = \sqrt{\frac{k}{\rho}} \quad (4.8)$$

Eq. (4.7) can be interpreted as the time taken for a wave to travel between two material points. This approach leads to a very conservative estimate of the time step for peridynamic models. This is because the maximum stable time step is limited by the horizon  $\delta$  and not

the grid spacing  $\Delta x$  [207]. The stable time step condition derived by Silling and Askari [207] is used in this work.

### 4.3.3 Quasi-static analysis

The peridynamic equation of motion is in a dynamic form and addressing static / quasi-static problems requires special considerations. For many problems, inertial effects are negligible, and suitable solution methods must be used to efficiently find the equilibrium state. Note that the static solution is simply the steady state of a dynamic problem with moderate damping. There are a number of techniques for obtaining the steady state solution of a dynamic simulation in a time efficient manner.

To obtain the static solution, the simplest method is to introduce a local damping term into the governing motion equation, as defined by Eq. (3.35). This method is sometimes referred to as dynamic relaxation. The local damping coefficient  $C$  is a positive real constant with units of  $\text{kg}/\text{m}^3\text{s}$ . The choice of damping coefficient will have a large effect on the convergence speed, as illustrated in Fig. 4.7. Huang et al. [118] provide further details. Determining the most effective damping coefficient  $C$  can be difficult in non-linear problems and this led to the introduction of an adaptive dynamic relaxation (ADR) method for quasi-static simulations using the peridynamic theory [131]. In ADR, the damping coefficient is changed adaptively in every time step and this can lead to a speed up in convergence. These methods are applicable to quasi-static load-controlled problems. To capture non-linear behaviour, the load must be applied over a number of sub-steps and an equilibrium solution is sought for each sub-step. For highly non-linear problems, a large number of sub-steps might be required.

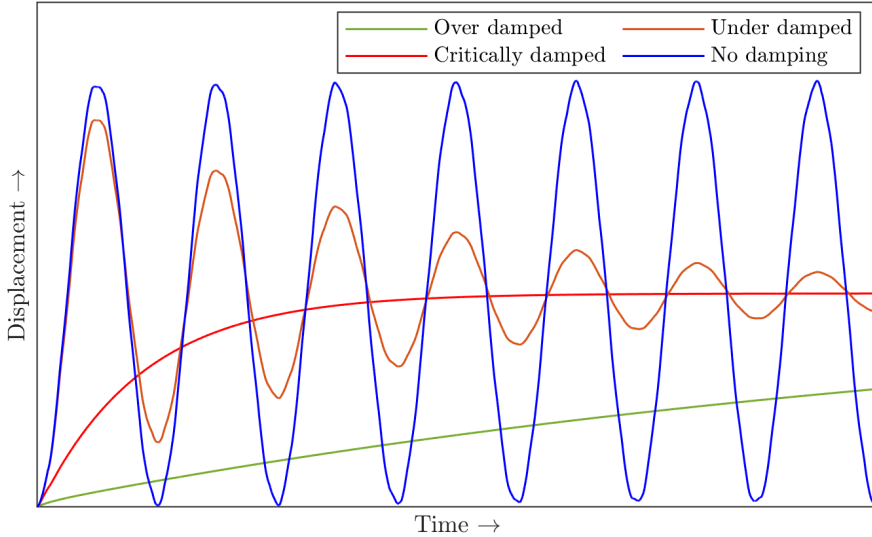


Fig. 4.7 Influence of the local damping coefficient on the convergence speed for load-controlled quasi-static analysis

For displacement-controlled quasi-static problems, the rate of applied loading should be smooth to reduce dynamic effects and improve accuracy. Discontinuities in the loading rate produce stress waves that introduce noise and errors into the solution. The applied displacement is increased incrementally using a smoothstep function. This allows for a faster loading rate whilst maintaining quasi-static conditions. This work uses a fifth-order smoothstep function defined by Eq. (4.9) and illustrated in Fig. 4.8, where  $A_t$  represents the applied displacement at time  $t$ . The function defines a smooth loading amplitude that ramps up from zero at the start of loading ( $t_0 = 0$  s,  $A_0 = 0$  mm) to the final value ( $t_1, A_1$ ). The first and second derivatives of the curve are continuous and are zero at  $t_0$  and  $t_1$ . There is minimal change in acceleration from one increment to the next. This method is based on that used by Abaqus, a commercial non-linear finite element analysis tool. A small to moderate damping coefficient can be used to further reduce unwanted dynamic effects.

$$A_t = A_0 + (A_1 - A_0)\gamma^3(10 - 15\gamma + 6\gamma^2) \quad \gamma = \frac{t - t_0}{t_1 - t_0} \quad (4.9)$$

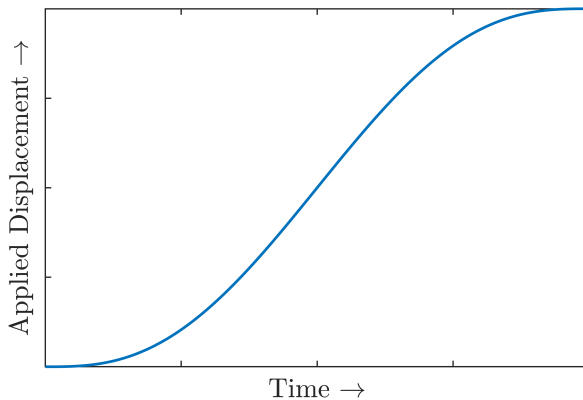


Fig. 4.8 Applied displacement against time using a smooth amplitude curve for displacement-controlled quasi-static analysis

To ensure that quasi-static conditions are met (i.e., dynamic effects are negligible), a general rule is to check that the kinetic energy in the system is less than 5% of the total internal energy. This approach is used in Abaqus for explicit analysis [1]. Rabczuk and Ren [183] used this approach in a peridynamic framework. Rabczuk states that by ensuring the kinetic energy is less than 1% of the total internal energy, quasi-static conditions are guaranteed. By removing the acceleration term in the equation of motion, it is possible to directly find a static solution. Details are provided in section 4.6.

## 4.4 Boundary conditions

In classical continuum mechanics, the solution of the governing differential equations must satisfy the natural boundary conditions (applied tractions) and essential boundary conditions (applied displacements) on the surface of the domain. This is known as a boundary value problem. The application of boundary conditions in the peridynamic theory is different to that in classical continuum mechanics. As shown by Silling [203], the formulation of the governing equations of peridynamics does not lead to natural and essential boundary conditions. Boundary conditions cannot be imposed on the boundary surface of a peridynamic body and must be applied directly to material points. In essence, boundary conditions must have a non-zero volume, otherwise they will integrate to zero. Madenci et al. [144] recently introduced a weak form of peridynamics for non-local essential and natural boundary conditions.

### 4.4.1 Force boundary condition

Surface tractions, which appear naturally in the classical theory, do not appear in the governing equations of peridynamics. Instead, external forces are applied as body forces  $\mathbf{b}$ . Surface tractions ( $\text{N/m}^2$ ) must be converted to a force per unit volume ( $\text{N/m}^3$ ). Conversion of an externally applied load to a body force is achieved using Eq. (4.10), where  $P$  is the applied load,  $n$  is the number of nodes over which the load is applied, and  $V$  is the cell volume.

$$\mathbf{b}(\mathbf{x}, t) = \frac{P(\mathbf{x}, t)}{nV(\mathbf{x})} \quad (4.10)$$

### 4.4.2 Displacement boundary condition

Displacement boundary conditions cannot be imposed on the boundary surface of a peridynamic body and must be applied directly to a material point. As noted by Mehrmashhadi et al. [151], applying imposed displacements to a single node will result in a large surface effect. Imposed displacements should be distributed over a number of nodes but this can also be problematic. Nodes subjected to the same applied displacement move together and forces in the connecting bonds are zero. To limit these issues, Mehrmashhadi applied the imposed displacements over a two by two node region.

#### Contact model

A contact model can be used to solve the issues associated with displacement boundary conditions. In this work, loading is applied using a displacement-controlled cylindrical rigid impactor. The contact algorithm described by Madenci and Oterkus [146] is used to model the interaction between the rigid impactor and deformable body. The cylindrical impactor is moved by a small displacement every time step. The displacement is defined by the fifth-order smoothstep function given in Eq. (4.9). When the rigid impactor and deformable body come into contact, there is initially an interpenetration of material points, as illustrated in Fig. 4.9. Material points that lie within the surface of the impactor are moved to the boundary. New particle positions are determined so that the displacement vector is equal to the shortest path between the particle and contact surface. This process develops a contact surface between the rigid penetrator and deformable body. See section 10.1.1 in [146] for the full implementation.

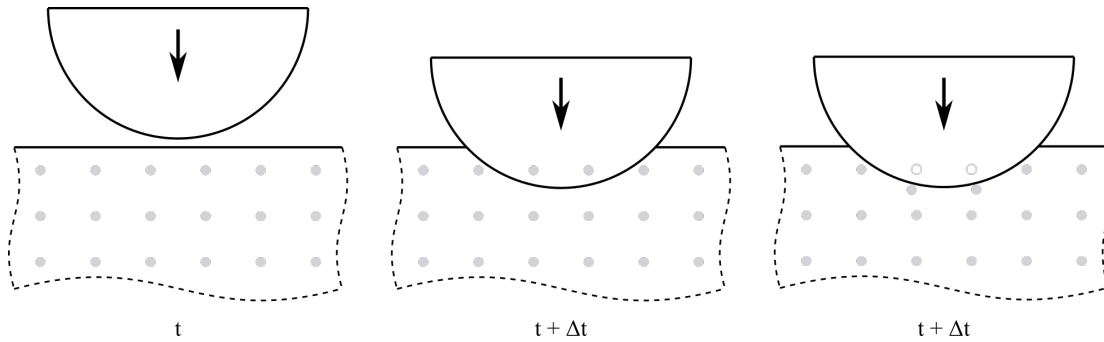


Fig. 4.9 Development of a contact surface between a rigid penetrator and deformable body. Displacement of a particle is equal to the length of the shortest path between the particle and penetrator surface.

## 4.5 Surface correction factors

The derivation of the peridynamic bond stiffness  $c$  is based on the assumption that the horizon of a material point  $\mathcal{H}_x$  is contained completely within the bulk of a body. This assumption does not hold true for nodes within a distance  $\delta$  of the body edge (see Fig. 4.10). Nodes within  $\delta$  of the body edge do not possess a full non-local neighbourhood. Consequently the material properties of nodes contained within the main bulk and nodes within a distance  $\delta$  of the body edge differs. This is known as the peridynamic surface effect.

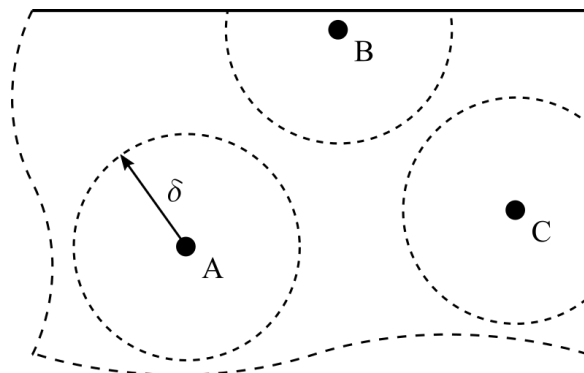


Fig. 4.10 Material point horizons. The horizon of Material Point A is contained completely within the material bulk. The horizon of Material Point B and C lies across the boundary of the peridynamic body.

Nodes that do not possess a full non-local neighbourhood have less interactions (bonds) and this leads to a reduction in material stiffness. Material behaviour is not accurately captured at the free surface of a peridynamic body, and displacements are larger than that

predicted by classical methods. Surface correction factors can be used to correct stiffness softening behaviour.

A number of surface correction schemes exist to correct stiffness softening behaviour. Surface correction schemes can be organised into two categories: (1) methods that modify the force between particle pairs; (2) methods that introduce fictitious nodes at the boundary. Methods in the first category include: the volume method [30], force density method [173, 146, 145], energy method [173, 145], and force normalisation method [143]. The second category contains the fictitious nodes method [93]. Fictitious nodes are added at the surface of a peridynamic body, so that real surface nodes have a full non-local neighbourhood. This is sometimes referred to as a ‘ghost domain’. This method is severely limited by the complexity of its implementation and can only be used to address trivial problems. For a detailed review and comparison of existing correction schemes, see the work of Le and Bobaru [133].

#### 4.5.1 Volume correction method

This work has implemented the volume correction method, first proposed in Chapter 2 of [30]. Le and Bobaru [133] found that the volume method is one of the most effective techniques for correcting surface effects and is relatively simple to implement. Stiffness softening behaviour is corrected by increasing the micromodulus of bonds connected to nodes within a distance  $\delta$  of the free surface. This is done by ensuring that nodes under homogeneous deformation have the same value of strain energy density when located near the surface or within the main bulk.

Fig. 4.11 illustrates the bond connecting node  $\mathbf{x}$  and  $\mathbf{x}'$ . The horizon area/volume of node  $\mathbf{x}$  is  $V(\mathbf{x})$  and the horizon area/volume of node  $\mathbf{x}'$  is  $V(\mathbf{x}')$ . The horizon of both node  $\mathbf{x}$  and  $\mathbf{x}'$  is intersected by the surface boundary and both nodes will experience stiffness softening. The bond that connects node  $\mathbf{x}$  and  $\mathbf{x}'$  must be stiffened to capture the correct material behaviour.

A dimensionless stiffening factor  $\lambda$  is defined by Eq. (4.11), where  $V_0$  is the horizon area/volume of a node within the main bulk. For 3D problems,  $V_0 = 4\pi\delta^3/3$ ; and for 2D problems,  $V_0 = \pi\delta^2$ . The stiffening factor  $\lambda$  will be greater than or equal to 1 because  $V_0$  will always be larger than or equal to  $V(\mathbf{x})$  and  $V(\mathbf{x}')$ . The micromodulus  $c$  of the bond connecting node  $\mathbf{x}$  and  $\mathbf{x}'$  is corrected by multiplying it with the dimensionless stiffening factor  $\lambda$ .

$$c_{corrected} = \lambda c \quad \lambda = \frac{2V_0}{V(\mathbf{x}) + V(\mathbf{x}')} \quad (4.11)$$

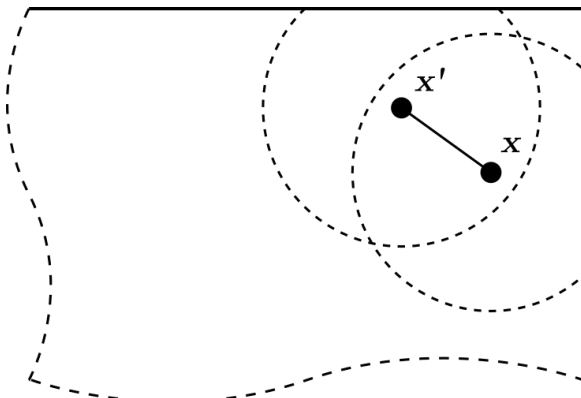


Fig. 4.11 Schematic to illustrate the computation of surface correction factors.

It is demonstrated in section 5.5.3 that the computation of stiffness correction factors is influenced by spatial integration errors.  $V(\mathbf{x})$  and  $V(\mathbf{x}')$  can not be determined exactly and this influences the accuracy of the calculated stiffness correction factor  $\lambda$ . If  $V(\mathbf{x})$  and  $V(\mathbf{x}')$  are underestimated,  $\lambda$  will be higher than expected.

Note that the critical stretch  $s_c$  of a bond has been derived using the assumption that every bond has the same value of stiffness  $c$ . This assumption does not hold true if a surface correction scheme that modifies bond properties is applied. It is shown in Chapter 5 that the application of surface correction factors produces a toughening effect. A critical stretch correction scheme is proposed that is simple to implement and yields improved results.

## 4.6 Implicit time integration

Implicit methods can be used to directly solve problems where dynamic effects are negligible. Due to the simplicity, computational efficiency, and robustness of explicit schemes, implicit methods are rarely found in the peridynamic literature. Significant time was spent developing an implicit solver but due to time constraints the code was not used. The code has been verified against the explicit solver but optimisation of the code would be required to address large scale problems with hundreds of thousands of particles. This section has been included to provide the reader with an understanding of the advantages and disadvantages of implicit schemes. Further to this, solution procedures are not readily available in the literature.

### 4.6.1 Static formulation

Often the static solution is of most interest and dynamic effects are negligible. By setting the acceleration component of the equation of motion to zero, it is possible to directly find a

solution by solving a system of linear equations [243]. The discretised form of the governing equation for static problems is defined by Eq. (4.12).

$$0 = \sum_p \mathbf{f}(\mathbf{u}_p^n - \mathbf{u}_i^n, \mathbf{x}_p - \mathbf{x}_i) dV_p + \mathbf{b}_i^n \quad (4.12)$$

The pairwise force function  $\mathbf{f}$  must be linearised. By linearising the pairwise force function, it becomes possible to study the behaviour of a non-linear function near a given point using tools from the analysis of linear systems. Linearisation of the bond-based peridynamic theory is discussed in [203, 248, 210]. A linearised form of Eq. (4.12) is given by Eq. (4.13). Eq. (4.13) is first given by Macek and Silling [143] and further details are provided in [197, 181].

$$0 = \sum_p \left[ c \frac{\xi \otimes \xi}{|\xi|^3} \eta \right]_{ip} dV_p + \mathbf{b}_i^n \quad (4.13)$$

#### 4.6.2 Local and global stiffness matrix

From the linearised force function, the local stiffness matrix of a bond can be defined. The element stiffness matrix in three-dimensions is defined by Eq. (4.14).

$$[\mathbf{K}]_{bond} = \frac{c}{|\xi|^3} (1-d) \alpha \Delta V_i \Delta V_p \begin{vmatrix} \xi_x^2 & \xi_x \xi_y & \xi_x \xi_z & -\xi_x^2 & -\xi_x \xi_y & -\xi_x \xi_z \\ \xi_x \xi_y & \xi_y^2 & \xi_y \xi_z & -\xi_x \xi_y & -\xi_y^2 & -\xi_y \xi_z \\ \xi_x \xi_z & \xi_y \xi_z & \xi_z^2 & -\xi_x \xi_z & -\xi_y \xi_z & -\xi_z^2 \\ -\xi_x^2 & -\xi_x \xi_y & -\xi_x \xi_z & \xi_x^2 & \xi_x \xi_y & \xi_x \xi_z \\ -\xi_x \xi_y & -\xi_y^2 & -\xi_y \xi_z & \xi_x \xi_y & \xi_y^2 & \xi_y \xi_z \\ -\xi_x \xi_z & -\xi_y \xi_z & -\xi_z^2 & \xi_x \xi_z & \xi_y \xi_z & \xi_z^2 \end{vmatrix} \quad (4.14)$$

Where  $\xi_x$ ,  $\xi_y$ , and  $\xi_z$  are the components of the bond vector between the particles  $i$  and  $p$ ,  $\alpha$  is the volume correction factor, and  $(1-d)$  controls the slope of the bond force-stretch relationship.  $d$  is a softening parameter that is required for constitutive models with softening behaviour. For a derivation of the local stiffness matrix, the reader is referred to [197, 45, 181].

The next step is to assemble the global stiffness matrix. See the work of Sarego [197] for a detailed description of the assembly procedure. Fig 4.12 illustrates the typical sparsity structure of the global stiffness matrix for a peridynamic model. This example contains 3,500 nodes and approximately 160,000 bonds. The global matrix provides a description of the coupling between nodes. The banded diagonals represent the non-local nature of the

peridynamic theory. The diagonals are banded because nodes in the peridynamic system are not coupled arbitrarily. The number of bands is related to the  $m$ -ratio (in this case  $m = 3$ ). To reduce the memory requirements, the sparse stiffness matrix is stored using the Compressed Sparse Column (CSC) storage format. Assuming a regular grid and constant horizon, the stiffness matrix will be symmetric and only the upper triangle need be stored [181].

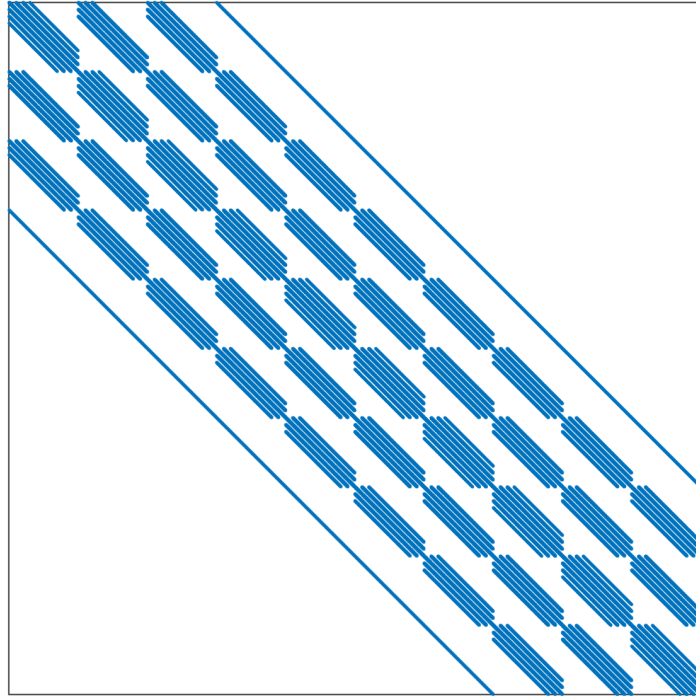


Fig. 4.12 Sparsity structure of the global stiffness matrix  $[\mathbf{K}]_{global}$

The global equilibrium equation of a bond-based peridynamic model in matrix form is given by Eq. (4.15), where  $\{\mathbf{F}_{ext}\}$  is the external force vector,  $[\mathbf{K}]_{global}$  is the global stiffness matrix and  $\{\mathbf{U}\}$  is the nodal displacement vector.

$$\{\mathbf{F}_{ext}\} = [\mathbf{K}]_{global}\{\mathbf{U}\} \quad (4.15)$$

The next step is to solve the sparse system of equations. For linear problems, the system of equations can be solved directly  $\mathbf{u} = \mathbf{K}^{-1}\mathbf{f}$ . For non-linear problems, an incremental-iterative procedure must be employed. The solution procedure is described in the next section.

### 4.6.3 Solution procedure

This section outlines the solution procedure for linear and non-linear problems. The use of implicit solvers for peridynamic models has been examined and discussed in [139, 197, 166, 181].

The aim of the solution procedure is to determine the displacement of all nodes (the displacement vector) so that the internal and external forces are in equilibrium ( $\mathbf{f}_{int} = \mathbf{f}_{ext}$ ), and the boundary conditions are satisfied. When the load-displacement relationship is linear, the solution (displacement vector) can be found in a single step. A system of equations in the form  $\mathbf{Ku} = \mathbf{F}$  can be solved directly by inverting the stiffness matrix to solve for the unknown displacements.

Generally, the load-displacement relationship will be non-linear. The two main sources of non-linearities are geometric non-linearity and material non-linearity. Material non-linearities occur when the stress-strain relationship is non-linear or due to crack nucleation and propagation. For non-linear problems, the system of equations must be solved with an incremental-iterative solution procedure.

To obtain a numerical solution, the system must be discretised in time. In static analysis, time is a pseudo-time that describes a sequence of events. The simulation is divided into a series of load steps at which static equilibrium is enforced. For every given time increment (load step), the boundary conditions are updated and the displacement vector that satisfies the equilibrium conditions must be determined.

After the external force vector is updated, the linear system of equations is solved to determine the nodal displacements. Iterative methods such as the biconjugate gradient method can be used to solve the sparse system of equations. The next step is to check that the solution satisfies the equilibrium equations. The residual force vector  $\mathbf{r}$  (out of balance force vector), defined by Eq. (4.16), must be equal or close to zero.

$$\mathbf{r} = \mathbf{f}_{ext} - \mathbf{f}_{int} = \mathbf{0} \quad (4.16)$$

For a non-linear solution, the system will be out of equilibrium, and an iterative procedure must be used to determine the nodal displacements so that equilibrium is satisfied. The convergence criteria for the non-linear solver are defined by the scalar-valued residual  $r$  and tolerance value. The scalar-valued residual is defined as the  $\ell_2$ -norm of  $\mathbf{r}$ . The tolerance is set to be 0.5% of the total force in the system. If the residual force is less than the tolerance, the next load step is applied. If the residual force is greater than the tolerance, a loop employing a Newton-Raphson convergence scheme is used until the desired tolerance is met. Once

the equilibrium conditions have been met, the next load step can be applied. The solution procedure is outlined in Fig. 4.13.

When using displacement-controlled loading, the external force vector is not increased directly. The prescribed displacements must be incorporated into the external force vector to obtain a first prediction of nodal displacements. The implemented displacement-controlled solver is based on that described by De Borst et al. [65]. For a detailed discussion of the merits of load and displacement controlled Newton-Raphson schemes, the reader is referred to the work of Rots [195].

A displacement-controlled Newton-Raphson solver will fail to converge when a strain-softening material model is used and a path-following method must be employed [65]. Sun et al. [213] implemented an arc-length method [189] within a peridynamic framework. The arc-length method is applied at the onset of energy dissipation. Concrete is a strain-softening material and a path-following method, such as the arc-length method, must be implemented to capture the full post-peak structural response.

Accurately predicting crack paths also requires some special considerations. When an unlimited number of bonds are allowed to fail in every iteration, the fracture pattern becomes smeared. Ni et al. [166] found that by limiting the number of bonds broken per iteration, predictions of the fracture behaviour are improved. Methods that limit the number of bonds broken per iteration will become extremely computationally expensive when the limit is small. High computational expense is a factor that is often cited against the use of implicit solvers. Prakash and Stewart [181] found that implicit schemes are an order of magnitude faster than explicit schemes for a simple static problem without damage. However, for a quasi-static fracture problem, implicit methods require a large number of load steps and iterations, and explicit schemes are significantly faster. There is still a significant amount of work that needs to be done before implicit schemes can be used to efficiently address large scale problems.

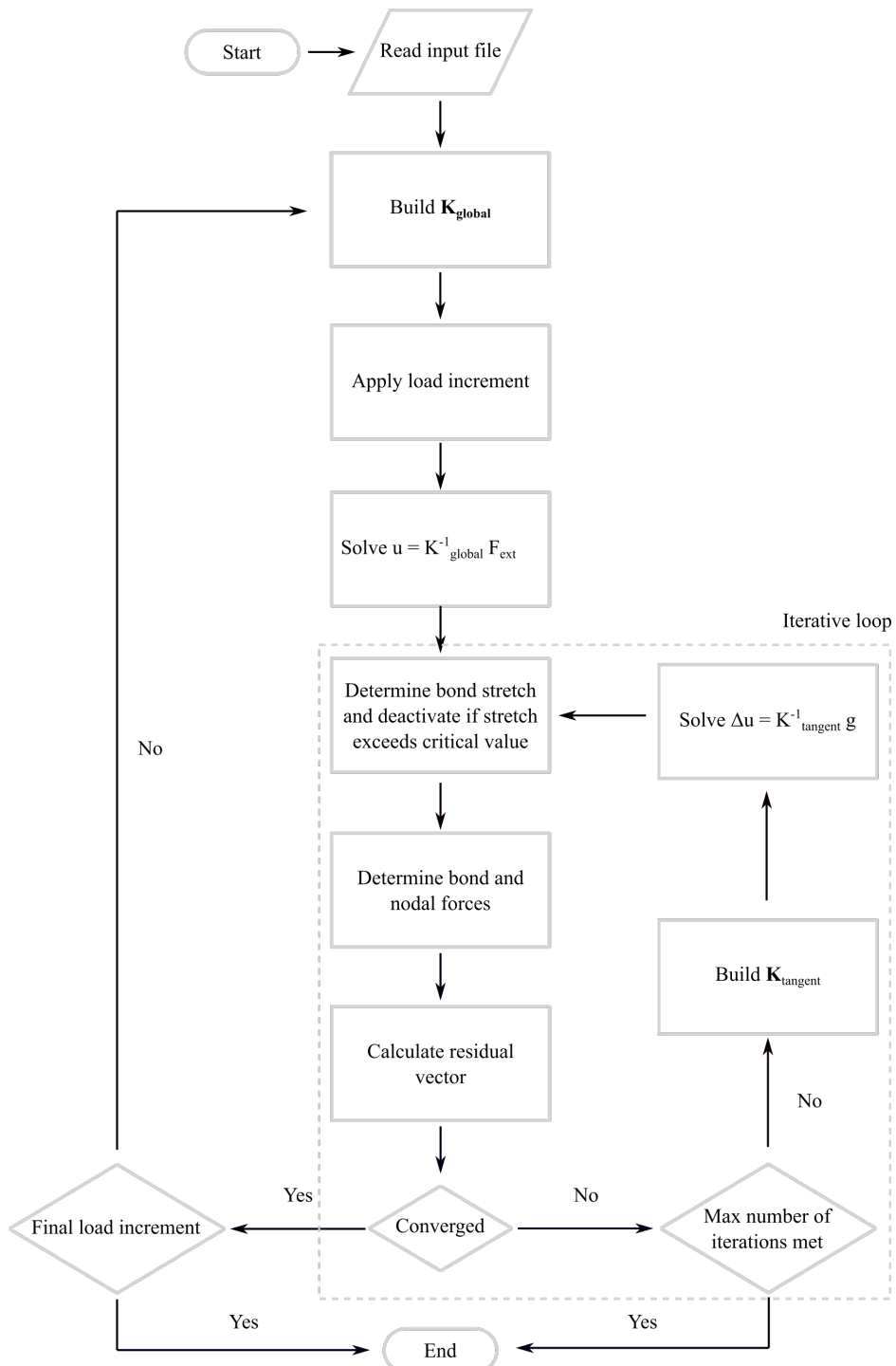


Fig. 4.13 Schematic of an implicit scheme with load-control. After every time *increment* (load step), an *iterative* solution algorithm must be used to determine the equilibrium state, hence the solution process is known as an *incremental-iterative* procedure.

## 4.7 Reducing computational expense

The computationally demanding nature of peridynamics is a major barrier to tackling large scale industry-motivated problems. Peridynamic models are computationally expensive due to the non-local nature of the governing equations. Simulating large problems of interest, on the order of hundreds of thousands to tens of millions of particles, requires vast computational resources. A number of strategies are available to minimise computational effort: (1) employ a multi-scale discretisation scheme and refine the mesh in areas of interest [187, 188, 117]; (2) adaptively refine the mesh at crack tips [33, 31, 71, 100]; (3) couple peridynamic and finite element meshes [141, 86]; (4) exploit parallel computing techniques and multi-thread processing.

### 4.7.1 Parallel processing

Peridynamics lends itself well to parallel processing techniques and solvers have been developed on distributed and shared memory architectures. The Message Passing Interface (MPI) has been the dominant parallel programming model for developing highly scalable codes on distributed memory platforms. MPI-based codes use spatial decomposition, in which the physical space is decomposed into multiple subdomains, and each subdomain is assigned to a unique compute node (each node has its own local memory). This approach is necessary for problems with large memory requirements. A number of peridynamic solvers have been developed that utilise MPI [204, 176, 177]. EMU, developed by Silling [204], was the first computational peridynamics code. EMU is a parallel MPI based Fortran code [42]. This code is not publicly available. The number of cores per compute node has rapidly increased in recent years and shared memory approaches have been widely adopted. OpenMP (Open Multi-Processing application programming interface) is the standard for developing shared memory multi-threaded code. OpenMP has been used in multiple works [130, 78, 134]. Parallelisation with OpenMP is efficient and simple to implement but is constrained by the memory of a single compute node. Hybrid applications can be developed for large scale clusters, where MPI is used for parallelism across compute nodes and OpenMP is used for parallelism within a multi-core compute node. Hybrid MPI/OpenMP approaches have been employed by Dalla Barba et al. [63] and Ha [103]. HPX (High Performance ParallelX) has recently been employed by Diehl et al. [68] to develop a scalable peridynamics code. Exploiting the ‘massively parallel’ nature of Graphics Processing Units (GPUs) provides opportunities for greater speedups. Mossaiby et al. [158] developed a GPU accelerated solver using OpenCL. Boys et al. [41] made further improvements by utilising local memory on a GPU.

In this work, the developed code makes use of shared memory parallelism using OpenMP. The scalability of the code has been tested on the University of Cambridge High Performance Cluster using a single Cascade Lake Node with 56 cores. The implementation is approximately 5-8 times faster than a serial implementation. The GPU implementation of Boys et al. [41] provides a 4-7 times performance gain over the OpenMP implementation. Scaling up to problems with tens of millions of particles requires the use of distributed memory architectures. The largest problem considered in this thesis consists of approximately one million particles.

#### 4.7.2 Family member search and data structures

A key step in a peridynamic simulation is the establishment of nodal family members. A naive implementation would calculate the distance between the current node and every node in the body. Nodes located within the horizon radius  $\delta$  would be added to the family members of the current node. This method is fine for small problems but becomes extremely computationally expensive as the problem size increases. The time complexity of a brute force method is  $\mathcal{O}(N^2)$  where  $N$  is the number of particles. Sophisticated data structures are used to provide efficient neighbour searches, fast data access, and overcome memory limitations. Space partitioning data structures, such as K-dimensional trees, provide an efficient method for finding all neighbours within a specified cut off distance. The computational complexity of the nearest neighbour search can be reduced from  $\mathcal{O}(N^2)$  to  $\mathcal{O}(N \log N)$  [158]. In this work, nodal families are determined using a K-d tree search. Building the nodal families for a problem with one million nodes takes less than 5 minutes as opposed to many hours when using a brute force method. For most problems, the family member search is only performed once when creating the input file. For some problems, such as dynamic impact problems, the family member search might be repeated multiple times as the simulation progresses. See the work of Vazic et al. [221] for a detailed examination of family search algorithms.

A neighbour list is used to efficiently store the particle families. A neighbour list is a data structure used to store a list of particles within a specified cut off distance of each other. Particles are stored in pairs (sometimes known as a bond list). The calculation of nodal forces can be carried out in a single loop rather than two loops when neighbour lists are stored as pairwise interactions [140]. Fraga Filho et al. [85] found that the storage of particles as pairwise interactions (bonds) leads to a significant reduction in computational expense.

## 4.8 Code structure

The author has developed a three-dimensional bond-based peridynamic code in MATLAB and C. The code is structured into three modules: (1) input module, (2) core computational kernel, (3) post-processing module. The input and output of data is controlled by a programme written in MATLAB. The core functions are written in C and called from MATLAB for optimal performance. The use of MATLAB as an interface makes the code more accessible to engineers and researchers. The code makes use of shared memory parallelism using OpenMP. The scalability of the code has been tested on a Cascade Lake Node with 56 cores.

### 4.8.1 Input module

The input module contains a number of tools to build an input file. The input file defines the entire model and includes nodal coordinates, node families, connectivity information (bond list), boundary conditions, and material properties. The input file is created and saved to disk before being loaded into the solver. The procedure to build an input file is as follows:

- Discretise spatial domain (build material point coordinates)
- Build node families
- Build bond list (neighbour list)
- Define boundary conditions
- Assign material properties to nodes and bonds
- Calculate partial volume correction factors (to improve spatial integration accuracy)
- Calculate surface correction factors (to correct the peridynamic surface effect)

### 4.8.2 Core computational kernel

This section describes the structure of the core computational kernel. A schematic of a time step in the explicit scheme for a quasi-static displacement controlled test is provided in Fig 4.14. This procedure has been used to generate all the results presented in this thesis. A load-controlled procedure can also be employed. An implicit scheme is available but has not been optimised for solving large problems. Code functionality is controlled by a configuration file that can be edited by the user.

Simulation parameters must be defined before run time. Parameters to be defined include: time step size, number of time steps, damping coefficient, and magnitude of applied displacement. During run-time, the steps depicted in grey are run in parallel. The number of threads for a parallel region needs to be defined before run time. The calculation of bond forces, and their reduction to nodal forces is the most computationally expensive part of a peridynamic code. For larger problems (100,000 nodes or greater), it was found that these two steps account for 80% or more of the runtime.

Simulation data is written to a text file at a specified frequency, the default is every 50 time steps. The text file contains a summary of the input file and time histories of relevant parameters: displacement, reaction force, total internal energy, kinetic energy. The print function can be easily modified to write other parameters. The overhead of writing data to a text file is relatively small. Output files are saved at a specified frequency, the default is every 1000 time steps. The output files contain nodal and bond data, including nodal displacements and damage. The overhead of saving output files to disk is large and this must be considered when defining the output frequency.

### 4.8.3 Post-processing module

The post-processing module provides a number of tools for the processing and visualisation of results. The module reads in output files from the solver and extracts and plots particle data. The most common use case is to visualise crack paths by plotting damage at nodal points. The post-processing module also provides functionality for determining stress and strain at nodal points. The peridynamic theory discards with the notion of stress and strain, however, it is still possible to relate peridynamic variables to the classical theory of solid mechanics. Using concepts from the state-based theory, the deformation gradient tensor at every node can be determined [208]. From this, it is possible to determine the stress and strain tensor at a material point. See the work of Ballarini et al. [7] and Fallah et al. [77] for more details on the non-local stress tensor.

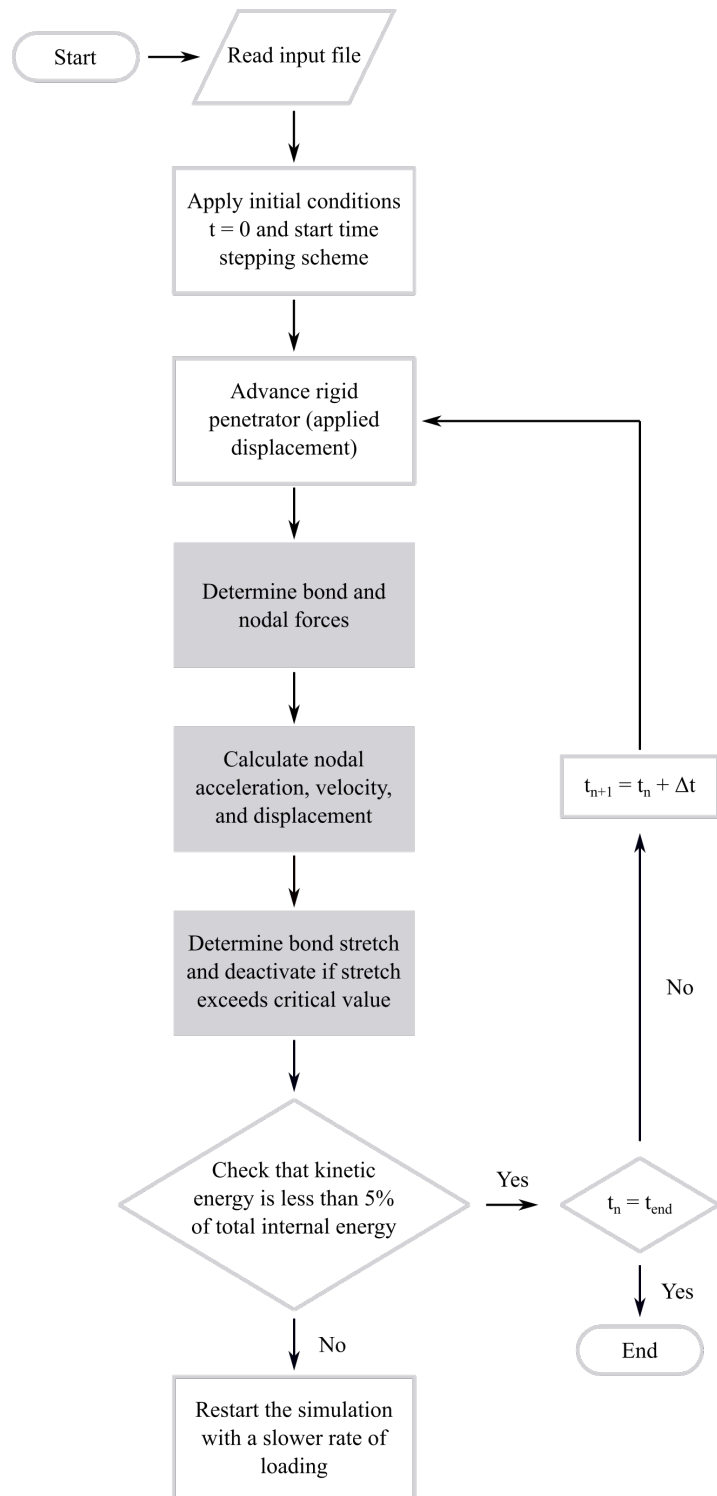


Fig. 4.14 Schematic of a quasi-static explicit solver with displacement-controlled loading



# Chapter 5

## Modelling of quasi-brittle materials

### 5.1 Introduction

This chapter examines the modelling of quasi-brittle materials using a three-dimensional bond-based peridynamic model. The aims of this chapter are as follows: (1) quantify the predictive accuracy of existing constitutive laws; (2) introduce a non-linear softening constitutive law; (3) validate the model against experimental data from the literature.

A detailed examination of constitutive laws is missing from the literature and this work addresses that gap. Notched and unnotched concrete beams are modelled to investigate the effect of different boundary types on the predictive accuracy of the peridynamic model. It is known that non-local models can fail to accurately capture the structural response for different boundary types [109]. Mode I and mixed-mode problems are considered to evaluate the generality of the model. Numerical predictions are validated against experimental results and the following validation metrics are used: load-CMOD response, ultimate load capacity, crack path and energy dissipation behaviour. To the best of the author's knowledge, this is the first time that energy dissipation in quasi-brittle materials has been investigated using a peridynamic model. The influence of mesh refinement on the load-CMOD response and damage energy dissipation is examined for notched and unnotched cases. All problems considered in this work are three-dimensional; the vast majority of papers in the literature only consider two-dimensional problems [69].

By following a rigorous validation process, new insights into the predictive capabilities of the bond-based model are gained. It is shown that the application of surface correction factors produces a toughening effect. The energy required to produce a fracture surface at the edge of a peridynamic body is significantly higher than the material fracture energy  $G_F$ . Consequently, a higher applied force is required to initiate and propagate a crack. This is the first time that this effect has been described. A correction scheme is proposed that is simple

to implement and yields improved results. This is perhaps the most important contribution of this chapter.

The chapter is organised as follows: Section 5.2 briefly reviews the failure of quasi-brittle materials. Section 5.3 reviews existing constitutive laws and a new non-linear softening model is introduced. Section 5.4 examines the predictive accuracy of different constitutive laws. The numerical results are validated against experimental data published by Grégoire et al. [98]. Notched and unnotched concrete beams are modelled to examine the effect of different boundary types on the predictive accuracy of a peridynamic model. Predictions with the newly proposed non-linear softening law improve upon existing laws. Section 5.5 presents a numerical examination of energy release rates in the discrete peridynamic model. It shows that the application of surface correction factors produces a toughening effect. A correction scheme is proposed that is simple to implement and yields improved results. Section 5.6 presents a mesh sensitivity study. Section 5.7 provides an examination of damage energy dissipation. Section 5.8 examines the accuracy and generality of the non-linear softening law against the mixed-mode fracture tests of García-Álvarez et al. [88]. Section 5.9 provides a discussion of the results and areas of future work are identified. Section 5.10 concludes the chapter and summarises the findings. All the results presented in this chapter were obtained using the explicit scheme outlined in Fig. 4.14.

## 5.2 Failure process

Fig. 5.1 illustrates the tensile stress-strain curve for concrete. Concrete is a quasi-brittle material, sometimes referred to as a cohesive-brittle material. After the peak stress is reached, the stress progressively decreases due to material cohesion and friction effects [179, 185]. The mechanical behaviour of quasi-brittle materials can be divided into three distinct stages: (1) linear elastic behaviour, (2) development of distributed micro-cracking, (3) localisation of damage and formation of macroscopic cracks [179]. The mesostructure of concrete is characterised by the random distribution of aggregates, voids, and mortar. The heterogeneous nature of concrete complicates efforts to accurately predict the mechanical behaviour, and capturing the physical mechanisms that govern the behaviour of quasi-brittle materials remains an open problem.

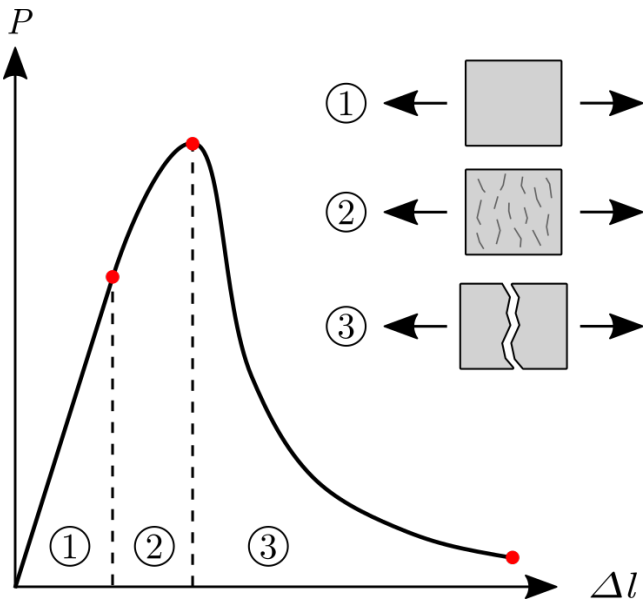


Fig. 5.1 Tensile stress-strain curve for concrete: (1) linear elastic behaviour, (2) development of distributed micro-cracking, (3) localisation of damage and formation of macroscopic cracks.

### 5.3 Constitutive laws

This section presents and discusses the different constitutive laws that have been proposed within the bond-based peridynamic framework and applied to the simulation of quasi-brittle materials.

A key advantage of using a bond-based peridynamic model is the simplicity of the constitutive law. It is generally assumed that the force-stretch ( $f$ - $s$ ) relationship of a peridynamic bond should be consistent with the macroscopic material response, and a failure mechanism is introduced into the model by eliminating the interaction between particle pairs when the stretch of the connecting bond exceeds a critical value. No additional methods are required to describe crack initiation and growth.

A number of constitutive laws have been proposed within the bond-based peridynamic framework, including: linear [207], bilinear [93, 243, 30, 194], trilinear [236], and decaying exponential [219] forms. A new non-linear softening model is introduced in this chapter that is more consistent with the tensile stress-strain behaviour of concrete. Detailed studies on the predictive accuracy of constitutive laws for quasi-brittle materials are still needed.

It should be noted that the compressive failure of bonds is not considered in any of the following models. The fracture behaviour of concrete at a micro and meso level is essentially a tensile phenomenon, even whilst under compression [154]. Cornelissen et al. [57] state

that the failure of concrete is induced by the initiation and propagation of cracks which are governed by the tensile properties.

### 5.3.1 Linear

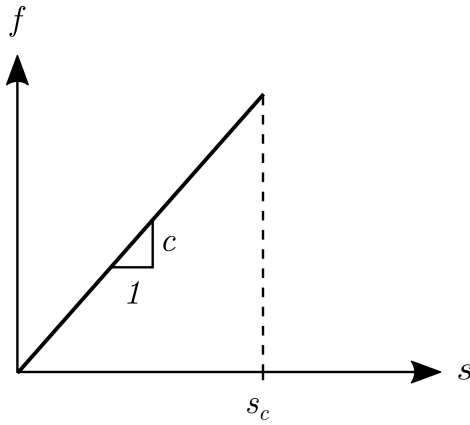


Fig. 5.2 Linear damage model ( $f$ - $s$ )

The linear elastic damage model, introduced by Silling and Askari [207] and illustrated in Fig. 5.2, was proposed for capturing the behaviour of ideal-brittle materials. The linear model has been used to accurately capture complex fracture patterns in glass and ceramic materials [104, 105]. The linear model has also been applied to the modelling of concrete structures and has achieved reasonable results [93, 141], but the use of linear damage models for concrete is primarily suited to the analysis of large structures (e.g. large dams with aggregate sizes up to 80mm). Due to the size effect law, the fracture behaviour of large concrete structures can be considered as brittle. This assumption can be made when the size of the fracture process zone is insignificant compared to the size of the structure [11]. Eq. (5.1) defines the critical stretch for a three-dimensional peridynamic material.

$$s_c = \sqrt{\frac{10G_F}{\pi c \delta^5}} = \sqrt{\frac{5G_F}{6E\delta}} \quad (5.1)$$

### 5.3.2 Bilinear

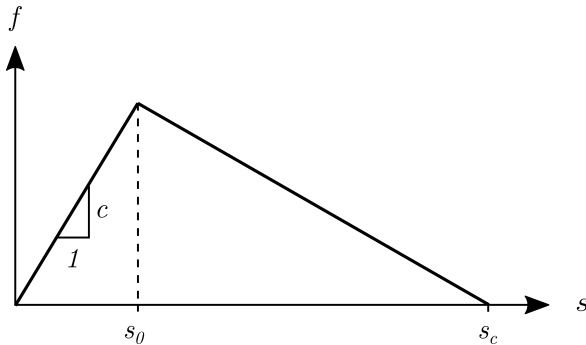


Fig. 5.3 Bilinear damage model ( $f$ - $s$ )

In small and medium sized structures, concrete acts as a quasi-brittle material and exhibits strain-softening behaviour when in tension. The linear damage model does not consider softening behaviour, and this limits its ability to capture the true behaviour of concrete structures.

Gerstle et al. [93] recognised this limitation and proposed a bilinear damage model, illustrated in Fig. 5.3. No details were provided for determining the value of the bond stretch at the linear elastic limit  $s_0$ , or the value of the bond stretch at failure  $s_c$ . Zaccariotto et al. [243] determined the parameters of the bilinear damage model with material fracture energy  $G_F$  and experimental load-displacement curves. The energy required to start the fracture process is defined as  $G_0$  and  $k_r$  is the ratio  $s_c/s_0$ . Note that in this case,  $G_0$  is different to the peridynamic energy release rate. The stretch at the linear elastic limit  $s_0$  is defined by Eq. (5.2) and  $k_r$  is determined from experimental load-displacement curves or through sensitivity studies. Examples of a concrete like material in three-point bending and a concrete four-point shear beam test were provided. For the concrete member,  $k_r$  is set at 20. All examples are two-dimensional and further validation of the bilinear damage model is required. A clear weakness of this method is the large degree of uncertainty in the selection of  $k_r$ .

$$s_0 = \sqrt{\frac{5G_0}{6E\delta}} \quad k_r = \frac{s_c}{s_0} = \frac{G_F}{G_0} \quad (5.2)$$

A bilinear damage model capable of reproducing fracture energy  $G_F$  and crack nucleation strain independently is introduced in Chapter 2 of [30]. According to the original linear damage model, bonds break when their stretch  $s$  exceeds a critical value  $s_c$  that has been calibrated to the material fracture energy  $G_F$ . This implies that  $s_c$  is the crack nucleation strain. The problem, as pointed out in [30], is that the critical stretch  $s_c$  depends strongly on the horizon  $\delta$  and cannot be specified independently of  $G_F$ . The fracture energy  $G_F$

and crack nucleation strain can be defined independently by adding a softening tail to the constitutive law. The crack nucleation strain is the linear elastic limit of a bond  $s_0$ , and can be approximated by  $f_t/E$ , where  $f_t$  is the tensile strength, and  $E$  is the elastic modulus. The critical stretch  $s_c$  can then be defined so that the energy release rate calculation agrees with  $G_F$  (see Eq. 5.3). This model assumes that  $s_c \geq s_0$ , which imposes a constraint on the selection of the horizon  $\delta$  and thus restricts the mesh spacing.

$$s_c = \frac{5G_F}{6E\delta s_0} \quad s_0 = \frac{f_t}{E} \quad (5.3)$$

Rossi Cabral et al. [194] recently proposed a bilinear model that introduces a material horizon related to the characteristic length of the material, and a numerical horizon that is chosen for convenience. It is claimed that the proposed model improves the flexibility of the model calibration and reduces the computational cost. The parameters in the constitutive model are defined independently of the horizon radius  $\delta$  (which is assumed to be a material property) and a convenient mesh discretisation can be used. Validation is performed on three-dimensional sandstone specimens subjected to uniaxial tension. Note that Rossi Cabral et al. [194] assumed that the peridynamic horizon is a material parameter, but the results presented in this thesis have revealed no evidence to support the hypothesis that the horizon is an intrinsic material property.

To capture the degradation in bond stiffness, a new damage parameter must be introduced into the bond force calculation. The stiffness of a damaged bond  $c_d$  is defined by Eq. (5.4), where  $d$  is a softening parameter given by Eq. (5.5). Note that the value of  $d$  will range from 0 to 1, where 0 indicates that the bond is still in the elastic range, and 1 represents a bond that has failed.

$$c_d = c(1 - d) \quad (5.4)$$

$$d = \begin{cases} 0 & \text{if } s < s_0 \\ \frac{s - s_0}{s} \cdot \frac{s_c}{s_c - s_0} & \text{if } s_0 \leq s < s_c \\ 1 & \text{if } s \geq s_c \end{cases} \quad (5.5)$$

### 5.3.3 Trilinear

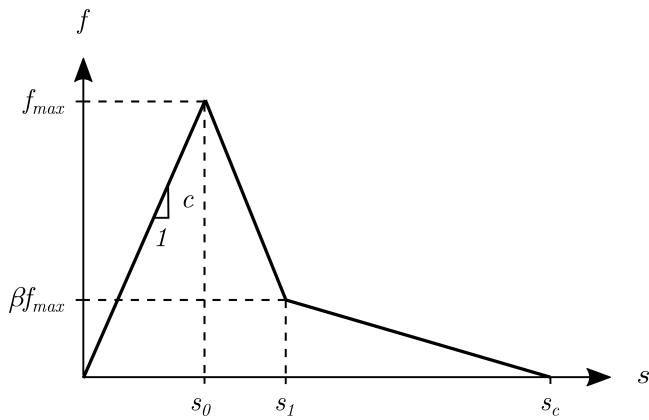


Fig. 5.4 Trilinear damage model ( $f$ - $s$ )

It is generally assumed that the behaviour of an individual bond should be consistent with the macroscopic material response. The tension softening branch of the bilinear damage model is not consistent with the true softening behaviour of concrete. The complete tensile stress-strain curve of concrete is illustrated in Fig. 5.1.

Yang et al. [236] established a new trilinear damage model within the bond-based peridynamic framework, illustrated in Fig. 5.4. The authors assume that the softening behaviour of a peridynamic bond is equivalent to the bilinear tension softening law proposed by Petersson [179], illustrated in Fig. 5.5. The bilinear softening stress-separation law has been widely adopted to predict the softening behaviour of quasi-brittle materials using cohesive zone models (CZM).  $f_t$  represents the tensile strength of concrete, and  $w$  represents the crack opening width. The area below the softening curve is assumed to be the material fracture energy  $G_F$ .

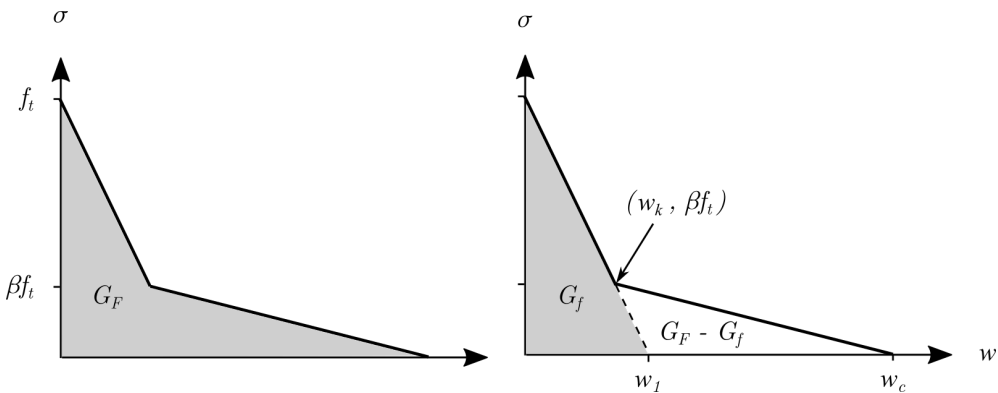


Fig. 5.5 Bilinear tension softening constitutive law ( $\sigma$ - $w$ ). Adapted from [10, 236].

A generalised method for determining the parameters  $s_0$ ,  $s_1$ , and  $s_c$  was proposed and only requires elastic modulus  $E$ , tensile strength  $f_t$ , and fracture energy  $G_F$ .

Bonds begin to damage when the stretch exceeds  $s_0$  and the initiation of micro-cracking occurs. The linear elastic limit  $s_0$  is defined empirically as  $f_t/E$ , and corresponds approximately to the ultimate tensile strain of concrete. This definition of  $s_0$  is a potential issue with the proposed model. The value of  $s_0$  is a constant for any mesh discretisation and is therefore not objective. Tong et al. [219] state that it is not physically reasonable to link the elastic limit  $s_0$  to the macroscopic tensile limit  $f_t$ .

The position of the kink point in the softening curve is determined with the initial fracture energy  $G_f$ , as proposed by Bažant [10]. The initial fracture energy  $G_f$  is the area under the initial descending slope of the softening curve, illustrated in Fig. 5.5, and controls the load capacity of a member. Therefore,  $w_1$  can be determined as follows:

$$w_1 = \frac{2G_f}{f_t} \quad (5.6)$$

Assuming that the gradient of the descending slope changes at  $\beta f_t$ , the critical crack opening width  $w_c$  can be defined as follows:

$$w_c = \frac{2}{\beta f_t} [G_F - (1 - \beta)G_f] \quad (5.7)$$

The stress at the kink point is generally considered to be between  $0.15f_t$  and  $f_t/3$  [10]. Yang et al. [236] set  $\beta$  to  $1/4$ . The material fracture energy  $G_F$  and initial fracture energy  $G_f$  are related through Eq. (5.8). This relationship is reported in the literature [10].

$$G_F \approx 2.5G_f \quad (5.8)$$

The position of the change in gradient can be determined as follows:

$$\beta = \frac{w_1 - w_k}{w_1} \rightarrow w_k = w_1(1 - \beta) \quad (5.9)$$

$$\frac{w_c}{w_k} = \frac{3 + 2\beta}{2\beta(1 - \beta)} \quad (5.10)$$

The position of the change in gradient in Fig 5.4 is defined by Eq. (5.11).

$$\gamma = \frac{s_c - s_0}{s_1 - s_0} = \frac{3 + 2\beta}{2\beta(1 - \beta)} \quad (5.11)$$

$s_1$  is defined by Eq. (5.12).

$$s_1 = s_0 + \frac{s_c - s_0}{\gamma} \quad (5.12)$$

The energy consumed by a bond during the softening stage is denoted by  $w$ . Eq. (5.13) is derived by determining the energy consumed between the limits  $s_0$  to  $s_c$ .

$$w = \frac{cs_0\xi(s_c - s_0)(1 + \gamma\beta)}{2\gamma} \quad (5.13)$$

By determining the critical energy release rate for a three-dimensional peridynamic body and rearranging, the critical bond stretch  $s_c$  is obtained.

$$s_c = \frac{10\gamma G_F}{\pi\delta^5 cs_0(1 + \gamma\beta)} + s_0 \quad s_0 = f_t/E \quad (5.14)$$

The softening parameter  $d$  for a trilinear model is defined by Eq. (5.15), where  $\eta = s_1/s_0$ .

$$d = \begin{cases} 0 & \text{if } s < s_0 \\ 1 - \frac{\eta - \beta}{\eta - 1} \cdot \frac{s_0}{s} + \frac{1 - \beta}{\eta - 1} & \text{if } s_0 \leq s < s_1 \\ 1 - \beta \cdot \frac{s_0}{s} \cdot \frac{s_c - s}{s_c - s_1} & \text{if } s_1 \leq s < s_c \\ 1 & \text{if } s \geq s_c \end{cases} \quad (5.15)$$

Yang et al. [236] validated the trilinear model against experimental data published in the literature. Plain concrete members in three-point bending were simulated using a two-dimensional numerical model. Concrete members with different strengths, dimensions, and notch-depth ratios were examined. Comparisons with a linear and bilinear damage model were provided. Predictions with the trilinear model show close agreement with experimental load-CMOD data. The bilinear model overestimates the peak load but the softening behaviour is similar to that observed experimentally. The linear damage model significantly overestimates the failure load of concrete members. This behaviour is observed in quasi-brittle materials (such as concrete), because fracture energy is predominantly the integral of the work consumed by the bond during the softening stage. This is effectively the opposite of an ideal-brittle material (such as glass), where all the fracture energy is consumed during the elastic stage.

The trilinear model has also been used by Diana et al. [67] within an implicit micropolar peridynamic framework. Numerical results were compared against experimental fracture data but load-deflection data was not provided. Work remains to validate the predictive accuracy of the trilinear constitutive model.

### 5.3.4 Non-linear

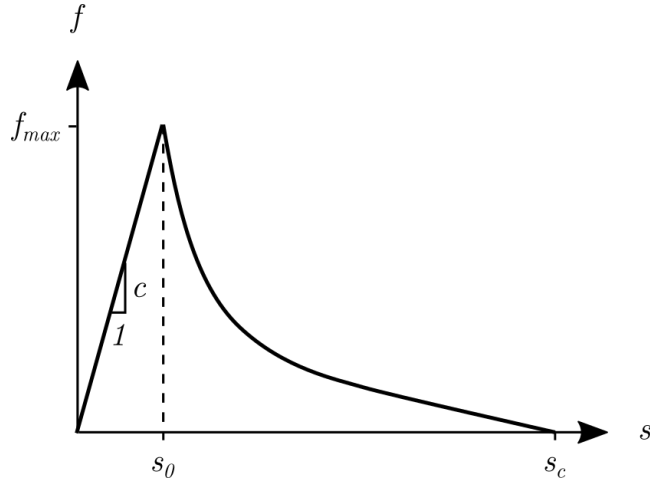


Fig. 5.6 Non-linear damage model ( $f$ - $s$ ). The force-stretch relationship is described by an exponentially decaying model with a linear term that forces the curve to intersect with the horizontal axis at  $s_c$ .

In 1976, Hillerborg et al. [113] made a major advance in the modelling of concrete fracture through the introduction of a cohesive crack model. Hillerborg defined the softening curve as a decaying exponential with a horizontal asymptote below the crack width  $w$  axis. For simplicity, the bilinear form was later introduced by Petersson [179] and has been widely adopted. Implementing a non-linear softening law within a bond-based peridynamic framework is relatively simple and might improve predictions of failure behaviour.

Tong et al. [219] recently introduced an exponentially decaying law for modelling quasi-brittle materials within a bond-based framework. Tong et al. [220] expanded this work to a state-based framework. The model is defined by three parameters: the linear elastic limit  $s_0$ , a bond force reduction parameter  $k$ , and a bond residual force parameter  $\alpha$ .  $k$  is essentially the rate of decay. The model proposed by Tong et al. [219] is not completely satisfactory as there is a degree of ambiguity surrounding the stretch value at which bond failure occurs. The proposed softening model is asymptotic with the horizontal axis and thus never intersects. This implies that bonds can always carry force. The softening function should be chosen so that there is an intersection point with the horizontal axis, and a unique critical stretch value can be defined. This corresponds with real material behaviour where fracture surfaces are completely separated at a certain crack opening value [115]. It is also evident that an explicit definition of critical stretch  $s_c$  is required so that an exact value for  $G_F$  can be defined.

Yang et al. [237] introduced an exponential softening model within an ordinary state-based peridynamic framework. Yang implemented the exponential degradation function

proposed by Reinhardt et al. [185]. By introducing a linear term to the exponential decay function, the softening curve can be forced to intersect with  $s_c$ . The degradation function contains a number of unexplained parameters and is not completely satisfactory.

### Proposed model

A new non-linear softening law, illustrated in Fig. 5.6, is introduced. It is assumed that the behaviour of an individual bond is consistent with the stress-crack width ( $\sigma$ - $w$ ) relationship, depicted in Fig. 5.7. The area under the stress-crack width curve is a measure of the material fracture energy  $G_F$ . This figure has been adapted from the work of Hordijk [115]. This relationship is based on the experimental work of Cornelissen et al. [57]. The stress-crack width relationship is described by an exponentially decaying model with a term that forces the curve to intersect with the horizontal axis at  $w_c$ . If the softening relationship is asymptotic with the horizontal axis, and thus never intersects, a unique value for  $s_c$  cannot be determined.

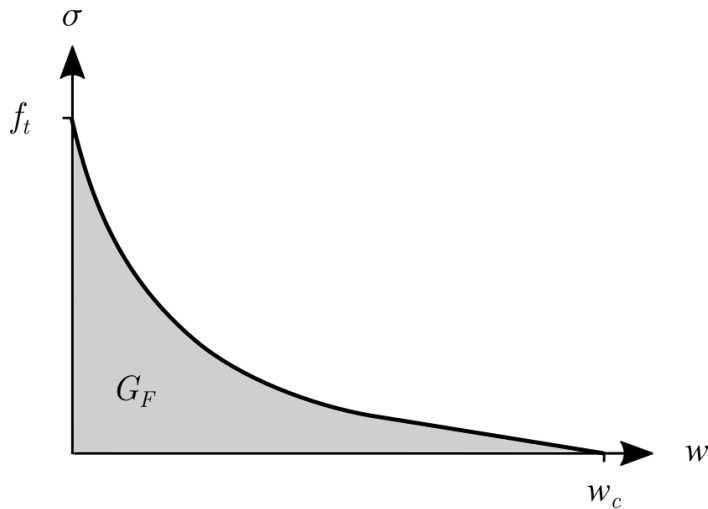


Fig. 5.7 Non-linear tension softening constitutive law ( $\sigma$ - $w$ ). Adapted from Fig. 6.1 in Hordijk [115].

The newly proposed model provides an explicit definition of the critical stretch  $s_c$  and an unambiguous relationship between  $s_c$ ,  $k$  and  $\alpha$ . The linear elastic limit  $s_0$  is defined empirically as  $f_t/E$ . This definition of  $s_0$  is not objective but it has been shown to provide good results. The evolution of the non-linear bond softening parameter  $d$  is defined by Eq. (5.16). This function describes an exponentially decaying curve with a linear term. As the bond stretch  $s$  approaches the critical stretch  $s_c$ , the linear term forces the softening curve to decay linearly and intersect with  $s_c$ .  $\alpha$  controls the position of the transition from exponential

to linear decay, and  $k$  controls the rate of exponential decay. Note that this definition of  $\alpha$  is different to that used by Tong et al. [219].

$$d = 1 - \frac{s_0}{s} \left( 1 - \frac{1 - \exp\left(-k \frac{s-s_0}{s_c-s_0}\right)}{1 - \exp(-k)} + \alpha \left( 1 - \frac{s-s_0}{s_c-s_0} \right) \right) \Big/ (1+\alpha) \quad (5.16)$$

The scalar bond force  $f$  is defined by Eq. (5.17), where  $c_d$  is the stiffness of a damaged bond.

$$f = c_d s \quad c_d = c(1-d) \quad (5.17)$$

The energy required to break a bond is defined by Eq. (5.18). Only the energy consumed during the softening stage is considered (between the limits  $s_0$  and  $s_c$ ). It is important that the softening curve intersects with  $s_c$  so that the integral in Eq. (5.18) can be evaluated. Tong et al. [219] take the limits of integration to be 0 and  $s$ , and a uniquely defined value of  $w$  does not exist.

$$w = \int_{s_0}^{s_c} f \xi ds = \frac{c s_0 \xi (s_0 - s_c) (2k - 2e^k + \alpha k - \alpha k e^k + 2)}{2k(e^k - 1)(1 + \alpha)} \quad (5.18)$$

Using Eq. (5.18), the material fracture energy  $G_F$  for a three-dimensional peridynamic body can be derived.

$$G_F = \int_0^\delta \int_0^{2\pi} \int_z^\delta \int_0^{\cos^{-1}(z/\xi)} w \xi^2 \sin\phi d\phi d\xi d\theta dz \quad (5.19)$$

$$G_F = \frac{\pi c s_0 \delta^5 (s_0 - s_c) (2k - 2e^k + \alpha k - \alpha k e^k + 2)}{10k(e^k - 1)(1 + \alpha)} \quad (5.20)$$

Rearranging Eq. (5.20), the critical stretch  $s_c$  can be defined in terms of  $s_0$ ,  $k$  and  $\alpha$ .

$$s_c = \frac{10k(1 - e^k)(1 + \alpha) \left( G_F - \frac{\pi c \delta^5 s_0^2 (2k - 2e^k + \alpha k - \alpha k e^k + 2)}{10k(e^k - 1)} \right)}{c \delta^5 s_0 \pi (2k - 2e^k + \alpha k - \alpha k e^k + 2)} \quad (5.21)$$

The proposed model provides an unambiguous approach for determining constitutive parameters and can be easily calibrated by adjusting  $k$  and  $\alpha$ . Calibrated values are provided in section 5.4.2.

### 5.3.5 Concrete fracture energy

The critical stretch of a peridynamic bond is highly dependent on fracture energy  $G_F$ . The selection of  $G_F$  is a major source of uncertainty in the peridynamic model and the value chosen will have a significant impact on the numerical results. Concrete material properties are typically determined through the testing of concrete compressive strength  $f_c$ . Additional material parameters such as elastic modulus  $E$ , tensile strength  $f_t$ , and fracture energy  $G_F$  are rarely tested and must be determined from empirical formulas. At present, there is no standard theory relating concrete compressive strength to fracture energy and Neville [163] states that fracture mechanics has not succeeded in developing parameters that adequately quantify the resistance of concrete to cracking. Furthermore, to paraphrase the *fib* [83]: defining and measuring the fracture energy of concrete is still a highly debated issue, despite the availability of many test results. *fib* Model Code 2010 does attempt to relate fracture energy to mean compressive strength  $f_{cm}$  through the empirical Eq. (5.22). Note that this equation is not dimensionally consistent and does not account for additional factors that are likely to play an important role such as maximum aggregate size.

$$G_F = 73f_{cm}^{0.18} \quad (5.22)$$

### 5.3.6 Summary

From the literature review (Table 2.1), it is evident that there is no broadly accepted constitutive model for quasi-brittle materials. This suggests that there is still a large degree of uncertainty surrounding the predictive accuracy of existing constitutive laws.

To the best of the authors knowledge, Yang et al. [236] provide the only comparison of different damage models within a bond-based peridynamic framework. They compare a linear, bilinear, and trilinear model against two concrete problems. Only mode I fracture is studied, all problems are two-dimensional, and mesh sensitivity is not examined. Details of the exact bilinear model used are not provided.

Tong et al. [219] recently introduced an exponentially decaying law for modelling quasi-brittle materials within a bond-based peridynamic framework. The proposed law is validated against experimental data, and mode I and mixed-mode problems are considered. All problems are two-dimensional, and mesh sensitivity is not examined. The model proposed by Tong et al. [219] does not provide an explicit definition of critical bond stretch  $s_c$ , resulting in a degree of ambiguity. Yu et al. [239] introduced a generalised bond-based micropolar peridynamic model with a non-linear softening law. Again, the critical bond stretch  $s_c$  is not defined.

It is generally assumed that the peridynamic force-stretch ( $f$ - $s$ ) constitutive relationship should have the same form as the macroscopic stress-crack width ( $\sigma$ - $w$ ) relationship. Motivated by the experimental and theoretical work of Cornelissen et al. [57] and Hordijk [115], a new non-linear constitutive damage law for quasi-brittle materials is introduced within a bond-based peridynamic framework. The proposed model is consistent with the macroscopic behaviour of concrete and overcomes the ambiguity of existing non-linear laws.

There are clear gaps in the literature that remain to be addressed: (1) a detailed examination of the predictive accuracy of existing constitutive laws is missing; (2) mesh sensitivity studies are required to assess the objectivity of constitutive laws; (3) three-dimensional problems need to be considered.

## 5.4 Comparison of constitutive laws

### 5.4.1 Validation problem

Validation of the model is performed against experimental data published by Grégoire et al. [98]. Geometrically similar notched and unnotched concrete members were tested in three-point bending to investigate size and boundary effects. Numerical results were also reported using a non-local finite element model. Numerical results have been reported by other researchers: Grassl et al. [96], Grégoire et al. [99], Feng and Wu [80], Rodrigues et al. [190], Barbat et al. [8]. It has been widely reported that non-local models struggle to accurately predict load-CMOD behaviour for different boundary types. Readers are referred to Havlásek et al. [109] for a detailed discussion. To the best knowledge of the author, the effect of different boundary types on the predictive accuracy of a peridynamic model has never been examined.

The smallest member (Beam 4) tested by Grégoire et al. [98] is used for validation in this study. The full set of tests is addressed in later size effect studies. A schematic diagram of the experimental setup is illustrated in Fig. 5.8. Three different notch configurations were used to investigate boundary effects: unnotched (notch-to-depth ratio  $\lambda$  of 0), fifth-notched (notch-to-depth ratio  $\lambda$  of 0.2), and half-notched (notch-to-depth ratio  $\lambda$  of 0.5). The member has the following dimensions: length  $l = 175$  mm; depth  $d = 50$  mm; and thickness  $b = 50$  mm. The span of the member is 125 mm. Every specimen was tested three times and there is a small degree of variability in the measured material properties. Standard compressive tests and splitting (Brazilian) tests were performed to characterise the material properties of each batch of concrete. 51 standard cylinders (with a height-to-diameter ratio of 2) were manufactured. The mean material properties are used for all computations: compressive

strength  $f_{cm,cyl} = 42.3$  MPa; modulus of elasticity  $E = 37.0$  GPa; splitting tensile strength  $f_t = 3.9$  MPa. The coefficient of variability for the mean material properties is 6.6%, 2.4%, and 6.0% respectively. The material fracture energy is estimated to be  $G_F = 73f_{cm}^{0.18} = 143.2$  N/m. The density of the concrete mixture was 2346 kg/m<sup>3</sup>.

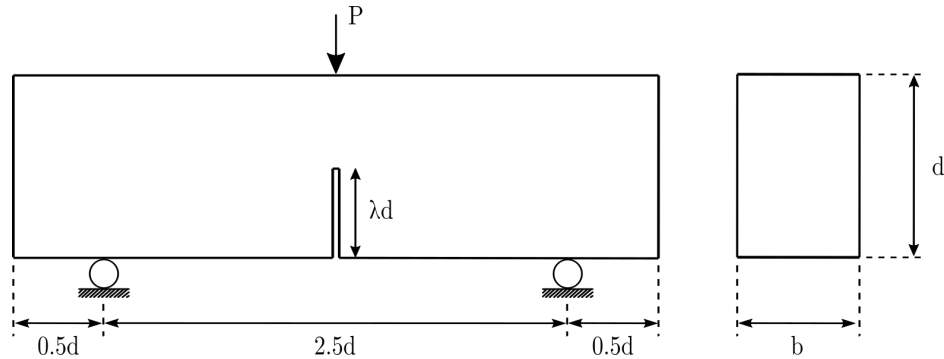


Fig. 5.8 Schematic of the experimental setup. Adapted from Grégoire et al. [98].

The experimental load-CMOD curves are illustrated in Fig. 5.9. Each member was tested multiple times and the range of results is plotted in grey. The experimental tests were CMOD controlled to avoid post-peak unstable crack propagation. All the results presented in this chapter were obtained using the explicit scheme outlined in Fig. 4.14. The applied displacement is increased incrementally using a fifth-order smoothstep function and there is no damping in the system. Implementing a CMOD controlled loading scheme would require the use of a computationally expensive implicit solver.

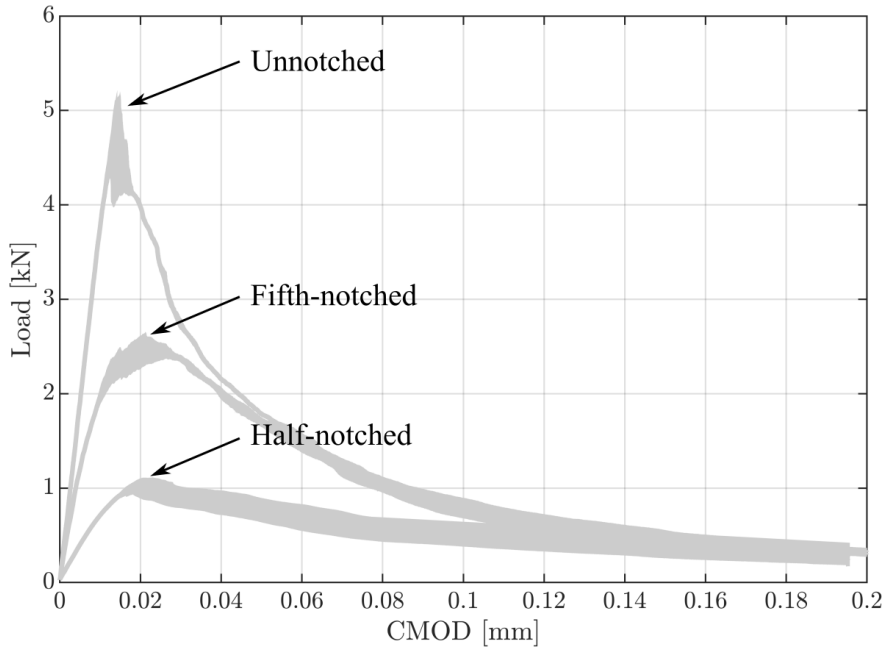


Fig. 5.9 Load-CMOD response for Beam 4 ( $d = 50$  mm): unnotched, fifth-notched, and half-notched [98]

### 5.4.2 Results

The first step was to investigate the accuracy of existing constitutive laws. Results from the testing of four different constitutive laws are presented: linear, bilinear, trilinear, and the newly proposed non-linear softening law. Uncertain parameters such as the position of the kink point in the trilinear model can be calibrated to fit the experimental results. The position of the kink point  $\beta$  in the trilinear model is set to 1/4, as proposed by Yang et al. [236]. For the non-linear softening model, the rate of decay  $k$  and the position of the transition from exponential to linear decay  $\alpha$  are calibrated to fit the experimental results for the unnotched member.  $k$  is set to 25, and  $\alpha$  is set to 1/4. The value of  $k_r$ , the ratio between the critical stretch  $s_c$  and the linear elastic limit  $s_0$  in the bilinear model is set to 25.

The following results have been obtained using a constant peridynamic horizon ( $\delta = 3.14\Delta x$ ) and regular grid spacing ( $\Delta x = 5$  mm). The constitutive model parameters are defined in Table 5.1. These parameters remain constant for all notch configurations. This is essential in a robust validation procedure. Adjusting model parameters to improve the agreement between numerical and experimental measurements does not constitute validation [218]. There is a lack of robust validation studies within the peridynamic literature and significant work remains to quantify the predictive accuracy of peridynamic models.

Table 5.1 Constitutive model parameters. Refer to Table 5.2 for a summary of the constitutive equations.

Law	$s_0$	$s_1$	$s_c$
Linear	-	-	4.53E-4
Bilinear	9.06E-5	-	2.27E-3
Trilinear	1.05E-4	6.90E-4	5.56E-3
Non-linear	1.05E-4	-	7.48E-3

Table 5.2 Constitutive equations

Law	$s_0$	$s_1$	$s_c$	$d$
Linear	-	-	Eq. (5.1)	-
Bilinear	Eq. (5.2)	-	Eq. (5.2)	Eq. (5.5)
Trilinear	$f_t/E$	Eq. (5.12)	Eq. (5.14)	Eq. (5.15)
Non-linear	$f_t/E$	-	Eq. (5.21)	Eq. (5.16)

Experimental and numerical load-CMOD results are presented in Fig. 5.10. The linear elastic response is correctly captured for all cases but the ultimate load capacity is overestimated by all the constitutive laws. This is partly addressed in the next section on critical stretch corrections. The highest predictive accuracy is achieved with the newly proposed non-linear softening model. The response predicted using the trilinear model is also in reasonable agreement with the experimental data. The bilinear model significantly overestimates the peak load. The initial slope of the softening relationship can be calibrated in the non-linear and trilinear model, and according to Alvaredo and Torrent [5], only the initial slope of the softening relationship plays a role in the prediction of peak loads. This explains the poor predictive performance of the bilinear model.

For purposes of clarity, results with the linear damage model have not been included in the following figures. The structural response using the linear model is perfectly linear elastic until failure occurs. For the unnotched member, failure is predicted at approximately 11,750 kN. It is clear that the linear damage model is not suitable for modelling quasi-brittle materials and the linear model will not be considered any further.

The shape of the softening branch in the constitutive law plays an important role in the macroscopic material behaviour. This has previously been noted by Yang et al. [236]. The post-peak softening behaviour predicted using the non-linear softening and trilinear model is in approximate agreement with the experimental data. The gradient of the softening response is consistent with the experimental data but the predicted load is shifted upwards. Qualitatively, the predictive accuracy of the non-linear softening law is superior. The softening response predicted using the bilinear model is steeper than that observed experimentally.

The accuracy of the predicted results is higher for the unnotched member with all constitutive laws. This could be explained by a number of factors. (1) The parameters in the non-linear softening model were calibrated against the unnotched member and higher accuracy is expected. This does not explain why the bilinear and trilinear law also show higher predictive accuracy. (2) The discretisation is not fine enough to properly capture the notch geometry and this might account for discrepancies between the experimental and numerical results. (3) The non-local nature of peridynamics influences the results for different boundary types. This is likely to be the main source of discrepancy between the experimental and numerical data. It is hypothesised that spurious strengthening occurs in the proximity of a notch due to the non-local interaction of particles above and below the notch tip. This is addressed in the discussion.

The computed fracture path is the same for all constitutive laws. The fracture initiates from the midspan of the beam and propagates vertically towards the applied load (see Fig. 5.23). For the unnotched case, a wide zone of softening damage develops in the highly stressed tensile region (see Fig. 5.24). This region of damage represents the development of micro-cracking. This occurs before the onset of strain localisation and development of a macroscopic fracture. This behaviour can only be captured when using a constitutive law with softening. A detailed examination of energy dissipation is provided in section 5.7.

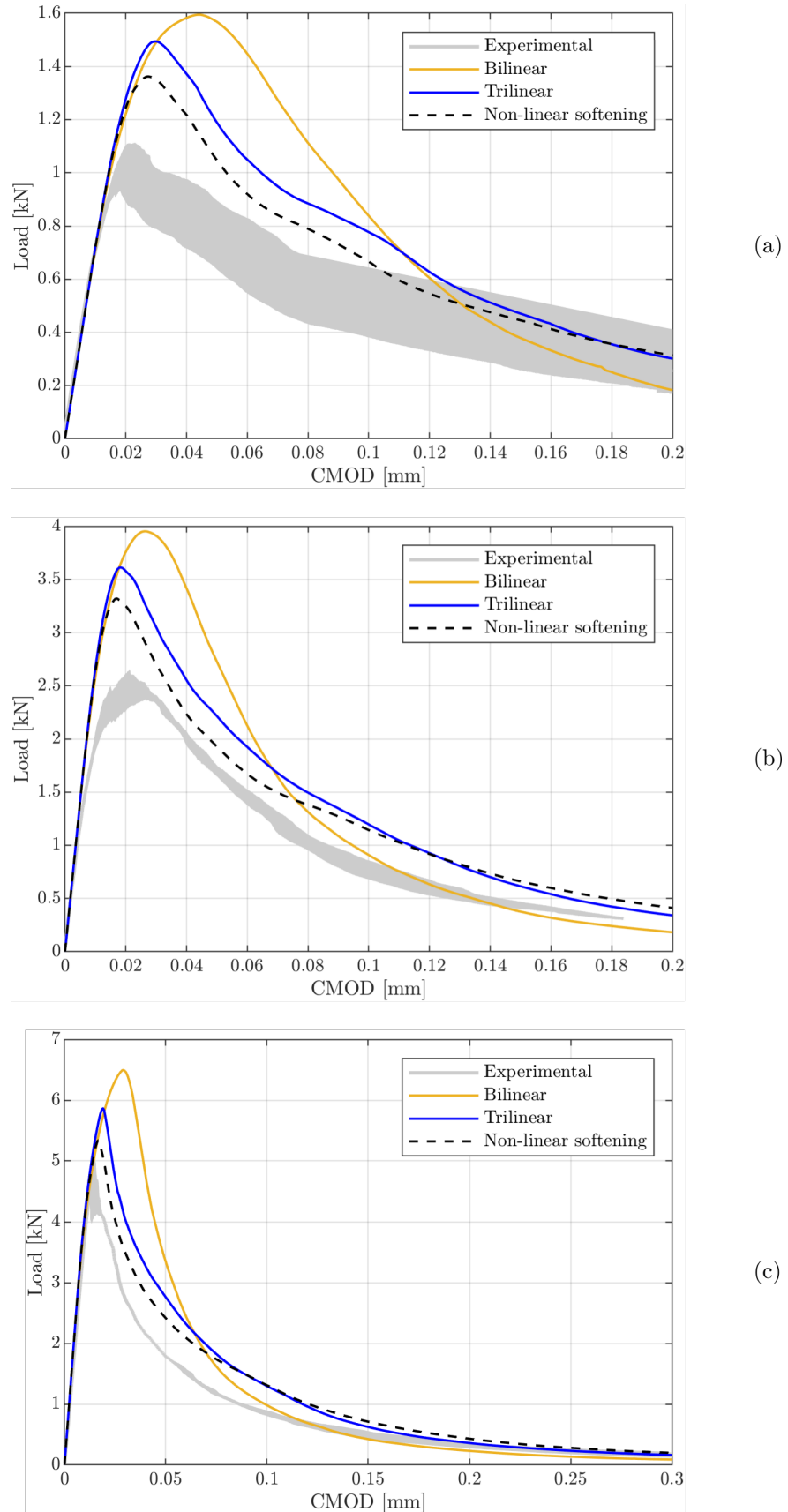


Fig. 5.10 Comparison of load-CMOD results predicted using different constitutive laws: (a) half-notched, (b) fifth-notched, (c) unnotched case.

## 5.5 Critical stretch corrections

It was observed in the previous section that the bond-based model overestimates the load capacity of concrete beams in three-point bending. For notched problems, the discrepancies can be primarily explained by the interaction of bonds above and below the notch tip. This does not explain the observed discrepancies for the unnotched case, and there must be another factor that accounts for the over-prediction.

This section presents a numerical examination of the energy release rate in a discrete peridynamic model. It is demonstrated that the application of surface correction factors produces a toughening effect. The energy required to produce a fracture surface at the edge of a peridynamic body is significantly higher than the material fracture energy  $G_F$ . A correction scheme is proposed that is simple to implement and yields improved results. The value of critical stretch  $s_c$  is not a constant across all bonds and depends on the applied surface correction factor.

This section is organised as follows: (1) The first section defines the problem; (2) The second section examines spatial integration accuracy in three-dimensions. This is essential to interpret the computed values of discrete fracture energy; (3) The third section examines the energy release rate in a discrete peridynamic model. It is demonstrated that the application of surface correction factors produces a toughening effect; (4) The fourth section presents a correction scheme to account for the toughening effect; (5) The fifth section presents results obtained using the correction scheme.

### 5.5.1 The problem

The work required to break all bonds per unit fracture area in a three-dimensional peridynamic body is given by Eq. (5.23) [207]. An infinitely large peridynamic body is completely separated into two halves and all the bonds that initially crossed the fracture surface are considered to have broken. The energy stored in a bond is known as the micropotential  $w$  and has units of energy per volume squared ( $J/m^6$ ). The energy required to break a bond is defined by Eq. (5.24).  $G_0$  ( $J/m^2$ ) can be interpreted as the energy needed to create a unit fracture surface in a peridynamic body. Note that the peridynamic energy release rate  $G_0$  has been determined from the calculation of the potential energy loss of an idealised infinite crack surface and is not related to any particular fracture mode [240].

$$G_0 = \int_0^\delta \int_0^{2\pi} \int_z^\delta \int_0^{\cos^{-1}(z/\xi)} \left( \frac{cs_c^2 \xi}{2} \right) \xi^2 \sin\phi d\phi d\xi d\theta dz \quad (5.23)$$

$$w_c = \frac{cs_c^2\xi}{2} \quad (5.24)$$

After evaluation of Eq. (5.23), the following definition of  $G_0$  is found.

$$G_0 = \frac{\pi cs_c^2\delta^5}{10} \quad (5.25)$$

It is assumed that the peridynamic energy release rate  $G_0$  is equal to the material fracture energy  $G_F$ . The material fracture energy  $G_F$  can be obtained experimentally or through empirical equations. The critical bond stretch  $s_c$  for a three-dimensional peridynamic body can then be defined as follows.

$$s_c = \sqrt{\frac{10G_F}{\pi c\delta^5}} \quad (5.26)$$

The critical stretch  $s_c$  has been derived using the assumption that every bond has the same micro-modulus  $c$ . This assumption does not hold true if a surface correction scheme that modifies bond properties is applied.

The derivation of the peridynamic bond stiffness  $c$  is based on the assumption that the horizon of a material point  $\mathcal{H}_x$  is contained completely within the bulk of the body. This assumption does not hold true for nodes within  $\delta$  of the body edge. Nodes within  $\delta$  of the body edge do not possess a full non-local neighbourhood. Consequently the material properties of nodes contained within the main bulk and nodes within a distance  $\delta$  of the body edge differ. This is known as the peridynamic surface effect. Nodes that do not possess a full non-local neighbourhood have less interactions (bonds) and this leads to a reduction in material stiffness. Material behaviour is not accurately captured at the free surface of a peridynamic body, and displacements are larger than that predicted by classical methods.

A number of surface correction schemes exist to correct stiffness softening behaviour. Surface correction schemes can be organised into two categories: (1) methods that modify the force between particle pairs; (2) methods that introduce fictitious nodes at the boundary. Le and Bobaru [133] provide a detailed review and comparison of existing correction schemes. The fictitious node method is severely limited by the complexity of its implementation and can only be used to address trivial problems. Le and Bobaru [133] found that the volume correction method, first proposed in Chapter 2 of Bobaru et al. [30], is one of the most effective correction schemes and is simple to implement. Softening behaviour is corrected by increasing the micro-modulus of bonds connected to nodes within a distance  $\delta$  of the free surface. This is done by ensuring that nodes under homogeneous deformation have the same value of strain energy density when located near the surface or within the main bulk.

It is clear that by increasing the micro-modulus of a bond, the energy required to break the bond will increase. Therefore, the energy required to initiate a fracture at the free surface of a peridynamic body is greater than the material fracture energy  $G_F$ .

To illustrate the problem, the computed load-CMOD response for the unnotched beam using a trilinear constitutive law with and without a surface correction scheme is presented in Fig. 5.11. To the best knowledge of the author, the effect of a surface correction scheme on the computed structural response has never been examined. The peridynamic model overestimates the ultimate load capacity when surface correction factors are applied, but the structural response in the linear elastic range is correctly captured. Without surface correction factors, the structural response is softer than that observed experimentally, resulting in a significant underestimation of the peak load.

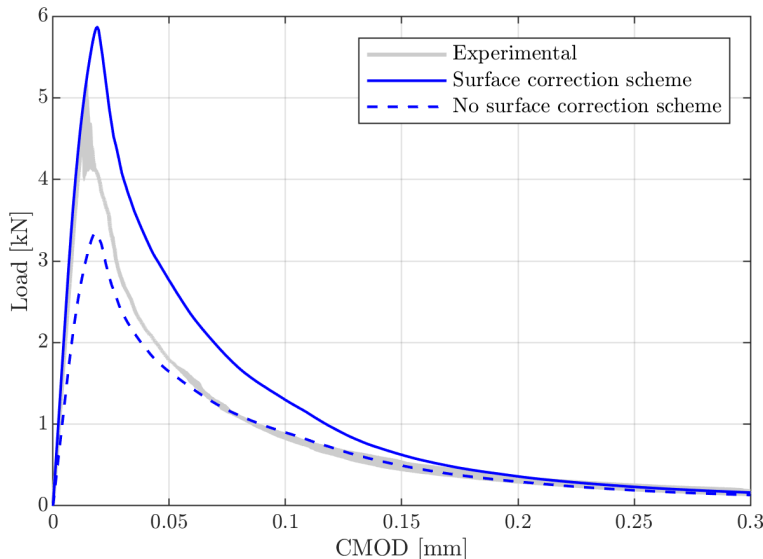


Fig. 5.11 Load-CMOD response for the unnotched beam ( $d = 50$  mm) using a trilinear constitutive law with and without surface correction factors.

### 5.5.2 Integration accuracy in three-dimensions

Before examining the energy release rate in a discrete peridynamic model, spatial integration accuracy in three-dimensions will be investigated. This will be of help when interpreting the computed values of discrete fracture energy.

Seleson [200] provide a detailed examination of one-point quadrature algorithms for two-dimensional peridynamic models. Hu et al. [116] also investigated algorithms for improving the accuracy of spatial integration in two-dimensional models. An equivalent examination of one-point quadrature algorithms for three-dimensional bond-based peridynamic models is missing in the literature. It should be noted that Seleson and Littlewood [201] considered

the accuracy and convergence behaviour of a 3D state-based linear peridynamic model under grid refinement, whilst keeping the horizon length  $\delta$  fixed. This section provides a short examination of the  $m$ -convergence properties of one-point quadrature algorithms in three-dimensions. Refer to Section 4.2.3 for further details of  $m$ -convergence.

Fig. 5.12 illustrates the  $m$ -convergence of the discrete volume approximation. Results using the Full Area (FA) and Partial Area (PA) algorithm introduced in the peridynamic code PD-LAMMPS [176] are presented. The value of  $m$  ranges from 2 to 10 with a step size  $\Delta m$  of 0.1. Convergence of the discrete volume approximation to the exact analytical volume is highly oscillatory. The FA algorithm oscillates around the exact value, often overestimating the volume. The value of the integral is always underestimated by the PA - PDLAMMPS algorithm and does not reach the exact volume. The convergence behaviour in three-dimensions is very similar to that observed in two-dimensional models.

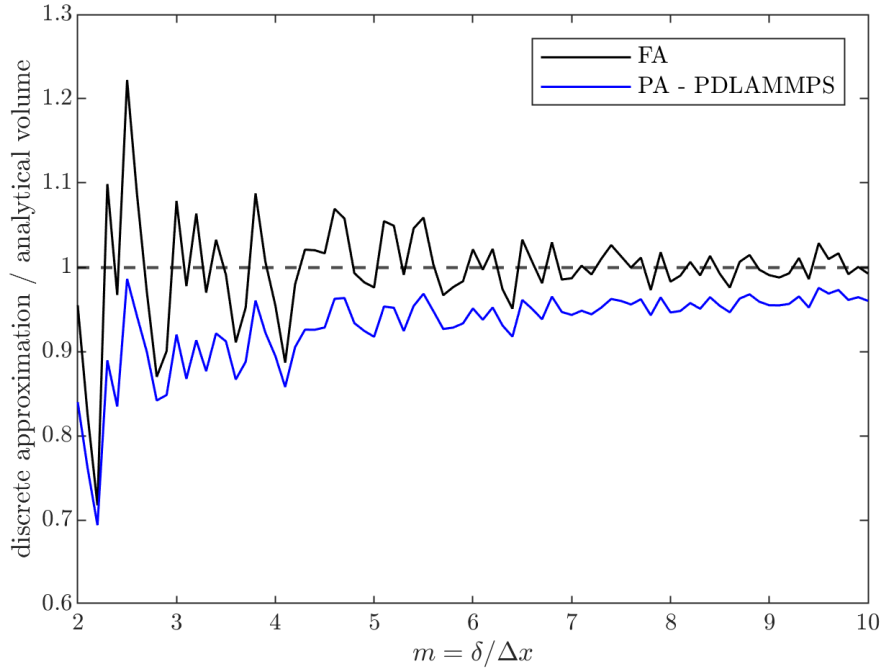


Fig. 5.12  $m$ -convergence of the discrete volume approximation.  $\Delta m = 0.1$

The  $m$ -convergence behaviour of the discrete approximation to the exact value of strain energy density  $W_{PD}$  is presented in Fig. 5.13. The dashed lines represent the discrete volume approximation. These are included to illustrate that the discrete volume approximation and the discrete strain energy density approximation are not in exact agreement.

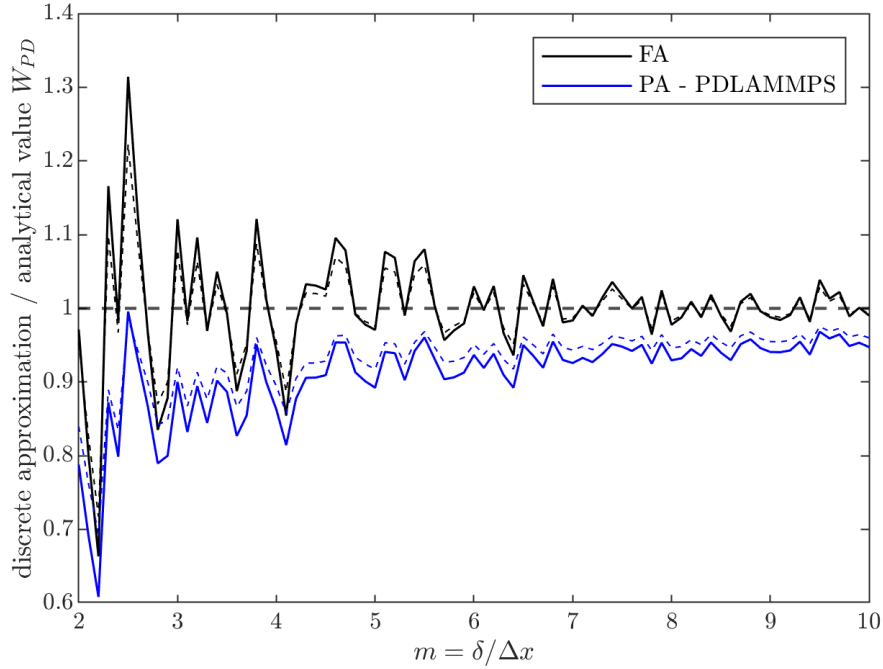


Fig. 5.13  $m$ -convergence of the discrete strain energy density approximation.  $\Delta m = 0.1$

### Influence function

The convergence behaviour of one-point quadrature algorithms to the correct value of strain energy density can be improved by using influence functions that reduce the weight of particles closer to the horizon edge. Fig. 5.14 illustrates a constant influence function and a conical influence function. The conical function reduces the integration errors caused by cells that are located near the boundary of a particle horizon  $\delta$ .

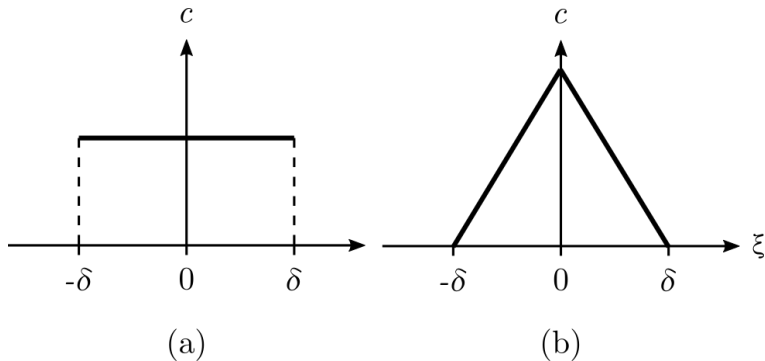


Fig. 5.14 Comparison of micro-modulus functions: (a) constant influence function; (b) triangular influence function (conical)

This idea was first proposed by Yu et al. [242] and was investigated in detail by Seleson [200] for two-dimensional problems. Smoother convergence is observed for influence func-

tions with a higher regularity (number of continuous derivatives). Seleson warns that different influence functions should be used with caution, as they may alter the behaviour of dynamic simulations. It was observed in [202] that different influence functions produce different dispersion relations and fracture patterns. This work is not concerned with dynamic problems and examining the dispersion behaviour of different influence functions in three-dimensions is beyond the current scope. The  $m$ -convergence behaviour of the discrete approximation using a conical influence function to the exact value of strain energy density  $W_{PD}$  is presented in Fig. 5.15. The micro-modulus function is defined as  $c(\xi, \delta) = c(0, \delta)\omega(\xi, \delta)$ . The conical influence function  $\omega(\xi, \delta)$  is given by Eq. (5.27) and the corresponding constant  $c(0, \delta)$  is given by Eq. (5.28). For a three-dimensional peridynamic material, the critical stretch  $s_c$  is given by Eq. (5.29), and the strain energy density  $W_{PD}$  is given by Eq. (5.30). The convergence behaviour is much improved and the exact solution is recovered. The difference in convergence behaviour between the FA and PA-PDLAMMPS algorithm is reduced. The dashed lines represent the discrete volume approximation. These are included to make the visual comparison with Fig. 5.13 easier.

$$\omega(\xi, \delta) = 1 - \frac{\xi}{\delta} \quad (5.27)$$

$$c(0, \xi) = \frac{60E}{\pi \delta^4} \quad (5.28)$$

$$s_c = \sqrt{\frac{60G_F}{\pi c \delta^5}} \quad (5.29)$$

$$W_{PD} = \frac{\pi c s_c^2 \delta^4}{20} \quad (5.30)$$

All the results in this thesis have been obtained using a constant influence function and further work is needed to examine the use of different influence functions for quasi-static problems. This subsection was included to demonstrate the potential benefits of using a non-constant influence function.

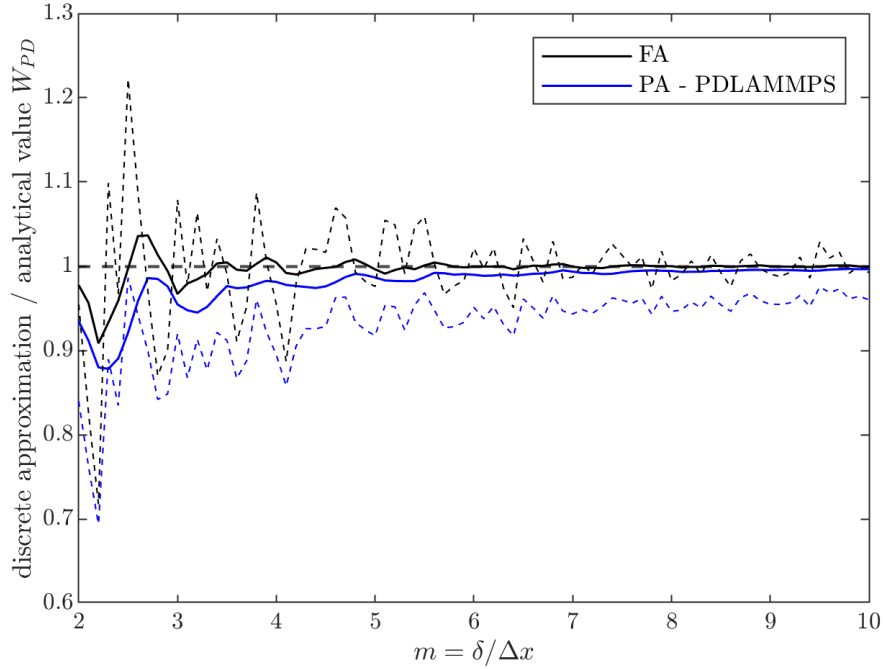


Fig. 5.15  $m$ -convergence of the discrete strain energy density approximation using a conical influence function.  $\Delta m = 0.1$

### 5.5.3 Numerical examination of discrete fracture energy

This section examines the energy release rate in a discrete peridynamic body. The energy required to create a discrete fracture surface is examined for three cases: (1) a fracture surface in a finite body, (2) a fracture surface in an infinite body, and (3) a fracture surface at the edge of a peridynamic body. It is shown that the application of surface correction factors produces a toughening effect.

#### Finite case

Consider a uniformly discretised unit cube, illustrated in Fig. 5.16 (a). By summing the energy required to break every bond that intersects with the theoretical unit fracture surface, as illustrated in Fig. 5.16 (b), the material fracture energy  $G_F$  should be approximately recovered. This value is referred to as the discrete fracture energy. The exact material fracture energy will not be recovered due to spatial integration errors, as shown in the previous section.

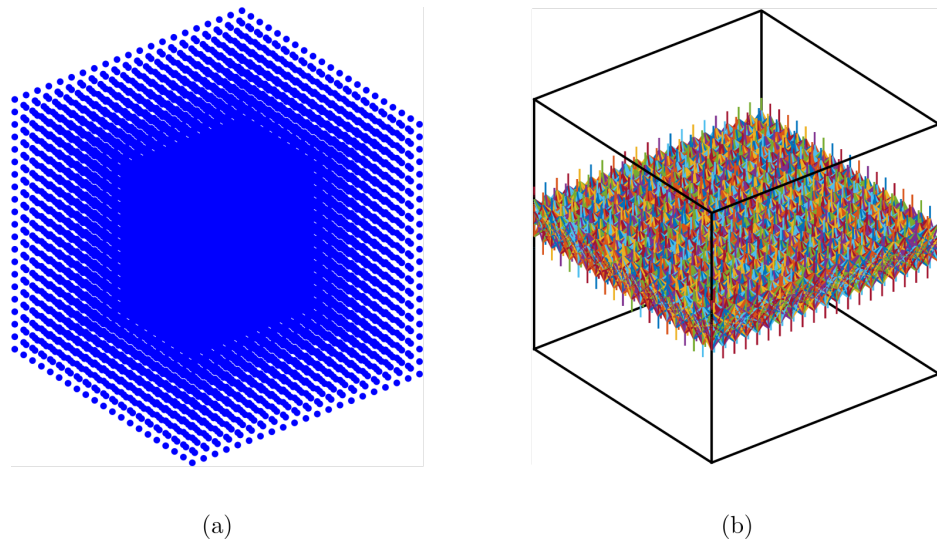


Fig. 5.16 (a) discretised unit cube; (b) all bonds that cross the theoretical unit fracture surface

Considering a linear elastic damage model, the energy required to break a bond is  $cs_c^2\xi/2$ . The material fracture energy  $G_F$  is set to 100 N/m, and the  $m$ -ratio ( $m = \delta/\Delta x$ ) is set to  $\pi$  and  $\Delta x = 50$  mm. Spatial integration is performed using the FA algorithm and the ratio of the discrete approximation to the analytical value of strain energy density  $W_{PD}$  is 0.93. The discrete fracture energy is examined with and without surface correction factors applied, and the surface correction scheme proposed in Chapter 2 of [30] is employed.

The discrete fracture energy without surface correction factors is 90.1 N/m. The material fracture energy  $G_F$  is not recovered exactly in the discrete model. This error is due to two factors: (1) spatial integration errors, (2) surface effects. Due to spatial integration errors, the discrete fracture energy is limited to a maximum accuracy of approximately  $0.93G_F$ . The remaining discrepancies can be accounted for by surface effects. The peridynamic energy release rate  $G_0$  is based on an idealised model that assumes that the fracture surface lies within an infinitely large body [240]. Fig. 5.17 illustrates the bonds that cross the unit fracture surface. The number of bonds intersecting the fracture surface is reduced at the edges. As a result, the discrete fracture energy will be less than the material fracture energy  $G_F$ . The discrete fracture energy with surface corrections is 106.5 N/m. The application of a surface correction scheme results in an increase in the value of discrete fracture energy.

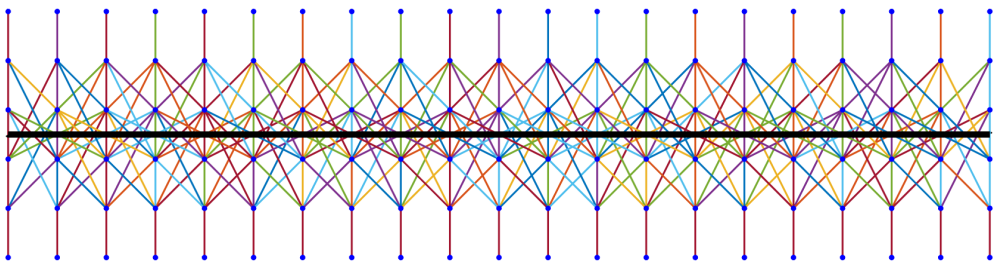


Fig. 5.17 Bonds that cross the theoretical unit fracture surface within a unit cube ( $\Delta x = 50$  mm)

### Infinite case

Now a unit fracture surface at the centre of a  $5\text{m} \times 5\text{m} \times 5\text{m}$  cube is considered, see Fig. 5.18. This represents the case of a unit fracture surface that lies within an infinitely large body. Surface effects will be eliminated and the discrete fracture energy should be approximately equal to  $0.93G_F$ . The discrete fracture energy without surface correction factors is  $93.3$  N/m. The discrete fracture energy with and without surface correction factors should be equal. Unexpectedly, the discrete fracture energy with surface correction factors is  $99.3$  N/m. This can be explained by the influence of spatial integration errors on the calculation of stiffness correction factors. This effect is relatively minor and will not be considered further in this work, but researchers should be aware of the influence of spatial integration errors on the computation of stiffness correction factors.

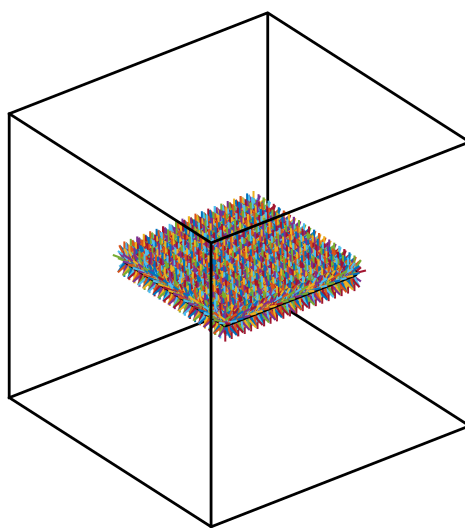


Fig. 5.18 Bonds that cross the theoretical unit fracture surface centred within a  $5\text{m} \times 5\text{m} \times 5\text{m}$  cube. The cube is not drawn to scale.

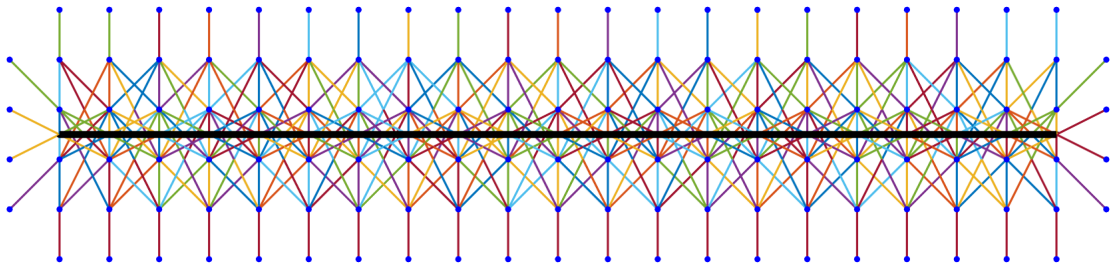


Fig. 5.19 Bonds that cross the theoretical unit fracture surface centred within a  $5\text{m} \times 5\text{m} \times 5\text{m}$  cube ( $\Delta x = 50\text{ mm}$ )

### Edge case

The two previous cases do not fully elucidate the problem. The issue is much more pronounced at the edge of a body. This is particularly problematic because mode I and mixed-mode cracks will generally initiate from the edge of a body. Fig. 5.20 illustrates a 25 mm wide strip at the edge of a peridynamic body. The discrete fracture energy without surface correction factors is 99.4 N/m. The discrete fracture energy with surface correction factors is 165.4 N/m. To state the problem clearly, for the presented edge case, when surface correction factors are applied, the discrete fracture energy at the edge of a peridynamic body is approximately 65% higher than the material fracture energy ( $100\text{ N/m} \rightarrow 165.4\text{ N/m}$ ). Consequently, a higher applied force is required to initiate and propagate a crack.

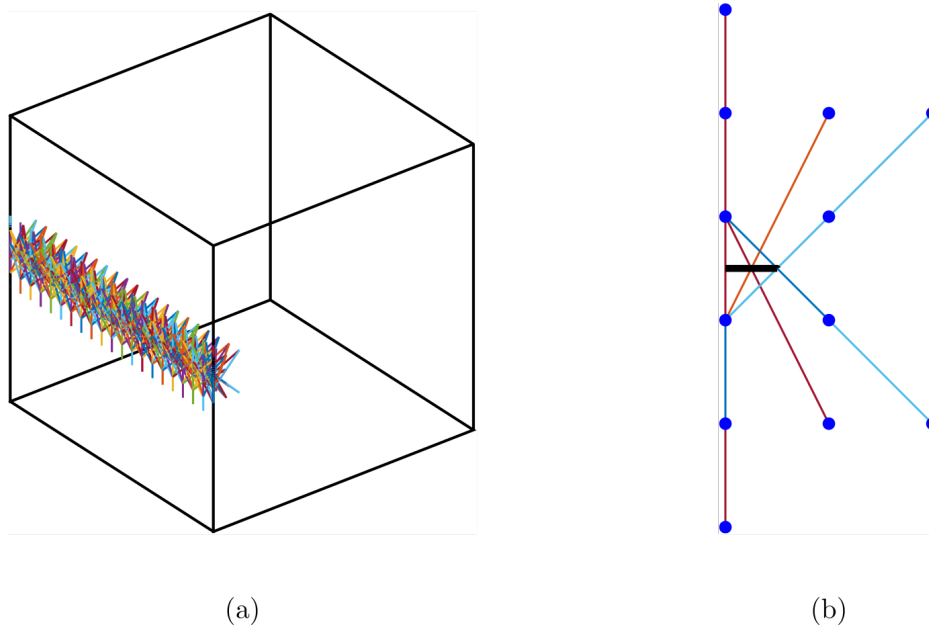


Fig. 5.20 Bonds that cross a theoretical fracture surface at the edge of a peridynamic body

### 5.5.4 Critical stretch correction scheme

A correction scheme is proposed to account for the increase in fracture energy at the edge of a peridynamic body. The proposed correction scheme is simple to implement and yields improved results. The critical stretch  $s_c$  should not be a constant across all bonds, and must be uniquely assigned depending on the applied surface correction factor. This can be easily achieved by using the corrected micro-modulus to calculate  $s_c$ .

Using the surface correction scheme proposed in Chapter 2 of [30], commonly referred to as the volume method. The micromodulus of a bond connecting node  $\mathbf{x}$  and  $\mathbf{x}'$  is corrected using Eq. (5.31), where  $\lambda$  is a dimensionless stiffening factor, and  $V_0$  is the horizon area/volume of a node within the main bulk. The horizon area/volume of node  $\mathbf{x}$  is  $V(\mathbf{x})$  and the horizon area/volume of node  $\mathbf{x}'$  is  $V(\mathbf{x}')$ . The stiffening factor  $\lambda$  will be greater than or equal to 1 because  $V_0$  will always be larger than or equal to  $V(\mathbf{x})$  and  $V(\mathbf{x}')$ .

$$c_{corrected} = \lambda c \quad \lambda = \frac{2V_0}{V(\mathbf{x}) + V(\mathbf{x}')} \quad (5.31)$$

Using the linear damage model as an example, the critical stretch  $s_c$  of a bond is defined as follows.

$$s_c = \sqrt{\frac{10G_F}{\pi\lambda c\delta^5}} \quad (5.32)$$

This method can be extended to more complex constitutive laws without any modification and the proposed correction scheme is tested in the next section. Note that this scheme leads to higher memory requirements as the critical stretch value  $s_c$  must be stored for every bond.

Lastly, Yu and Li [240] recently studied energy release rates in peridynamics. The authors systematically investigated the fracture energy release rate in peridynamics for a number of finite crack models, and they concluded that the critical bond stretch should not be a constant value across all bonds. The same conclusion has been reached independently in this work. The author was not aware of the work of Yu and Li [240] and a distinct approach has been used to reach a similar conclusion.

### 5.5.5 Results

Results using the critical stretch correction scheme proposed in the previous section are presented in Fig. 5.21. The test cases presented in section 5.4 are used for validation. Only the trilinear and proposed non-linear softening law are considered.

The critical stretch correction scheme improves the accuracy of the computed results. For the unnotched case, using the proposed non-linear softening model, the predicted peak load lies within the experimental range and the post-peak softening behaviour is in very good agreement with the experimental envelope. The critical stretch correction scheme reduces the predicted peak load by approximately 11% ( $5336\text{ N} \rightarrow 4748\text{ N}$ ). The peak load is overestimated for the fifth and half-notched members but the post-peak softening behaviour is in reasonable agreement with the experimental data. The critical stretch correction scheme reduces the predicted peak load for the fifth-notched case by 6.7% ( $3320\text{ N} \rightarrow 3097\text{ N}$ ), and for the half-notched case by 6% ( $1362\text{ N} \rightarrow 1280\text{ N}$ ). The computed fracture paths are as expected.

It is important to compare the results obtained using the non-local peridynamic model against advanced numerical methods. Comparisons are made with numerical results from Barbat et al. [8]. The failure process is modelled using a crack band approach with an isotropic damage constitutive law. The material parameters have been reverse fitted to improve agreement between the experimental and numerical results. The material parameters are within 10% of the experimentally measured values. The crack band approach does not suffer from spurious strengthening within the proximity of a notch, and for the notched cases, the predicted peak loads are in better agreement with the experimental data. Qualitatively, the softening response predicted using the peridynamic model is in better agreement with the experimental results. It is important to note that this was achieved without fitting the material parameters. Barbat et al. [8] examined the sensitivity of the results to mesh refinement and orientation. The results were found to be mesh objective, and the predicted structural response converges on a unique solution as the mesh is refined. Xenos and Grassl [232] reported that crack band models are mesh dependent for more complex reinforced concrete problems. The influence of the mesh resolution is examined in the next section.

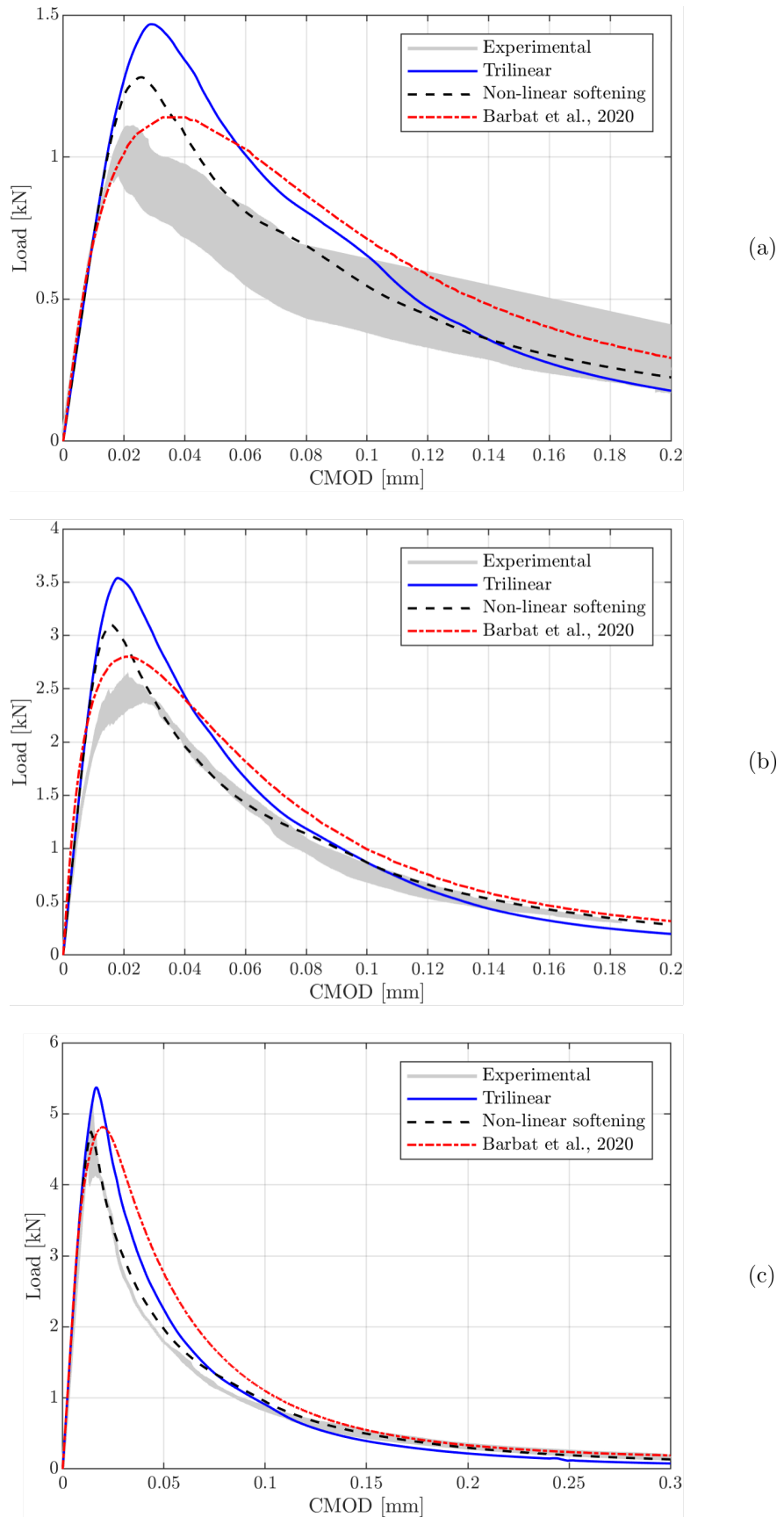


Fig. 5.21 Load-CMOD results with critical stretch corrections: (a) half-notched, (b) fifth-notched, (c) unnotched case.

## 5.6 Mesh sensitivity study

This section presents a mesh sensitivity study. The predicted results (load-deflection response, peak load and crack path) should be independent of the mesh resolution. This is a basic test of the adequacy of any numerical model.

The ratio  $m = \delta/\Delta x$  is fixed and  $\Delta x$  is refined. This is known as  $\delta$ -convergence in the peridynamic literature. Three different levels of mesh refinement are examined:  $\Delta x = 1.25$  mm, 2.5 mm, and 5 mm. The predicted results should converge to a unique solution upon refinement of the discretisation. Only the proposed non-linear softening law is considered. It has already been discussed that the definition of  $s_0$  remains constant for all discretisation levels and it is unclear how this will influence the computed results.

It has been shown in the previous section that spurious strengthening occurs with the peridynamic model for notched cases. The mesh used in the previous simulations is too coarse to accurately capture the notch width (2 mm) and the spurious strengthening effect might be reduced when using a finer mesh. Bobaru and Hu [32] and Zhao et al. [244] note that the size of the horizon should be defined by the smallest geometrical feature. In this work the smallest relevant geometrical feature is the notch width. A maximum horizon size of 2 mm is not reasonably practicable due to high computational expense. A horizon size of 2 mm would require that  $\Delta x$  is approximately 0.6 mm.

Results from the mesh sensitivity study are presented in Fig. 5.22. The most notable feature of the results for the unnotched case is the progressive increase in the predicted peak load as the mesh is refined. For the notched cases, the predicted peak load is independent of the mesh discretisation. Isolating the cause of the mesh dependency is difficult as the sensitivity is not consistent across notched and unnotched cases. The results for the notched cases cast doubt on the claim of Tong et al. [219] that it is not physically reasonable to link the elastic limit  $s_0$  to the macroscopic tensile limit  $f_t$ .

Displacement controlled methods can fail to follow the structural response when large instabilities occur. The release of a large amount of stored elastic energy in the unnotched member results in sudden and uncontrolled fracture propagation. When using the finest mesh, the full post-peak structural response is not captured and oscillations occur in the load-CMOD curve. Path-following methods are required to follow the structural response throughout the fracture propagation. Implementing a path-following method requires a computationally expensive implicit solver.

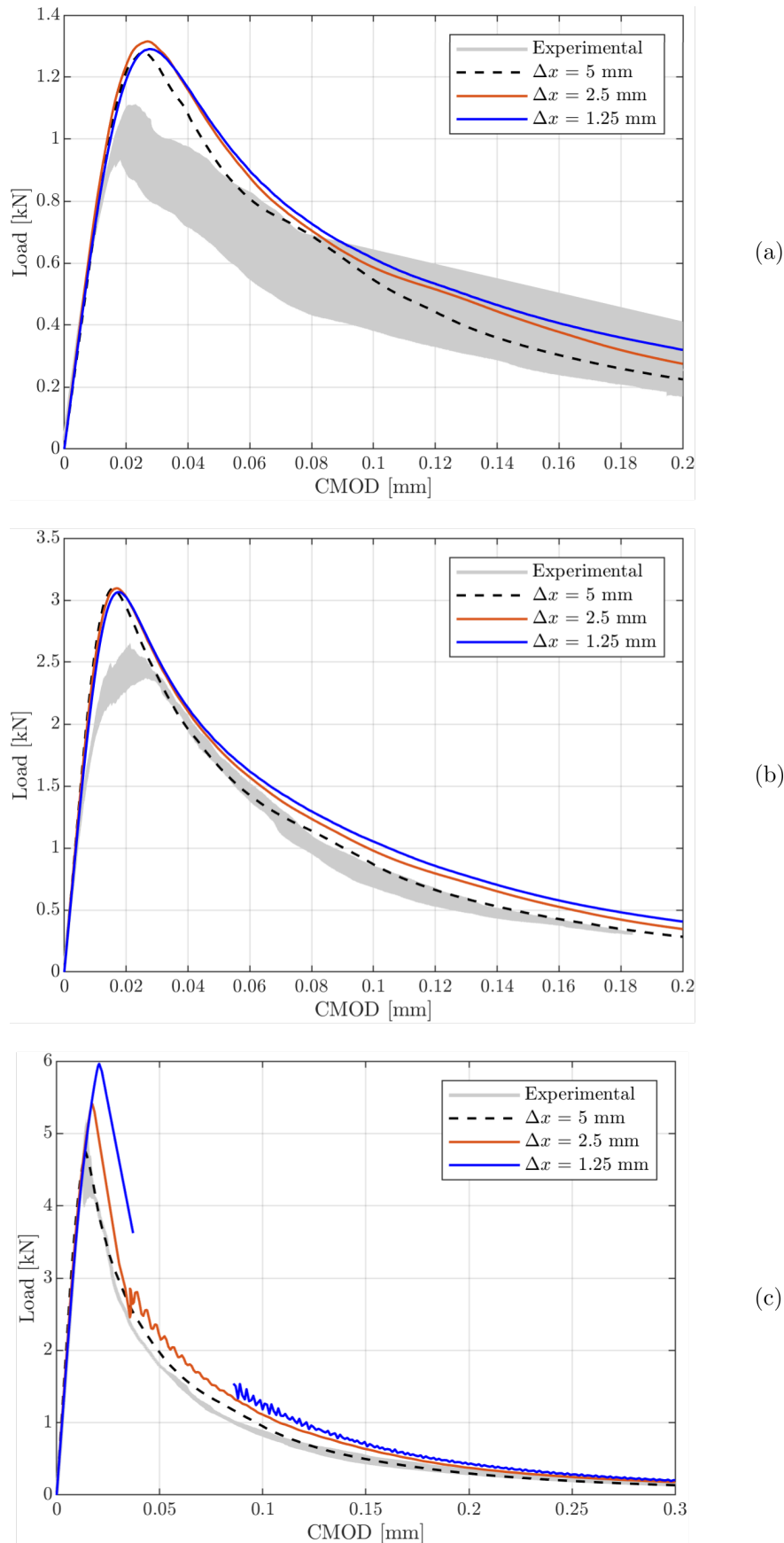


Fig. 5.22 Mesh sensitivity study. Load-CMOD response for three levels of mesh refinement ( $\Delta x = 1.25 \text{ mm}$ ,  $2.5 \text{ mm}$ , and  $5 \text{ mm}$ ). (a) half-notched, (b) fifth-notched, (c) unnotched.

Fig. 5.23 illustrates the fracture path at 0.5mm of applied displacement using the finest mesh  $\Delta x = 1.25$  mm. The numerical fracture path is identical for all levels of mesh refinement. By only considering the macroscopic fracture behaviour, the underlying mechanisms driving the failure process are hidden. Examining the development of micro-cracking might provide insights into the observed numerical results and the next section provides an examination of the damage energy dissipation.

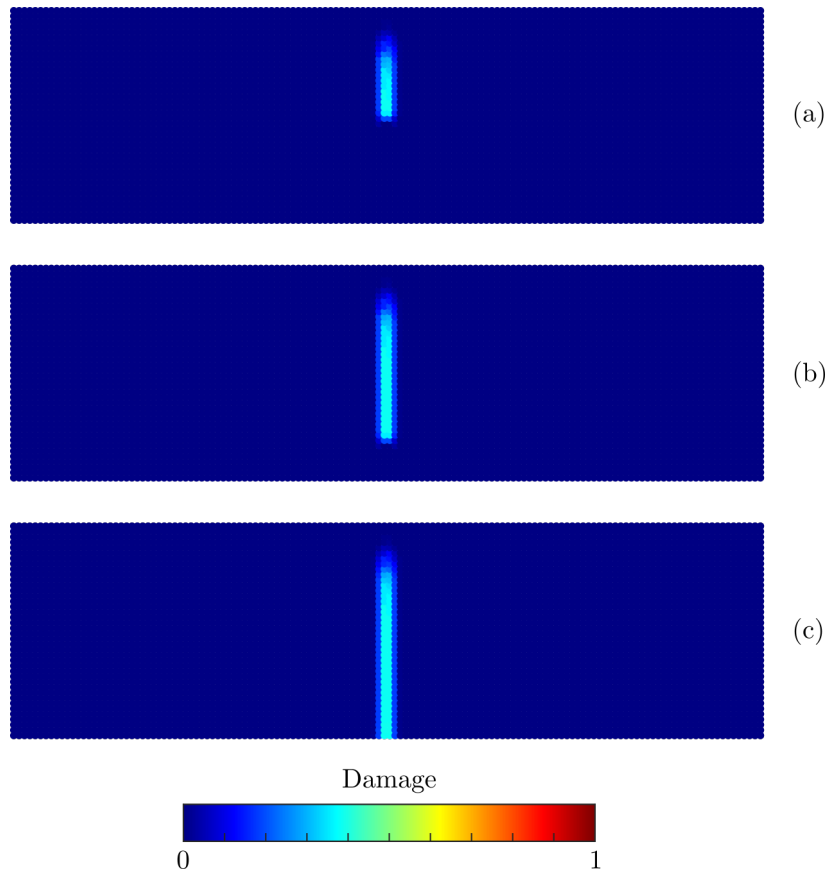


Fig. 5.23 Numerical fracture path at 0.5 mm of applied displacement. The residual load carrying capacity is approximately 30 N for each member. (a) half-notched, (b) fifth-notched, (c) unnotched.

## 5.7 Examination of damage energy dissipation

This section provides an examination of the damage energy dissipation. Investigating the energy dissipation provides insights into the observed mesh sensitivity. To the best knowledge of the author, this is the first time that energy dissipation has been investigated using a peridynamic model.

The spatial distribution of energy dissipation represents the growth of micro-cracks. In quasi-brittle materials, the initiation, propagation and coalescence of micro-cracks is the main physical mechanism governing the inelastic deformation and failure. Failure occurs due to the formation of localised macro-cracks that occur through the coalescence of diffuse micro-cracks [245]. The size and shape of the damage zone has been determined experimentally and numerically, and Eliáš and Vorechovský [74] provide a short review. A number of studies have examined energy dissipation using numerical methods [96, 75, 74].

Fig. 5.24 illustrates the softening damage at 0.5 mm of applied displacement using the finest mesh  $\Delta x = 1.25$  mm. The softening damage at a material point  $x$  is defined as the ratio of bonds that have exceeded the linear elastic limit to the total number of bonds. The spatial distribution of dissipated energy is very different if a fracture initiates from a flat surface (unnotched specimen) or from a notch. A wide zone of distributed micro-cracking develops prior to the peak load in unnotched members, and at the peak load, the micro-cracks localise into a distinct single macroscopic fracture. Predicting fracture initiation in unnotched members is considered to be a harder problem due to the complex behaviour of energy dissipation and localisation. Vorel et al. [228] compared four continuum-based models and a lattice discrete particle model for modelling concrete. For all models, the predictive accuracy was found to be significantly lower for unnotched problems.

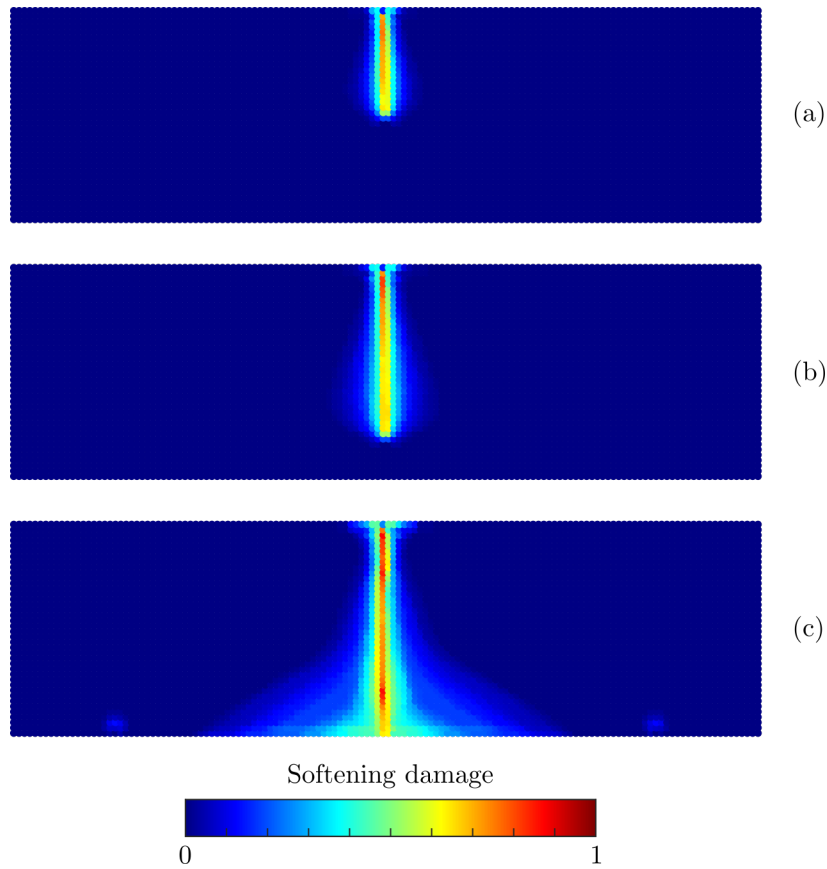


Fig. 5.24 Numerical softening damage at 0.5 mm of applied displacement using the finest mesh  $\Delta x = 1.25$  mm. (a) half-notched, (b) fifth-notched, (c) unnotched.

Grassl et al. [96] modelled the fracture process zone (FPZ) in concrete using a discrete lattice approach. They defined the FPZ as the zone in which energy is dissipated at a certain stage of analysis. The numerical results are compared to the experimental results of Grégoire et al. [98]. The predicted spatial distribution of damage energy was later validated against acoustic emission data [99]. The numerical model is in good agreement with the acoustic emission data. Grassl mapped the meso-structure of concrete on the discrete lattice by employing a field of spatially varying material properties. 100 simulations were conducted for every beam with randomly generated meso-structures and the average width of the region of energy dissipation was determined. For the half-notched member, the region of energy dissipation is approximately 18 mm wide. For the fifth-notched member, the width of the region of energy dissipation increases to approximately 24 mm. For the unnotched member, the width of the region of energy dissipation significantly increases to approximately 100 mm, with most of the energy dissipation occurring within a region approximately 40 mm wide.

Similar to the work of Grassl et al. [96], the region of energy dissipation is determined using the mid-point of bonds that have exceeded the elastic limit. Fig. 5.25 illustrates the zone of energy dissipation immediately after the peak load using the finest mesh  $\Delta x = 1.25$  mm. Each point represents the mid-point of a damaged bond. For the notched cases, the width of the region of energy dissipation remains approximately equal across all levels of mesh refinement. For the unnotched case, the width of the region of energy dissipation increases as the mesh is refined. The results, presented in Table 5.3, are in close agreement with those of Grassl et al. [96]. For the unnotched member, most of the energy dissipation occurs within a region approximately 35 mm wide (see Fig. 5.25 (c)).

The dependency of the energy dissipation on the mesh resolution for the unnotched case is believed to be the source of the peak load sensitivity. The cause of the mesh sensitivity is not yet fully understood but an important factor has been identified. It is hypothesised that the inclusion of spatially varying material properties might be important for capturing the correct behaviour in unnotched cases. Eliáš et al. [75] found that the energy dissipation in unnotched beams is significantly influenced by the inclusion of randomness. In later work, Eliáš and Vorechovský [74] found that spatial variability in material properties does not influence the peak load for notched cases. These observations are consistent with the presented results and support the hypothesis that statistical variability in material properties plays an important role.

Table 5.3 Width of the region of damage energy dissipation at peak load (mm)

$\Delta x$ (mm)	$\delta$ (mm)	Half-notched	Fifth-notched	Unnotched
5	15.7	15.0	25.0	62.5
2.5	7.9	15.0	22.5	76.3
1.25	3.9	16.3	24.4	85.0

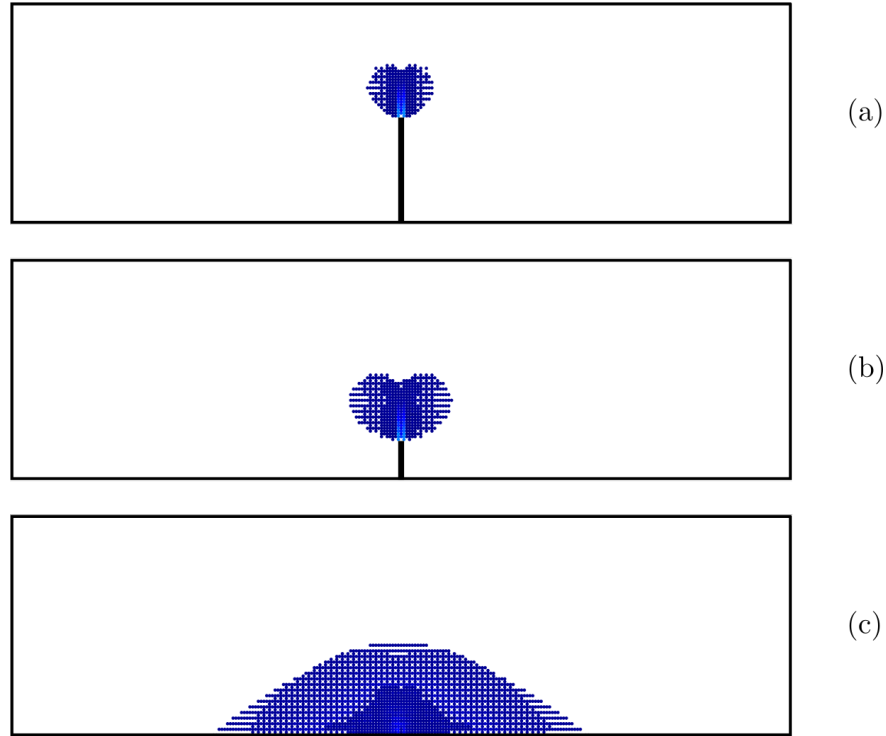


Fig. 5.25 Region of damage energy dissipation at peak load using the finest mesh  $\Delta x = 1.25$  mm. Each point represents the mid-point of a bond that has exceeded the elastic limit. (a) half-notched, (b) fifth-notched, (c) unnotched.

Fig. 5.26 illustrates the region of energy dissipation at the peak load for the fifth-notched member. This figure is included to qualitatively demonstrate the capability of the model. The peridynamic model could be used to provide a greater understanding of the fracture process zone in quasi-brittle materials. Benkemoun et al. [26] concluded that the volume (width) of the fracture process zone is correlated to the aggregate size and this is an area that requires further investigation.

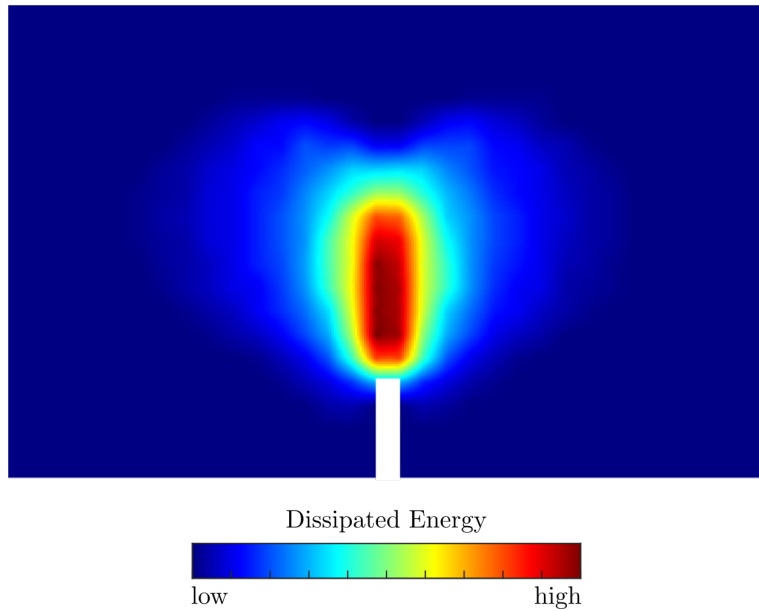


Fig. 5.26 Region of energy dissipation (fracture process zone) at the peak load for the fifth-notched beam.

## 5.8 Mixed-mode problem

This section provides an examination of mixed-mode fracture problems. The ability to accurately predict mixed-mode fracture is an important check on the validity of a numerical model. Many problems of interest (industrially motivated problems) will exhibit mixed-mode behaviour. Constitutive laws have been introduced in the framework of finite element analysis to capture the complex behaviour of mixed-mode fracture behaviour. Xie and Waas [233] introduced a cohesive constitutive law that separates the crack propagation criteria into tension (mode I) and shear (mode II) components. This requires separating the fracture energy into mode I and mode II components. The existence of mode II fracture energy has been questioned by Carpinteri et al. [44] and there still exists no consensus. The proposed non-linear softening law does not explicitly consider shear behaviour (mode II behaviour).

The mixed-mode fracture tests of García-Álvarez et al. [88] are simulated. Eccentrically notched concrete beams in three-point bending were experimentally tested. Numerical results have been reported by the authors who used a non-linear finite element model with interface elements to model the experimental tests. Numerical results have also been reported by Feng and Wu [80], Mendonça et al. [152] and Barbat et al. [8]. A schematic diagram of the experimental setup is illustrated in Fig. 5.27. The smallest member (depth  $d = 80$  mm) is

used for validation. The full set of tests is addressed in later size effect studies (see Chapter 6).

The member has the following dimensions: length  $l = 250$  mm; depth  $d = 80$  mm; and thickness  $b = 50$  mm. The span of the member is 200 mm. The notch-to-depth ratio  $\lambda$  is fixed at 0.25 and three different notch eccentricities  $\mu d$  are considered:  $0.0d$ ,  $0.3125d$ , and  $0.625d$ . The material properties used for computation are as follows: cylindrical compressive strength  $f_{cm,cyl} = 20$  MPa; modulus of elasticity  $E = 33.8$  GPa; tensile strength  $f_t = 3.5$  MPa; material fracture energy  $G_F = 125.2$  N/m. The cylindrical compressive strength  $f_{cm,cyl}$  and modulus of elasticity  $E$  were determined experimentally. The value of tensile strength  $f_t$  was determined numerically by García-Álvarez et al. [88]. The specimens were cured for 720 days in a fog room. The long curing period and high moisture content explains the high tensile strength  $f_t$  [83]. The material fracture energy  $G_F$  was determined empirically using Eq. (5.22).

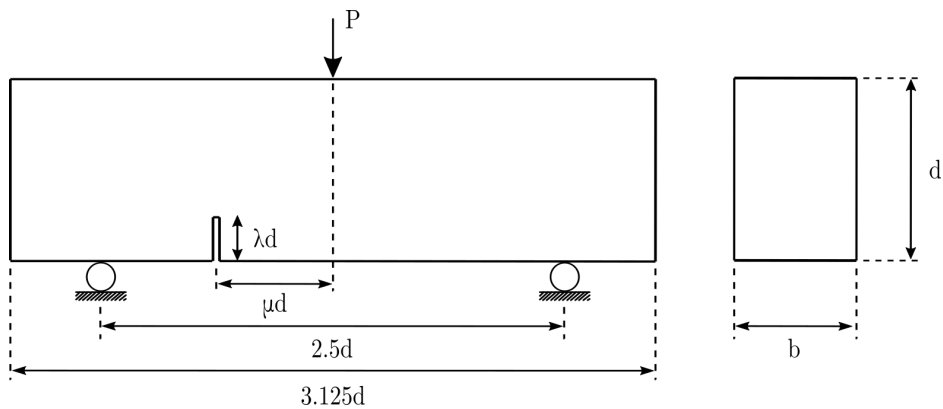


Fig. 5.27 Schematic of the experimental setup. Adapted from García-Álvarez et al. [88].

Only the newly proposed non-linear softening law is considered. Predictions using the finest mesh resolution  $\Delta x = 1.25$  mm are reported. The model parameters remain the same; only the material properties change. Results are presented in Fig. 5.28 and predictions from Barbat et al. [8] are included for comparison. Every case was tested multiple times and the range of experimental results is plotted in grey. The predicted load-CMOD response is in good agreement with the experimental data, and the peak load is accurately predicted. This is somewhat unexpected. As previously observed for notched cases, it was expected that the predicted peak load would be higher than the experimental value. This might be a result of uncertainty in the material properties that has a favourable impact on the predictions. To improve the robustness of the numerical predictions, load-CMOD results should be bounded with an upper and lower limit.

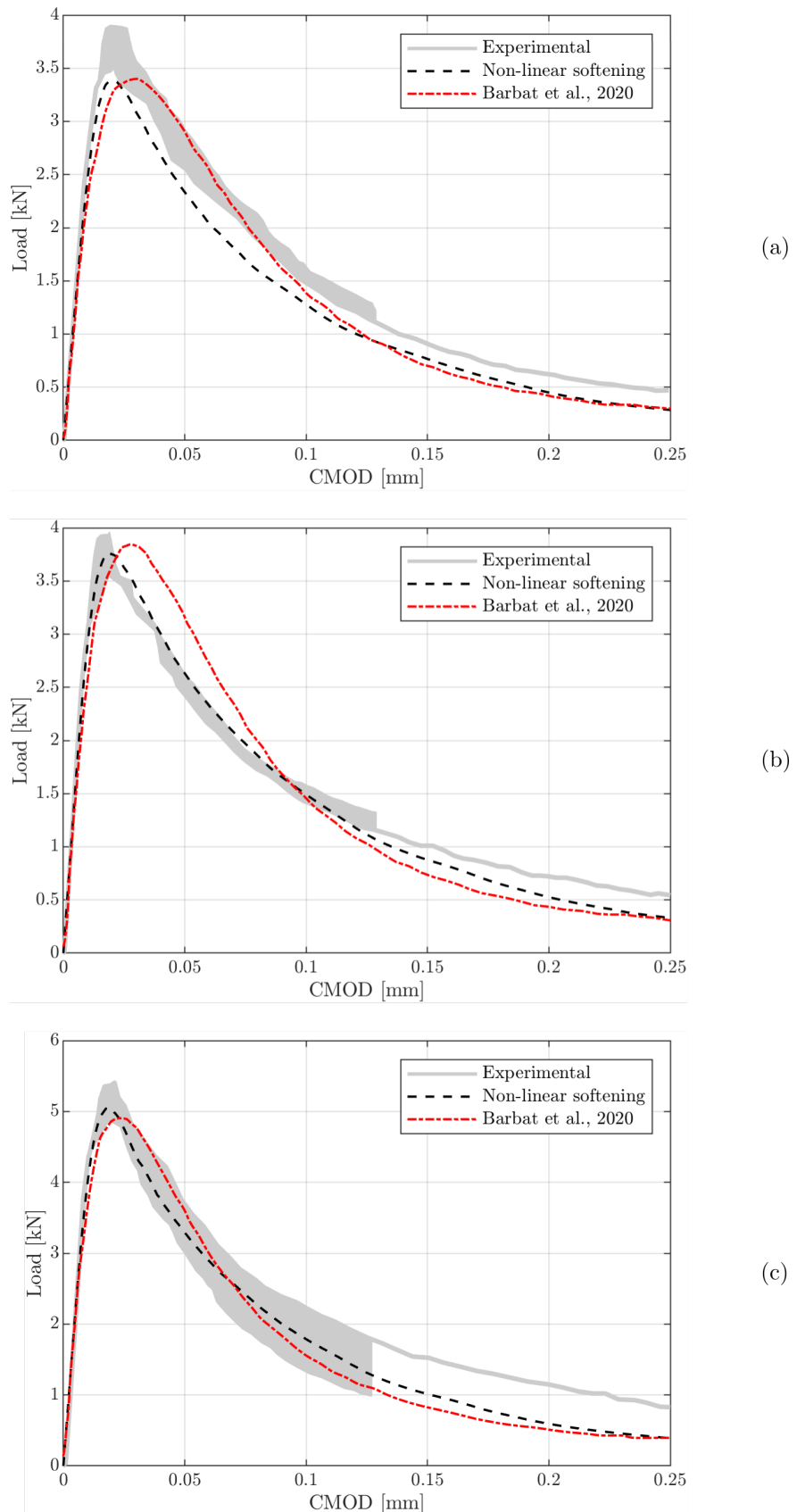


Fig. 5.28 Load-CMOD response for the mixed mode fracture tests. Notch eccentricity  $\mu d$ : (a) 0d, (b) 0.3125d, and (c) 0.625d

The computed fracture paths are illustrated in Fig. 5.29, Fig. 5.30 and Fig. 5.31. Results for the mode I case ( $\mu d = 0.0d$ ) have not been included to avoid repetition. For the mode I case, the fracture initiates from the notch (mid-span) and propagates vertically towards the applied load. For the mixed-mode problems, the fracture initiates from the notch and propagates at an angle towards the applied load. The three-dimensional mixed-mode fracture paths are depicted in Fig. 5.29. This figure is included to demonstrate the ability of the peridynamic model to accurately capture three-dimensional crack paths. More complex three-dimensional problems are addressed in Chapter 7. Fig. 5.31 compares the computed fracture path against the experimental data. A good agreement is observed, and the results do not show any mesh bias. The predicted crack paths are independent of the mesh resolution, demonstrating the robustness of the model.

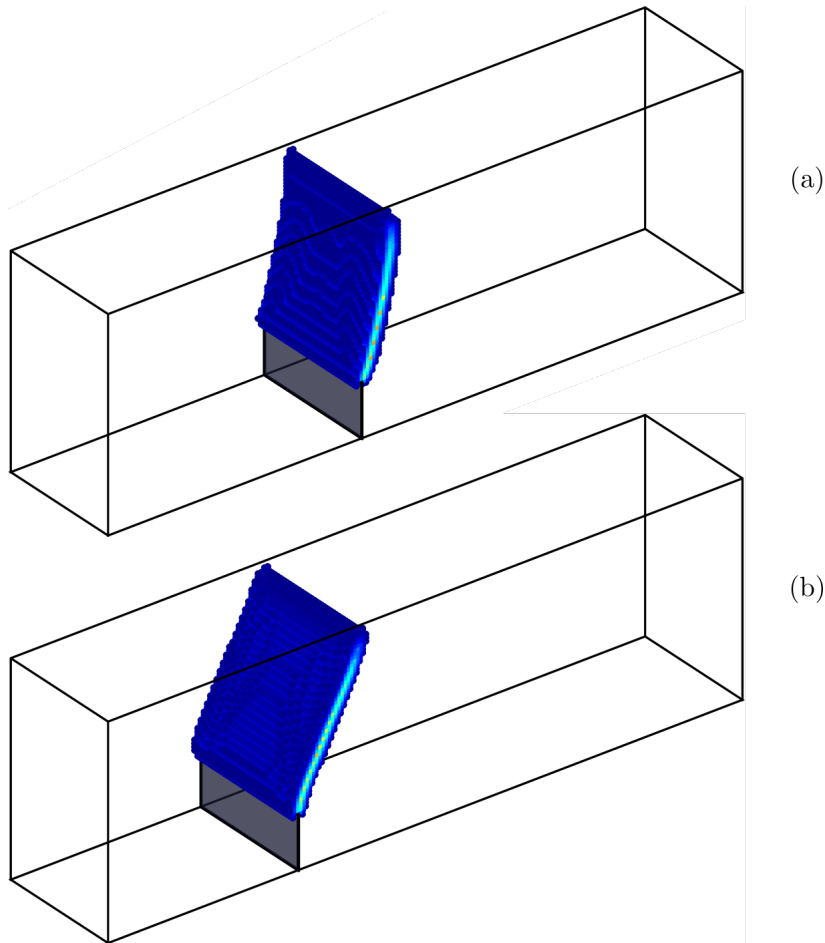


Fig. 5.29 3D crack paths for the mixed-mode fracture tests. Notch eccentricity  $\mu d$ : (a) 0.3125d, and (b) 0.625d

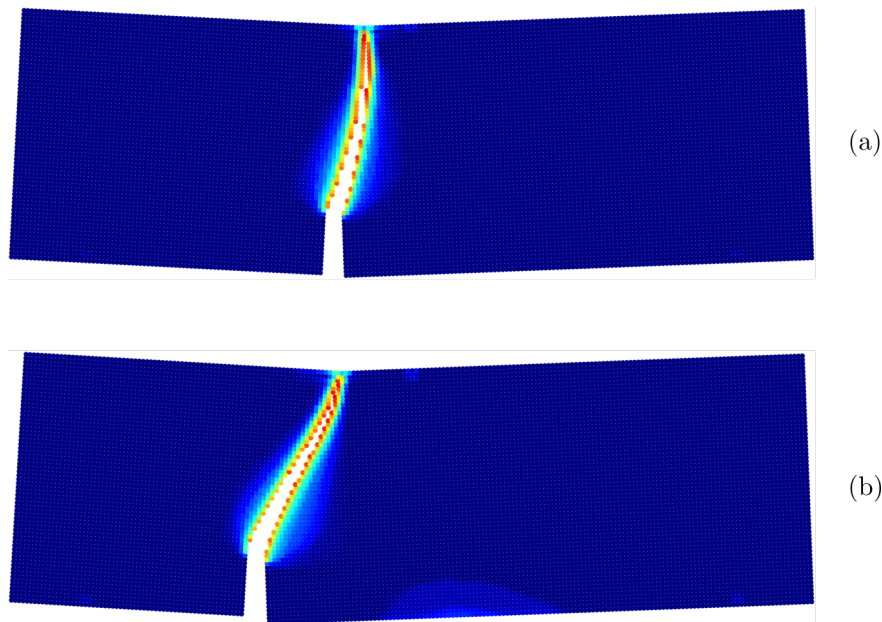


Fig. 5.30 Numerical softening damage for the mixed-mode fracture tests. Notch eccentricity  $\mu d$ : (a) 0.3125d, and (b) 0.625d. Displacement is scaled by a factor of 10.

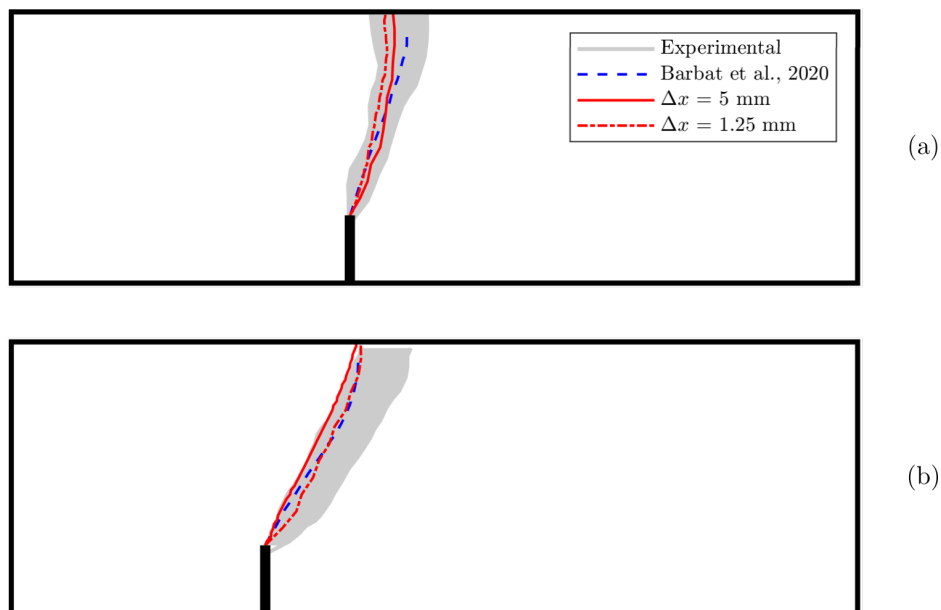


Fig. 5.31 Experimental and numerical crack paths for the mixed-mode fracture tests. Notch eccentricity  $\mu d$ : (a) 0.3125d, and (b) 0.625d

## 5.9 Discussion and future work

Overall, the numerical results are in good agreement with the experimental data, but the peridynamic model overestimates the load capacity of the notched beams tested by Grégoire et al. [98]. This discrepancy can be explained by the non-local interaction of particles above and below the notch tip. This effect might be reduced by using a non-constant micro-modulus function where the weight of a particle is inversely proportional to the bond length.

The use of a non-constant micro-modulus function might provide a number of benefits: (1) an improved representation of the physical reality of non-local forces; (2) reduced surface effects [31]; (3) improved numerical convergence [33, 116, 200]. Ha and Bobaru [104], Chen et al. [51], and Li et al. [136] have studied the influence of different micro-modulus functions. These studies predominantly focussed on brittle fracture and dynamic crack branching and all problems examined are two-dimensional. Further examination of influence functions is required and additional validation metrics need to be considered, such as load-deflection response and ultimate load capacity. Three-dimensional problems must also be investigated. This work has demonstrated that using a conical influence function improves the convergence behaviour for a three-dimensional peridynamic model (see Fig. 5.15).

An obvious step is to examine the size effect in quasi-brittle materials using a peridynamic framework. The capability of the peridynamic model to predict size effect has not been investigated and remains a major question. There are two primary sources of size effect [14]: (1) release of stored energy and (2) statistical variability in material properties. The release of stored energy is the primary mechanism controlling size effect [8]. The results presented in this chapter show that the predicted region of energy dissipation is in good agreement with experimental results. This suggests that the model will be able to capture size effect. The influence of spatially varying material properties must also be examined. A clearer understanding of the effect of material micro-structure on energy dissipation and fracture initiation and propagation is needed.

The post-peak softening response is steeper for larger structural members. Efficient path-following methods are required to follow the complete structural response. Sun et al. [213] recently implemented an arc-length method within a peridynamic framework. The arc-length method is applied at the onset of energy dissipation. This approach is capable of following the entire equilibrium path.

## 5.10 Conclusions

The aim of this chapter was to quantify the predictive accuracy of existing constitutive laws for modelling quasi-brittle materials. Existing laws were found to be unsatisfactory, and a new non-linear softening law has been introduced. In an attempt to explain the cause of discrepancies between experimental and numerical results, it was determined that the application of surface correction factors increases the energy required to produce a fracture surface. A correction scheme is proposed that is simple to implement and yields improved results. A sensitivity study was performed to investigate the dependency of the results on the mesh resolution and this was followed by an examination of damage energy dissipation. The key findings are as follows:

1. The newly proposed non-linear softening law can be used to accurately predict the behaviour of quasi-brittle materials. The predicted load-CMOD response, ultimate load capacity, crack path and energy dissipation behaviour are in good agreement with experimental results.
2. The non-local nature of peridynamics influences the results for different boundary types. Spurious strengthening occurs in the proximity of a notch due to the non-local interaction of particles above and below the notch tip.
3. The critical stretch value is not a constant for all bonds and is dependent on the corrected bond stiffness. This is perhaps the most novel contribution of the chapter.
4. For notched problems, the predicted peak load is independent of the mesh discretisation. For unnotched problems, the predicted peak load progressively increases as the mesh is refined.
5. The region of energy dissipation is generally in good agreement with experimental results. The dependency of the energy dissipation on the mesh resolution for the unnotched case is believed to be the source of the peak load sensitivity.
6. The model accurately captures the development of diffuse micro-cracking and the formation of localised macro-cracks. This is achieved without explicitly modelling the meso-structure. An investigation of the damage process at the micro-scale has been missing in the peridynamic literature.
7. Mode I and mixed-mode problems are considered to evaluate the generality of the model. A good agreement is observed between the experimental and numerical results and the predictive accuracy is similar to more advanced approaches. The predicted

crack paths are independent of the mesh resolution, demonstrating the robustness of the model.

In spite of its relative simplicity, the bond-based peridynamic model can accurately capture the complex mechanisms that govern the behaviour of quasi-brittle materials. The model correctly describes the progressive development of distributed micro-cracking, the localisation of damage and formation of macroscopic cracks, and the structural response after localisation. It is possible that the peridynamic model could be used to provide a greater understanding of fracture processes in quasi-brittle materials.



# Chapter 6

## Size effect

### 6.1 Introduction

This chapter examines size effect in quasi-brittle materials using a three-dimensional bond-based peridynamic model. The capability of a peridynamic model to capture size effect in quasi-brittle materials has not been investigated yet and remains a major question. As stated by Bažant [19], the capability to correctly reproduce the size effect is an important check on the validity of any computational model. The aims of this chapter are: (1) quantify the predictive accuracy of the bond-based peridynamic model in capturing size effect; (2) validate the model against experimental data from the literature.

Capturing the structural size effect is essential for safe predictions of load capacity. Existing analytical formulas for predicting size effect in geometrically similar structures are extremely limited, and they generally employ empirical parameters that must be determined through best-fit procedures [155]. Numerical methods offer the only practicable approach for addressing complex industry motivated problems. Understanding the predictive capabilities of the peridynamic model is essential for further application to more complex problems.

There are two primary sources of size effect in quasi-brittle materials [14]: (1) release of stored energy (deterministic size effect), and (2) statistical variability in material properties (statistical size effect). The release of stored energy is the primary mechanism controlling size effect and this work only considers the deterministic component. Considering the spatial randomness of material properties was not practicable due to the high computational cost of peridynamic simulations.

The predictive capabilities of the peridynamic model are quantified against experimental data. Geometrically similar beams of different sizes are modelled. Notched and unnotched concrete beams are modelled to examine the effect of boundary types on the predictive accuracy of the peridynamic model, and mode I and mixed-mode problems are considered

to evaluate the generality of the model. The chapter is organised as follows: Section 6.2 provides a review of structural size effect and the mechanisms behind size effect are examined. Section 6.3 briefly outlines the numerical framework. Mode I problems are examined in section 6.4 and the effect of boundary types is explored. Mixed-mode problems are examined in section 6.5. Section 6.6 provides a discussion of the results and areas of future work are identified. Section 6.7 concludes the chapter.

## 6.2 Structural size effect

### 6.2.1 What is size effect?

According to the classical failure theories, such as elasticity with a material strength limit and plasticity theory, the nominal strength  $\sigma_n$  of a structure is independent of size when geometrically similar structures are considered. The classical theories express the material failure criterion in terms of stress and strain and the nominal strength  $\sigma_n$  is defined as the maximum stress that a structure can resist [19]. For a concrete beam in bending, the limiting nominal strength  $\sigma_n$  is given by the ultimate tensile strength  $f_t$ . Any deviation from predictions made using stress failure criteria is known as the structural size effect. A size effect is observed in many materials.

To clarify further, the basic theory of strength of materials predicts that a small and large beam made of the same material will fail at the same value of stress. In reality, the larger beam will fail at a lower stress. The post-peak behaviour of quasi-brittle materials also exhibits a size effect. At a small scale, concrete behaves like a ductile material and the post-peak load deflection curve descends slowly. At a sufficiently large scale, concrete becomes perfectly brittle, and the load-deflection curve descends rapidly and may exhibit snap-back behaviour [18]. Clearly, a proper understanding of structural size effect is essential for safe predictions of load capacity. For a detailed examination of size effect in quasi-brittle materials, see the work of Bažant and Planas [14] and Bažant [18, 19].

### 6.2.2 Size effect mechanisms

In brittle and quasi-brittle materials, the size effect can primarily be explained by two mechanisms [14, 19]: (1) release of stored energy, and (2) statistical variability in material properties. These effects are often referred to as the deterministic and statistical size effect. Secondary factors that influence the size effect include the boundary layer effect, diffusion phenomena, and hydration heat [8]. The influence of these secondary factors is insignificant and will not be considered any further. The release of stored energy is by far the most

important factor influencing the size effect on structural strength. The influence of statistical variability in material properties is less significant. But until the late 1980's, the primary cause of size effect was generally believed to be of statistical origin [20].

When a fracture initiates and begins to propagate, the elastic strain energy stored in the structure is consumed by the fracture propagation. In quasi-brittle materials, energy is dissipated in a non-linear zone of micro-cracking formed at the crack tip. This damage zone is known as the fracture process zone (FPZ). The ratio between the elastic energy stored in the structure and the energy consumed by the fracture process varies with the size of the structure. This is the main mechanism responsible for structural size effect. The mechanism by which the statistical size effect occurs is simpler to comprehend. As the size of a structure increases, so does the probability that a defect will be present from which a fracture will initiate.

Studying the mechanisms that govern size effect is limited by the physical size of the experiments that can be performed within a reasonable timescale and budget. Many structures of interest, such as dams and reactor containment buildings, are far beyond the scale of laboratory experiments. Numerical methods provide new ways to explore size effect without the aforementioned limitations.

### 6.2.3 Size effect laws

Numerous analytical expressions have been developed to describe the size effect of quasi-brittle materials. Size effect laws provide predictions of nominal strength as a function of the characteristic size of the structure for geometrically similar structures, with and without notches. These expressions have been developed from experimental observations and theoretical considerations.

The central characteristic of quasi-brittle materials is that there exists a sizeable fracture process zone and area of softening damage. The size effect is governed by the size of the fracture process zone relative to the size of the structure and depending on the structure size, different theories are applicable for predicting strength. At a sufficiently small scale, the theory of plasticity, which assumes no size effect, is applicable. The theory of plasticity is valid when the size of the fracture process zone is comparable to the structural size. At a sufficiently large scale, the theory of linear elastic fracture mechanics, which predicts the strongest possible deterministic size effect, is applicable. The theory of linear elastic fracture mechanics is valid when the size of the fracture process zone is negligible with respect to the structural size. Many attempts have been made to bridge the gap between the theory of plasticity and the theory of linear elastic fracture mechanics.

Numerous expressions have been proposed to combine the different theories and provide a general size effect law. The analytical expressions defined by Eq. 6.1 were proposed by Bažant [16] and Bažant and Planas [14] to describe the deterministic size effect. Two types of size effect law are defined: Type 1 - structures with no notches or pre-existing cracks (fracture initiates from a smooth surface); Type 2 - structures with a notch. Notched problems are representative of reinforced concrete structures, where due to the reinforcement, the stable growth of cracks occurs prior to the ultimate load.

$$\sigma_N(D) = \begin{cases} f_r^\infty \left(1 + r \frac{D_b}{D + l_p}\right)^{1/r} & \text{Type 1 (unnotched case)} \\ \frac{Bf_t}{\sqrt{1 + \frac{D}{D_0}}} & \text{Type 2 (notched case)} \end{cases} \quad (6.1)$$

$\sigma_N$  is the nominal strength and  $D$  is the characteristic size of the structure. For Type 1 structures,  $f_r^\infty$ ,  $D_b$ ,  $l_p$ , and  $r$  are positive constants representing unknown empirical parameters.  $f_r^\infty$  represents the elastic-brittle strength reached for large structures,  $D_b$  is a deterministic characteristic length set principally by the material inhomogeneity size (aggregate size in concrete),  $l_p$  is a second deterministic characteristic length controlling the centre of transition to a horizontal asymptote of the  $\log \sigma_N$  versus  $\log D$  curve, and  $r$  controls the curvature and shape of the law. For Type 2 structures,  $f_t$  represents the tensile strength, and  $B$  and  $D_0$  are positive constants representing unknown empirical parameters.  $B$  is a dimensionless constant, and  $D_0$  represents the transitional size at which the power laws of plasticity and LEFM intersect. It should be noted these definitions are not exact and different interpretations can be found within the literature. The size effect laws are illustrated in Fig. 6.1 and it becomes clear that Type 1 and Type 2 structures have different asymptotic properties when  $D \rightarrow \infty$ .

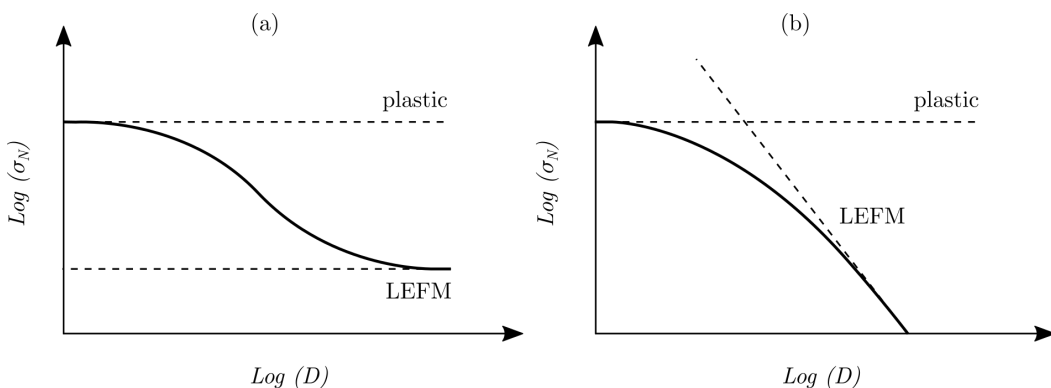


Fig. 6.1 Size effect laws in a log-log scale: (a) Type 1 (unnotched case); (b) Type 2 (notched case). Adapted from Fig. 1 in [216].

An extended analytical expression was proposed by Bažant et al. [24] to describe the combined deterministic-stochastic size effect for Type 1 structures.

$$\sigma_N(D) = f_r^\infty \left( \left( \frac{l_s}{D + l_s} \right)^{\frac{m}{m}} + r \frac{D_b}{D + l_p} \right)^{1/r} \quad (6.2)$$

$l_s$  is a stochastic scaling length,  $m$  is the dimensionless Weibull modulus (shape parameter of the Weibull distribution), and  $n$  is the number of spatial dimensions in which the structure is scaled. The proposed expression accounts for the stochastic and deterministic component of size effect.

The practical applicability of size effect laws is limited. This has been noted by Moallemi et al. [155]. Many of the parameters are empirical and there is no systematic method to determine the parameter values. A precise definition for the characteristic length is lacking and this ambiguity further undermines the general applicability of the size effect laws. This is discussed further in the following section. The nominal strength is influenced by multiple factors including the geometry of the structure, boundary conditions, and material properties. It is unlikely that it will be possible to develop a general size effect law that can be reliably applied to a wide range of non-trivial problems. Numerical methods offer the only practicable approach for addressing complex industry motivated problems.

#### 6.2.4 Numerical methods

A significant body of work has been published on the numerical simulation of size effect in quasi-brittle materials, and models can be broadly categorised as deterministic or stochastic. In a deterministic model, the material properties are constant over the spatial domain. Deterministic models have been employed by many researchers including Moallemi et al. [155], Feng and Wu [80] and Barbat et al. [8]. In a stochastic model, the spatial variability of the material properties is considered. Stochastic models have been used by Gutiérrez and De Borst [101], Vorechovský [227], Bažant et al. [24], Yang and Frank Xu [238], Bobiński et al. [34], Grassl et al. [96], Syroka-Korol et al. [216], Syroka-Korol et al. [217], Zhou and Chen [246], Eliáš et al. [75] and Eliáš and Vorechovský [74]. These references are not exhaustive. A stochastic model is required for a complete examination of the mechanisms that govern the size effect, and allows the magnitude of the deterministic and stochastic components to be determined.

Capturing the correct energy dissipation as a crack forms and propagates is essential to accurately model structural size effect [48, 8]. Many existing numerical methods use a localisation limiter that governs the width of the softening zone. Examples include crack

band, gradient enhanced, non-local, and phase-field models. For further details, the reader is referred to [14, 21, 211, 8]. The use of a localisation limiter is necessary to prevent damage from localising into a zone of zero volume [22]. The localisation limiter is chosen to ensure correct energy dissipation when a crack forms and is determined by an internal characteristic length  $l_c$  that is a property of the material being modelled. Note that the correlation length in a probabilistic framework plays a role equivalent to the characteristic length [53]. Bažant and Pijaudier-Cabot [22] define the characteristic length as a material property that governs the minimum possible width of a zone of strain-softening damage. The characteristic length  $l_c$  is the ratio of the fracture energy (energy dissipated per unit area) to the energy dissipated per unit volume. For concrete, the characteristic length is determined to be approximately 2.7 times the maximum aggregate size [22]. Nguyen et al. [165] states that a clear physical interpretation and direct link between the length parameter in the numerical model and the characteristic length of the material is debatable. Moallemi et al. [155] also note that the definition of the characteristic length is ambiguous. In different works it has loosely been interpreted as the size of the fracture process zone or the size of material inhomogeneities. The peridynamic model is non-local and material particles interact over a length-scale determined by the horizon  $\delta$ . The peridynamic model differs from existing approaches as the size of the peridynamic horizon  $\delta$  is not explicitly related to material properties.

### 6.3 Numerical framework

All the results presented in this chapter were obtained using the explicit scheme outlined in Fig. 4.14. The applied displacement is increased incrementally using a fifth-order smooth step function and there is no damping in the system. The non-linear softening law, first proposed in Chapter 5, is used for all simulations, as is the critical stretch correction scheme, also first proposed in Chapter 5. The non-linear softening model was calibrated to fit the experimental results for the smallest unnotched specimen ( $d = 50$  mm). Model parameters are then fixed for all test cases. This is essential in a robust validation procedure [218].

### 6.4 Mode I problem

Validation is performed against the full set of experimental results published by Grégoire et al. [98]. Geometrically similar notched and unnotched concrete members were tested in three-point bending to investigate size and boundary effects. The aim of the experiments was (1) to provide suitable experimental data for the validation of constitutive models, and (2)

to provide a benchmark for assessing the accuracy of non-linear finite element models in capturing size effect. It should be noted that Hoover et al. [114] independently performed a similar experimental study that has also widely been used for validation.

A schematic diagram of the experimental setup is illustrated in Fig. 5.8. Four different sizes of geometrically similar specimens were considered: depth  $d = 50$  mm, 100 mm, 200 mm, and 400 mm; constant thickness of 50mm; and fixed span-to-depth ratio of 2.5. Member dimensions can be found in Table 6.1. The smallest member ( $d = 50$  mm) was examined in the previous chapter. To examine boundary effects, three different notch configurations were considered: unnotched (notch-to-depth ratio  $\lambda$  of 0), fifth-notched (notch-to-depth-ratio  $\lambda$  of 0.2), and half-notched (notch-to-depth ratio  $\lambda$  of 0.5). The mean material properties are used for all computations: compressive strength  $f_{cm,cyl} = 42.3$  MPa; modulus of elasticity  $E = 37.0$  GPa; splitting tensile strength  $f_t = 3.9$  MPa. The coefficient of variability for the mean material properties is 6.6%, 2.4%, and 6.0% respectively. The material fracture energy is estimated to be  $G_F = 73f_{cm}^{0.18} = 143.2$  N/m. The density of the concrete mixture was 2346 kg/m<sup>3</sup> and the maximum aggregate diameter was 10 mm.

The results from the experiments of Grégoire et al. [98] have been used to validate a wide range of numerical models. Grégoire used an integral-type non-local damage model within a finite element framework. The model failed to capture the size effect over the full range of experiments. Grassl et al. [96] modelled the full experimental series using a two-dimensional discrete lattice approach. Rodrigues et al. [191] modelled the fifth-notched beams using a two-dimensional mesoscale model in a finite element framework. Crack propagation was modelled by means of a mesh fragmentation technique in which interface elements were inserted along the potential crack path. Rodrigues et al. [190] recently extended this work to three-dimensions and again modelled the fifth-notched beams. Feng and Wu [80] used a phase-field regularised cohesive zone model (CZM) to model the complete experimental set. Eliáš and Vorechovský [74] used a lattice discrete particle model with spatially varying material properties. The authors use trial and error to determine the modulus of elasticity  $E$ , and an optimisation method to determine the tensile strength  $f_t$  and material fracture energy  $G_F$ . This approach is unsatisfactory and the obtained parameters differ considerably from the experimentally determined values. Calibrating the material parameters to obtain a good fit does not constitute validation. Predictions obtained using the peridynamic model are compared against results recently published by Barbat et al. [8]. The authors employ a crack band model in a smeared crack framework. This is the most widely used approach for modelling the failure of concrete [10, 8]. Comparing the predictive accuracy of the peridynamic model against established numerical methods is an essential step in validation.

The above discussion is not exhaustive and numerical results have been reported by many other authors.

Table 6.1 Member dimensions

Specimen:	1	2	3	4
Length $l$ (mm)	1400	700	350	175
Depth $d$ (mm)	400	200	100	50
Width $t$ (mm)	50	50	50	50
Span $s$ (mm)	1000	500	250	125

### 6.4.1 Results: notched cases

The predicted load-CMOD response for the full set of notched tests is illustrated in Fig. 6.3 (a) and (b). Results from Barbat et al. [8] are included for comparison. The numerical and experimental results are in good agreement. The peak-load and softening response is accurately captured for almost all notched specimens, and the correct fracture behaviour is predicted for all cases. The computed fracture paths for the half-notched specimens are illustrated in Fig. 6.2. Results for the fifth-notched specimens have not been included to avoid repetition of similar results. For all problems, the fracture initiates from the mid-span of the beam and propagates vertically towards the applied load. The results demonstrate that a bond-based peridynamic model can capture a deterministic size effect. The statistical size effect is negligible in notched specimens [34]. The influence of randomness in material properties is lessened due to the high concentration of stress at the notch tip.

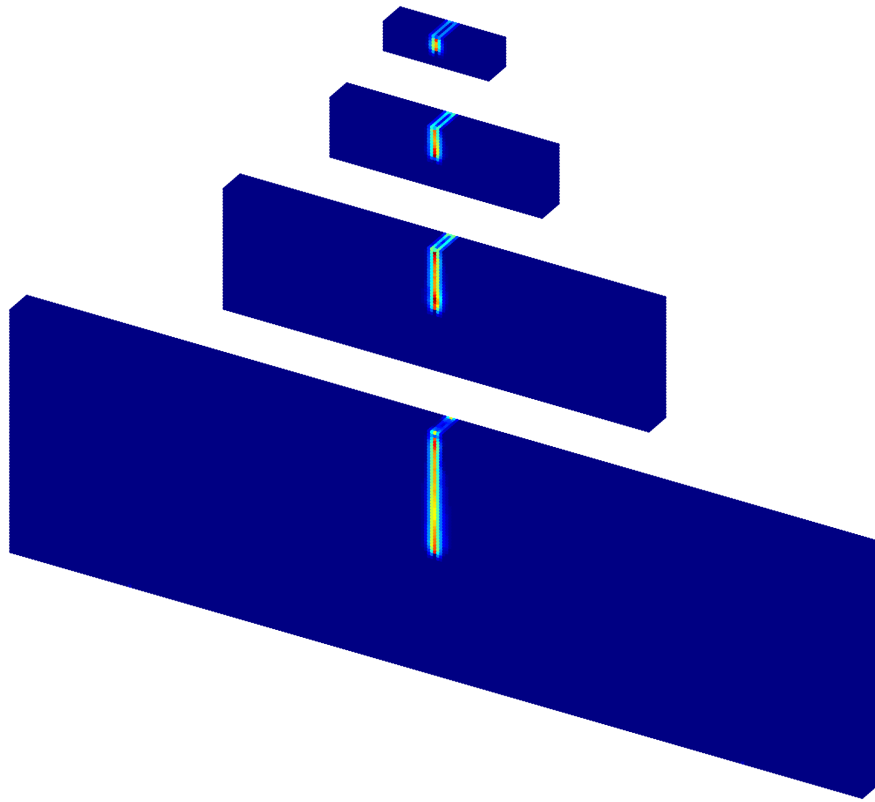


Fig. 6.2 Numerical softening damage for the half-notched specimens

### 6.4.2 Results: unnotched case

The predicted load-CMOD response for the full set of unnotched tests is illustrated in Fig. 6.3 (c). As the structure size increases, so does the over-prediction of structural strength for unnotched members. For Beam 3, the predictive error between the experimental and predicted failure load is approximately +10%; for Beam 2, the predictive error is approximately +20%; and for Beam 1, the predictive error is approximately +40%. To some extent, this behaviour was expected. For notched problems, statistical variability in material properties can largely be ignored, but for unnotched problems, the randomness of material properties has a significant effect on structural strength [216, 74]. For unnotched specimens, the probability that a defect is present in the region of highly stressed material is much higher. The load-CMOD response does not reveal all. The size effect on structural strength is illustrated much more clearly by plotting the predicted nominal strength against beam depth, see Fig. 6.4. A strong deterministic size effect is predicted for the notched problems, but for the unnotched problems, the nominal strength  $\sigma_n$  remains approximately constant for all beam depths. It was expected that the deterministic model would overestimate the nominal strength, but it is surprising that no size effect is observed.

The deterministic model significantly over-predicts the load capacity of Beam 1 and 2 and the obvious question is: does the omission of statistical variability in material properties account for the entire discrepancy between the experimental and numerical results? The degree to which material randomness influences structural strength is unclear and the only way to definitively answer this question would be to model the spatial variability in material properties. This is beyond the scope of this work due to the high computational expense (further details are provided in the discussion). Despite this, some useful understanding can be attained by considering the existing literature.

Vorechovský [227], Bobiński et al. [34], Syroka-Korol et al. [216], and Eliáš et al. [75] found that the difference between the deterministic and mean statistical strength increases for larger structures (mean statistical strength is always smaller). The predicted results are consistent with this observation. Syroka-Korol et al. [216] modelled unnotched concrete beams in three point bending using a deterministic and stochastic approach. The deterministic and mean stochastic strength start to diverge when the beam depth is greater than 50 - 60 mm. Their results showed that the mean stochastic strength is 12% smaller than the deterministic strength for a beam depth of 320 mm. The observed reduction in strength is not large enough to explain all the difference between the experimental and numerical results obtained using the peridynamic model. However, the work of Syroka-Korol is limited by the lack of comparison with experimental data, and there is evidence that the difference between mean stochastic strength and deterministic strength should be greater.

Syroka-Korol et al. [216] compared the stochastic and deterministic numerical results with size effect laws proposed in the literature [14]. The deterministic-stochastic size effect law of Bažant et al. [24] was fitted to the stochastic numerical results using a Weibull modulus of 48 (see Fig. 21 in [216]). The Weibull modulus  $m$  is a dimensionless parameter of the Weibull distribution, used to describe the variability in material properties. For concrete, the Weibull modulus is generally in the range of 5 - 24, where a higher value signifies less variability [13]. The degree of variability in the material parameters ( $m = 48$ ) does not agree with experimental data ( $m = 5 - 24$ ) and this will have a significant influence on the predicted strength. The difference between the mean stochastic strength and deterministic strength would be much greater if the stochastic model captured the true variability in material properties. Using a Weibull modulus of 12, the statistical size effect would reduce the nominal strength of a 320 mm deep beam by approximately 30% (see Fig. 21 in [216]). This suggests that the omission of statistical variability in material properties might account for almost all of the observed discrepancies.

It is important to be transparent about the limitations of the peridynamic model. The peridynamic model does not predict any deterministic size effect for the unnotched problems,

and whilst it is expected that the inclusion of statistical variability in material properties would significantly improve the predictive accuracy, a small deterministic size effect should have been captured. Feng and Wu [80] and Barbat et al. [8] captured the correct failure load for the unnotched cases without considering randomness in material properties. These results run counter to the previous arguments and require examination. In this work, the spatial domain has been discretised using a regular mesh. Feng and Wu [80] used an unstructured mesh and it is hypothesised that randomness in the mesh structure might improve the localisation behaviour for unnotched problems. However, Barbat et al. [8] used a regular mesh and correctly predicted the peak load for all unnotched problems. Moallemi et al. [155] also demonstrated a deterministic size effect in unnotched problems using a structured triangular mesh. However, there is no comparison with experimental data which makes it difficult to assess the correctness of the results. Eliáš et al. [75] modelled a similar set of unnotched beams using a discrete meso-scale model. Deterministic calculations were performed using a random spatial arrangement of particles and a small size effect was predicted, but the reduction in nominal strength was significantly less than that observed experimentally.

The above analysis does not provide any definitive conclusions and clearly the next step is to model the spatial variability in material properties. This is beyond the scope of the current work but implementation details are provided in the discussion. The influence of an unstructured discretisation also requires further study.

Computed crack paths for the unnotched specimens have not been included to avoid repetition of similar results. As illustrated in Fig. 5.24, a wide zone of softening damage develops in the tensile region prior to the peak load. At the peak load, the damage localises, and a fracture initiates from the mid-span of the beam and propagates vertically towards the applied load.

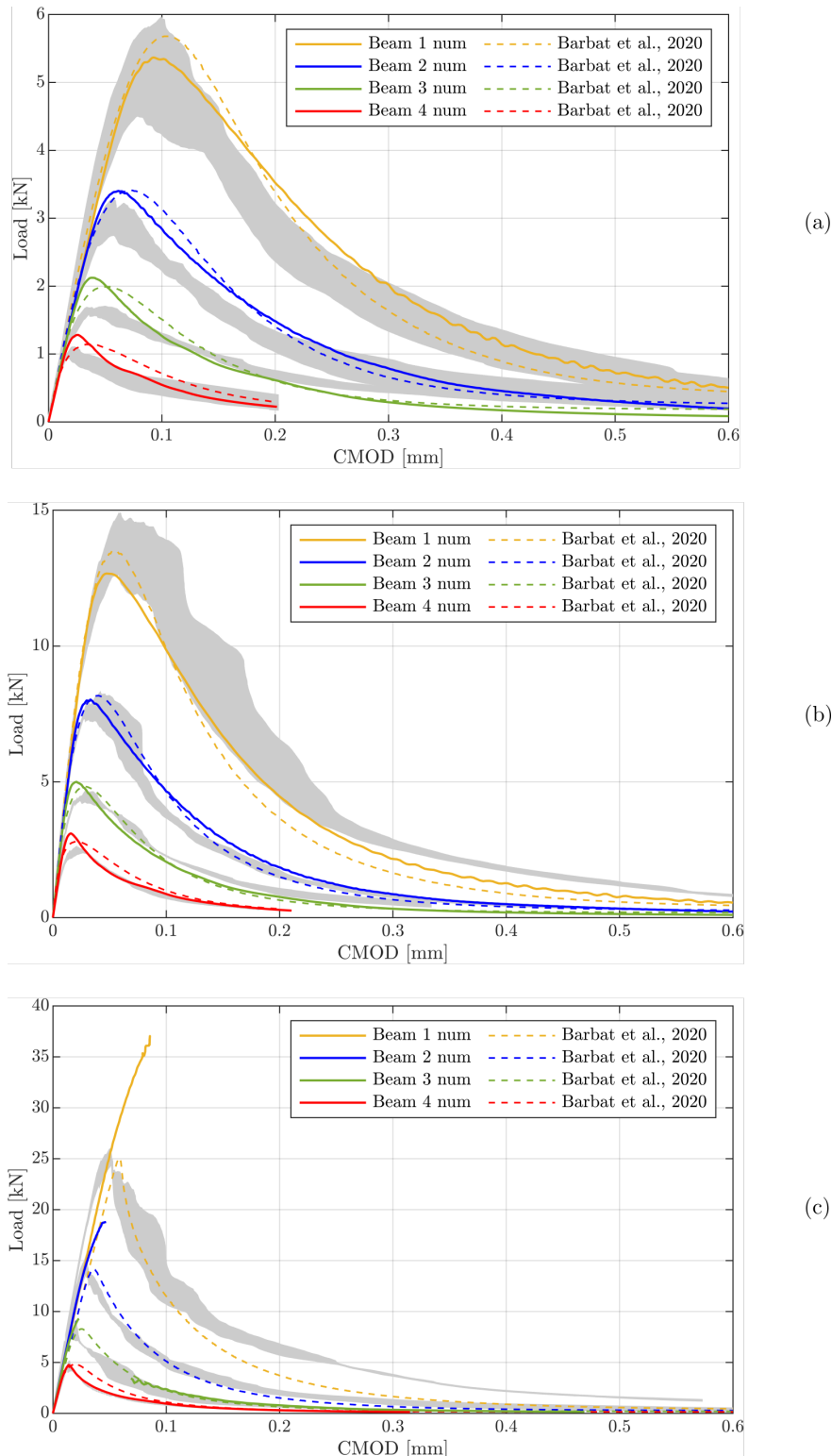


Fig. 6.3 Load-CMOD response for the mode I fracture tests: (a) half-notched, (b) fifth-notched, (c) unnotched case.

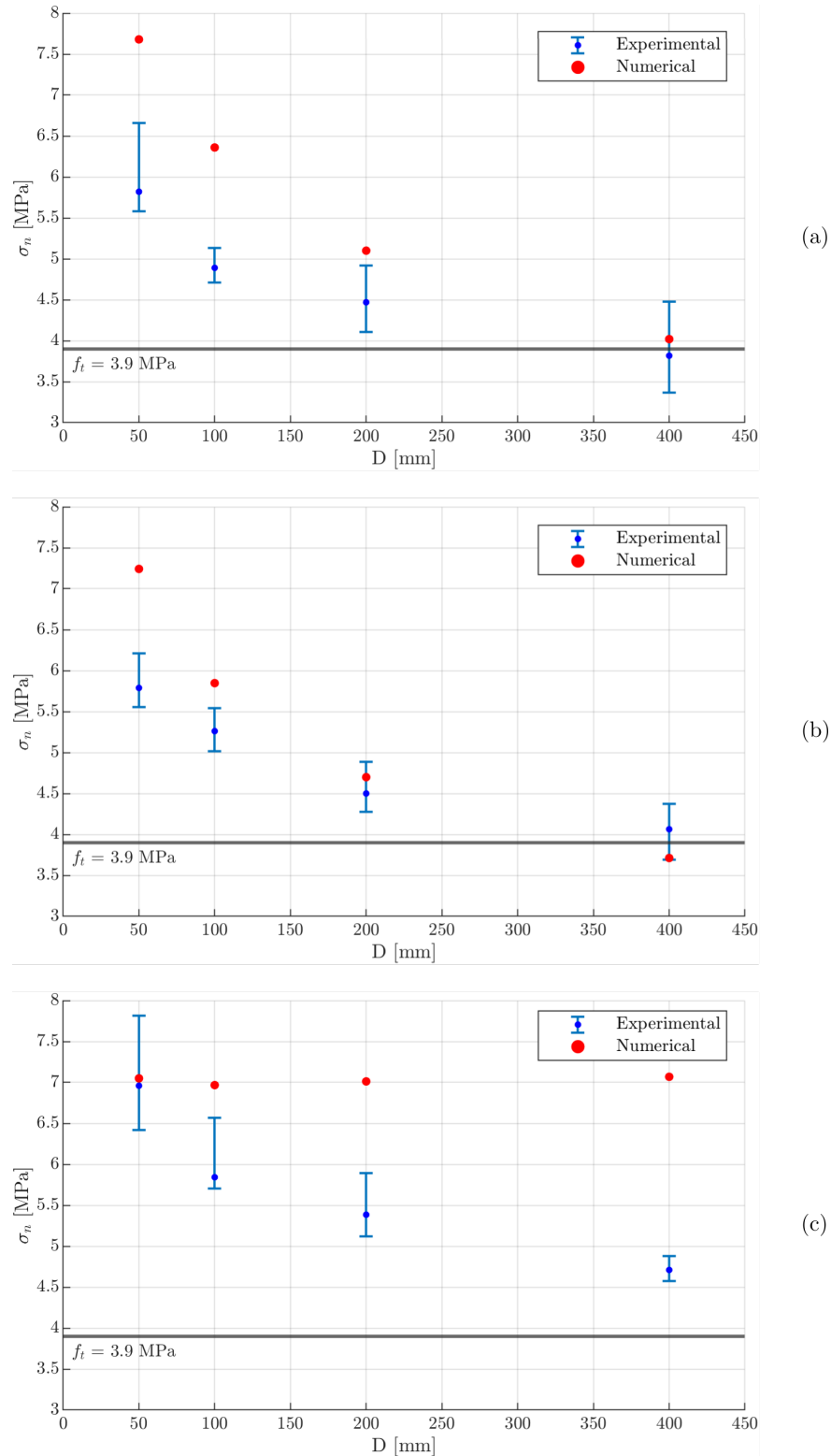


Fig. 6.4 Nominal strength versus depth (characteristic dimension) for the mode I fracture tests: (a) half-notched, (b) fifth-notched, (c) unnotched case. For large unnotched structures, the nominal strength should converge on the tensile strength  $f_t = 3.9$  MPa.

### 6.4.3 Energy dissipation

This section provides an examination and discussion of the damage energy dissipation. Stress redistribution and the associated energy release caused by micro-cracking is the primary mechanism influencing the size effect on structural strength [20]. Investigating the energy dissipation might help to explain why the numerical model fails to predict a deterministic size effect for the unnotched problems.

For every specimen, the width of the region of energy dissipation at peak load has been determined and the results are presented in Table 6.2. See section 5.7 for an explanation of how the region of energy dissipation is determined and for detailed discussion and figures. The width of the region of energy dissipation depends on the depth of the beam and the boundary type.

Table 6.2 Width of the region of damage energy dissipation at peak load (mm). Mesh resolution  $\Delta x = 5$  mm.

Depth	$\lambda$		
	0.5	0.2	0
50	15.0	25.0	62.5
100	22.5	30.0	127.5
200	27.5	40.0	267.5
400	35.0	45.0	553.0

For notched problems, the width of the region of damage is less dependent on the depth of the beam. For the half-notched specimens, the width increases from 15 mm for the smallest beam ( $d = 50$  mm) to 35 mm for the largest beam ( $d = 400$  mm). The results are in good agreement with the numerical predictions of Grassl et al. [96]; approximately 18 mm for the smallest beam and 40 mm for the largest beam. A good agreement is also observed for the fifth-notched beams.

For the unnotched beams, the width of the region of energy dissipation is strongly influenced by the depth of the beam, increasing from 62.5 mm for the smallest beam ( $d = 50$  mm) to 553 mm for the largest beam ( $d = 400$  mm). For the largest beam ( $d = 400$  mm), Grassl et al. [96] determined that the region of energy dissipation is approximately 200 mm wide. This prediction was later validated against acoustic emissions data [99]. As illustrated in Fig. 6.5, the region of energy dissipation scales linearly with the depth. The width of the

region of energy dissipation to beam depth ratio is approximately constant for all unnotched specimens and this is believed to be the source of the over-prediction of peak load. It is hypothesised that a source of randomness must be introduced to trigger the localisation of damage in unnotched specimens. This hypothesis requires further study.

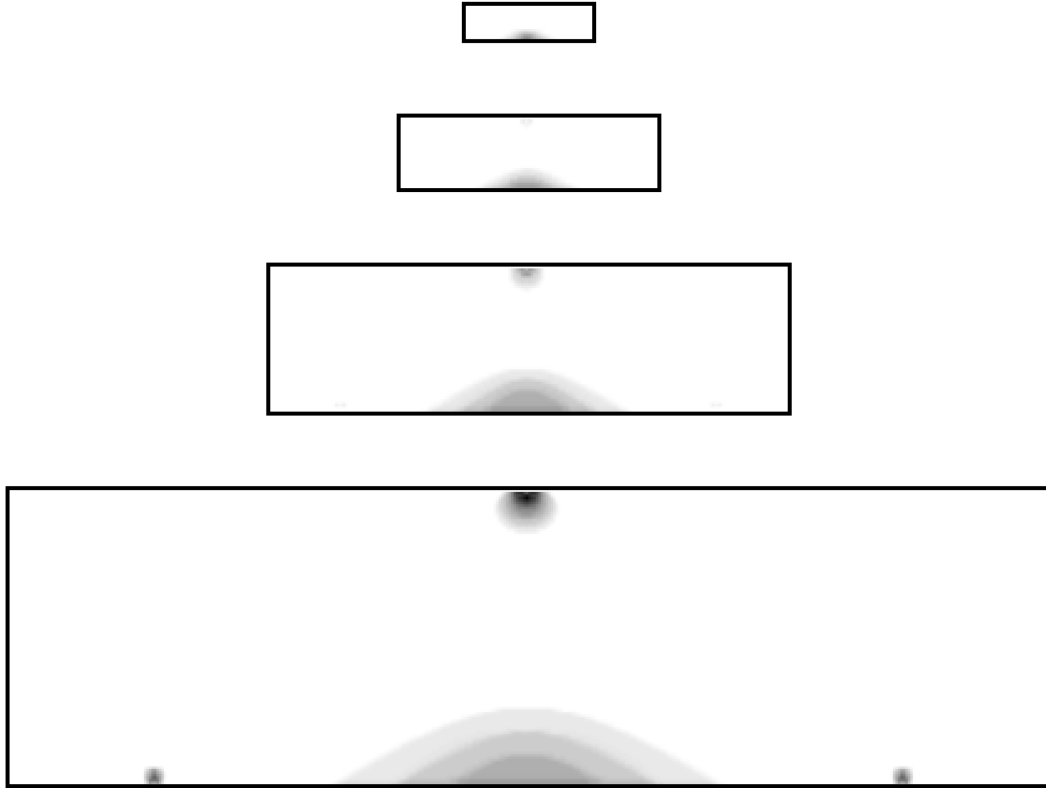


Fig. 6.5 Region of damage energy dissipation at peak load for unnotched members. Mesh resolution  $\Delta x = 5$  mm. Note that a grey colour scale is used to improve the clarity of the figure.

## 6.5 Mixed-mode problem

To test the generality of the model, the mixed-mode fracture tests of García-Álvarez et al. [88] are simulated. Feng and Wu [80] noted that the overwhelming majority of numerical studies only considerer mode I problems. Accurately predicting mixed-mode fracture behaviour is generally considered to be a harder problem than predicting mode I fracture behaviour, and most problems of practical relevance will be subject to mixed-mode loading conditions.

Eccentrically notched concrete beams in three-point bending were experimentally tested. A schematic diagram of the experimental setup is illustrated in Fig. 5.27. Three different sizes of geometrically similar specimens were considered: depth  $d = 80$  mm, 160 mm, and

320 mm. The smallest member (depth  $d = 80$  mm) was examined in the previous chapter. The notch-to-depth ratio  $\lambda$  was fixed at 0.25, and three different notch eccentricities  $\mu d$  were considered:  $0.0d$ ,  $0.3125d$ , and  $0.625d$ . The material properties used for computations are as follows: cylindrical compressive strength  $f_{cm,cyl} = 20$  MPa; modulus of elasticity  $E = 33.8$  GPa; tensile strength  $f_t = 3.5$  MPa; material fracture energy  $G_F = 125.2$  N/m. The cylindrical compressive strength  $f_{cm,cyl}$  and modulus of elasticity  $E$  were determined experimentally. The value of tensile strength  $f_t$  was determined numerically by García-Álvarez et al. [88]. The specimens were cured for 720 days in a fog room. The long curing period and high moisture content explains the high tensile strength  $f_t$  [83]. The material fracture energy  $G_F$  was determined empirically using Eq. (5.22).

Numerical results have been reported by García-Álvarez et al. [88] who used a non-linear finite element model with interface elements and a cohesive crack model to simulate the experimental tests. Interface elements are placed along the crack path, requiring pre-existing knowledge of the fracture behaviour and limiting this method to simplistic problems. Numerical results have also been reported by Feng and Wu [80], Mendonça et al. [152] and Barbat et al. [8]. The methods used in these works are more generally applicable and do not require pre-existing knowledge of the fracture path. Mendonça et al. [152] used the boundary element method to model the beam of depth 160 mm. Feng and Wu [80] and Barbat et al. [8] modelled the full set of experiments using a phase-field regularised cohesive zone model and a smeared crack approach respectively. All previously reported results are two-dimensional. Results reported in this work were obtained using a three-dimensional model.

### 6.5.1 Results

Fig. 6.10 illustrates the predicted load-CMOD response for the mixed-mode fracture tests of García-Álvarez et al. [88]. The numerical results are in very good agreement with the experimental data. The peak load is correctly predicted in almost all cases and the softening response shows good agreement with the experimental response. Results from Barbat et al. [8] are included for comparison. It would be fair to say that the predictive accuracy of the peridynamic model is equivalent, if not superior, to the smeared crack approach employed by Barbat. The smeared crack approach, first introduced over 50 years ago by Rashid [184], in combination with the crack band theory [12], is the most widely used method for modelling the failure of concrete. The relative immaturity of the peridynamic model and the high predictive accuracy support the argument that this is a method worthy of further investigation.

The correct fracture behaviour is predicted for all cases and the computed crack paths are illustrated in Fig. 6.6 and Fig. 6.7. Results for the mode I case ( $\mu d = 0.0d$ ) have not been included to avoid repetition. For all mode I problems, the fracture initiates from the

notch (mid-span) and propagates vertically towards the applied load. For the mixed-mode problems, the fracture initiates from the notch and propagates at an angle towards the applied load. Fig. 6.8 and Fig. 6.9 compare the computed fracture paths against the experimental data and numerical results of Barbat et al. [8]. All the results are in approximate agreement with the experimental range. The degree to which the crack path depends on the spatial variability in material properties requires examination.

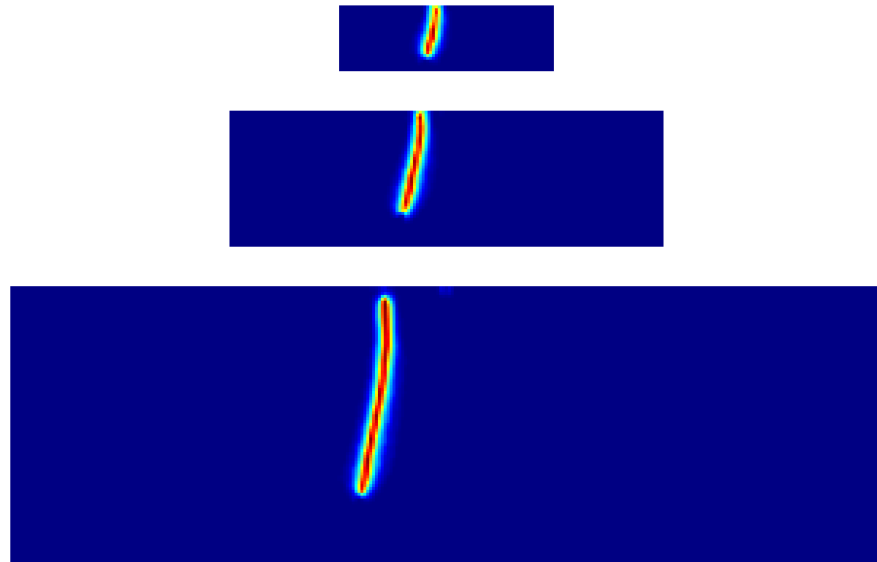


Fig. 6.6 Numerical softening damage for notch eccentricity  $\mu d = 0.3125d$ .

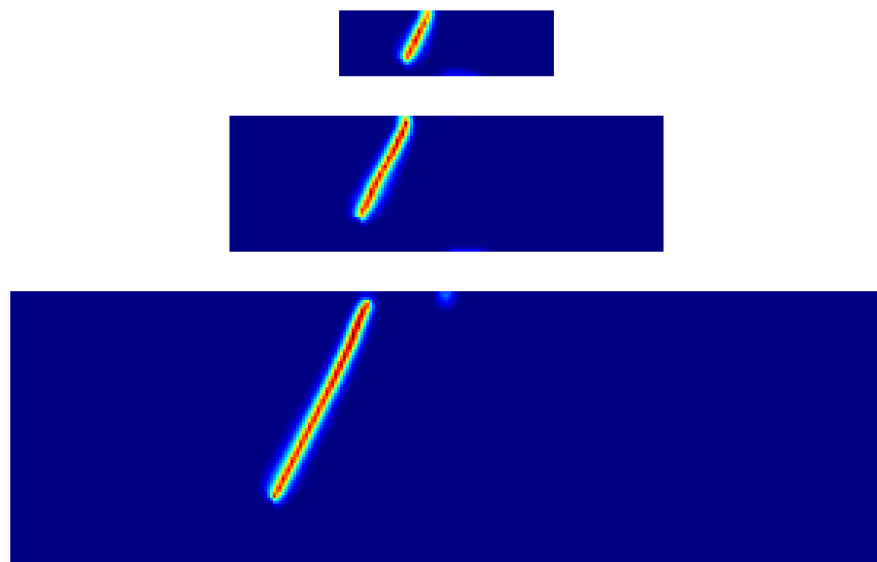


Fig. 6.7 Numerical softening damage for notch eccentricity  $\mu d = 0.625d$ .

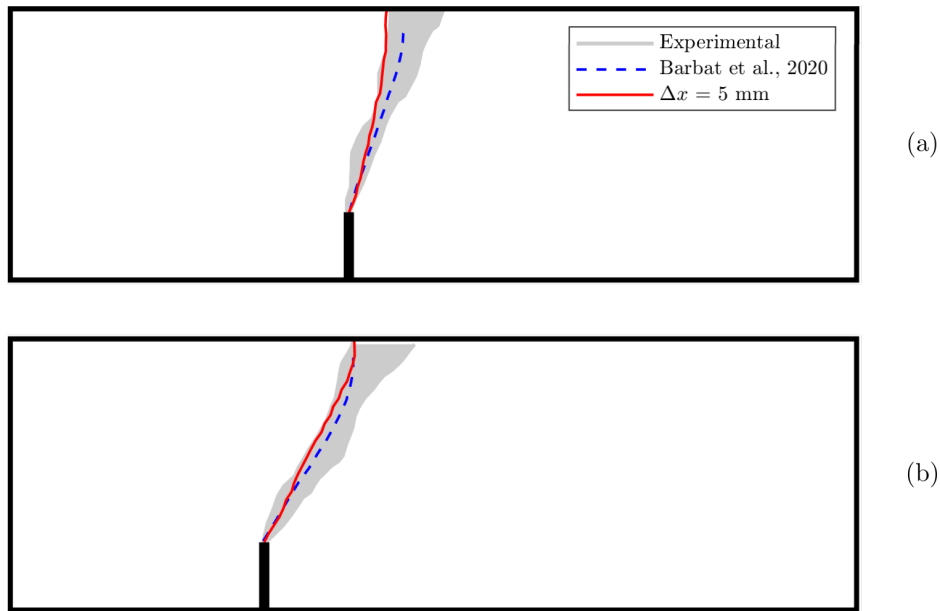


Fig. 6.8 Experimental and numerical crack paths for the mixed mode fracture tests ( $d = 160\text{mm}$ ). Notch eccentricity  $\mu d$ : (a)  $0.3125d$ , and (b)  $0.625d$

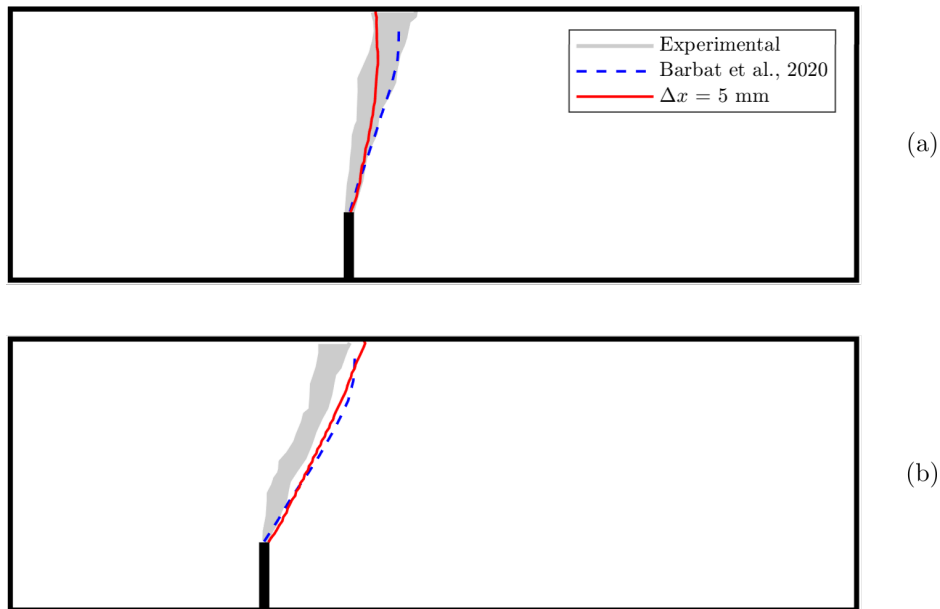


Fig. 6.9 Experimental and numerical crack paths for the mixed mode fracture tests ( $d = 320\text{mm}$ ). Notch eccentricity  $\mu d$ : (a)  $0.3125d$ , and (b)  $0.625d$

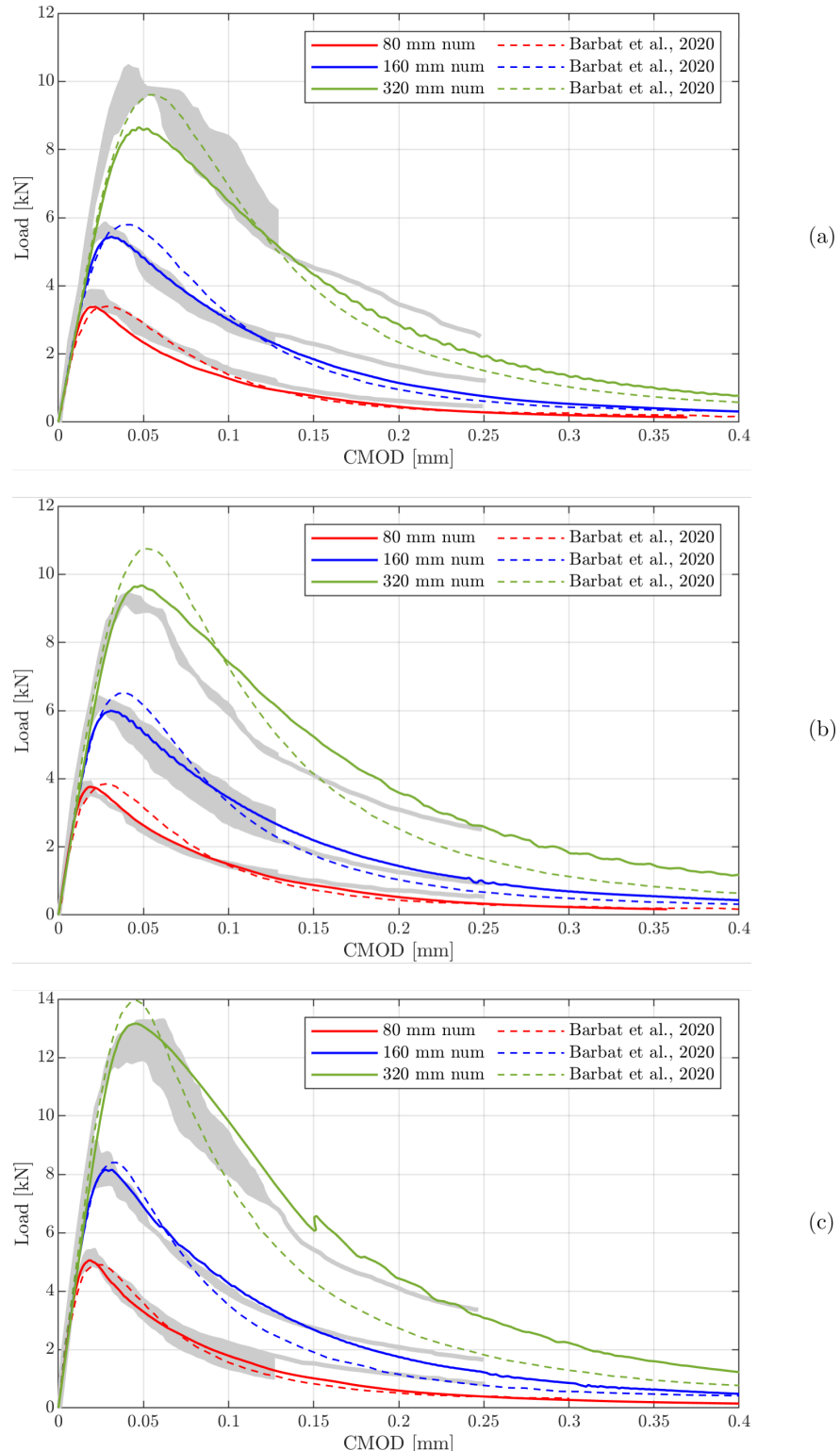


Fig. 6.10 Load-CMOD response for the mixed-mode fracture tests. Notch eccentricity  $\mu d$ : (a) 0d, (b) 0.3125d, and (c) 0.625d

## 6.6 Discussion and future work

### 6.6.1 Spatial variability of material properties

In general, the numerical results are in good agreement with the experimental data; however, a significant disagreement is observed for the unnotched cases. The peridynamic model does not predict any deterministic size effect for the unnotched problems, and the magnitude of the statistical size effect remains to be examined. Extending the model to account for spatial variability in material properties is the obvious next step, and implementation details are discussed here.

There are a limited number of papers that have explored the application of spatially varying material properties in a peridynamic framework. Demmie and Ostoja-Starzewski [66] modelled wave propagation in geologic materials. The material properties (density, bulk modulus, and yield strength) are represented as spatially correlated random fields. The generated random fields depend on the assumed correlation structure and probability distribution. It should be noted that the accuracy of the random field depends on the mesh resolution and the discretisation should approximately correspond to the mesoscale of the material. The authors only consider a single realisation of the random field. In most problems of practical interest, the mean failure load is of limited concern and a probability distribution of the load capacity is required. Calculating structural failure probabilities requires sampling the entire probability distribution using Monte Carlo methods. Monte Carlo methods require thousands of simulations and are currently prohibitively expensive. The number of samples can be reduced by using variance reduction methods such as Latin hypercube sampling. Syroka-Korol et al. [216] examined the statistical size effect in concrete beams and used Latin hypercube sampling to reduce the number of samples required from thousands to less than a hundred. Multilevel Monte Carlo schemes, similar to those proposed by Blondeel et al. [29] and Dodwell et al. [72], offer another approach. These schemes employ a hierarchy of mesh discretisations, with many samples taken on cheaper coarse meshes, and relatively few samples on expensive fine meshes.

Chen et al. [50] recently proposed a new model, referred to as the Intermediately Homogenized Peridynamic (IH-PD) model. The explicit modelling of the material microstructure is avoided and only essential details of the microstructure, such as void volume, are required by applying material properties directly to bonds. The authors modelled the failure behaviour of porous materials by deleting bonds to achieve a defined pore volume. Bonds are selected for deletion using a random uniform distribution. Mehrmashhadi et al. [151] adopted the same method and modelled fibre-reinforced composites by stochastically assigning bond properties to achieve a specific fibre volume fraction. This method has also been used by

Zhao et al. [244] and Wu et al. [230] to model concrete. Bonds are randomly assigned properties to produce a defined volume fraction of aggregates and cement. Oterkus and Madenci [174] used a comparable method to model nuclear fuel pellets. Randomness was introduced into the model by assigning a Young's Modulus value to bonds using a random Gaussian distribution. These methods are computationally cheap but they lack a robust theoretical basis. By introducing randomness, realistic crack paths and crack tortuosity are predicted, but the failure probability distribution cannot be determined. Jones et al. [127] note that these methods are generally used to avoid problems related to symmetry, and they do not attempt to capture the true material behaviour by implementing an experimentally measured probability distribution of material properties.

After addressing computational expense, there are further issues. Jones et al. [127] found that naively randomising the properties of bonds affects the results in unexpected ways, for example producing very narrow failure distributions. Accurately reproducing strength distributions, such as the Weibull distribution, requires a correction scheme. The authors proposed a scheme that successfully generates a Weibull strength distribution in a one-dimensional peridynamic body. The proposed method is only applicable to one-dimensional problems, and expansion to two and three-dimensional peridynamic problems is still required. The preceding discussion demonstrates that the inclusion of spatially varying material properties is not a trivial problem, and further work is required to reduce computational expense and to accurately reproduce strength distributions.

### 6.6.2 Load path following

The direct displacement-controlled loading scheme fails to capture the post-peak structural response for large unnotched beams, see Fig. 6.3 (c). This behaviour was expected, as direct displacement control is not capable of passing limit points of vertical tangent ('snap-back') [195]. The post-peak response of large structures is steeper than small structures, and for very large structures snap-back behaviour will occur [18, 216, 8]. Path-following techniques, such as the arc-length method [189], can be used to capture the full equilibrium path of materials that exhibit strain-softening behaviour. Sun et al. [213] have implemented an arc-length method within a peridynamic framework.

A displacement-controlled Newton Raphson solver has been implemented in the developed analysis code, and introducing an arc-length solver would be relatively simple due to the similarities with the Newton Raphson solver. Construction of the stiffness matrix and the iterative solution of the system of equations is computationally expensive. Optimising the code to run large problems is an obvious future step.

### 6.6.3 Localisation limiter

In strain-softening materials, damage localisation occurs. The localisation of damage into a band that is one element wide is a major issue when using a finite element model. Results from finite element models lack objectivity, because upon mesh refinement, damage localises into a infinitely small volume and the energy dissipation tends to zero. Furthermore, capturing the correct energy dissipation as a crack forms and propagates is essential to accurately model structural size effect. A localisation limiter, defined by a characteristic length of the material, is used to enforce a minimum width of the strain localisation band [211]. This prevents the damage from localising into a zone of zero volume upon mesh refinement.

As stated by Bažant [18], the fundamental feature of any model capable of bridging the gap between the theory of plasticity and the theory of linear elastic fracture mechanics is the presence of some form of characteristic length. Due to the non-locality of the peridynamic model, a size effect is naturally captured. In the peridynamic model, the horizon  $\delta$  defines the range over which particles interact. The peridynamic horizon  $\delta$  is not an intrinsic material property. This differentiates the peridynamic model from common numerical approaches, and the use of an ambiguous characteristic length parameter is avoided. The non-locality of the peridynamic model prevents both damage localisation into a zone of zero volume and zero energy dissipation upon mesh refinement. Note that a crack band model prevents zero energy dissipation upon refinement, but damage localisation still occurs in a single row of elements, even if the size of the elements becomes infinitely small [211]. The peridynamic model is physically consistent, and therefore is more fundamental than a crack band model.

### 6.6.4 Additional comments

The high computational expense prevented a mesh sensitivity study for all members. For completeness, the influence of the mesh resolution on the predictive accuracy should be examined. Detailed mesh sensitivity studies will become increasingly practicable as solvers advance and computational power increases. The influence of an unstructured mesh discretisation also requires examination. It is hypothesised that an unstructured mesh might influence the localisation behaviour and improve the predictive accuracy for unnotched problems. Molinari et al. [157] used a cohesive zone model to show that by introducing randomness into the mesh structure, the total energy dissipated converges significantly faster. Finally, the mode II energy dissipation component in the mixed-mode fracture tests is minor [88], and further problems should be tested to improve the robustness of the validation.

## 6.7 Conclusions

Bažant [17] stated that correct modelling of the size effect on material strength should be adopted as the basic criterion of acceptability of any numerical model. This chapter has demonstrated the capability of a bond-based peridynamic model to capture the size effect in quasi-brittle materials. This is the first time that a peridynamic model has been used to examine the size effect, and provides an important check on the validity of the numerical model. The key findings are as follows:

1. The peridynamic model accurately captures the deterministic size effect in notched problems and the predicted load-CMOD response and crack paths are in close agreement with the observed experimental data. Comparisons with leading numerical models are provided, and the predictive accuracy of the peridynamic model is equivalent, if not superior.
2. In conventional numerical models, capturing size effect requires a localisation limiter that governs the width of the softening zone. The localisation limiter is determined by an internal characteristic length that is a property of the material. The definition of the characteristic length is highly ambiguous and its value can not be determined experimentally. The non-local length scale in the peridynamic model is not related to material properties and avoids the aforementioned problems.
3. The peridynamic model fails to accurately capture the structural strength for all unnotched specimens. As the structure size increases, so does the over-prediction of structural strength. To some extent, this behaviour was expected. For notched problems, statistical variability in material properties can largely be ignored, but for unnotched problems, the randomness of material properties has a significant effect on structural strength.
4. The peridynamic model does not predict any deterministic size effect for the unnotched problems, and whilst it is expected that the inclusion of statistical variability in material properties would significantly improve the predictive accuracy, a small deterministic size effect should have been observed.
5. To trigger the localisation of damage in unnotched specimens, it is hypothesised that a source of randomness must be introduced.

In 1999, Bažant [18] stated that discrete element models will be needed to help explain the mechanics of size effect and to separate the important processes from the unimportant

ones. A complete understanding of size effect is still lacking and peridynamic models might help to clarify the underlying mechanics. The developed model could be used to inform a greater understanding of the physical basis of size effect, and extending the model to account for spatial variability in material properties is the obvious next step.

# Chapter 7

## Shear failure

### 7.1 Introduction

This chapter examines the predictive capabilities of the bond-based peridynamic model against a series of reinforced concrete beams. The aims of this chapter are to: (1) quantify the predictive accuracy of the model for determining the shear strength of reinforced concrete beams; (2) validate the model against a systematically arranged set of experimental tests that encompasses a wide range of structural behaviours; (3) explain any discrepancies between the experimental and numerical results.

There are a limited number of published papers that address reinforced concrete problems using a peridynamic model. Gerstle and Sau [91] were the first to model concrete and reinforced concrete using a two-dimensional bond-based peridynamic model. Gerstle et al. [94] later introduced a micropolar peridynamic model that accounts for the bending stiffness of bonds. The model is applied to a reinforced concrete cantilever failing in shear [92] and a simply supported reinforced concrete beam, with and without shear reinforcement [89]. Numerical results are compared against predictions from design codes and a good agreement is observed. Significant work remains to quantify the confidence and predictive accuracy of peridynamic models. Section 2.4.1 provides a brief review of the development of peridynamics for quasi-brittle materials and structures. For a thorough review of the development of peridynamics and applications to concrete and reinforced concrete problems, readers are referred to the work of Hattori et al. [108].

The experimental test series by Leonhardt and Walther [135] is chosen as a benchmark due to the wide range of failure modes exhibited. The chosen series of tests has been carefully selected to provide a robust and methodical validation of the bond-based peridynamic framework. The shear-span-to-depth ratio is systematically varied from 1 to 8 to facilitate a study of different load-transfer mechanisms and failure modes. The change in load-

transfer behaviour and the important influence of fracture behaviour on the redistribution of stresses makes this a challenging benchmark. To the best of the authors knowledge, a robust quantitative examination such as this has until now been missing in the peridynamic literature. The chapter is organised as follows: Section 7.2 describes the numerical framework and the steel and interface constitutive models. Section 7.3 provides a comprehensive validation study against a series of nine beams. Four validation metrics are used: load-deflection response, ultimate load capacity, failure mode, and fracture behaviour. Section 7.4 provides a discussion of the results and deficiencies within the model are identified. Section 7.5 concludes the chapter and summarises the findings. Future research and development needs are listed.

## 7.2 Numerical framework

All the results presented in this chapter were obtained using the explicit scheme outlined in Fig. 4.14. The imposed displacement is increased incrementally using a fifth-order smooth step function and a small amount of damping is applied. The bilinear damage model proposed by Zaccariotto et al. [243] is used in this chapter and critical stretch corrections are not applied. The bilinear law was chosen as it is the simplest constitutive model that accounts for softening behaviour. Details of the bilinear model are provided in section 5.3.2. By using the simplest possible model, it is easier to gain insight into any discrepancies. Note that the model is equivalent to that used in section 5.4.2 (see Fig. 5.10).

### 7.2.1 Steel constitutive model

The microplastic material model introduced by Macek and Silling [143] is used to capture the yielding behaviour of steel reinforcing bars, see Fig. 7.1. Plasticity is introduced by assuming that a bond has a yielding stress. At an individual bond level the material is elastic perfectly plastic. At a macroscopic level, the material shows a strain hardening effect due to bonds yielding at different values of bulk strain. In the microplastic model, the force magnitude  $f$  is defined by Eq. (7.1), where  $s_p(t)$  is the plastic stretch history defined by Eq. (7.2), and  $s_y$  is the yielding stretch.

$$f = \begin{cases} c(s - s_p(t)) & \text{if } |\mathbf{x}' - \mathbf{x}| \leq \delta \\ 0 & \text{otherwise} \end{cases} \quad (7.1)$$

$$s_p(0) = 0, \quad \frac{d}{dt}s_p = \begin{cases} 0 & \text{if } |s - s_p| < s_y \\ \frac{d}{dt}s & \text{otherwise} \end{cases} \quad (7.2)$$

The bond yield stretch  $s_y$  can be related to the ultimate yield strength  $\sigma_{ult}$  by considering that all bonds will have yielded when the ultimate strength is reached. By following the same process used to derive the critical bond stretch in the original linear elastic material model, the bond yield stretch is defined by Eq. (7.3), where  $K$  is bulk modulus.

$$s_y \approx \frac{\sigma_{ult}}{3K} \quad (7.3)$$

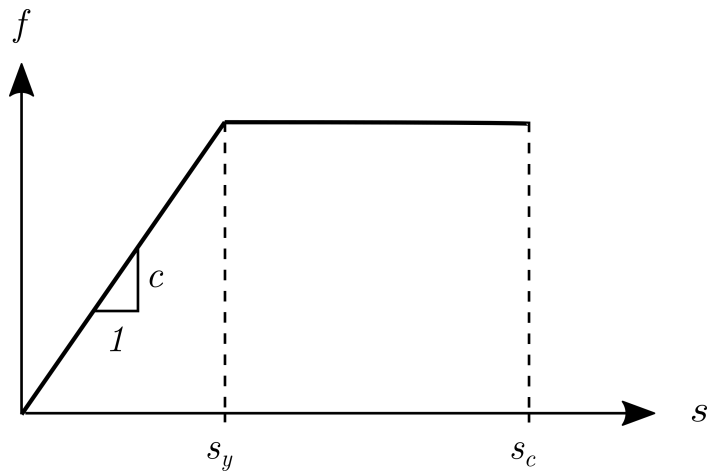


Fig. 7.1 Microplastic Model

### 7.2.2 Interface constitutive model

The bond between the steel reinforcing bars and concrete plays an important role in the behaviour of a reinforced concrete member. Within the peridynamic framework there are a limited number of papers that explicitly discuss the steel-concrete interface model. Gerstle et al. [90] modelled a reinforced concrete lap splice problem and treated the steel-to-concrete interface bonds as modified concrete bonds. The calculated pairwise force and pre-defined critical stretch value in the modified bonds are multiplied by a factor of three. This factor accounts for the toughening effect of the ribs on the reinforcing bars. Lu et al. [142] simulate anchor bolt pullout in concrete by introducing a short-range interaction force to reproduce the interaction between the concrete and steel anchor bolt. Li and Guo [138] recently used a dual-horizon peridynamic model to simulate the debonding process in fibre-reinforced polymer (FRP)-to-concrete bonded joints. A multi-scale discretisation scheme is used and

the mesh is refined at the bond interface. Using a linear elastic damage model, the captured interfacial slip is in accordance with experimental results.

The interface behaviour has been investigated by many researchers using conventional numerical methods. Jendele and Červenka [123] presented a bond slip model for simulating the interface between reinforcing bars and concrete within a non-linear finite element model. They found that when bond slip is neglected, a finer mesh is required to capture the correct behaviour. More recently, Xenos and Grassl [232] modelled the failure behaviour of a reinforced concrete member with non-local and crack band approaches using a damage-plasticity model and they assumed perfect bond between the steel reinforcement and concrete. This idealisation of the interface behaviour leads to reasonable results and simplifies the problem. This work also assumes perfect bond between the reinforcement and concrete and bond slip is not accounted for. It is not the purpose of this chapter to study the interface in detail. The stiffness of steel-to-concrete bonds are set equivalent to concrete bonds and bond failure can not occur.

### 7.3 Model validation

The goal of this chapter is to develop and benchmark the capabilities of a three-dimensional bond-based peridynamic model for the simulation of failure behaviour in reinforced concrete members. Whilst peridynamic models have been studied fairly extensively, a rigorous validation study for reinforced concrete problems is missing. Limitations of previous studies include: (1) a dependency on qualitative validation through visual comparisons of fracture behaviour, (2) simulations are restricted to two-dimensions but the complex interaction between reinforcing bars and concrete is three-dimensional, (3) validation is limited to a narrow range of problems and fails to provide sufficient insight into the generality of the model. Proving that a model can correctly capture all possible scenarios is not feasible but a sufficiently wide range of problems should be addressed so that the limitations of a model can be identified. The influence of the discretisation on the structural response and fracture behaviour is also investigated.

The predictive capabilities of the peridynamic model are quantified by comparison with experimental results. The model is evaluated against the following criteria: load-deflection curve, ultimate load capacity, failure mode, and fracture behaviour. The generality of the model is assessed by simulating a comprehensive range of reinforced concrete members that exhibit distinct failure modes. Members failing in flexure and shear are considered. Shear failure is distinguished from flexural failure by the development of inclined cracks. The flexural behaviour of reinforced concrete members is well understood and the ultimate

flexural strength can be accurately predicted using analytical methods based on simplified rectangular stress blocks. Failure loads predicted by analytical methods match closely with experimental results and form the basis of modern design codes. Correctly capturing flexural failure behaviour still remains an important test for any numerical model. The shear behaviour of reinforced concrete members is much more complex and predictions of shear strength rely on empirical methods that lack a robust theoretical basis [55]. The ultimate shear capacity is governed by the combined resistance to shear force offered by (1) the uncracked compressive zone, (2) arch or direct strut action, (3) aggregate interlock, (4) dowel action, and (5) the residual tensile strength in the fracture process zone. The contribution of each action to the overall shear resistance is related to parameters such as shear span, beam depth, and reinforcement ratio [119, 111]. There is no consensus on the relational theory between shear failure and the many influencing parameters. This uncertainty is highlighted by the variability that exists within different design codes. Bentz et al. [27] state that predictions of ultimate shear strength can vary by a factor of more than two when using different design codes, whilst the flexural strength predicted by the same codes does not vary by more than 10%. Correctly capturing different modes of shear failure is an essential test for any numerical model due to the sudden and catastrophic nature of members failing in shear.

### 7.3.1 Stuttgart shear tests

The peridynamic model is validated against a series of reinforced concrete beams tested by Leonhardt and Walther [135], commonly referred to as the Stuttgart Shear Tests. Ten beams subjected to four-point loading were tested to investigate the influence of the shear-span-to-depth ratio ( $a_v/d$ ) upon the shear strength of simply supported prismatic beams. Shear reinforcement was not considered so that the development of diagonal shear cracks could be studied. Extensive testing has shown that the shear-span-to-depth ratio is one of the most important factors affecting the failure behaviour of reinforced concrete beams. Kani [128] proved experimentally that the load transfer behaviour changes at a value of  $a_v/d$  approximately equal to 2.5. If the value of  $a_v/d$  is less than 2.5, beams develop an internal arch and shear capacity increases. For values of  $a_v/d$  greater than 2.5, beam action becomes dominant and sudden and brittle failure in diagonal-tension is expected. Full flexural capacity,  $M_{fl}$ , is not obtained for values of  $a_v/d$  between 1.5 to 5. The largest reduction in flexural capacity is observed for  $a_v/d = 2.5$ , and the moment at failure,  $M_u$ , is approximately 50% lower than the theoretical capacity. The observed reduction in flexural strength due to shear is often referred to as ‘Kani’s valley of shear failure’ and is illustrated in Fig. 7.2. The wide range of failure modes, the multiple influencing parameters, the complex load transfer

mechanisms, and the important role of fracture behaviour on stress redistribution make this series of tests a suitable challenge for model validation.

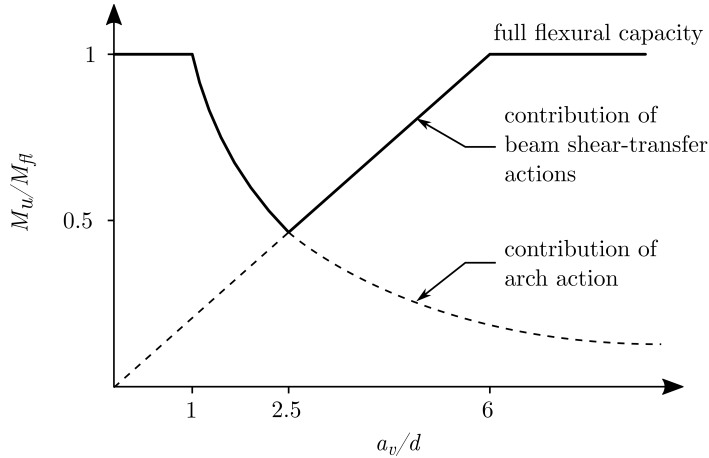


Fig. 7.2 Kani's shear valley

Four broad categories of failure mode can be defined: shear-web failure ( $a_v/d < 1$ ), shear-compression failure ( $1 < a_v/d < 2.5$ ), shear-flexural failure ( $2.5 < a_v/d < 6$ ), and flexural failure ( $a_v/d > 6$ ) [132, 167]. For RC members within the same category, the expected failure behaviour (sequence of events and fracture characteristics) will be approximately the same. The results section is divided into these categories and a detailed description of each failure mode is provided within the discussion. It should be noted that providing an exact definition of the different shear failure modes that may occur in a reinforced concrete beam is not trivial and the terminology used within the literature is often conflicting. Fig. 7.5 illustrates the experimental fracture behaviour from the series of tests by Leonhardt and Walther [135]. This is one of the best examples available that clearly demonstrates the influence of  $a_v/d$  on fracture behaviour. Beam 4, 5, and 6 were repaired on one side after the occurrence of shear failure and further loaded until failure occurred on the other side.

A schematic diagram of the experimental setup is illustrated in Fig. 7.3 and member dimensions and material properties can be found in Table 7.1. The shear span,  $a_v$ , is defined as the distance between the applied point load and the point of nearest restraint. The shear force remains constant throughout the shear span. The effective depth,  $d$ , is defined as the distance from the top compression fibre to the centre of the tensile reinforcement and is constant across all members ( $d = 270$  mm). All members have the same cross sectional area (320 mm  $\times$  190 mm) and reinforcement ratio ( $\rho \approx 2.05\%$ ). Longitudinal reinforcement is provided in the form of two ribbed steel bars of 26 mm diameter ( $A_s = 1062$  mm $^2$ ). The reinforcing bars were manufactured from high yield steel and possess the following properties: modulus of elasticity  $E_s = 208,000$  MPa, yield strength  $f_y = 465$  MPa, and yield strain  $s_y = 0.2\%$ .

Input parameters for the concrete constitutive model have been determined using empirical formulas from *fib* Model Code 2010 [83], that relate the experimentally measured cubic compressive strength to common concrete properties. For every test, the mean cube strength  $f_{cm,cube}$  was determined from twenty test cubes 200 mm in size. Model Code 2010 relates the compressive strength of cubes 150 mm in size to cylindrical compressive strength, thus introducing a degree of error. The value of  $k_r$ , the ratio between the critical stretch and the linear elastic limit, has been set at 25, and was determined using experimental load-deflection curves from Barr et al. [9]. The value of 25 is approximate and there is a large degree of uncertainty. Yang et al. [236] note that it is not easy to determine the exact point at which linearity is lost in a load-deflection curve and this is a weakness of the calibration method proposed by Zaccariotto et al. [243].

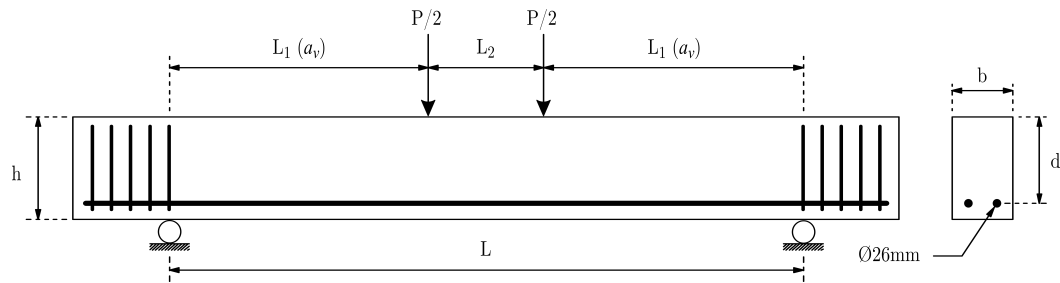


Fig. 7.3 Experimental setup.  $L_1$  is the shear span  $a_v$ . Adapted from Leonhardt and Walther [135].

Table 7.1 Stuttgart Shear Tests - experimental parameters

Designation	$L$ (m)	$L_1$ (m)	$L_2$ (m)	$a_v/d$	$f_{cm,cube}$ (MPa)	$f_{cm,cyl}$ (MPa)	$G_F$ (N/m)	$E_c$ (MPa)
1	0.90	0.27	0.36	1.0	35	28.6	133	30,500
2	1.15	0.40	0.35	1.5	35	28.6	133	30,500
3	1.45	0.54	0.37	2.0	35	28.6	133	30,500
4	1.70	0.67	0.36	2.5	35	28.6	133	30,500
5	1.95	0.81	0.33	3.0	35	28.6	133	30,500
6	2.55	1.10	0.35	4.0	35	28.6	133	30,500
7	3.10	1.35	0.40	5.0	36.5	29.6	134	30,900
8	3.60	1.62	0.36	6.0	36.6	29.7	134	30,900
10	4.70	2.16	0.38	8.0	35.4	28.9	134	30,600

All members have been modelled with a constant peridynamic horizon  $\delta = 3.14\Delta x$  and regular grid spacing  $\Delta x = 11.5$  mm. To study mesh sensitivity, Beam 3, 5, and 7 have also been modelled using a finer mesh with regular grid spacing  $\Delta x = 7.67$  mm. The grid spacing has been chosen so that the correct area of steel can be modelled. Experimental load-deflection curves are available for Beam 3, 5 and 7. The concrete constitutive model parameters for the two levels of mesh refinement are defined in Table 7.2. The loading configuration of Beam 9 is not consistent with the remainder of the test series and has been omitted from the simulations.

Peridynamic model parameters remain the same across all tests. This is essential in a robust validation procedure. Adjusting model parameters to improve the agreement between numerical and experimental measurements does not constitute validation [218].

Table 7.2 Simulation Parameters. Stretch is a dimensionless scalar.

Mesh	Grid Spacing	Bilinear Model Parameters	
	$\Delta x$ (mm)	$s_0$	$s_c$
Normal	11.5	6.34E-5	1.60E-3
Fine	7.67	7.78E-5	1.95E-3

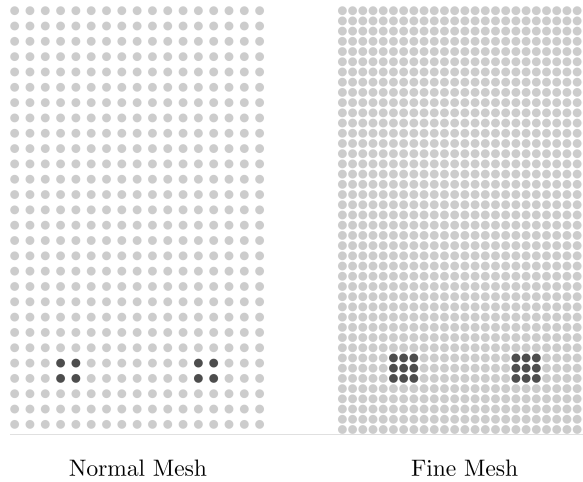


Fig. 7.4 Discretised cross-section. The nodal spacing for the normal mesh is 11.5 mm, and for the fine mesh is 7.67 mm. The area of steel  $A_s$  is approximately 1060 mm<sup>2</sup> in both meshes.

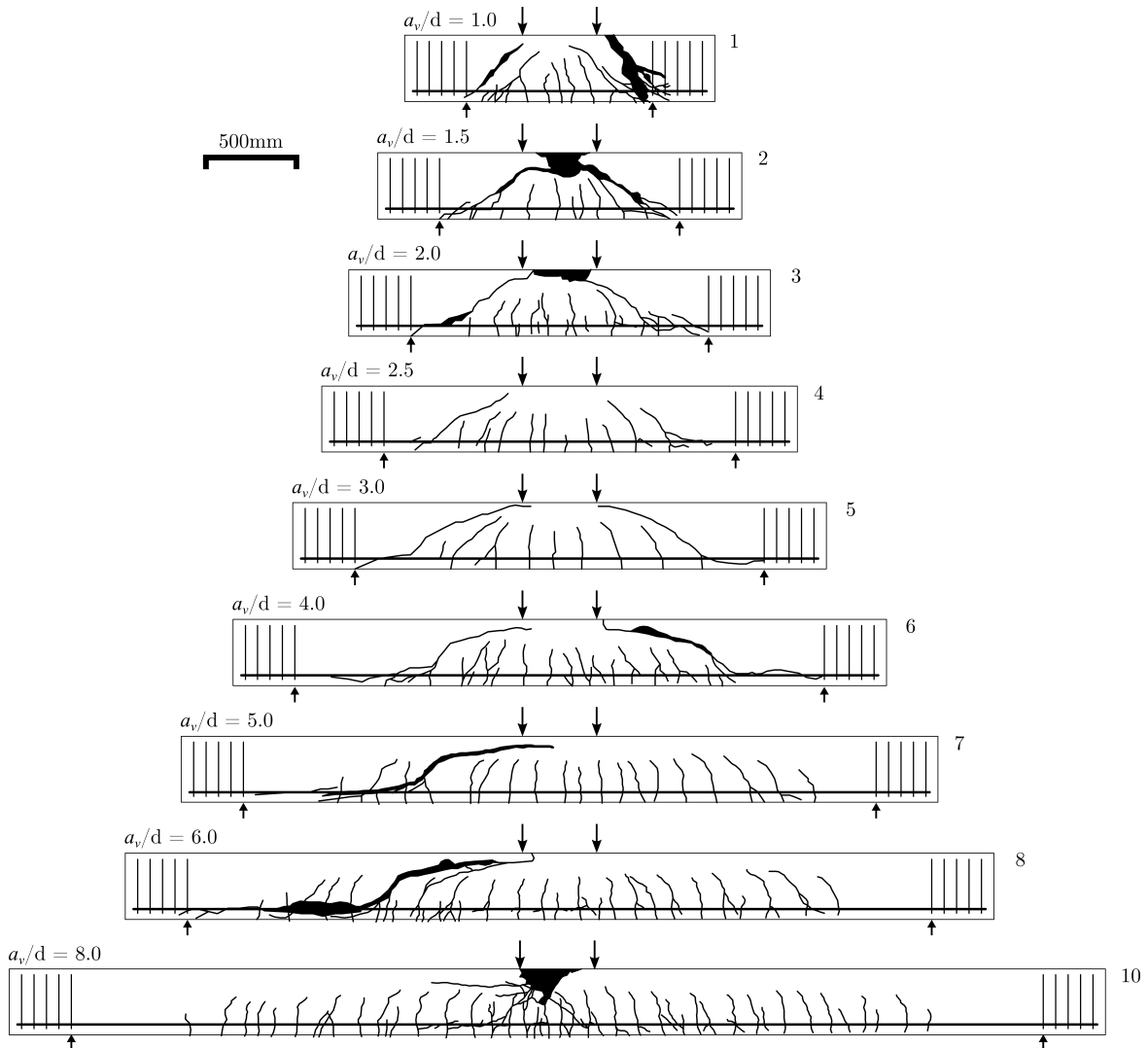


Fig. 7.5 Failure behaviour in beams tested by Leonhardt and Walther [135]. Refer to Table 7.1 for dimensions.

### 7.3.2 Results

This section presents the numerical results. The experimental and predicted failure loads are summarised in Table 7.3. Fig. 7.6 plots the experimental and numerical shear force and moment at failure against  $a_v/d$ . The numerical fracture pattern at failure for all beams can be found in Fig. 7.7. Numerical fracture patterns using the fine mesh are provided in Fig. 7.8. Load-deflection results for Beam 3, 5, and 7 are plotted in Fig. 7.9, Fig. 7.10, and Fig. 7.11. Interpretation of the results is saved for the discussion.

Table 7.3 Comparison of experimental results, design code predictions, and numerical predictions

Specimen	1	2	3	4	5	6	7	8	10
<b>Experimental</b>									
<i>P</i> (kN)	777	520	294	161	118	118	120 131 <sup>1</sup>	126 126 <sup>1</sup>	94 103 <sup>1</sup>
Failure Mode <sup>2</sup>	s	s	s	s	s	s	s	s	f
<b>Eurocode 2</b>									
<i>P</i> (kN)	287	194	144	144	144	144	144	125	93
Failure Mode	s	s	s	s	s	s	s	f	f
% Error	-63%	-63%	-51%	-10%	+22%	+22%	+20%	-1%	+1%
<b>Normal Mesh</b>									
<i>P</i> (kN)	335	253	170	131	112	85	87	76	56
Failure Mode	s	s	s	s	s	s	s	f	f
% Error	-57%	-51%	-42%	-19%	-5%	-28%	-28%	-40%	-41%
<b>Fine Mesh</b>									
<i>P</i> (kN)	-	-	181	-	122	-	92	-	-
Failure Mode	-	-	s	-	s	-	s	-	-
% Error	-	-	-38%	-	+3%	-	-23%	-	-

<sup>1</sup> Beam 7, 8, and 10 were tested twice using identical material properties<sup>2</sup> Failure mode - shear (s), flexural (f)

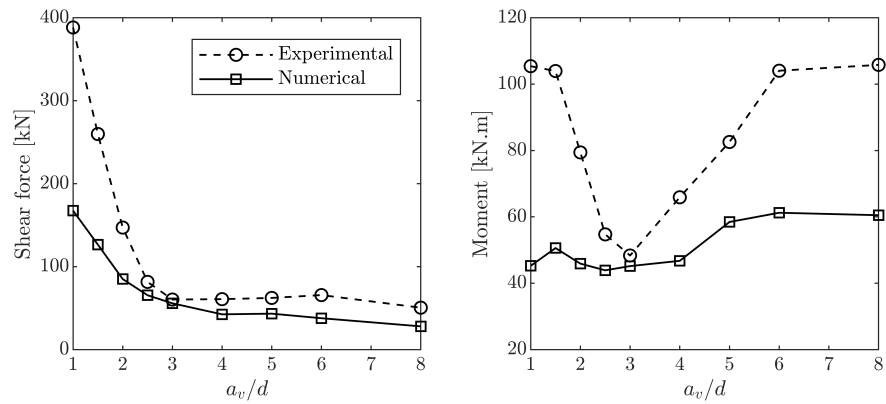
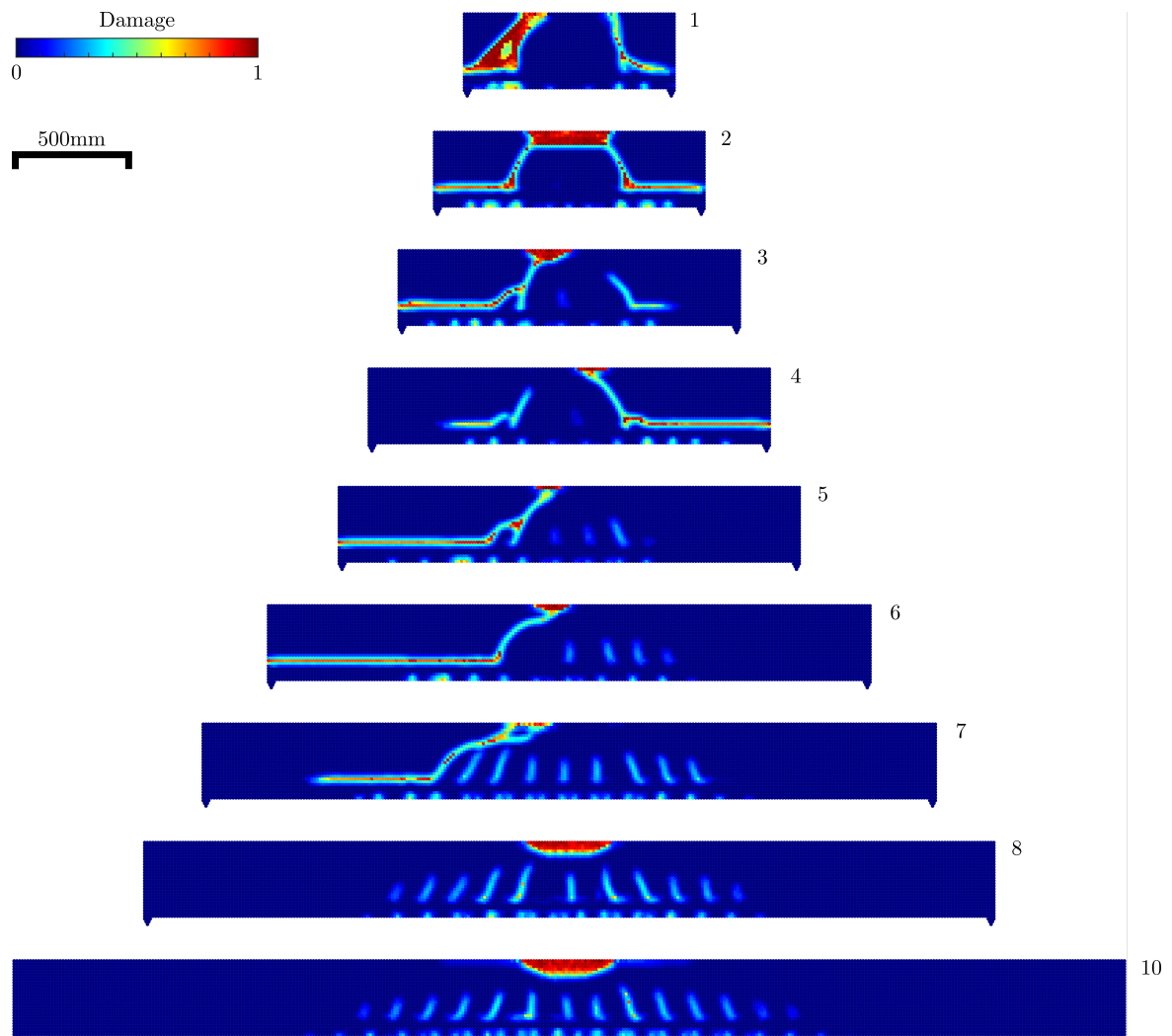
Fig. 7.6 Shear force and moment at failure against  $a_v/d$ 

Fig. 7.7 Numerical fracture pattern at failure using the normal mesh. The cross-section is taken through a reinforcing bar

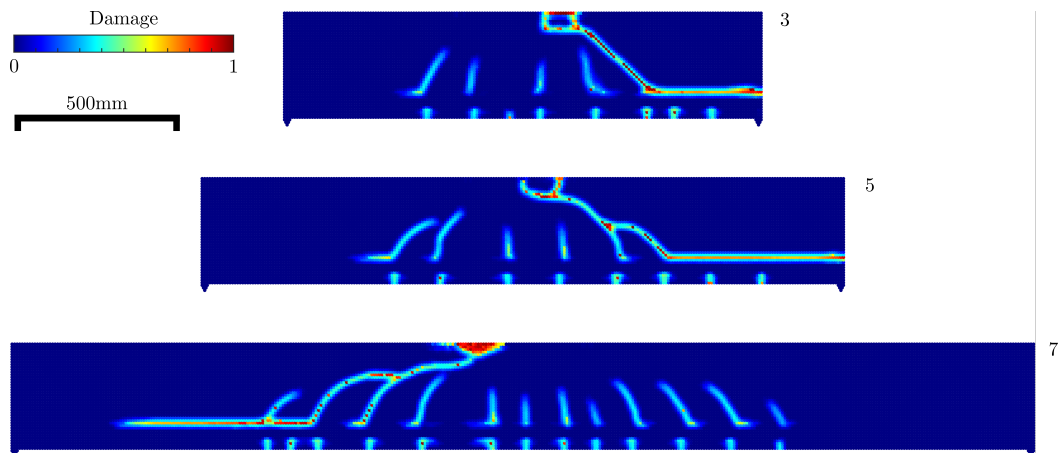


Fig. 7.8 Numerical fracture pattern at failure for Beam 3, 5, and 7 using the fine mesh

### **Shear-web failure: Beam 1**

Shear-web failure, sometimes referred to as true shear failure, deep beam failure, or splitting failure, occurs when the shear span is less than the effective depth,  $0 < a_v/d < 1$ . Diagonal shear cracks form in the web and propagate in an approximately direct line between the applied load and support. This is due to the splitting action of the compressive force between the load and support. The shear force cannot transfer across the crack, and members behave like a truss. The compression zones act as struts and the longitudinal reinforcement ties the struts together. Final failure can be caused by splitting, compression failure at the supports, or reinforcement anchorage failure due to the large tensile forces generated. Flexural cracking is limited.

Beam 1 has a shear-span-to-depth ratio of 1 and lies at the boundary of shear-web and shear-compression failure. The experimental fracture behaviour is typical of shear-web failure. Beam 1 failed experimentally at a load of 777 kN. Failure is predicted at a load of 335 kN and a mid-span deflection of approximately 1.1 mm. The experimental mid-span deflection is not known. The percentage error between the actual and predicted failure load is -57%; the largest error observed across all tests. The potential reasons for this error are numerous and analysis is provided within the discussion. The numerical and experimental fracture behaviour are in reasonable agreement but there are clear differences that might provide insight into the reasons for premature failure. Uniformly spaced flexural cracks form in the span of constant bending. As the applied load is increased, symmetric cracks propagate vertically towards the point of load application. The numerical and experimental fracture behaviour then start to diverge. In the numerical model, splitting between the steel-concrete interface occurs. This behaviour was not observed in the experimental work. Final failure

occurs with the formation of a diagonal crack in the web that propagates suddenly between the load and support. In the numerical model, propagation of the diagonal crack is stopped by the reinforcement. The numerical model correctly captures that no concrete crushing occurs in the compression zone.

### **Shear-compression failure: Beam 2, 3**

Shear-compression failure typically occurs in the range  $1 < a_v/d < 2.5$  and is characterised by crushing failure of the concrete at the point of load application. This mode of failure can occur suddenly and at a substantially lower load than that seen in shear-web failure. Flexural cracks will form initially before a diagonal crack starts from the last flexural crack and turn gradually towards the applied load. With few exceptions, diagonal cracks are extensions of flexural cracks. High vertical compressive stresses directly beneath the applied load halt the propagation of the diagonal crack. Internal forces are then redistributed and the member is able to carry additional load before compression failure finally occurs adjacent to the applied loads. Similarly, high vertical compressive stresses near the supports prevent the further propagation of splitting failure between the reinforcing bars and concrete. Fracture behaviour is generally symmetric with two diagonal cracks forming. The experimental failure behaviour observed in Beam 2 and 3 is typical of shear-compression failure.

The experimental failure load for Beam 2 is 520 kN. Failure is predicted to occur at a load of 253 kN and a mid-span deflection of 1.9 mm. The prediction error of -51% is smaller than the error observed in Beam 1. The experimental and numerical fracture behaviour are in reasonable agreement. The numerical model captures the crushing failure between the applied loads and symmetrical diagonal cracks form as expected. The location and angle of the diagonal cracks is incorrect, initiating closer to the applied load and at a steeper angle than that observed experimentally. Again, splitting between the steel-concrete interface occurs and propagates to the supports. This behaviour was not seen experimentally. High compressive forces beneath the applied load halt the direct propagation of the crack toward the point of load application.

The experimental failure load for Beam 3 is 294 kN. The numerical model predicts that failure will occur at a load of 170 kN and a mid-span deflection of 1.8 mm. The prediction error is -42%. The predicted deflection at failure is similar for Beam 2 and 3. Experimental load-deflection results are available for Beam 3 and the numerical load-deflection behaviour in Fig. 7.9 is in good agreement with the experimental results until premature failure occurs. The peridynamic model accurately reproduces the structural stiffness in the initial stages of loading. The model captures the stiffness softening observed at the start of crack initiation and there is very good agreement between the numerical and experimental results until

premature failure occurs. The mesh size does not influence the structural response during the initial loading period. The predicted structural response diverges moderately in the later stages of loading. Using the fine mesh, the predicted failure load is 181 kN and mid-span deflection is approximately 1.8 mm. In Beam 3, crushing occurs between the applied loads but only a single diagonal crack forms. The degree of crushing in the model is less than that observed experimentally. Using the normal mesh, the location and angle of the diagonal crack is incorrect. The fine mesh is more accurate in capturing the correct location and angle but errors remain. Splitting at the steel-concrete interface occurs when using the normal and fine mesh. Beam 3 and 5 have been modelled by Malm [147] using two commercial finite element codes, ATENA and Abaqus. The best correlation was achieved with Abaqus and the results have been included in Fig. 7.9. The results have been included for completeness but a fair comparison is difficult. The material properties for Beam 3 and 5 are identical but Malm adjusts the simulation parameters to improve agreement with the experimental data. This is calibration not validation.

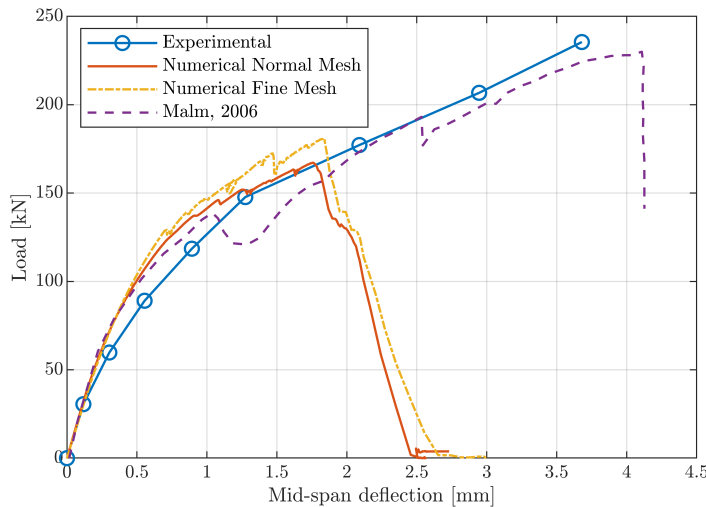


Fig. 7.9 Beam 3 load-displacement curve ( $a_v/d = 2$ )

### Shear-flexural failure: Beam 4, 5, 6, 7, 8

Shear-flexural failure occurs in the range  $2.5 < a_v/d < 6.0$ . Flexural cracks form during the early stages of loading. As the loading process progresses, a critical diagonal shear crack initiates from a flexural crack and travels towards the applied load. The diagonal crack rotates as the fracture propagates further into the compression zone. For members subjected to shear and bending, cracks will vary in slope from  $90^\circ$  at the extreme fibre (pure bending) to  $45^\circ$  at the neutral axis (pure shear). For beams in the range  $2.5 < a_v/d < 4$ , the diagonal crack meets resistance as it propagates upwards into the compression zone and

progression of the crack may be halted. With a further increase in loading, the fracture gradually extends along a shallow slope until sudden failure occurs when the arch mechanism is no longer capable of sustaining the applied load, leading to failure. This mode of failure is sometimes referred to as diagonal tension failure. For beams that lie within the range  $4 < a_v/d < 6$ , additional flexural cracks might form between the critical diagonal crack and the support and failure is typically very sudden. Leonhardt and Walther [135] remarked that the failure of Beam 7 and 8 was sudden. Fracture behaviour is typically asymmetrical and failure occurs at a load approximately half that observed in shear-web failure. Shear-flexural failure is also characterised by splitting between the concrete and longitudinal reinforcement. The experimental failure behaviour exhibited in Beam 4, 5, 6, 7, and 8 is characteristic of shear-flexural failure.

Beam 4 has a shear-span-to-depth ratio of 2.5 and lies at the boundary of shear-compression and shear-flexural failure. The experimental failure load is 161 kN, and the numerical model predicts that failure will occur at a load of 131 kN and mid-span deflection of 2.24 mm. The prediction error is -19%. The experimental fracture pattern demonstrates characteristics of shear-compression and shear-flexural failure. The slope of the critical diagonal crack is approximately constant with limited crack rotation. Concrete crushing does not occur. The numerical model correctly captures that crushing failure does not occur in Beam 4 but the location and angle of the diagonal crack is incorrect. The diagonal crack initiates closer to the applied load and at a steeper angle than that exhibited experimentally. The crack travels under the applied load and into the span of constant bending, this behaviour was not observed in the experiment.

Beam 5 failed experimentally at a load of 118 kN and the numerical model predicted the peak load to be 112 kN at a mid-span deflection of 2.5 mm. Final failure occurs at a mid-span deflection of 2.8 mm. The numerical prediction error is -5%. This is the best prediction achieved across all tests using the normal mesh. The difference between the actual and predicted failure load reduces as the internal behaviour switches from arch action to beam action. The numerical structural response, plotted in Fig. 7.10, is in good agreement with the experimental load-displacement curve. The initial structural stiffness is captured correctly. As loading progresses, structural stiffness is moderately overestimated. Concrete softening and the initiation of damage reduce the stiffness of the structural member and good agreement is observed near the peak load. The mesh size does not impact on the structural response until the later stages of loading. The failure load predicted using the fine mesh is 122 kN and mid-span deflection is approximately 2.9 mm. Beam 5 has previously been modelled by Most [159], Malm [147], Jendele and Červenka [123], Červenka and Papanikolaou [222], and more recently by Xenos and Grassl [232]. Xenos and Grassl [232] modelled the failure

of Beam 5 with non-local and crack band approaches using the damage-plasticity model CDPM2, originally introduced by Grassl et al. [97]. The results for the non-local model with a fine mesh from Xenos and Grassl [232] are included in Fig. 7.10. The member was modelled in two-dimensions and planes of symmetry were exploited, with only half of the beam considered. This is not strictly valid due to the asymmetrical failure behaviour of reinforced concrete members in the range  $2.5 < a_v/d < 6.0$ . The two models show good agreement until approximately 100 kN where the results diverge and the model of Xenos and Grassl [232] underestimates the peak load. The peridynamic model reproduces the expected asymmetrical failure mode and the fracture pattern is in reasonable agreement with the experimentally observed behaviour. Using the normal mesh, the location and angle of the diagonal crack is incorrect. The distance between the fracture origin and applied load is only 0.2 m. Experimentally this distance is measured to be approximately 0.5 m. Using the fine mesh improves the fracture results. As the diagonal crack propagates into the compression zone, the characteristic rotation behaviour is seen and the distance between the fracture origin and applied load is over 0.3 m.

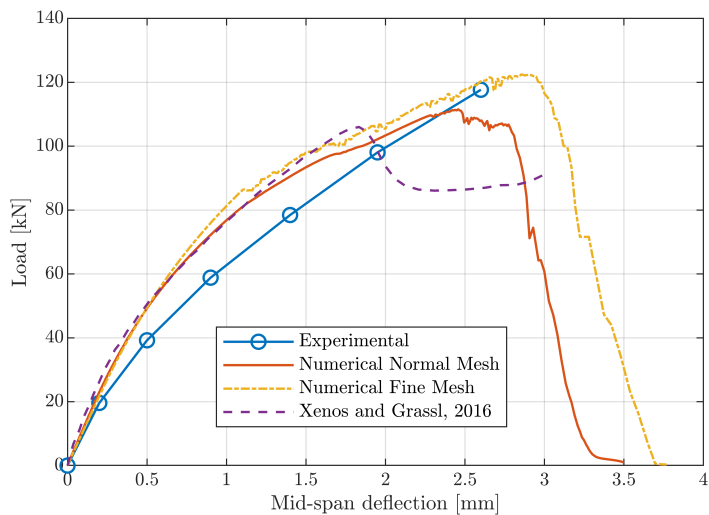


Fig. 7.10 Beam 5 load-displacement curve ( $a_v/d = 3$ )

Beam 6 fails experimentally at a load of 118 kN and the numerical model predicts that failure will occur at a load of 85 kN and mid-span deflection of 4.5 mm. The prediction error is -28%. This is a notable increase in the error of the numerical prediction. The numerical model captures the asymmetrical fracture behaviour but the location of the diagonal crack is wrong. The diagonal crack initiates closer to the applied load than that observed in the physical test. This behaviour has been observed in Beam 2, 3, 4, and 5.

Beam 7 was tested twice using identical material parameters. The first specimen failed experimentally at a load of 120 kN and the second specimen failed at 131 kN. The results

demonstrate the inherent variability of ultimate strength in identical reinforced concrete elements. Herbrand [111] notes that the exact replication of flexural shear tests is unreliable and the coefficient of variation of repeated tests is typically between 6 to 12%. Failure is predicted at a load of 87 kN and a mid-span deflection of approximately 8.1 mm. Using the lower failure load of 120 kN, the prediction error is -28%. The numerical and experimental load-deflection behaviour, plotted in Fig. 7.11, are in good agreement during the early stages of loading. As the applied load is increased, the model predicts a stiffer response than the experimental results. After damage, the numerical model overestimates the reduction in member stiffness. The member carries additional load until premature failure occurs. The predicted structural response using the normal and fine mesh is in good agreement until the peak. The peak load is mesh dependent and the failure load predicted using the fine mesh is 92 kN and mid-span deflection is 9.1 mm. Herbrand et al. [112] modelled the failure of Beam 7 using a plastic damage material model with Abaqus. Full bond is assumed between the concrete and reinforcement. The two models show good agreement during the initial stages of loading. The model of Herbrand et al. [112] better captures the structural stiffness after the onset of damage. The peridynamic model captures the expected asymmetrical failure behaviour and the fracture behaviour is in good agreement with the experimental results. Fig. 7.12 illustrates the three-dimensional fracture path. Using the normal and fine mesh, the location and angle of the critical diagonal crack is approximately correct. The predicted distance between the fracture origin and applied load is 0.45 m. The characteristic rotation behaviour of the shear crack is captured and the fracture propagates at a shallow angle beneath the applied load. The flexural crack width spacing also shows good agreement with the experimental results. In the experimental test, additional flexural cracks form between the critical diagonal crack and the support. This behaviour is only observed when using the fine mesh. Fig. 7.13 displays the deformed shape of Beam 7 at failure and illustrates the opening of the diagonal crack.

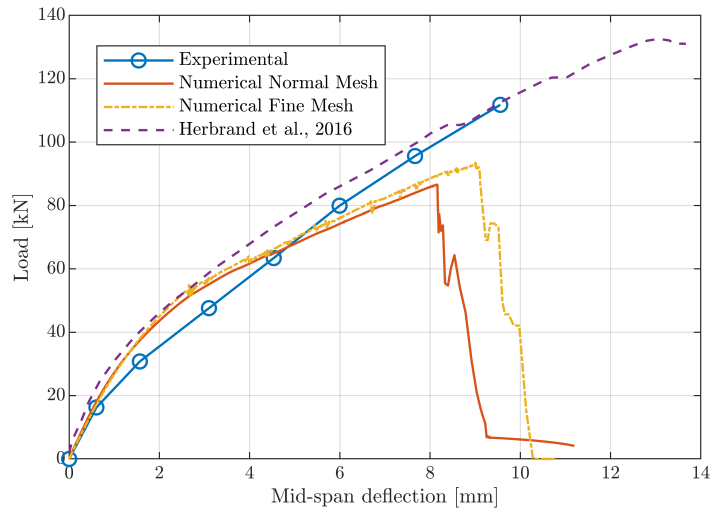


Fig. 7.11 Beam 7 load-displacement curve ( $a_v/d = 5$ )

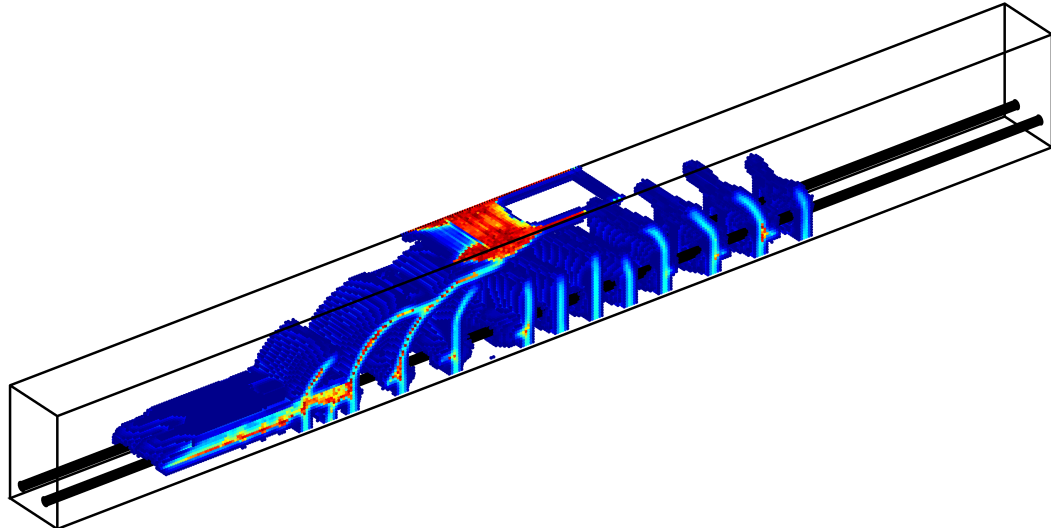


Fig. 7.12 Fracture paths in Beam 7 using the fine mesh

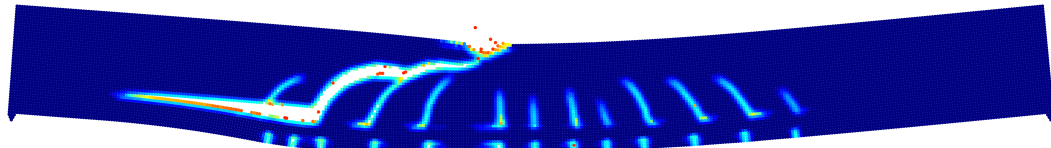


Fig. 7.13 Deformed shape of Beam 7 at failure. Displacement is scaled by a factor of 10

Beam 8 has a shear span-to-depth ratio  $a_v/d$  of 6 and lies at the boundary of shear-flexural and flexural failure. The experimental failure behaviour is typical of shear-flexural failure. Beam 8 was tested twice using identical material parameters and both specimens failed at

126 kN. Failure is predicted at a load of 76 kN and a mid-span deflection of 11 mm. The prediction error is -40%. The numerical model fails to capture the correct failure mode and the fracture behaviour is typical of flexural failure. Uniformly spaced flexural cracks form and grow proportionally with increases in applied load. Compressive failure of the concrete occurs between the applied loads resulting in a complete loss of load carrying capacity. Yielding of steel reinforcement does not occur.

### Flexural failure: Beam 10

Members with a shear-span-to-depth ratio greater than 6 are expected to reach their full theoretical flexural capacity. The failure behaviour of a slender beam under constantly increasing load is well known. Narrow flexural cracks will begin to appear well before the ultimate load. If proper bond is provided, the steel and concrete will attain the same strain. As the loading is increased, the width and length of the flexural cracks will increase and the area of the compression zone will decrease. This behaviour will become more pronounced after yielding of the reinforcing steel. The area of the compression zone will continue to decrease and the compressive stresses will eventually reach a level where crushing failure of the concrete occurs [129].

Beam 10 was also tested twice. The first specimen failed at 94 kN and the second specimen failed at 103 kN. Both specimens failed in flexure. The numerical model predicts failure at 56 kN and a mid-span deflection of 18.4 mm. Using the lower failure load of 94 kN, the prediction error is -41%. The numerical fracture behaviour is in good agreement with the experimental results. The average crack spacing in the experimental test is approximately 110 mm and the maximum flexural crack length is 230 mm. In the numerical model, the average crack spacing is 120 mm and the maximum flexural crack length is 218 mm. Leonhardt and Walther [135] note that Beam 10 fails due to the crushing of concrete before the yield point was reached in the reinforcement. This behaviour is observed in the numerical model and yielding of the reinforcement does not occur.

## 7.4 Discussion

### 7.4.1 Shear-transfer actions

The numerical results are in fair agreement with the experimental results but the ultimate load capacity is underestimated in all cases. Insight into the behaviour of the numerical model can be gained through examination of the variation in error for different values of  $a_v/d$ . The prediction error between the numerical and experimental results decreases as  $a_v/d$  changes

from 1 to 3 (-57% → -5%). Unexpectedly the prediction error then increases as  $a_v/d$  changes from 3 to 8 (-5% → -41%). The potential reasons for these differences are numerous and it is probable that no single issue is solely responsible for the observed errors. The results suggest that the peridynamic model captures some but not all of the factors that contribute to shear resistance. Isolating sources of discrepancy between experimental and numerical results is challenging. By considering how the contribution of different shear-transfer actions changes for a range of  $a_v/d$  values, and relating to variations in prediction error, it is possible to identify specific areas of deficiency within the model. A number of recent papers have examined the contribution of the various shear-transfer actions in members without web reinforcement [119, 111, 46, 47]. These works are used to guide the discussion but it should be noted that there is no clear consensus on the exact relationship between the individual shear-transfer mechanisms and influencing parameters.

The largest prediction errors are observed in members where load transfer occurs predominantly through arch action ( $a_v/d < 2.5$ ). This is not completely unexpected as this behaviour is observed within existing design codes and numerical models. The degree of uncertainty in shear strength predictions increases as  $a_v/d$  approaches 0 and the ultimate shear strength of a deep beam ( $a_v/d < 1$ ) can be four times greater than that predicted by Eurocode 2 (EC2) [193]. Červenka et al. [224] used non-linear finite element analysis to simulate 33 experimental tests of reinforced concrete elements and found that model uncertainty is higher for members failing in shear. Fig. 7.6 shows that the numerical model does capture an increase in shear capacity for members in the range  $a_v/d < 2.5$  but the degree of increase is smaller than expected. It is hypothesised that the failure to capture the correct ultimate load and fracture behaviour could be due to (1) limitations of the concrete damage model, and/or (2) the assumption of perfect bond between the steel reinforcement and concrete.

Potential shortcomings of the concrete damage model include the absence of compressive softening, and difficulty capturing mode II fracture. It might be necessary to include compressive softening behaviour in the concrete constitutive model. Fig. 7.14 illustrates the principal compressive strain distribution in Beam 1 before the onset of damage. Bottle-shaped compressive struts appear to be forming correctly but damage does not form within the strut as expected. Claus [52] found that the inclusion of compressive softening is important for the accurate representation of the formation and degradation of the compressive struts within a non-linear finite element model. In shear-compression and shear-flexural failure, the critical diagonal crack initiates from a flexural crack (mode I type fracture). In shear-web failure, the critical diagonal crack is expected to initiate within the web and the exact fracture mode or combination of modes is not clear but mode II type fracture potentially plays a significant role. The prediction error between the numerical and experimental results is highest for Beam

1 ( $a_v/d = 1$ ), and this might imply that the concrete constitutive model does not properly account for mode II fracture behaviour. Ren et al. [187] proposed a new damage rule based on the maximal deviatoric bond strain. They report that this damage rule is compatible with the three modes of brittle failure, and compared with the classic maximum bond stretch rule, the proposed damage model can predict in-plane and out-of-plane shear failure with ease. This requires further investigation.

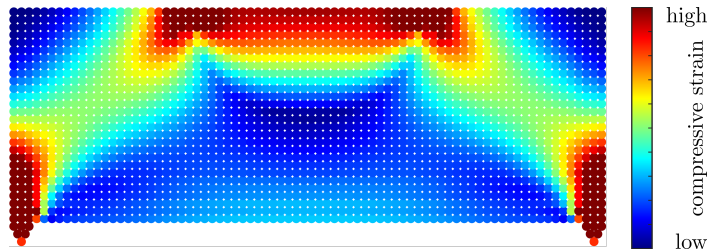


Fig. 7.14 Principal compressive strain distribution in Beam 1. The purpose of this figure is to illustrate the formation of compressive struts and the inclusion of strain values is considered to be redundant.

The load-deflection results for Beam 3 in Fig. 7.9 provide useful insight into the numerical behaviour of a beam under arch action. The peridynamic model accurately reproduces the structural response in the initial stages of loading and correctly captures the reduction in stiffness observed at the start of crack initiation. The results are in good agreement until premature failure occurs. This suggests that the model fails to capture an important aspect of structural behaviour. Fenwick and Pauley [81] found that arch action can only occur at the expense of slip (complete loss of bond transfer). Swamy et al. [214] also showed that arch action can be developed in a beam only when the steel is fully unbonded between strong end anchorages. It was found that arch action enhances the shear resistance of an unbonded beam beyond that of a bonded beam failing in shear but also increases deflection. This evidence suggests that the assumption of perfect bond between the reinforcement and concrete is a likely source of error for beams that transfer load primarily through arch action. Work is needed to develop a constitutive model for bonds that interface between reinforcement and concrete.

Beam 5 ( $a_v/d = 3$ ) is the most brittle member tested (lowest moment capacity) and lies at the bottom of Kani's shear valley. Fig. 7.6 plots the ultimate moment at failure from the experimental and numerical tests. It is interesting to observe that the numerical shear valley is much shallower than the experimental shear valley. The predicted ultimate moment capacity ranges from 44 kNm to 62 kNm, whereas the experimental ultimate moment capacity ranges from 48 kNm to 105 kNm. The predicted failure load for Beam 5 is also the most accurate across all tests and the key question is why? The shear force resistance of the inclined

compressive strut and aggregate interlock is expected to be limited. The contribution of the inclined compressive strut is vanishingly small in members with a shear-span-to-depth ratio greater than 3. This is well known. The exact contribution of aggregate interlock to the shear strength is much less certain but the following points suggest that it is comparatively low: (1) Large aggregate interlock stresses are expected when the angle of the diagonal crack is greater than  $45^\circ$  [46]. For Beam 5, the angle of the diagonal crack is approximately  $28^\circ$  at the steepest point. (2) Aggregate interlock is much more pronounced in deep beams [119]. It is assumed that the shear force is resisted primarily by a combination of the uncracked compressive zone, residual tensile stresses at flexural crack tips, and dowel action. For Beam 7, Herbrand [111] determined that approximately 30% of the shear force at failure is resisted by the uncracked compressive zone. As the contribution of the uncracked compressive zone is mainly governed by the reinforcement ratio  $\rho$ , a similar value is expected for Beam 5. The contribution of the residual tensile stresses at flexural crack tips to the shear strength is estimated to be approximately 20 - 40% of the shear capacity [119, 111], and the contribution of the dowel action to the shear strength is estimated to be approximately 10 - 20% of the shear capacity [119, 47]. The high predictive accuracy suggests that the peridynamic model does a good job of capturing these shear-transfer actions.

According to Červenka et al. [224], the uncertainty in a non-linear finite element model of a reinforced concrete member decreases as the failure mode changes from shear to flexural. Unexpectedly, the prediction error in the peridynamic model increases as the failure mode transitions from shear to flexural. It is theorised that for members in the range  $3 < a_v/d < 6$ , discrepancies between the experimental and numerical results can be partly accounted for by the neglect of crack friction within the numerical model. Aggregate interlock is known to have an important role in the transfer of shear forces. As a crack opens, sliding occurs and contact between the faces produces normal and tangential stresses. Huber et al. [119] found that the crack opening and sliding behaviour is directly correlated with the shape of the critical shear crack, and aggregate interlock is more pronounced in members with steeply inclined shear cracks. The steep inclination of the shear crack at mid-span in Beam 7 and 8 (see Fig. 7.5) produces a large aggregate lock effect. Cavagnis et al. [47] used digital image correlation to investigate the role of various shear-transfer actions in members without web reinforcement. It was found that for members governed by beam shear-transfer actions, the contribution of aggregate interlock is dominant. Herbrand [111] developed a mechanical model to predict the shear strength of reinforced concrete members without web reinforcement. Herbrand used the model to determine the contribution of each shear transfer action to the overall shear resistance of Beam 7 at every load step. At failure, aggregate interlock carries 43% of the shear force. Unbroken bonds that cross between fracture faces

introduce a degree of resistance to crack sliding and the numerical prediction error is -28%. Contact between crack faces stiffens the structural response and the reduced numerical stiffness observed in Beam 7 (see Fig. 7.11) further supports the theory that crack friction must be accounted for. The numerical fracture pattern predicted by the peridynamic model (see Fig. 7.12 and 7.13) is superior to that of Herbrand et al. [112] and it is interesting to note that the asymmetrical failure is captured with homogeneous material properties.

Correctly predicting the ultimate flexural capacity of a reinforced concrete member is a key test when evaluating model robustness. The principles governing flexural strength are clearly understood and accurately predicting the bending capacity of a reinforced concrete member is trivial. The size of the prediction error between the actual and predicted failure load for Beam 10 is somewhat unexpected. Unfortunately there is no experimental load-displacement graph from which insight into the numerical behaviour might be gained. The numerical fracture behaviour is in good agreement with the experimental results and the failure is governed by concrete crushing in the compression zone. This suggests that early compressive failure might be responsible for the disagreement between the numerical and experimental results. According to Eurocode 2 (EC2) [43], concrete reaches its maximum compressive stress when compressive strain is approximately 0.002 and crushing failure occurs at an ultimate strain of 0.0035. The maximum compressive strain in Beam 10 reaches 0.0013 shortly before failure occurs. This value is consistent with the prediction error. Beam 8 failed experimentally in shear but the numerical fracture displays the characteristics of flexural failure. Crushing failure of concrete in the compression zone occurs before a diagonal shear crack can form. The numerical failure mechanism and prediction error in Beam 8 and 10 is almost identical.

#### 7.4.2 Loading system

Differences in obtained structural behaviour and failure load can also be partly explained by the loading system. Leonhardt and Walther [135] tested all members with a discrete load-controlled system. Beams were loaded in incremental stages of approximately 1/10th of the predicted failure load. In discrete load-controlled testing, the precise failure load and corresponding displacement are not measured. In the numerical simulations, all members were loaded with a forced displacement. Displacement-controlled testing has some important advantages. The exact failure load is identified and the structural response of the member can be studied continuously, including the post-peak behaviour. To explain the problem; the final loading step prior to failure for Beam 3 was 235 kN, and shear failure occurred between this load step and the final load step of 294 kN. The exact failure load is not known and

the potential prediction error between the experimental and numerical results ranges from a minimum of -28% to a maximum of -42%.

### 7.4.3 Discretisation

The mesh discretisation is another source of error and uncertainty. Mesh dependency has been investigated using two levels of mesh refinement. The load-deflection curves are independent of the mesh refinement until the peak load is approached (see Fig. 7.9, 7.10, and 7.11). The structural response at the peak load is mesh dependent, and the fine mesh provides better predictions of load capacity. The mesh refinement influences the fracture patterns. The average crack spacing between flexural cracks remains approximately the same for both meshes, but the location and path of the diagonal shear crack improves as the mesh is refined. The improved shear crack location and path could explain the increased prediction accuracy. Bobaru and Hu [32] and Zhao et al. [244] note that the size of the horizon should be defined by the smallest relevant geometrical feature. In this work the maximum horizon size should ideally be smaller than the diameter of the steel reinforcing bars. This was not reasonably practicable due to the high computational expense. This is a clear limitation and the interaction between the reinforcing bars and concrete might not be captured correctly. Computational expense and time limits prevented further examination of the mesh dependency. Ren et al. [186, 187, 188] recently introduced a dual-horizon peridynamic formulation which allows for an irregular discretisation. Using a multi-scale discretisation scheme, it would be possible to refine the mesh at critical locations such as the bond interface, similar to the work of Lu et al. [142]. This is a promising area of future research.

### 7.4.4 Material parameters

There is a significant degree of uncertainty in the selection of material parameters and this will influence the reliability of the predicted failure load and behaviour. This uncertainty can be investigated by considering a probabilistic model of material properties. Červenka et al. [225] modelled fracture energy  $G_F$  as a random field over the domain of a concrete member. The introduction of randomly distributed material properties reduced discrepancies between numerical and experimental results. Future work should consider the micro-structure and spatial variability of concrete.

### 7.4.5 Comparison with design codes

Load capacity and failure mode predictions using EC2 [43] are provided in Table 7.3. All safety factors have been set to 1. The poor prediction accuracy demonstrates the uncertainty that surrounds shear failure. The peridynamic model offers an appreciable improvement in accuracy for members failing in shear, and in all cases, the model provides safe predictions of load capacity. The design code predictions are unconservative for Beam 5, 6, and 7, and the predicted load capacity is up to 22% higher than that observed experimentally. EC2 predicts that Beam 8 will fail in flexure at 125 kN. The predicted load capacity is correct but the failure mode is wrong. It is interesting that the failure mode in the numerical analysis agrees with EC2. Predicting the correct failure type for members that lie at the boundary of distinct failure modes is challenging. As has already been stated, EC2 provides accurate predictions of flexural capacity.

### 7.4.6 Importance of further validation

As pointed out by Diehl et al. [69], the majority of papers calibrate model parameters against a single experiment and only a few addressed further validation. This work has demonstrated the importance of further validation and areas of future research have emerged. The experimental test series by Leonhardt and Walther [135], modelled in this chapter, is proposed as a benchmark problem for modelling the failure of reinforced concrete elements. To the best of the authors knowledge, this is the first work to consider the full series of tests. Good benchmark problems help facilitate the fair comparison of different numerical models and provide the required credibility to make definitive conclusions. Validation against the complete test series will provide a robust investigation of the ability of a numerical model to capture a range of load-transfer and failure mechanisms.

When viewing the load-deflection graphs in isolation it can be difficult to discern how the structural response differs between members. Fig. 7.15 combines the experimental and numerical load-displacement curves for Beam 3, 5, and 7 using the normal mesh. The horizontal line indicates the load capacity predicted by EC2. This figure illustrates the capability of the peridynamic model to predict a range of structural responses.

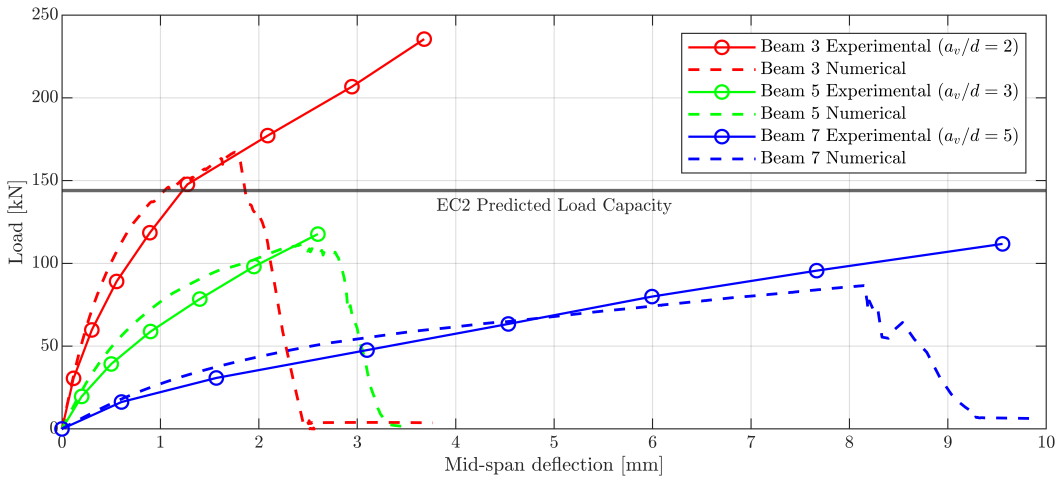


Fig. 7.15 Comparison of experimental and numerical load-displacement curves. The horizontal line indicates the load capacity predicted by EC2.

#### 7.4.7 Summary

The preceding results discussion has identified a number of potential areas of deficiency within the model and provided evidence to support the interpretation of results. There are multiple other factors that may introduce errors and detailed uncertainty quantification studies are needed. The presented approach has demonstrated significant promise for predicting the shear capacity of reinforced concrete members, and the peridynamic model possesses a number of features that justify further development:

1. Crack initiation, propagation and coalescence naturally emerge from the governing equations. Asymmetrical failure modes (as illustrated in Fig. 7.13) are predicted without explicitly modelling the microstructure.
2. Non-planar three-dimensional crack paths are captured with ease (see Fig. 7.12). This is important when considering more complex problems such as reinforced slabs.
3. The constitutive model that has been employed is very simple and has few parameters, and in some cases, as illustrated in Fig. 7.10, the results are better than that of well-established numerical methods. Xenos and Grassl [232] used the damage-plasticity model CDPM2, and they note that this model requires a large number of input parameters. Vorel et al. [228] recently compared four state of the art concrete constitutive models in a standard continuum-based framework. The average number of model parameters is 25, and many of these parameters have no credible justification. The simplicity of the presented approach should be regarded as an advantage.

## 7.5 Conclusions

Determining the shear capacity of reinforced concrete members is notoriously difficult. In this work, a three-dimensional bond-based peridynamic framework has been developed and validated for predicting shear failure in reinforced concrete beams. This is the first study to comprehensively validate the predictive capability of a peridynamic model against a series of problems. The experimental test series by Leonhardt and Walther [135] was chosen as a benchmark due to the wide range of failure modes exhibited. It was hypothesised that this series of beams would be difficult to simulate due to the change in load-transfer behaviour as shear slenderness is increased, and the important influence of fracture behaviour on the redistribution of stresses. The predictive error between the experimental and numerical results ranges from +3% to -57%, highlighting the importance of validation against a series of problems. The results demonstrate that the model captures many, but not all, of the factors that contribute to shear and bending resistance. The main findings are listed:

1. The model successfully captures many of the key features of shear and flexural failure. This is achieved using a simple bilinear constitutive model, a regular mesh discretisation, and without the need for prior knowledge of fracture behaviour. The predicted fracture patterns are generally in good agreement with the experimental results. Using the fine mesh, the predicted fracture behaviour is equivalent to, if not better than that found elsewhere in the literature.
2. The model accurately predicts the load capacity of Beam 5 and the numerical structural response is in good agreement with the experimental load-deflection curve. This suggests that the model captures the following load-transfer actions: shear transfer in the uncracked compressive zone, residual tensile stresses at flexural crack tips, and dowelling action of the tensile reinforcement.
3. The assumption of perfect bond between the steel reinforcement and concrete is a likely source of error for beams that transfer load primarily through arch action. Arch action can only occur at the expense of slip and development of an interface constitutive model is needed. Factors such as bond-slip need to be considered.
4. The results for short members suggest that there are limitations with the concrete constitutive model. Potential shortcomings of the concrete damage model include the absence of compressive softening, and difficulty capturing mode II fracture. It remains unclear to which degree the prediction error can be attributed to these factors but they are worthy of further investigation. The early compressive failure of concrete

in slender beams could be linked to the identified shortcomings. It is also possible that there are unknown factors at play.

5. Discrepancies between the experimental and numerical results can be partly accounted for by the neglect of crack friction within the numerical model. For members governed by beam shear-transfer actions the contribution of aggregate interlock is dominant, and the numerical model should be expanded to explicitly account for crack friction.

In addition, there are a number of areas that have not been addressed by this work but likely play an important role: (1) the influence of size effect on structural strength, and (2) the influence of concrete micro-structure on fracture initialisation and growth. Further challenges include addressing computational efficiency with a multi-scale mesh discretisation, and bounding predictions with upper and lower limits using uncertainty quantification methods. The results presented in this study help to elucidate where future avenues of research lie for the application of peridynamics to reinforced concrete problems. With further research and development, it is conceivable that the peridynamic model might enable a better understanding of shear failure and the multitude of influencing factors.

# **Chapter 8**

## **Conclusions and future work**

The peridynamic theory provides a powerful framework for modelling fracture and damage in quasi-brittle materials. There has been an exponential growth in interest from the research community and industry since Silling [203] introduced the theory in 2000, however, there has been a lack of robust validation studies and this is potentially limiting the application of peridynamic models.

The main aim of this thesis was to develop a three-dimensional bond-based peridynamic framework for modelling quasi-brittle structural elements and to quantify the predictive accuracy of the model by employing a thorough validation procedure. By carefully selecting validation problems that tested a wide range of behaviours, this work has delivered new insights into the capabilities and deficiencies of the peridynamic model. Furthermore, this work has presented a number of new developments that have improved the predictive accuracy of the bond-based peridynamic model.

### **8.1 Conclusions**

#### **8.1.1 Constitutive model**

A comparative study to quantify the predictive accuracy of existing constitutive laws for modelling quasi-brittle materials was needed. From the literature review, it was evident that there is no broadly accepted constitutive model for quasi-brittle materials. This suggests that there is still a large degree of uncertainty surrounding the predictive accuracy of existing constitutive laws.

A number of constitutive laws have been proposed within the bond-based peridynamic framework but a detailed examination of the predictive accuracy of different models was missing from the literature. The results demonstrated that the behaviour of a peridynamic

bond should be consistent with the macroscopic material response and a new non-linear softening law was introduced that addressed the ambiguity of existing non-linear laws. The predictive accuracy of the proposed non-linear softening law is superior to existing constitutive laws, and the numerical results are in good agreement with experimental data.

### 8.1.2 Mode I and mixed-mode fracture

The model has been validated against both mode I and mixed-mode fracture problems. The chosen test problems have been examined by many researchers, making it easy to compare the results with existing numerical models.

To test the predictive capabilities of the model for mode I fracture, validation was performed against the full set of experimental results published by Grégoire et al. [98]. Geometrically similar notched and unnotched concrete members were tested in three-point bending to investigate size and boundary effects. It was shown that the non-local nature of peridynamics influences the results for different boundary types, and spurious strengthening occurs in the proximity of a notch due to the non-local interaction of particles above and below the notch tip. This effect is reduced as the size of the beam is increased.

To test the generality of the model, the mixed-mode fracture tests of García-Álvarez et al. [88] were simulated. Accurately predicting mixed-mode fracture behaviour is considered to be a harder problem than predicting mode I fracture behaviour, and most problems of practical relevance will be subject to mixed-mode loading conditions. In all presented cases, the computed load-CMOD response is in good agreement with the experimental data, and the peak load is accurately predicted. The computed fracture paths are also in good agreement with experimental results and demonstrate the robustness and generality of the bond-based model.

Predictions obtained using the peridynamic model were compared against results from more advanced models. Results recently published by Barbat et al. [8] were selected for comparison as the authors employed a crack band model in a smeared crack framework, and this is the most widely used and successful approach for modelling the failure of quasi-brittle materials. Comparing the predictive capabilities of the peridynamic model against established numerical methods is an essential step in validation, and it was demonstrated that the accuracy of the developed model is equivalent for the presented test cases.

### 8.1.3 Size effect

Accurately capturing the structural size effect is essential for safe predictions of load capacity. The capability of a peridynamic model to capture size effect in quasi-brittle materials had yet

to be examined and remained a major question. As stated by Bažant [19], the capability to correctly reproduce the size effect is an important check on the validity of any computational model.

The peridynamic model accurately captures the deterministic size effect in notched problems and the predicted load-CMOD response and crack paths are in close agreement with the observed experimental data. Comparisons with leading numerical models are provided, and the predictive accuracy of the peridynamic model is equivalent, if not superior.

In conventional numerical models, capturing size effect requires a localisation limiter that governs the width of the softening zone. The localisation limiter is determined by an internal characteristic length that is a property of the material. The definition of the characteristic length is highly ambiguous and its value can not be determined experimentally. The non-local length scale in the peridynamic model is not related to material properties and avoids the aforementioned problems.

The peridynamic model fails to accurately capture the structural strength for all unnotched specimens. As the structure size increases, so does the over-prediction of structural strength. To some extent, this behaviour was expected. For notched problems, statistical variability in material properties can largely be ignored, but for unnotched problems, the randomness of material properties has a significant effect on structural strength.

The peridynamic model does not predict any deterministic size effect for the unnotched problems, and whilst it is expected that the inclusion of statistical variability in material properties would significantly improve the predictive accuracy, a small deterministic size effect should have been observed. To trigger the localisation of damage in unnotched specimens, it is hypothesised that a source of randomness must be introduced.

### 8.1.4 Shear strength

Correctly predicting the shear strength of a reinforced concrete element is an essential test for any numerical model due to the sudden and catastrophic nature of shear failure. To quantify the predictive accuracy of a peridynamic model, the model was tested against a systematically arranged set of element-level benchmark tests that exhibited a wide range of failure modes.

The experimental test series by Leonhardt and Walther [135] was chosen as a benchmark due to the wide range of failure modes exhibited. It was hypothesised that this series of beams would be difficult to simulate due to the change in load-transfer behaviour as shear slenderness is increased, and the important influence of fracture behaviour on the redistribution of stresses. The predictive error between the experimental and numerical results ranges from +3% to -57%, highlighting the importance of validation against a series

of problems. The results demonstrate that the model captures many, but not all, of the factors that contribute to shear and bending resistance.

Discrepancies between the experimental and numerical failure loads might appear to be substantial, but as has been shown, predictions with Eurocode 2 are worse for shear critical members. Comparisons with numerical results from three earlier studies are provided but a fair comparison is difficult as these studies did not follow a robust validation process.

It should be emphasised that the employed constitutive model (bilinear) is very simple and has few parameters, and in some cases, as illustrated in Fig. 7.10, the results are better than that of well-established numerical methods. Xenos and Grassl [232] used the damage-plasticity model CDPM2, and they noted that this model requires a large number of input parameters. The simplicity of the presented approach should be regarded as an advantage, and the use of complex models with many parameters that have no physical justification should be avoided if possible. Simpler models are preferable because they are easier to validate and less prone to overfitting during calibration. It is worth restating the following principle: the simplest model should be examined first, and only if the model is found to be deficient should the complexity be increased.

### 8.1.5 Mesh sensitivity

Mesh sensitivity studies were performed to investigate the dependency of the results on the mesh resolution. The predicted results (load-deflection response, peak load and crack path) should be independent of the mesh resolution. This is a basic test of the adequacy of any numerical model. To the best of the authors knowledge, mesh sensitivity studies are missing from the existing literature.

For notched problems, the predicted peak load is independent of the mesh discretisation, but for unnotched problems, the predicted peak load progressively increases as the mesh is refined. In an attempt to understand this behaviour, an examination of the damage energy dissipation is provided. To the best knowledge of the author, this is the first time that energy dissipation has been investigated using a peridynamic model. For the unnotched case, the width of the region of energy dissipation increases as the mesh is refined. The dependency of the energy dissipation on the mesh resolution for the unnotched case is believed to be the source of the peak load sensitivity. The cause of the mesh sensitivity is not yet fully understood, but an important factor has been identified. It is hypothesised that the inclusion of spatially varying material properties might be important for capturing the correct behaviour in unnotched cases.

Mixed-mode problems were considered to examine the dependency of the predicted crack path on the mesh resolution. The computed fracture paths are independent of the mesh resolution, demonstrating the robustness of the model (see Fig. 5.31).

The peridynamic model prevents the localisation of damage into a zone of infinitely small volume as the mesh is refined. Both the total energy dissipation and the volume of the damage zone remain approximately constant across different levels of mesh refinement. A crack band model prevents zero energy dissipation upon refinement, but damage localisation occurs in a single row of elements, even if the mesh elements become infinitely small. This is not physically consistent, and in this sense, the peridynamic model is more fundamental than a crack band model.

Mesh sensitivity was also examined for reinforced concrete members. The assessment is complicated by the presence of two materials with very different properties. Mesh dependency was investigated using two levels of mesh refinement. The computed load-deflection curves are independent of the mesh resolution until the peak load is approached. The structural response at the peak load is mesh dependent, and the fine mesh provides better predictions of load capacity. The mesh refinement influences the fracture patterns. The average crack spacing between flexural cracks remains approximately the same for both meshes, but the location and path of the diagonal shear crack improves as the mesh is refined. The improved shear crack location and path could explain the increased prediction accuracy. Computational expense and time limits prevented further examination of the mesh dependency, and this is an area that needs additional work. It remains to be established if the results will converge upon further mesh refinement.

### 8.1.6 Physical meaning of the horizon

The results presented in this thesis have demonstrated that non-locality is essential in a physically consistent model, but at the macroscale, the horizon radius  $\delta$  is not an intrinsic material property. This differentiates the peridynamic model from existing non-local models, and the use of an ambiguous characteristic length parameter is avoided. There are two key factors that support the conclusion that the horizon radius  $\delta$  is not an intrinsic material property:

1. For notched problems, the region of energy dissipation remains approximately equal across three levels of mesh refinement ( $\Delta x = 1.25, 2.5, 5$  mm and  $\delta = \pi\Delta x$ ). If  $\delta$  is a intrinsic material length (characteristic length), related to material heterogeneities and independent of the mesh refinement, then one would expect that the region of energy dissipation would change for different values of  $\delta$ .

2. Capturing the correct energy dissipation as a crack forms and propagates is essential to accurately model structural size effect. Many existing numerical methods use a localisation limiter to prevent damage from localising into a zone of zero volume. The localisation limiter is chosen to ensure correct energy dissipation when a crack forms and is determined by an internal characteristic length  $l_c$  that is a property of the material being modelled. If  $\delta$  is a material property, then one would have expected the predictions of size effect to be inaccurate.

It might be fair to argue that the two factors are negative claims, i.e. there is no evidence to suggest that  $\delta$  is an intrinsic material property, but this does not conclusively prove that  $\delta$  is a numerical parameter. From the available data, the author strongly suspects that  $\delta$  is not an intrinsic material property, but further work is required to conclusively prove this. It should also be noted that the above arguments are only valid for quasi-static problems and might not hold true for dynamic problems.

### 8.1.7 Critical stretch corrections

It was shown that the application of surface correction factors produces a toughening effect. The energy required to produce a fracture surface at the edge of a peridynamic body is significantly higher than the material fracture energy  $G_F$ . Consequently, a higher applied force is required to initiate and propagate a crack. This is the first time that this effect has been described. A correction scheme is proposed that is simple to implement and yields improved results. The value of critical stretch  $s_c$  is not a constant across all bonds and is dependent on the applied surface correction factor.

## 8.2 Future work

This thesis employed the bond-based theory. It was a deliberate choice not to consider the more complex state-based theory and this was justified as follows: (1) the simplest model should be examined first and only if the model is found to be deficient should the complexity be increased, and (2) the developed numerical framework serves as a good baseline form which to measure any improvements obtained from more sophisticated models. The capabilities of the presented framework have been robustly examined, and the predictive accuracy of the model is found to be equivalent to well-established methods. With further research and development, it is conceivable that the peridynamic model could become a leading method for modelling quasi-brittle materials and structures. The results presented in this thesis have helped to identify future areas of research:

- **Material heterogeneity:** Extending the model to account for spatial variability in material properties is an obvious future step. Implementation details and complexities are discussed in section 6.6.1. The discussion demonstrates that the inclusion of spatially varying material properties is not a trivial problem, and further work is required to reduce computational expense and to accurately reproduce strength distributions. Accounting for material heterogeneity is important for a number of reasons:
  - **Statistical size effect:** The model fails to accurately capture the structural strength for all unnotched specimens (see Fig. 6.3). As the structure size increases, so does the over-prediction of structural strength. To some extent, this behaviour was expected. For notched problems, statistical variability in material properties can largely be ignored, but for unnotched problems, the randomness of material properties has a significant effect on structural strength. The magnitude of the statistical size effect remains to be examined.
  - **Probability distribution of strength:** In most problems of practical interest, the mean failure load is of limited concern and a probability distribution of the load capacity is required. By running many repeated simulations that sample the probability distribution of material properties, it is possible to determine the reliability of a structure (probability of failure).
  - **Fracture behaviour:** It is hypothesised that by considering spatial variability in the material properties, the complex fracture behaviour of reinforced concrete members will be captured more accurately.
- **Constitutive model:** The results for short members suggest that there are limitations with the concrete constitutive model. Potential shortcomings of the concrete damage model include the absence of compressive softening, and difficulty capturing mode II fracture. It remains unclear to which degree the prediction error can be attributed to these factors but they are worthy of further investigation. The early compressive failure of concrete in slender beams could be linked to the identified shortcomings. It is also possible that there are unknown factors at play.
- **Steel-concrete interface model:** The assumption of perfect bond between the steel reinforcement and concrete is a likely source of error for beams that transfer load primarily through arch action. Arch action can only occur at the expense of slip and development of an interface constitutive model is needed. Factors such as bond-slip need to be considered.

- **Aggregate interlock:** Discrepancies between the experimental and numerical results can be partly accounted for by the neglect of crack friction within the numerical model. For members governed by beam shear-transfer actions the contribution of aggregate interlock is dominant, and the numerical model should be expanded to explicitly account for crack friction.
- **Influence function:** The use of a non-constant micro-modulus function might provide a number of benefits: (1) an improved representation of the physical reality of non-local forces, (2) reduced surface effects, and (3) improved numerical convergence. This work has demonstrated that using a conical influence function improves the convergence behaviour for a three-dimensional peridynamic model (see Fig. 5.15) but further examination of influence functions is required.
- **Mesh sensitivity:** The influence of an unstructured mesh discretisation requires examination. It is hypothesised that an unstructured mesh might influence the localisation behaviour and improve the predictive accuracy for unnotched problems.
- **Load path following:** Path-following techniques, such as the arc-length method [189], can be used to capture the full equilibrium path of materials that exhibit strain-softening behaviour. A displacement-controlled Newton Raphson solver has been implemented in the developed analysis code, and introducing an arc-length solver would be relatively simple due to the similarities with the Newton Raphson solver.
- **Reducing computational expense:** If peridynamic models are to become viable for simulating complex industry motivated problems, the computational cost must be further reduced. A number of strategies are available to minimise computational effort: (1) employ a multi-scale discretisation scheme and refine the mesh in areas of interest, (2) adaptively refine the mesh at crack tips, and (3) couple peridynamic and finite element meshes. All three strategies require further research, in particular, mesh sensitivity and rigorous validation studies are needed.
- **Uncertainty quantification:** Quantifying the uncertainty in model outputs is essential if peridynamics is to become a viable method for designing novel structures. Uncertainty arises from many sources, including input parameters and numerical approximation methods. The development of a probabilistic peridynamic model that can reliably account for uncertainties would be a major step towards addressing complex real world problems.

### 8.3 A comment on the importance of validation

It was established from the literature review that significant work remained to quantify the confidence and predictive accuracy of the bond-based peridynamic model. The lack of rigorous validation studies is an issue that is prevalent throughout the peridynamic literature and is also observed in the wider computational mechanics literature. Calibration and validation are often conceptually misunderstood and many papers fail to make a clear distinction between the two. It is common to see bad practices such as the adjustment of material parameters that have been determined through experimentation. This only serves to obfuscate the predictive capabilities of a model.

By following a rigorous validation process, this work has delivered new insights into the capabilities and deficiencies of the bond-based model. The reporting of poor results is vitally important, and it is out of such discrepancies that scientific knowledge is discovered. By isolating sources of error, it is possible to gain meaningful insights into the predictive capabilities of a model and to identify future areas of research. Validation is an ongoing process as complete validation over the entire domain of applicability is an impossibility.



# References

- [1] ABAQUS (2006). *ABAQUS/Explicit User's Manual, Version 6.6*. Dassault Systèmes Simulia Corp, Providence, RI, US.
- [2] ACI Committee 318 (2019). Building code requirements for structural concrete (aci 318-19): An aci standard; commentary on building code requirements for structural concrete (aci 318r-19).
- [3] Alali, B. and Lipton, R. (2012). Multiscale Dynamics of Heterogeneous Media in the Peridynamic Formulation. *Journal of Elasticity*, 106(1):71–103.
- [4] Allwood, J. M., Ashby, M. F., Gutowski, T. G., and Worrell, E. (2011). Material efficiency: A white paper. *Resources, Conservation and Recycling*, 55(3):362–381.
- [5] Alvaredo, A. M. and Torrent, R. J. (1987). The effect of the shape of the strain-softening diagram on the bearing capacity of concrete beams. *Materials and Structures*, 20(6):448–454.
- [6] Aydin, B. B., Tuncay, K., and Binici, B. (2019). Simulation of Reinforced Concrete Member Response Using Lattice Model. *Journal of Structural Engineering*, 145(9):04019091.
- [7] Ballarini, R., Diana, V., Biolzi, L., and Casolo, S. (2018). Bond-based peridynamic modelling of singular and nonsingular crack-tip fields. *Meccanica*, 53(14):3495–3515.
- [8] Barbat, G. B., Cervera, M., Chiumenti, M., and Espinoza, E. (2020). Structural size effect: Experimental, theoretical and accurate computational assessment. *Engineering Structures*, 213:110555.
- [9] Barr, B. I. G., Lee, M. M., de Place Hansen, E. J., Dupont, D., Erdem, E., Schaerlaekens, S., Schnütgen, B., Stang, H., and Vandewalle, L. (2003). Round-robin analysis of the RILEM TC 162-TDF beam-bending test: Part 2—Approximation of  $\delta$  from the CMOD response. *Materials and Structures*, 36(9):621–630.
- [10] Bažant, Z. (2001). Concrete fracture models: Testing and practice. *Engineering Fracture Mechanics*, 69(2):165–205.
- [11] Bažant, Z. and Kazemi, M. T. (1990). Size effect in fracture of ceramics and its use to determine fracture energy and effective process zone length. *Journal of the American Ceramic Society*, 73(7):1841–1853.
- [12] Bažant, Z. and Oh, B. H. (1983). Crack band theory for fracture of concrete. *Matériaux et Construction*, 16(3):155–177.

- [13] Bazant, Z. P. (2001). Probabilistic modeling of quasibrittle fracture and size effect. In *Proc., 8th Int. Conf. on Structural Safety and Reliability (ICOSSAR)*, pages 1–23. Swets and Zeitinger, Balkema.
- [14] Bažant, Z. P. and Planas, J. (1998). *Fracture and Size Effect in Concrete and Other Quasibrittle Materials*. Routledge, New York.
- [15] Bazant, Z. P., Xi, Y., and Reid, S. G. (1991). Statistical size effect in quasi-brittle structures: I. Is weibull theory applicable? *Journal of engineering Mechanics*, 117(11):2609–2622.
- [16] Bažant, Z. P. (1984). Size Effect in Blunt Fracture: Concrete, Rock, Metal. *Journal of Engineering Mechanics*, 110(4):518–535.
- [17] Bažant, Z. P. (1991). Why Continuum Damage is Nonlocal: Micromechanics Arguments. *Journal of Engineering Mechanics*, 117(5):1070–1087.
- [18] Bažant, Z. P. (1999). Size effect on structural strength: a review. *Archive of Applied Mechanics*, 69(9):703–725.
- [19] Bažant, Z. P. (2000). Size effect. *International Journal of Solids and Structures*, 37(1):69–80.
- [20] Bažant, Z. P. (2004). Probability distribution of energetic-statistical size effect in quasibrittle fracture. *Probabilistic Engineering Mechanics*, 19(4):307–319.
- [21] Bažant, Z. P. and Jirásek, M. (2002). Nonlocal Integral Formulations of Plasticity and Damage: Survey of Progress. *Journal of Engineering Mechanics*, 128(11):1119–1149.
- [22] Bažant, Z. P. and Pijaudier-Cabot, G. (1989). Measurement of Characteristic Length of Nonlocal Continuum. *Journal of Engineering Mechanics*, 115(4):755–767.
- [23] Bažant, Z. P., Tabbara, M. R., Kazemi, M. T., and Pijaudier-Cabot, G. (1990). Random Particle Model for Fracture of Aggregate or Fiber Composites. *Journal of Engineering Mechanics*, 116(8):1686–1705.
- [24] Bažant, Z. P., Vorechovský, M., and Novák, D. (2007a). Asymptotic Prediction of Energetic-Statistical Size Effect from Deterministic Finite-Element Solutions. *Journal of Engineering Mechanics*, 133(2):153–162.
- [25] Bažant, Z. P., Yu, Q., Gerstle, W., Hanson, J., and Ju, J. W. (2007b). Justification of ACI 446 Proposal for Updating ACI Code Provisions for Shear Design of Reinforced Concrete Beams. *Structural Journal*, 104(5):601–610.
- [26] Benkemoun, N., Poullain, P., Al Khazraji, H., Choinska, M., and Khelidj, A. (2016). Meso-scale investigation of failure in the tensile splitting test: Size effect and fracture energy analysis. *Engineering Fracture Mechanics*, 168:242–259.
- [27] Bentz, E. C., Vecchio, F. J., and Collins, M. R. (2006). Simplified modified compression field theory for calculating shear strength of reinforced concrete elements. *ACI Structural Journal*, 103(4):614–624.

- [28] Bessa, M. A., Foster, J. T., Belytschko, T., and Liu, W. K. (2014). A meshfree unification: reproducing kernel peridynamics. *Computational Mechanics*, 53(6):1251–1264.
- [29] Blondeel, P., Robbe, P., van hoorickx, C., Lombaert, G., and Vandewalle, S. (2018). Multilevel Monte Carlo for uncertainty quantification in structural engineering. *arXiv:1808.10680 [cs]*.
- [30] Bobaru, F., Foster, J., Geubelle, P., and Silling, S. (2017). *Handbook of Peridynamic Modeling*. Chapman and Hall/CRC, New York, 1<sup>st</sup> edition.
- [31] Bobaru, F. and Ha, Y. D. (2011). Adaptive refinement and multiscale modeling in 2d peridynamics. *Journal for Multiscale Computational Engineering*, 9(635-659).
- [32] Bobaru, F. and Hu, W. (2012). The meaning, selection, and use of the peridynamic horizon and its relation to crack branching in brittle materials. *International Journal of Fracture*, 176(2):215–222.
- [33] Bobaru, F., Yang, M., Alves, L. F., Silling, S. A., Askari, E., and Xu, J. (2009). Convergence, adaptive refinement, and scaling in 1D peridynamics. *International Journal for Numerical Methods in Engineering*, 77(6):852–877.
- [34] Bobiński, J., Tejchman, J., and Górska, J. (2009). Notched concrete beams under bending-calculations of size effects within stochastic elasto-plasticity with non-local softening. *Archives of Mechanics*, 61:1–25.
- [35] Boresi, A. P., Chong, K., and Lee, J. D. (2010). *Elasticity in engineering mechanics*. Wiley, New York, 3<sup>rd</sup> edition.
- [36] Borst, R. (1997). Some recent developments in computational modelling of concrete fracture. *International Journal of Fracture*, 86(1-2):5–36.
- [37] Borst, R., Remmers, J. J. C., Needleman, A., and Abellán, M.-A. (2004). Discrete vs smeared crack models for concrete fracture: bridging the gap. *International Journal for Numerical and Analytical Methods in Geomechanics*, 28(7-8):583–607.
- [38] Borst, R. and Rots, J. G. (1989). Occurrence of spurious mechanisms in computations of strain-softening solids. *Engineering Computations*, 6(4):272–280.
- [39] Borst, de, R. and Pamin, J. (1996). Gradient plasticity in numerical simulation of concrete cracking. *European Journal of Mechanics. A, Solids*, 15(2):295–320.
- [40] Bourdin, B., Francfort, G. A., and Marigo, J.-J. (2000). Numerical experiments in revisited brittle fracture. *Journal of the Mechanics and Physics of Solids*, 48(4):797–826.
- [41] Boys, B., Dodwell, T. J., Hobbs, M., and Girolami, M. (2021). PeriPy - A high performance OpenCL peridynamics package. *Computer Methods in Applied Mechanics and Engineering*, 386:114085.
- [42] Breitenfeld, M. S., Geubelle, P. H., Weckner, O., and Silling, S. A. (2014). Non-ordinary state-based peridynamic analysis of stationary crack problems. *Computer Methods in Applied Mechanics and Engineering*, 272:233–250.

- [43] BSI (2004). Eurocode 2: Design of concrete structures. General rules and rules for buildings. BS EN 1992-1-1:2004.
- [44] Carpinteri, A., Valente, S., Ferrara, G., and Melchiorrl, G. (1993). Is mode II fracture energy a real material property? *Computers & Structures*, 48(3):397–413.
- [45] Casolo, S. and Diana, V. (2018). Modelling laminated glass beam failure via stochastic rigid body-spring model and bond-based peridynamics. *Engineering Fracture Mechanics*, 190:331–346.
- [46] Cavagnis, F., Fernández Ruiz, M., and Muttoni, A. (2015). Shear failures in reinforced concrete members without transverse reinforcement: An analysis of the critical shear crack development on the basis of test results. *Engineering Structures*, 103:157–173.
- [47] Cavagnis, F., Ruiz, M. F., and Muttoni, A. (2018). An analysis of the shear-transfer actions in reinforced concrete members without transverse reinforcement based on refined experimental measurements. *Structural Concrete*, 19(1):49–64.
- [48] Cervera, M. and Chiumenti, M. (2009). Size effect and localization in J2 plasticity. *International Journal of Solids and Structures*, 46(17):3301–3312.
- [49] Chen, H. (2019). A comparison study on peridynamic models using irregular non-uniform spatial discretization. *Computer Methods in Applied Mechanics and Engineering*, 345:539–554.
- [50] Chen, Z., Niazi, S., and Bobaru, F. (2019a). A peridynamic model for brittle damage and fracture in porous materials. *International Journal of Rock Mechanics and Mining Sciences*, 122:104059.
- [51] Chen, Z., Woody Ju, J., Su, G., Huang, X., Li, S., and Zhai, L. (2019b). Influence of micro-modulus functions on peridynamics simulation of crack propagation and branching in brittle materials. *Engineering Fracture Mechanics*, 216:106498.
- [52] Claus, T. (2009). Non-Linear Finite Element Analysis of Shear Critical Reinforced Concrete Beams. Master's thesis, Delft University of Technology, Delft.
- [53] Colliat, J.-B., Hautefeuille, M., Ibrahimbegovic, A., and Matthies, H. G. (2007). Stochastic approach to size effect in quasi-brittle materials. *Comptes Rendus Mécanique*, 335(8):430–435.
- [54] Collins, M. P., Bentz, E. C., Quach, P. T., and Proestos, G. T. (2015). The challenge of predicting the shear strength of very thick slabs. *Concrete International*, 37(11).
- [55] Collins, M. P., Bentz, E. C., Sherwood, E. G., and Xie, L. (2008). An adequate theory for the shear strength of reinforced concrete structures. *Magazine of Concrete Research*, 60(9):635–650.
- [56] Collins, M. P., Vecchio, F. J., and Mehlhorn, G. (1985). An international competition to predict the response of reinforced concrete panels. *Canadian Journal of Civil Engineering*, 12(3).

- [57] Cornelissen, H., Hordijk, D., and Reinhardt, H. (1986). Experimental determination of crack softening characteristics of normalweight and lightweight concrete. *Heron*, 31(2):45–46.
- [58] Courant, R., Friedrichs, K., and Lewy, H. (1928). Über die partiellen Differenzengleichungen der mathematischen Physik. *Mathematische Annalen*, 100:32–74.
- [59] Cromer, A. (1981). Stable solutions using the Euler approximation. *American Journal of Physics*, 49:455–459.
- [60] CSA (2014). CSA A23.3-14 - design of concrete structures.
- [61] Cusatis, G., Mencarelli, A., Pelessone, D., and Baylot, J. (2011a). Lattice Discrete Particle Model (LDPM) for failure behavior of concrete. II: Calibration and validation. *Cement and Concrete Composites*, 33(9):891–905.
- [62] Cusatis, G., Pelessone, D., and Mencarelli, A. (2011b). Lattice Discrete Particle Model (LDPM) for failure behavior of concrete. I: Theory. *Cement and Concrete Composites*, 33(9):881–890.
- [63] Dalla Barba, F., Campagnari, P., Zaccariotto, M., Galvanetto, U., and Picano, F. (2018). A fluid-structure interaction model based on peridynamics and navier-stokes equations for hydraulic fracture problems. In *6th European Conference on Computational Mechanics (ECCM 6), 7th European Conference on Computational Fluid Dynamics (ECFD 7)*.
- [64] Das, S., Hoffarth, C., Ren, B., Spencer, B., Sant, G., Rajan, S. D., and Neithalath, N. (2019). Simulating the fracture of notched mortar beams through extended finite-element method and peridynamics. *Journal of Engineering Mechanics*, 145(7):04019049.
- [65] De Borst, R., Crisfield, M. A., Remmers, J. J. C., and Verhoosel, C. V. (2012). *Non-linear finite element analysis of solids and structures*.
- [66] Demmie, P. N. and Ostoja-Starzewski, M. (2016). Local and nonlocal material models, spatial randomness, and impact loading. *Archive of Applied Mechanics*, 86(1):39–58.
- [67] Diana, V., Labuz, J. F., and Biolzi, L. (2020). Simulating fracture in rock using a micropolar peridynamic formulation. *Engineering Fracture Mechanics*, 230:106985.
- [68] Diehl, P., Jha, P. K., Kaiser, H., Lipton, R., and Levesque, M. (2020). An asynchronous and task-based implementation of Peridynamics utilizing HPX – the C++ standard library for parallelism and concurrency. *arXiv:1806.06917 [physics]*. arXiv: 1806.06917.
- [69] Diehl, P., Prudhomme, S., and Lévesque, M. (2019). A review of benchmark experiments for the validation of peridynamics models. *Journal of Peridynamics and Nonlocal Modeling*, 1(1):14–35.
- [70] Dipasquale, D., Sarego, G., Zaccariotto, M., and Galvanetto, U. (2016). Dependence of crack paths on the orientation of regular 2D peridynamic grids. *Engineering Fracture Mechanics*, 160:248–263.
- [71] Dipasquale, D., Zaccariotto, M., and Galvanetto, U. (2014). Crack propagation with adaptive grid refinement in 2d peridynamics. *International Journal of Fracture*, 190(1-2):1–22.

- [72] Dodwell, T. J., Kynaston, S., Butler, R., Haftka, R. T., Kim, N. H., and Scheichl, R. (2021). Multilevel Monte Carlo simulations of composite structures with uncertain manufacturing defects. *Probabilistic Engineering Mechanics*, 63:103116.
- [73] Dutler, N., Nejati, M., Valley, B., Amann, F., and Molinari, G. (2018). On the link between fracture toughness, tensile strength, and fracture process zone in anisotropic rocks. *Engineering Fracture Mechanics*, 201:56–79.
- [74] Eliáš, J. and Vorechovský, M. (2020). Fracture in random quasibrittle media: I. Discrete mesoscale simulations of load capacity and fracture process zone. *Engineering Fracture Mechanics*, 235:107160.
- [75] Eliáš, J., Vorechovský, M., Skocek, J., and Bažant, Z. P. (2015). Stochastic discrete meso-scale simulations of concrete fracture: Comparison to experimental data. *Engineering Fracture Mechanics*, 135:1–16.
- [76] Emmrich, E. and Weckner, O. (2007). On the well-posedness of the linear peridynamic model and its convergence towards the Navier equation of linear elasticity. *Communications in Mathematical Sciences*, 5(4):851–864.
- [77] Fallah, A. S., Giannakeas, I. N., Mella, R., Wenman, M. R., Safa, Y., and Bahai, H. (2020). On the Computational Derivation of Bond-Based Peridynamic Stress Tensor. *Journal of Peridynamics and Nonlocal Modeling*.
- [78] Fan, H. and Li, S. (2017). Parallel peridynamics–SPH simulation of explosion induced soil fragmentation by using OpenMP. *Computational Particle Mechanics*, 4(2):199–211.
- [79] Fayyad, T. M. (2016). *Reinforced concrete fracture*. PhD thesis, University of Cambridge.
- [80] Feng, D.-C. and Wu, J.-Y. (2018). Phase-field regularized cohesive zone model (CZM) and size effect of concrete. *Engineering Fracture Mechanics*, 197:66–79.
- [81] Fenwick, R. C. and Pauley, T. (1968). Mechanism of shear resistance of concrete beams. *Journal of the Structural Division*, 94(10):2325–2350.
- [82] fib (2008). *fib Bulletin No. 45 Practitioner's guide to finite element modelling of reinforced concrete structures*. State-of-art report, Fédération Internationale du Béton (*fib*), Lausanne, Switzerland.
- [83] fib (2010). *fib Model Code for Concrete Structures 2010*. Technical Report, Fédération Internationale du Béton (*fib*), Lausanne, Switzerland.
- [84] fib (2018). *Towards a rational understanding of shear in beams and slabs*. Technical Report (*fib*) Bulletin 85, Fédération Internationale du Béton (*fib*), Lausanne, Switzerland.
- [85] Fraga Filho, C. A. D., Schuina, L. L., and Porto, B. S. (2020). An Investigation into Neighbouring Search Techniques in Meshfree Particle Methods: An Evaluation of the Neighbour Lists and the Direct Search. *Archives of Computational Methods in Engineering*, 27(4):1093–1107.

- [86] Galvanetto, U., Mudric, T., Shojaei, A., and Zaccariotto, M. (2016). An effective way to couple FEM meshes and Peridynamics grids for the solution of static equilibrium problems. *Mechanics Research Communications*, 76:41–47.
- [87] Ganzenmüller, G. C., Hiermaier, S., and May, M. (2015). On the similarity of meshless discretizations of Peridynamics and Smooth-Particle Hydrodynamics. *Computers & Structures*, 150:71–78.
- [88] García-Álvarez, V. O., Gettu, R., and Carol, I. (2012). Analysis of mixed-mode fracture in concrete using interface elements and a cohesive crack model. *Sadhana*, 37(1):187–205.
- [89] Gerstle, W., Gheitanbaf, H. H., and Asadollahi, A. (2013). Computational simulation of reinforced concrete using the micropolar peridynamic lattice model. In *Proceedings of the 8<sup>th</sup> International Conference on Fracture Mechanics of Concrete and Concrete Structures, FraMCoS-8*, pages 272–281, Barcelona, Spain.
- [90] Gerstle, W., Sakhavand, N., and Chapman, S. (2010). Peridynamic and continuum models of reinforced concrete lap splice compared. In *Proceedings of the 7<sup>th</sup> International Conference on Fracture Mechanics of Concrete and Concrete Structures, FraMCoS-7*, Jeju, South Korea.
- [91] Gerstle, W. and Sau, N. (2004). Peridynamic modeling of concrete structures. In *Proceedings of the 5<sup>th</sup> International Conference on Fracture Mechanics of Concrete Structures, FraMCoS-5*, volume 2, pages 949–956, Vail, Colorado.
- [92] Gerstle, W., Sau, N., and Aguilera, E. (2007a). Micropolar peridynamic modeling of concrete structures. In *Proceedings of the 6<sup>th</sup> International Conference on Fracture Mechanics of Concrete and Concrete Structures, FraMCoS-6*, volume 1, pages 475–481, Catania, Italy.
- [93] Gerstle, W., Sau, N., and Silling, S. (2005). Peridynamic modeling of plain and reinforced concrete structures. In *SMiRT18: 18<sup>th</sup> International Conference on Structural Mechanics in Reactor Technology*, Beijing, China. IASMiRT.
- [94] Gerstle, W., Sau, N., and Silling, S. (2007b). Peridynamic modeling of concrete structures. *Nuclear Engineering and Design*, 237(12-13):1250–1258.
- [95] Gould, H., Tobochnik, J., and Christian, W. (2007). *An introduction to computer simulation methods*. Addison-Wesley, MA, third edition edition.
- [96] Grassl, P., Grégoire, D., Solano, L. R., and Pijaudier-Cabot, G. (2012). Meso-scale modelling of the size effect on the fracture process zone of concrete. *International Journal of Solids and Structures*, 49(13):1818–1827.
- [97] Grassl, P., Xenos, D., Nyström, U., Rempling, R., and Gylltoft, K. (2013). CDPM2: A damage-plasticity approach to modelling the failure of concrete. *International Journal of Solids and Structures*, 50(24):3805–3816.
- [98] Grégoire, D., Rojas-Solano, L. B., and Pijaudier-Cabot, G. (2013). Failure and size effect for notched and unnotched concrete beams. *International Journal for Numerical and Analytical Methods in Geomechanics*, 37(10):1434–1452.

- [99] Grégoire, D., Verdon, L., Lefort, V., Grassl, P., Saliba, J., Regoin, J.-P., Loukili, A., and Pijaudier-Cabot, G. (2015). Mesoscale analysis of failure in quasi-brittle materials: comparison between lattice model and acoustic emission data. *International Journal for Numerical and Analytical Methods in Geomechanics*, 39(15):1639–1664.
- [100] Gu, X., Zhang, Q., and Xia, X. (2017). Voronoi-based peridynamics and cracking analysis with adaptive refinement. *International Journal for Numerical Methods in Engineering*, 112(13):2087–2109.
- [101] Gutiérrez, M. A. and De Borst, R. (1999). Deterministic and stochastic analysis of size effects and damage evolution in quasi-brittle materials. *Archive of Applied Mechanics*, 69(9):655–676.
- [102] Gálvez, J. C., Cervenka, J., Cendón, D. A., and Saouma, V. (2002). A discrete crack approach to normal/shear cracking of concrete. *Cement and Concrete Research*, 32(10):1567–1585.
- [103] Ha, Y. D. (2020). An extended ghost interlayer model in peridynamic theory for high-velocity impact fracture of laminated glass structures. *Computers & Mathematics with Applications*, 80(5):744–761.
- [104] Ha, Y. D. and Bobaru, F. (2010). Studies of dynamic crack propagation and crack branching with peridynamics. *International Journal of Fracture*, 162(1-2):229–244.
- [105] Ha, Y. D. and Bobaru, F. (2011). Characteristics of dynamic brittle fracture captured with peridynamics. *Engineering Fracture Mechanics*, 78(6):1156–1168.
- [106] Hadjab, H., Chabaat, M., and Thimus, J.-F. (2007). Use of Scanning Electron Microscope and the Non-local Isotropic Damage Model to Investigate Fracture Process Zone in Notched Concrete Beams. *Experimental Mechanics*, 47(4):473–484.
- [107] Hai, L. and Ren, X. (2020). Computational investigation on damage of reinforced concrete slab subjected to underwater explosion. *Ocean Engineering*, 195:106671.
- [108] Hattori, G., Hobbs, M., and Orr, J. (2021). A review on the developments of peridynamics for reinforced concrete structures. *Archives of Computational Methods in Engineering*.
- [109] Havlásek, P., Grassl, P., and Jirásek, M. (2016). Analysis of size effect on strength of quasi-brittle materials using integral-type nonlocal models. *Engineering Fracture Mechanics*, 157:72–85.
- [110] Henke, S. F. and Shanbhag, S. (2014). Mesh sensitivity in peridynamic simulations. *Computer Physics Communications*, 185(1):181–193.
- [111] Herbrand, M. (2017). *Shear Strength Models for Reinforced and Prestressed Concrete Members*. PhD, RWTH Aachen University, Aachen.
- [112] Herbrand, M., Kueres, D., Stark, A., and Classen, M. (2016). Numerische simulation von balken- und plattenförmigen bauteilen aus stahlbeton und UHPC mit einem plastischen schädigungsmodell. *Bauingenieur*, 91:46–46.

- [113] Hillerborg, A., Modéer, M., and Petersson, P. E. (1976). Analysis of crack formation and crack growth in concrete by means of fracture mechanics and finite elements. *Cement and Concrete Research*, 6(6):773–781.
- [114] Hoover, C. G., Bažant, Z. P., Vorel, J., Wendner, R., and Hubler, M. H. (2013). Comprehensive concrete fracture tests: description and results. *Engineering fracture mechanics*, 114:92–103.
- [115] Hordijk, D. A. (1991). *Local approach to fatigue of concrete*. PhD thesis, Delft University of Technology.
- [116] Hu, W., Ha, Y. D., and Bobaru, F. (2010). Numerical integration in peridynamics. Technical report, University of Nebraska-Lincoln.
- [117] Hu, Y., Chen, H., Spencer, B. W., and Madenci, E. (2018). Thermomechanical peridynamic analysis with irregular non-uniform domain discretization. *Engineering Fracture Mechanics*, 197:92–113.
- [118] Huang, D., Lu, G., and Qiao, P. (2015). An improved peridynamic approach for quasi-static elastic deformation and brittle fracture analysis. *International Journal of Mechanical Sciences*, 94-95:111–122.
- [119] Huber, P., Huber, T., and Kollegger, J. (2016). Investigation of the shear behavior of RC beams on the basis of measured crack kinematics. *Engineering Structures*, 113:41–58.
- [120] Ingraffea, A. R. and Saouma, V. (1985). Numerical modeling of discrete crack propagation in reinforced and plain concrete. In *Fracture mechanics of concrete: Structural application and numerical calculation*, Engineering Application of Fracture Mechanics, pages 171–225. Springer, Dordrecht.
- [121] Ismail, K. S. (2016). *Shear behaviour of reinforced concrete deep beams*. PhD thesis, University of Sheffield.
- [122] Javili, A., Morasata, R., Oterkus, E., and Oterkus, S. (2019). Peridynamics review. *Mathematics and Mechanics of Solids*, 24(11):3714–3739.
- [123] Jendele, L. and Červenka, J. (2006). Finite element modelling of reinforcement with bond. *Computers & Structures*, 84(28):1780–1791.
- [124] Jirásek, M. (1998). Nonlocal models for damage and fracture: Comparison of approaches. *International Journal of Solids and Structures*, 35(31):4133–4145.
- [125] Jirásek, M. (2004). Non-local damage mechanics with application to concrete. *Revue Française de Génie Civil*, 8(5-6):683–707.
- [126] Jones, B. D. and Williams, J. R. (2017). Fast computation of accurate sphere-cube intersection volume. *Engineering Computations*, 34(4):1204–1216.
- [127] Jones, L. D., Vandepitte, L. J., Haynes, T. A., and Wenman, M. R. (2020). Theory and application of Weibull distributions to 1D peridynamics for brittle solids. *Computer Methods in Applied Mechanics and Engineering*, 363:112903.

- [128] Kani, G. N. J. (1964). The riddle of shear failure and its solution. *Journal Proceedings*, 61(4):441–468.
- [129] Kani, M. W., Huggins, M. W., and Wittkopp, R. R. (1979). *Kani on shear in reinforced concrete*. University of Toronto, Dept. of Civil Engineering, Toronto.
- [130] Kilic, B. (2008). *Peridynamic Theory for Progressive Failure Prediction in Homogeneous and Heterogeneous Materials*. PhD, University of Arizona.
- [131] Kilic, B. and Madenci, E. (2010). An adaptive dynamic relaxation method for quasi-static simulations using the peridynamic theory. *Theoretical and Applied Fracture Mechanics*, 53(3):194–204.
- [132] Kotsovos, M. D. (1983). Mechanisms of ‘shear’ failure. *Magazine of Concrete Research*, 35(123):99–106.
- [133] Le, Q. V. and Bobaru, F. (2018). Surface corrections for peridynamic models in elasticity and fracture. *Computational Mechanics*, 61(4):499–518.
- [134] Lee, J., Oh, S. E., and Hong, J.-W. (2017). Parallel programming of a peridynamics code coupled with finite element method. *International Journal of Fracture*, 203(1):99–114.
- [135] Leonhardt, F. and Walther, R. (1964). *The Stuttgart Shear Tests, 1961: Contributions to the treatment of the problems of shear in reinforced concrete construction. A translation of articles that appeared in "Beton- und Stahlbetonbau". Vol. 56, No. 12, 1961, and V.57, No. 2, 3, 6, 7, and 8, 1962*. Cement and Concrete Association, London.
- [136] Li, S., Jin, Y., Huang, X., and Zhai, L. (2020). An extended bond-based peridynamic approach for analysis on fracture in brittle materials. *Mathematical Problems in Engineering*, 2020(9568015).
- [137] Li, W. and Guo, L. (2018). Meso-fracture simulation of cracking process in concrete incorporating three-phase characteristics by peridynamic method. *Construction and Building Materials*, 161:665–675.
- [138] Li, W. and Guo, L. (2019). Dual-horizon peridynamics analysis of debonding failure in FRP-to-concrete bonded joints. *International Journal of Concrete Structures and Materials*, 13(1):26.
- [139] Littlewood, D. (2015). Roadmap for Peridynamic Software Implementation. Technical Report SAND2015-9013, Sandia National Laboratories, Albuquerque, NM and Livermore, CA.
- [140] Liu, G.-R. and Liu, M. B. (2003). *Smoothed particle hydrodynamics: a meshfree particle method*. World scientific, Singapore.
- [141] Liu, W. and Hong, J.-W. (2012). A coupling approach of discretized peridynamics with finite element method. *Computer Methods in Applied Mechanics and Engineering*, 245-246:163–175.

- [142] Lu, J., Zhang, Y., Muhammad, H., and Chen, Z. (2018). Peridynamic model for the numerical simulation of anchor bolt pullout in concrete. *Mathematical Problems in Engineering*.
- [143] Macek, R. W. and Silling, S. A. (2007). Peridynamics via finite element analysis. *Finite Elements in Analysis and Design*, 43(15):1169–1178.
- [144] Madenci, E., Dorduncu, M., Barut, A., and Phan, N. (2018). Weak form of peridynamics for nonlocal essential and natural boundary conditions. *Computer Methods in Applied Mechanics and Engineering*, 337:598–631.
- [145] Madenci, E. and Oterkus, E. (2014a). Coupling of the Peridynamic Theory and Finite Element Method. In *Peridynamic Theory and Its Applications*, pages 191–202. Springer, New York, NY.
- [146] Madenci, E. and Oterkus, E. (2014b). *Peridynamic Theory and Its Applications*. Springer, New York.
- [147] Malm, R. (2006). *Shear cracks in concrete structures subjected to in-plane stresses*. Doctoral Thesis, KTH Royal Institute of Technology, Stockholm.
- [148] Marti, P. (1985a). Basic Tools of Reinforced Concrete Beam Design. *Journal Proceedings*, 82(1):46–56.
- [149] Marti, P. (1985b). Truss Models in Detailing. *Concrete International*, 7(12):66–73.
- [150] Mauludin, L. M. and Oucif, C. (2020). Computational modeling of fracture in concrete: A review. *Frontiers of Structural and Civil Engineering*, 14(3):586–598.
- [151] Mehrmashhadi, J., Chen, Z., Zhao, J., and Bobaru, F. (2019). A stochastically homogenized peridynamic model for intraply fracture in fiber-reinforced composites. *Composites Science and Technology*, 182:107770.
- [152] Mendonça, T. S., Peixoto, R. G., and Ribeiro, G. O. (2018). Crack propagation using the continuum strong discontinuity approach by the BEM: some numerical remarks. *Journal of the Brazilian Society of Mechanical Sciences and Engineering*, 40(11):520.
- [153] Miehe, C., Hofacker, M., and Welschinger, F. (2010). A phase field model for rate-independent crack propagation: Robust algorithmic implementation based on operator splits. *Computer Methods in Applied Mechanics and Engineering*, 199(45):2765–2778.
- [154] Mier, J. G. M. v. (1996). *Fracture Processes of Concrete*. CRC Press.
- [155] Moallemi, S., Pietruszczak, S., and Mróz, Z. (2017). Deterministic size effect in concrete structures with account for chemo-mechanical loading. *Computers & Structures*, 182:74–86.
- [156] Moës, N., Dolbow, J., and Belytschko, T. (1999). A finite element method for crack growth without remeshing. *International Journal for Numerical Methods in Engineering*, 46(1):131–150.

- [157] Molinari, J. F., Gazonas, G., Raghupathy, R., Rusinek, A., and Zhou, F. (2007). The cohesive element approach to dynamic fragmentation: the question of energy convergence. *International Journal for Numerical Methods in Engineering*, 69(3):484–503.
- [158] Mossaiby, F., Shojaei, A., Zaccariotto, M., and Galvanetto, U. (2017). OpenCL implementation of a high performance 3D Peridynamic model on graphics accelerators. *Computers & Mathematics with Applications*, 74(8):1856–1870.
- [159] Most, T. (2005). *Stochastic crack growth simulation in reinforced concrete structures by means of coupled finite element and meshless methods*. Doctoral Thesis, Bauhaus-Universität Weimar, Weimar.
- [160] Muttoni, A. and Fernández Ruiz, M. (2008). Shear strength of members without transverse reinforcement as function of critical shear crack width. *ACI Structural Journal*, 105(2):163.
- [161] Muttoni, A. and Ruiz, M. F. (2019). From experimental evidence to mechanical modeling and design expressions: The Critical Shear Crack Theory for shear design. *Structural Concrete*, 20(4):1464–1480.
- [162] Needleman, A. (1988). Material rate dependence and mesh sensitivity in localization problems. *Computer Methods in Applied Mechanics and Engineering*, 67(1):69–85.
- [163] Neville, A. M. (2011). *Properties of concrete*. Pearson Education Limited, London, 5<sup>th</sup> edition edition.
- [164] Ngo, D. and Scordelis, A. C. (1967). Finite Element Analysis of Reinforced Concrete Beams. *Journal Proceedings*, 64(3):152–163.
- [165] Nguyen, G. D., Nguyen, C. T., Nguyen, V. P., Bui, H. H., and Shen, L. (2016). A size-dependent constitutive modelling framework for localised failure analysis. *Computational Mechanics*, 58(2):257–280.
- [166] Ni, T., Zaccariotto, M., Zhu, Q.-Z., and Galvanetto, U. (2019). Static solution of crack propagation problems in Peridynamics. *Computer Methods in Applied Mechanics and Engineering*, 346:126–151.
- [167] O’Brien, E. J. and Dixon, A. S. (1995). *Reinforced and Prestressed Concrete Design: The Complete Process*. Longman Scientific & Technical, Harlow.
- [168] Oliver, J. (1996a). Modelling Strong Discontinuities in Solid Mechanics Via Strain Softening Constitutive Equations. Part 1: Fundamentals. *International Journal for Numerical Methods in Engineering*, 39(21):3575–3600.
- [169] Oliver, J. (1996b). Modelling Strong Discontinuities in Solid Mechanics Via Strain Softening Constitutive Equations. Part 2: Numerical Simulation. *International Journal for Numerical Methods in Engineering*, 39(21):3601–3623.
- [170] Orr, J., Bras, A., and Ibello, T. (2017). Effectiveness of design codes for life cycle energy optimisation. *Energy and Buildings*, 140:61–67.

- [171] Orr, J., Darby, A., Ibello, T., Evernden, M., and Otlet, M. (2011). Concrete structures using fabric formwork. *The Structural Engineer*, 89:20–26.
- [172] Orr, J., Ibello, T. J., Darby, A. P., and Evernden, M. (2014). Shear behaviour of non-prismatic steel reinforced concrete beams. *Engineering Structures*, 71:48–59.
- [173] Oterkus, E. (2010). *Peridynamic Theory for Modeling Three-Dimensional Damage Growth in Metallic and Composite Structures*. PhD, University of Arizona.
- [174] Oterkus, S. and Madenci, E. (2017). Peridynamic modeling of fuel pellet cracking. *Engineering Fracture Mechanics*, 176:23–37.
- [175] Otsuka, K. and Date, H. (2000). Fracture process zone in concrete tension specimen. *Engineering Fracture Mechanics*, 65(2):111–131.
- [176] Parks, M., Lehoucq, R. B., Plimpton, S. J., and Silling, S. A. (2008). Implementing peridynamics within a molecular dynamics code. *Computer Physics Communications*, 179(11):777–783.
- [177] Parks, M., Littlewood, D., Mitchell, J. A., and Silling, S. (2012). Peridigm Users' Guide. Technical Report SAND2012-7800, Albuquerque, New Mexico.
- [178] Peerlings, R. H. J., Borst, R. D., Brekelmans, W. a. M., and Vree, J. H. P. D. (1996). Gradient Enhanced Damage for Quasi-Brittle Materials. *International Journal for Numerical Methods in Engineering*, 39(19):3391–3403.
- [179] Petersson, P. E. (1981). *Crack growth and development of fracture zones in plain concrete and similar materials*. PhD thesis, University of Lund.
- [180] Pijaudier-Cabot, G. and Bažant, Z. P. (1987). Nonlocal Damage Theory. *Journal of Engineering Mechanics*, 113(10):1512–1533.
- [181] Prakash, N. and Stewart, R. J. (2020). A Multi-threaded Method to Assemble a Sparse Stiffness Matrix for Quasi-static Solutions of Linearized Bond-Based Peridynamics. *Journal of Peridynamics and Nonlocal Modeling*.
- [182] Rabczuk, T. (2013). Computational Methods for Fracture in Brittle and Quasi-Brittle Solids: State-of-the-Art Review and Future Perspectives.
- [183] Rabczuk, T. and Ren, H. (2017). A peridynamics formulation for quasi-static fracture and contact in rock. *Engineering Geology*, 225:42–48.
- [184] Rashid, Y. R. (1968). Ultimate strength analysis of prestressed concrete pressure vessels. *Nuclear Engineering and Design*, 7(4):334–344.
- [185] Reinhardt, H. W., Cornelissen, H. A. W., and Hordijk, D. A. (1986). Tensile tests and failure analysis of concrete. *Journal of Structural Engineering*, 112(11):2462–2477.
- [186] Ren, H., Zhuang, X., Cai, Y., and Rabczuk, T. (2016a). Dual-horizon peridynamics. *International Journal for Numerical Methods in Engineering*, 108(12):1451–1476.

- [187] Ren, H., Zhuang, X., and Rabczuk, T. (2016b). A new peridynamic formulation with shear deformation for elastic solid. *Journal of Micromechanics and Molecular Physics*, 01(02):1650009.
- [188] Ren, H., Zhuang, X., and Rabczuk, T. (2017). Dual-horizon peridynamics: A stable solution to varying horizons. *Computer Methods in Applied Mechanics and Engineering*, 318:762–782.
- [189] Riks, E. (1972). The application of Newton's Method to the problem of elastic stability. *Journal of Applied Mechanics*, 39(4):1060–1065.
- [190] Rodrigues, E. A., Manzoli, O. L., and Bitencourt, L. A. G. (2020). 3D concurrent multiscale model for crack propagation in concrete. *Computer Methods in Applied Mechanics and Engineering*, 361:112813.
- [191] Rodrigues, E. A., Manzoli, O. L., Bitencourt Jr., L. A. G., and Bittencourt, T. N. (2016). 2D mesoscale model for concrete based on the use of interface element with a high aspect ratio. *International Journal of Solids and Structures*, 94-95:112–124.
- [192] Rombach, G. and Nghiep, V. H. (2011). Versuche zur querkrafttragfähigkeit von gevouteten stahlbetonbalken ohne querkraftbewehrung. *Beton- und Stahlbetonbau*, 106(1):11–20.
- [193] Rombach, G. A., Kohl, M., and Nghiep, V. H. (2011). Shear design of concrete members without shear reinforcement - a solved problem? *Procedia Engineering*, 14:134–140.
- [194] Rossi Cabral, N., Invaldi, M. A., Barrios D'Ambra, R., and Iturrioz, I. (2019). An alternative bilinear peridynamic model to simulate the damage process in quasi-brittle materials. *Engineering Fracture Mechanics*, 216:106494.
- [195] Rots, J. G. (1988). *Computational modeling of concrete fracture*. Doctoral Thesis, Delft University of Technology, Delft.
- [196] Rots, J. G. and Blaauwendraad, J. (1989). Crack Models for Concrete, Discrete or Smeared? Fixed, Multi-Directional or Rotating? *HERON*, 34 (1), 1989.
- [197] Sarego, G. (2016). *Structural material damage: novel methods of analysis*. PhD, University of Padua, Padua.
- [198] Sau, N., Medina-Mendoza, J., and Borbon-Almada, A. C. (2019). Peridynamic modelling of reinforced concrete structures. *Engineering Failure Analysis*, 103:266–274.
- [199] Schlangen, E. and van Mier, J. G. M. (1992). Simple lattice model for numerical simulation of fracture of concrete materials and structures. *Materials and Structures*, 25(9):534–542.
- [200] Seleson, P. (2014). Improved one-point quadrature algorithms for two-dimensional peridynamic models based on analytical calculations. *Computer Methods in Applied Mechanics and Engineering*, 282:184–217.

- [201] Seleson, P. and Littlewood, D. J. (2016). Convergence studies in meshfree peridynamic simulations. *Computers & Mathematics with Applications*, 71(11):2432–2448.
- [202] Seleson, P., Parks, M., et al. (2011). On the role of the influence function in the peridynamic theory. *International Journal of Multiscale Computational Engineering*, 9(6):689–706.
- [203] Silling, S. A. (2000). Reformulation of elasticity theory for discontinuities and long-range forces. *Journal of the Mechanics and Physics of Solids*, 48(1):175–209.
- [204] Silling, S. A. (2003). Dynamic fracture modeling with a meshfree peridynamic code. In Bathe, K. J., editor, *Proceedings Second MIT Conference on Computational Fluid and Solid Mechanics*, pages 641–644. Elsevier.
- [205] Silling, S. A. (2014). Origin and effect of nonlocality in a composite. *Journal of Mechanics of Materials and Structures*, 9(2):245–258.
- [206] Silling, S. A. (2017). Stability of peridynamic correspondence material models and their particle discretizations. *Computer Methods in Applied Mechanics and Engineering*, 322:42–57.
- [207] Silling, S. A. and Askari, E. (2005). A meshfree method based on the peridynamic model of solid mechanics. *Computers & Structures*, 83(17):1526–1535.
- [208] Silling, S. A., Epton, M., Weckner, O., Xu, J., and Askari, E. (2007). Peridynamic states and constitutive modeling. *Journal of Elasticity*, 88(2):151–184.
- [209] Silling, S. A. and Lehoucq, R. B. (2008). Convergence of Peridynamics to Classical Elasticity Theory. *Journal of Elasticity*, 93(1):13.
- [210] Silling, S. A. and Lehoucq, R. B. (2010). Peridynamic Theory of Solid Mechanics. In Aref, H. and Giessen, E. v. d., editors, *Advances in Applied Mechanics*, volume 44 of *Advances in Applied Mechanics*, pages 73–168. Elsevier.
- [211] Slobbe, A. T. (2015). *Propagation and band width of smeared cracks*. PhD thesis, Delft University of Technology.
- [212] Sluys, L. J. (1992). *Wave propagation, localisation and dispersion in softening solids*. PhD thesis, Delft University of Technology.
- [213] Sun, W., Fish, J., and Zhang, G. (2020). Superposition of non-ordinary state-based peridynamics and finite element method for material failure simulations. *Meccanica*, 55(4):681–699.
- [214] Swamy, R., Andriopoulos, A., and Adepegba, D. (1970). Arch action and bond in concrete shear failures. *Journal of the Structural Division*, 96(ST6).
- [215] Swope, W. C., Andersen, H. C., Berens, P. H., and Wilson, K. R. (1982). A computer simulation method for the calculation of equilibrium constants for the formation of physical clusters of molecules: Application to small water clusters. *The Journal of Chemical Physics*, 76(1):637–649.

- [216] Syroka-Korol, E., Tejchman, J., and Mróz, Z. (2013). FE calculations of a deterministic and statistical size effect in concrete under bending within stochastic elasto-plasticity and non-local softening. *Engineering Structures*, 48:205–219.
- [217] Syroka-Korol, E., Tejchman, J., and Mróz, Z. (2015). FE investigations of the effect of fluctuating local tensile strength on coupled energetic–statistical size effect in concrete beams. *Engineering Structures*, 103:239–259.
- [218] Thacker, B. H., Doebling, S. W., Hemez, F. M., Anderson, M. C., Pepin, J. E., and Rodriguez, E. A. (2004). Concepts of model verification and validation. Technical Report LA-14167, Los Alamos.
- [219] Tong, Y., Shen, W., Shao, J., and Chen, J. (2020a). A new bond model in peridynamics theory for progressive failure in cohesive brittle materials. *Engineering Fracture Mechanics*, 223:106767.
- [220] Tong, Y., Shen, W.-Q., and Shao, J.-F. (2020b). An adaptive coupling method of state-based peridynamics theory and finite element method for modeling progressive failure process in cohesive materials. *Computer Methods in Applied Mechanics and Engineering*, 370:113248.
- [221] Vazic, B., Diyaroglu, C., Oterkus, E., and Oterkus, S. (2020). Family Member Search Algorithms for Peridynamic Analysis. *Journal of Peridynamics and Nonlocal Modeling*, 2(1):59–84.
- [222] Červenka, J. and Papanikolaou, V. K. (2008). Three dimensional combined fracture–plastic material model for concrete. *International Journal of Plasticity*, 24(12):2192–2220.
- [223] Červenka, J., Červenka, V., and Laserna, S. (2018a). On crack band model in finite element analysis of concrete fracture in engineering practice. *Engineering Fracture Mechanics*, 197:27–47.
- [224] Červenka, V., Červenka, J., and Kadlec, L. (2018b). Model uncertainties in numerical simulations of reinforced concrete structures. *Structural Concrete*, 19(6):2004–2016.
- [225] Červenka, V., Červenka, J., Pukl, R., and Sajdlova, T. (2016). Prediction of shear failure of large beam based on fracture mechanics. In *Computational Modeling*, Berkeley, California. 9<sup>th</sup> International Conference on Fracture Mechanics of Concrete and Concrete Structures, FraMCoS-9.
- [226] Vecchio, F. J. and Collins, M. P. (1986). The Modified Compression-Field Theory for Reinforced Concrete Elements Subjected to Shear. *Journal Proceedings*, 83(2):219–231.
- [227] Vorechovský, M. (2007). Interplay of size effects in concrete specimens under tension studied via computational stochastic fracture mechanics. *International Journal of Solids and Structures*, 44(9):2715–2731.
- [228] Vorel, J., Marcon, M., Cusatis, G., Caner, F., Di Luzio, G., and Wan-Wendner, R. (2021). A comparison of the state of the art models for constitutive modelling of concrete. *Computers & Structures*, 244:106426.

- [229] Whitney, C. S. (1937). Design Of Reinforced Concrete Members Under Flexure Or Combined Flexure And Direct Compression. *Journal Proceedings*, 33(3):483–498.
- [230] Wu, P., Zhao, J., Chen, Z., and Bobaru, F. (2020). Validation of a stochastically homogenized peridynamic model for quasi-static fracture in concrete. *Engineering Fracture Mechanics*, 237:107293.
- [231] Wu, Y.-F. (2016). Theorems for Flexural Design of RC Members. *Journal of Structural Engineering*, 142(5):04015172.
- [232] Xenos, D. and Grassl, P. (2016). Modelling the failure of reinforced concrete with nonlocal and crack band approaches using the damage-plasticity model CDPM2. *Finite Elements in Analysis and Design*, 117-118:11–20.
- [233] Xie, D. and Waas, A. M. (2006). Discrete cohesive zone model for mixed-mode fracture using finite element analysis. *Engineering Fracture Mechanics*, 73(13):1783–1796.
- [234] Xu, C., Yuan, Y., Zhang, Y., and Xue, Y. (2021). Peridynamic modeling of pre-fabricated beams post-cast with steelfiber reinforced high-strength concrete. *Structural Concrete*, 22(1):445–456.
- [235] Yaghoobi, A. and Chorzepa, M. (2015). Meshless modeling framework for fiber reinforced concrete structures. *Computers & Structures*, 161:43–54.
- [236] Yang, D., Dong, W., Liu, X., Yi, S., and He, X. (2018). Investigation on mode-I crack propagation in concrete using bond-based peridynamics with a new damage model. *Engineering Fracture Mechanics*, 199:567–581.
- [237] Yang, D., He, X., Yi, S., and Liu, X. (2019). An improved ordinary state-based peridynamic model for cohesive crack growth in quasi-brittle materials. *International Journal of Mechanical Sciences*, 153-154:402–415.
- [238] Yang, Z. and Frank Xu, X. (2008). A heterogeneous cohesive model for quasi-brittle materials considering spatially varying random fracture properties. *Computer Methods in Applied Mechanics and Engineering*, 197(45):4027–4039.
- [239] Yu, H., Chen, X., and Sun, Y. (2020). A generalized bond-based peridynamic model for quasi-brittle materials enriched with bond tension–rotation–shear coupling effects. *Computer Methods in Applied Mechanics and Engineering*, 372:113405.
- [240] Yu, H. and Li, S. (2020). On energy release rates in Peridynamics. *Journal of the Mechanics and Physics of Solids*, 142:104024.
- [241] Yu, K. (2011). *Enhanced integration methods for the peridynamic theory*. PhD thesis, Kansas State University, Kansas.
- [242] Yu, K., Xin, X. J., and Lease, K. B. (2011). A new adaptive integration method for the peridynamic theory. *Modelling and Simulation in Materials Science and Engineering*, 19(4):045003.

- [243] Zaccariotto, M., Luongo, F., Sarego, G., and Galvanetto, U. (2015). Examples of applications of the peridynamic theory to the solution of static equilibrium problems. *The Aeronautical Journal*, 119(1216):677–700.
- [244] Zhao, J., Chen, Z., Mehrmashhadi, J., and Bobaru, F. (2020). A stochastic multiscale peridynamic model for corrosion-induced fracture in reinforced concrete. *Engineering Fracture Mechanics*, 229:106969.
- [245] Zhao, L.-Y., Shao, J.-F., and Zhu, Q.-Z. (2018). Analysis of localized cracking in quasi-brittle materials with a micro-mechanics based friction-damage approach. *Journal of the Mechanics and Physics of Solids*, 119:163–187.
- [246] Zhou, R. and Chen, H.-M. (2019). Mesoscopic investigation of size effect in notched concrete beams: The role of fracture process zone. *Engineering Fracture Mechanics*, 212:136–152.
- [247] Zhou, X.-P. and Wang, Y.-T. (2021). State-of-the-Art Review on the Progressive Failure Characteristics of Geomaterials in Peridynamic Theory. *Journal of Engineering Mechanics*, 147(1):03120001.
- [248] Zimmermann, M. (2005). *A continuum theory with long-range forces for solids*. PhD thesis, Massachusetts Institute of Technology.
- [249] Zubelewicz, A. and Bażant, Z. P. (1987). Interface Element Modeling of Fracture in Aggregate Composites. *Journal of Engineering Mechanics*, 113(11):1619–1630.

# Appendix A

## Code performance

The performance of the developed code is dependent on the hardware, compiler, number of threads, and the problem size (Table A.1 details the number of nodes and bonds for every problem presented in this thesis). Approximate run times for three problems are detailed below. The code was compiled using gcc-6.3.0 for Linux and the MATLAB version used was R2018b. The computations were performed using a single Skylake node with 32 OMP threads with the Cambridge Service for Data Driven Discovery (CSD3) Peta4 platform operated by the University of Cambridge Research Computing Service.

- For a problem with 1,000 nodes, the approximate run time for 5,000 time steps is 25 seconds.
- For a problem with 100,000 nodes, the approximate run time for 5,000 time steps is 160 seconds.
- For a problem with 1,000,000 nodes, the approximate run time for 5,000 time steps is 1400 seconds.

The length of a simulation (the number of time steps) is determined by the loading rate required to ensure quasi-static conditions. The simulation length varied from 50,000 to 300,000 time steps depending on the problem. For more details on code performance and memory constraints, the reader is referred to the work of Boys et al. [41].

Table A.1 Input file data

	Mesh resolution	Nodes <sup>1</sup>	Bonds <sup>2</sup>
<b>Grégoire et al. [98]</b>			
Beam 1 UN <sup>3</sup>	5 mm	224,000	11,871,304
Beam 1 FN	5 mm	224,000	11,855,208
Beam 1 HN	5 mm	224,000	11,830,152
Beam 2 UN	5 mm	56,000	2,911,984
Beam 2 FN	5 mm	56,000	2,904,240
Beam 2 HN	5 mm	56,000	2,891,712
Beam 3 UN	5 mm	14,000	700,324
Beam 3 FN	5 mm	14,000	696,756
Beam 3 HN	5 mm	14,000	690,492
Beam 4 UN	5 mm	3,500	161,494
Beam 4 FN	5 mm	3,500	160,014
Beam 4 HN	5 mm	3,500	156,882
Beam 4 UN	2.5 mm	28,000	1,492,064
Beam 4 FN	2.5 mm	28,000	1,487,860
Beam 4 HN	2.5 mm	28,000	1,479,904
Beam 4 UN	1.25 mm	224,000	12,784,204
Beam 4 FN	1.25 mm	224,000	12,764,656
Beam 4 HN	1.25 mm	224,000	12,731,944
<b>García-Álvarez et al. [88]</b>			
$d = 80 \text{ mm } \mu = 0.0d$	5 mm	8,000	387,780
$d = 80 \text{ mm } \mu = 0.3125d$	5 mm	8,000	389,364
$d = 80 \text{ mm } \mu = 0.3125d$	1.25 mm	512,000	29,577,864
$d = 80 \text{ mm } \mu = 0.625d$	5 mm	8,000	389,364
$d = 80 \text{ mm } \mu = 0.625d$	1.25 mm	512,000	29,577,864
$d = 160 \text{ mm } \mu = 0.0d$	5 mm	32,000	1,638,288

---

$d = 160 \text{ mm } \mu = 0.3125d$	5 mm	32,000	1,638,288
$d = 160 \text{ mm } \mu = 0.625d$	5 mm	32,000	1,638,288
$d = 320 \text{ mm } \mu = 0.0d$	5 mm	128,000	6,731,304
$d = 320 \text{ mm } \mu = 0.3125d$	5 mm	128,000	6,737,816
$d = 320 \text{ mm } \mu = 0.625d$	5 mm	128,000	6,737,816

---

**Stuttgart shear tests**

Beam 1	11.5 mm	37,332	2,002,474
Beam 2	11.5 mm	47,804	2,573,594
Beam 3	11.5 mm	60,180	3,248,554
Beam 3	7.67 mm	198,750	11,175,940
Beam 4	11.5 mm	70,652	3,819,674
Beam 5	11.5 mm	83,232	4,504,138
Beam 5	7.67 mm	267,000	15,039,150
Beam 6	11.5 mm	105,876	5,740,714
Beam 7	11.5 mm	128,724	6,986,794
Beam 7	7.67 mm	424,000	23,954,250
Beam 8	11.5 mm	149,192	8,103,074
Beam 10	11.5 mm	194,888	10,595,234

---

<sup>1</sup> Number of nodes<sup>2</sup> Number of bonds<sup>3</sup> UN - unnotched, FN - fifth-notched, HN - half-notched